MECHANICS AND APPLICATIONS OF PRESSURE ADAPTIVE HONEYCOMB

by

Submitted to the graduate degree program in Aerospace Engineering
and the Graduate Faculty of the University of Kansas
in partial fulfillment of the requirements for the degree of
Doctor of Philosophy.

Committee:

_____

Dr. Ron M. Barrett (chairperson)

_____

Dr. Jan Roskam

_____

Dr. Mark S. Ewing

_____

Dr. Richard D. Hale

_____

Dr. Albert Romkes

Date Defended:_____

ABSTRACT

A novel adaptive aerostructure is presented that relies on certified aerospace materials and can therefore be applied in conventional passenger aircraft. This structure consists of a honeycomb material which' cells extend over a significant length perpendicular to the plane of the cells. Each of the cells contains an inelastic pouch (or bladder) that forms a circular tube when the cell forms a perfect hexagon. By changing the cell differential pressure (CDP) the stiffness of the honeycomb can be altered. Using an external force or the elastic force within the honeycomb material, the honeycomb can be deformed such that the cells deviate from their perfect-hexagonal shape. It can be shown that by increasing the CDP, the structure eventually returns to a perfect hexagon. By doing so, a fully embedded pneumatic actuator is created that can perform work and substitute conventional low-bandwidth flight control actuators. It is shown that two approaches can be taken to regulate the stiffness of this embedded actuator:

- The first approach relies on the pouches having a fixed amount of air in them and stiffness is altered by a change in ambient pressure. Coupled to the ambient pressure-altitude cycle that aircraft encounter during each flight, this approach yields a true adaptive aerostructure that operates independently of pilot input and is controlled solely by the altitude the aircraft is flying at.

- The second approach relies on a controlled constant CDP. This CDP could be supplied from one of the compressor stages of the engine as a form of bleed air. Because of the air-tight pouches there would essentially be no mass flow, meaning engine efficiency would not be significantly affected due to this application. By means of a valve system the pilot could have direct control over the pressure and, consequently, the stiffness of the structure. This allows for much higher CDPs (on the order of 1MPa) than could physically be achieved by relying on the ambient pressure decrease with altitude. This option does require more infrastructure like tubing, valves, and supporting electronics from the cockpit.

Applications of pressure adaptive honeycomb are tailored primarily towards low-bandwidth applications like secondary flight control. The most profound application is the morphing of an entire wing section, from leading to trailing edge, due to the adaptive honeycomb. On a smaller scale, other examples include a solid state pressure adaptive flap, a pressure adaptive

droop nose, a pressure adaptive Gurney flap and a pressure adaptive engine inlet. Each of these applications is based on the same principle of stiffness alteration with pressure and can be used with either actuation option (constant mass or constant pressure).

A model that relates the volumetric change of the honeycomb cells to the external blocked stress was shown to correlate well to experiments that were carried out on several test articles. Based on this model it was estimated that pressure adaptive honeycomb has a maximum mass-specific energy density of 12.4J/g, for the case of an externally applied CDP of 0.9MPa (can be supplied from a high-pressure compressor stage of a gas turbine). In addition, it was shown that a maximum strain of 76% can be achieved and that the maximum blocked stress amounts to 0.82MPa. In the case of a 40kPa drop in atmospheric pressure and constant mass of air in the pouches, the maximum mass specific energy amounts to 1.1J/g and a maximum blocked force of 70kPa can be attained.

Pressure adaptive honeycomb was embedded into a 25%c adaptive flap on a NACA2412 wing section with a chord of 1.08m. Wind tunnel tests at Reynolds number of 1 million demonstrated a shift in the $c_l - \alpha$ curve upwards by an average of 0.3, thereby increasing the maximum lift coefficient from 1.27 to 1.52. This successfully demonstrated the application of pressure adaptive honeycomb embedded in a morphing aircraft structure.

ACKNOWLEGDEMENTS

TABLE OF CONTENTS

TABLE OF CONTENTS (cont.)

TABLE OF CONTENTS (cont.)

TABLE OF CONTENTS (cont.)

LIST OF SYMBOLS

Symbol	Description	Units
A	Aspect ratio	~
$\boldsymbol{A}$	Surface area vector	m
b	Span	m
$\boldsymbol{B}$	Surface area vector	m
c	Chord	m
c_d	Section drag coefficient	~
c_l	Section lift coefficient	~
c_m	Section moment coefficient	~
c_p	Pressure coefficient	~
c_v	specific heat constant at constant volume	J/K
C	Constant	~
C_D	Dissipation or Drag coefficient	~
C_f	Friction coefficient	~
C_L	Wing or vehicle lift coefficient	~
C_τ	Shear stress coefficient	~
D	Drag	N
e	Internal energy	J
E	Young's modulus or energy	N/m^2, J
$\boldsymbol{E}$	Fourth order stiffness tensor	N/m^2
$\widehat{\boldsymbol{E}}$	Linearized stiffness vector	N/m^2
$\boldsymbol{f}$	Body force vector field	N/m^3
F	Force	N
g	Volume ratio	~
G	Shear stiffness modulus	N/m^2
h	Geometric altitude or enthalpy	m, J
k	Spring stiffness	N/m
l	Honeycomb face length or arc length	m
L	Lift	N
m	Mass	kg

LIST OF SYMBOLS (cont.)

Symbol	Description	Units
M	Moment or Mach number	Nm, ~
n	Displacement of grid node perpendicular to streamline	m
$\tilde{n}$	Amplification factor	~
$\boldsymbol{n}$	Unit normal vector	~
$\boldsymbol{N}$	Average normal-to-streamline surface area vector	m
p	Pressure	N/m^2
Pr	Prandtl number	~
R	Gas constant for air	J/kg/K
Re	Reynolds number	~
s	Displacement	m
S	Surface area	m^2
$\boldsymbol{S}$	Average streamwise surface area vector	m
t	Thickness	m
$\boldsymbol{t}$	Distributed traction field vector	N/m^2
T	Temperature	℃
u	Velocity component	m/s
$\boldsymbol{u}$	Displacement field vector	m
v	Velocity component	m/s
V	Velocity or volume	$m/s, m^3$
W	Work or weight	J, kg

Greek Symbols

Symbol	Description	Units
α	Angle of Attack	deg
γ	Ratio of specific heats or shear strain	~, ~
δ	Elevator deflection	deg
δ^*	Displacement thickness	m
δ^{**}	Density thickness	m
ε	Strain	~
ζ	Pouch-to-honeycomb volume ratio	~
θ	Honeycomb angle or momentum thickness	deg, m

LIST OF SYMBOLS (cont.)

Symbol	Description	Units
θ^*	Kinetic energy thickness	m
Λ	Sweep or body shape factor	deg, ~
μ	Viscosity	Pa·s
ρ	Density	kg/m^3
σ	Standard deviation or normal stress	~, Pa
τ	Shear stress	N/m^2
υ	Poisson's Ratio	~
ξ	Tested-to-modeled volume ratio	~
Π	Streamline nodal pressure	Pa
φ	Latitude or force angle	deg
ϕ	Structural rotation	deg
ψ	Base function	~

Subscripts and Superscripts

0	Zero altitude, zero lift, or stagnation
a	Ambient
apr	Approach
cr	Cruise
e	Boundary layer edge
f	Flap
ea	Engagement altitude
eq	equivalent
ex	External
gp	Geopotential
h	Horizontal stabilizer
i	Initial
lat	Lateral
lin	Linear
lon	Longitudinal
m	Constant mass

LIST OF SYMBOLS (cont.)

Symbol	Description
p	Pressure
s	Structural
sb	Solid blockage
t	total or stagnation
u	Uncorrected
v	Volumetric
x, y, z	Principal axes directions
∞	Free stream

Acronyms

AAW	Active aeroelastic Wing
cs	Carbon steel
d.s.	Double slotted
CDP	Cell Differential Pressure
CTE	Coefficient of Thermal Expansion
CMT	Cellular Material Theory
FAA	Federal Aviation Authority
FAR	Federal Aviation Regulations
FE	Finite Element
FEA	Finite Element Analysis
gp	Geopotential
ISA	International Standard Atmosphere
Kr	Kruger flap
LSA	Light Sport Aircraft
LHS	Left-Hand Side
MAW	Mission Adaptive Wing
MLW	Maximum Landing Weight
MTOW	Maximum Take-Off Weight
ODE	Ordinary Differential Equation
PAX	Number of passengers

LIST OF SYMBOLS (cont.)

PBP	Post-Buckled Precompressed
PDE	Partial Differential Equation
RHS	Right-Hand Side
SMA	Shape Memory Alloy
sl	Slat
ss	Stainless steel
s.s.	Single slotted
SST	Supersonic Transport
SVG	Smart Vortex Generator
t.s.	Triple slotted
UAV	Uninhabited Aerial Vehicle
VAR	Variation
VG	Vortex Generator

LIST OF FIGURES

LIST OF FIGURES (cont.)

LIST OF FIGURES (cont.)

LIST OF FIGURES (cont.)

LIST OF FIGURES (cont.)

LIST OF FIGURES (cont.)

LIST OF FIGURES (cont.)

LIST OF FIGURES (cont.)

LIST OF TABLES

CHAPTER 1   MOTIVATION AND INTRODUCTION

1.1   <u>Motivation for Present Research</u>

During its flight regime an aircraft's wing needs to accommodate for two extreme conditions. During cruise its lift-to-drag ratio should be maximized in order to allow for the longest range. These quantities are directly coupled in the Breguet (cruise) range formula [1]:

$$R = \frac{V}{c_T}\frac{L}{D}\ln\frac{W_1}{W_2} \tag{1.1}$$

The range, R, is a function of the Mach number, M, local speed of sound, a, the specific fuel consumption, c_T, the lift-to-drag ratio, L/D, and the natural logarithm of the weight ratio, W_1/W_2. To maximize the range, the wing is shaped for a maximum lift-to-drag ratio. A high-L/D wing is thin and sharp, exhibits little camber, has a high aspect ratio, and is tapered and swept (in case transonic conditions apply).

Photo Credit: Boeing Aircraft Company   Photo Credit: Sander Wever

Maximum L/D at Cruise (Sonic Cruiser)   Maximum C_L at Landing (B747-400)

Figure 1.1   Disparate Requirements Driving Wing Design

At landing a significantly lower speed is required to bring the aircraft to a standstill within the length of the runway. As throughout the entire flight regime, during landing the following fundamental balance holds:

$$W = L = C_L\frac{1}{2}\rho V^2 S \tag{1.2}$$

where V is velocity, and S is a reference surface area (close to the wing surface area). To increase the maximum lift coefficient, a desirable wing would have a large wetted surface area, be unswept, have a high camber and thickness, and a relatively blunt leading edge.

1

In order to satisfy these disparate requirements of a high lift-to-drag ratio at cruise and a high maximum lift coefficient at landing, aircraft are generally equipped with high lift devices such as leading and trailing edge flaps and/or slats (see Figure 1.2, conventional approach). However, present-day high lift devices still rely heavily on complex mechanisms that consist of thousands of individual parts and heavy actuators to displace and/or rotate the whole assembly [2]. The present research focuses on an integrated adaptive structure that can carry structural loads and simultaneously change the shape of the wing such that it is optimal in both the cruise and the landing regime, while part count, complexity, and power consumption are minimized. This is schematically shown in the bottom morphing airfoil of Figure 1.2.

Maximum L/D   Maximum Lift Coefficient

Current/conventional approach

Proposed/morphing approach
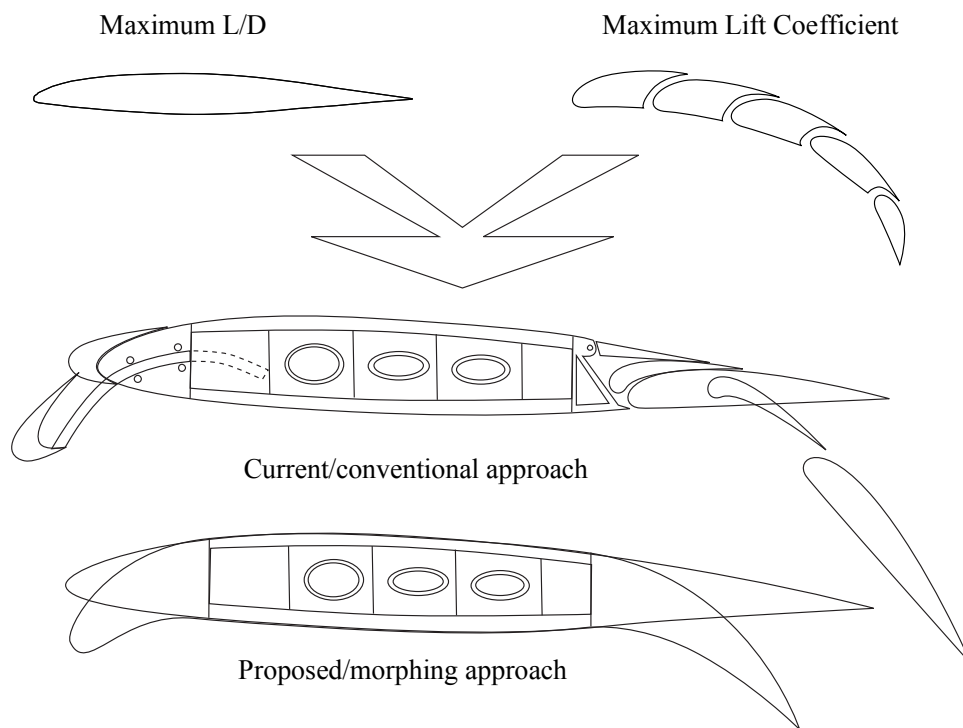
Figure 1.2   Conventional and Morphing Approach to Satisfy Maximum-L/D and Maximum-Lift-Coefficient Requirements

1.2   <u>Introduction and Hypothesis</u>

Adaptive structures can be used to enhance flight performance of aircraft. Nature can be an inspiration for engineers that need to design wings that perform equally well in the cruise and in the landing regime. Sweep, twist, dihedral and aspect ratio, a bird can change each of them in a split second to change its flight path, and what is more impressive, it hardly takes any

effort and the mechanism is low in complexity [3]. Figure 1.3 demonstrates wing morphing among seagulls. The reader can observe how the individual birds change their wing geometry to soar, hover, or maneuver.

Photo Credit: R. M. Barrett

Figure 1.3   Example of Wing Morphing among Seagulls

Matching the performance of bird morphing in combination with a low weight/energy/complexity penalty has proven to be very challenging. An important reason for this is that changes in the wing architecture do not only impact aerodynamics but also have an effect on the weight, structural integrity, and manufacturability of the aircraft. For the same set of requirements, the individual groups that form the entire design team all have different takes on which aircraft geometry satisfies these requirements best (see Figure 1.4). These individual outlooks are synthesized into a complete aircraft design. Morphing wing design is especially challenging because its multidisciplinary nature impacts each of the individual groups directly. For example, a swing wing can be beneficial from an aerodynamic standpoint; it also comes with a weight penalty and requires a completely different structural arrangement, which impacts the production and stress engineering groups.

Figure 1.4 of the page shows several hand-drawn aircraft sketches with the following labels:

- Attach wing "A" here
- Attach tail here
- Attach wing "B" here
- Aerodynamics group
- Production engineering group
- Powerplant group
- Unobtanium (1mil)
- Stress group
- Weight group
- Fuselage group
- Wing group
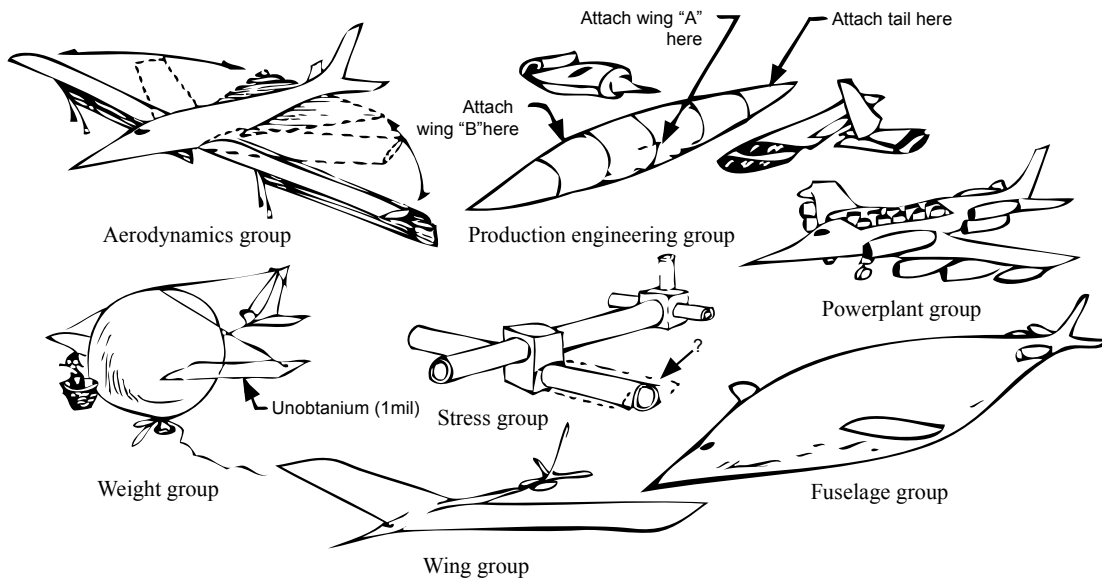
Figure 1.4   Each Group of Envisions a Different Aircraft for the Same Specifications (reproduced from Ref. 4)

Most efforts to mimic wing morphing have concentrated on UAVs as will be detailed in the next chapter. However, few of the morphing technologies have transferred to the civil realm of aviation. One of the prohibiting factors is the fact that the adaptive materials that are often employed in morphing structures are not FAR 23, 25, 27 or 29 certified.

In this dissertation it is hypothesized that an adaptive structure can be developed that relies on conventional aerospace materials, has low power consumption, has low complexity and can be easily integrated into aircraft structures to enable optimal performance in both the cruise and landing regime by changing the outer geometry of the wing.

In Chapter 2 previous research in the field of wing morphing is discussed. In addition, it is investigated what wing shapes are beneficial to morph into. In other words, a qualitative discussion is presented where the reader gets a feel for how wings should be altered in order to create beneficial aerodynamic performance. Against this background, Chapter 3 presents a new concept of wing morphing that satisfies the previously mentioned requirements. Possible applications of this adaptive structure are discussed in a qualitative manner. In Chapter 4 an analytical model is introduced that can be used to get a first cut at the mechanical properties of this adaptive structure. In addition, it is shown how the structure can be modeled using finite element analysis. Chapter 5 describes the experimental setups that were created to dem-

onstrate the workings of the adaptive structure and verify the models of Chapter 4. The adaptive structure was integrated into an adaptive flap that was aerodynamically tested in a subsonic wind tunnel. The results of the structural and aerodynamic tests are presented, discussed, and correlated to a CFD model in Chapter 6. Finally, Chapter 7 presents the overall conclusions of the present research and answers the research questions. It also discusses recommendations for future research. A schematic overview of the present dissertation is shown in Figure 1.5.
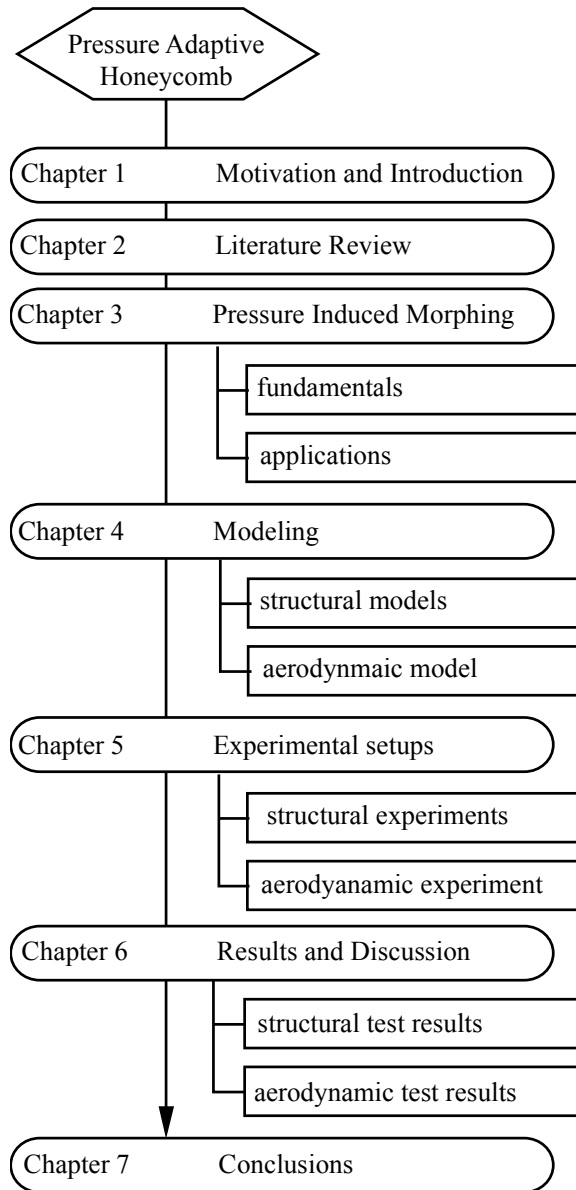
Figure 1.5   Outline of Dissertation Structure

CHAPTER 2   LITERATURE REVIEW

When adaptivity is addressed in terms of aircraft structural deformation, it should be apparent what condition the wing adapts to and what stimulus is required to achieve good adaptation. For commercial aircraft there are two extreme circumstances that the wing needs to adapt to: (1) maximum lift coefficient during landing and (2) maximum lift-to-drag ratio during cruise. Extensive research has been targeted towards making wings that perform well in both realms resulting in particular geometric characteristics. These characteristics are discussed in Section 2.2 and related to past efforts in morphing the wing to those desired geometries. With respect to the stimulus, this can either be gained from sources within the aircraft (as is conventional for aircraft of today) or extracted from external sources like temperature or pressure differences. The latter option results in a higher degree of adaptivity since the aircraft truly adapts to its surroundings without the interference of a pilot. It should be noted that this could also be perceived as a disadvantage because the pilot has no control over the adaptation of the aircraft. In addition, sources within the aircraft are common and well understood. To be able to say the same about the external stimuli, Section 2.3 researches how atmospheric conditions can be utilized to act as a stimulus for adaptive aerostructures.

2.1   Adaptive Structures and Materials

From Ref. 5 an adaptive structure is defined as: *A structure which uses highly integrated, normally load-bearing, adaptive materials to undergo a change in mechanical, thermal, optical, chemical, electrical, or magnetic properties as a function of a given stimulus*. With respect to aircraft structures, a change in mechanical properties is often most desirable since it allows for the ability to deform wing or empennage structure, influencing aircraft performance. The given definition incorporates the use of adaptive materials (materials that change their physical state as a function of a given stimulus). The most commonly used adaptive materials that change their mechanical state (strain) are shape memory alloy (SMA) and piezoelectric materials [5]. This section highlights the characteristics of these two adaptive materials, how they have been incorporated in aerospace applications, and what their advantages have been with respect to conventional alternatives.

2.1.1 Shape Memory Materials

Shape memory materials have the ability to return to their shape after being plastically deformed. The most commonly used shape memory materials are shape memory alloys (SMAs). The Nickel-Titanium based SMAs can be fabricated to almost any shape or form. Plastic deformation in shape memory alloys induces the martensitic atomic structure to deform significantly. By increasing the temperature of the material, the atomic structure changes to austenitic, thereby returning the material to its original shape. When the material is subsequently cooled, the geometry is maintained and the atomic structure becomes martensitic again (see Figure 2.1). If the material is in a particular form (e.g. rod, wire, bar) and loaded by a force, work can be performed.
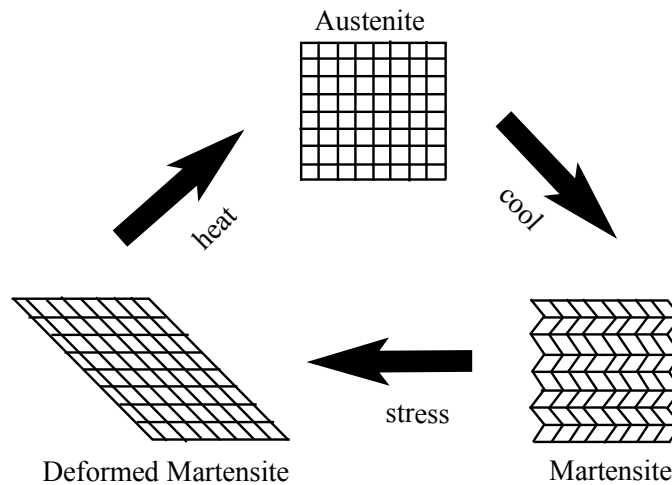
Figure 2.1   Microstructural Changes due to Shape Memory Effect (reproduced from Ref. 6)

SMAs have the highest single-stroke work density of the adaptive structures. They can exhibit great strains and apply considerable force. However, they generally exhibit a large power draw due to energy dissipation and their hysteresis can amount to 38%. Moreover, their bandwidth is generally poor because of thermal saturation issues [5].

Examples of the use of SMA in an aircraft application can be found as substitutes for conventional actuators in subscale uninhabited aerial vehicles (UAVs) [7]. An investigation into the use of adaptive materials in morphing structures demonstrated the effective use of highly integrated SMA materials for leading and trailing edge deformation on a wind-tunnel model of a contemporary fighter [8-11]. Several morphing wing concepts based on SMA tendon (wire)

7

actuators were conceived [12-14]. Although these designs accomplish large deformations the structure of multiple parts, hinges, and actuators is complex and occupies most of the internal wing volume (see Figure 2.2).
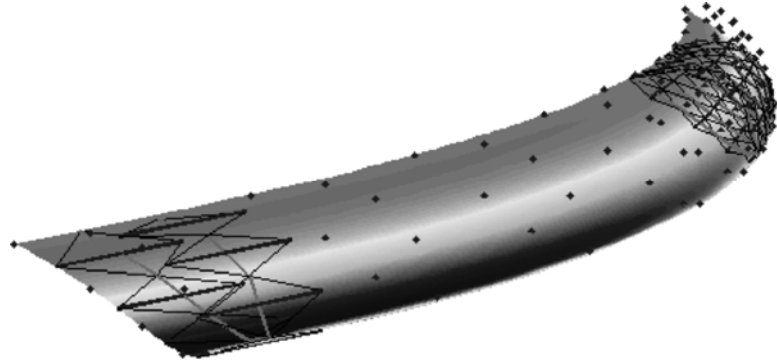
Figure 2.2   **Example of Morphing Wing Design based on SMA-Tendon-Actuated Cellular-Truss Structure [13]**

A successful application of SMA was presented by Boeing in 2006. They used SMA actuators to deform their jet-noise-reduction chevrons during flight. These chevrons are positioned at the rear of the engine cowling and often have a zig-zag geometry (see Figure 2.3). By pushing the chevrons slightly into the jet stream noise levels were significantly reduced at sealevel. Due to the large temperature difference, at cruise altitude the SMA actuators ensured the chevrons bent out of the jet stream, thereby giving the engine its maximum performance [15-17].

Figure 2.3   **SMA-Actuated Variable Geometry Chevron for Jet Noise Reduction [17]**

8

2.1.2 Piezoelectric Materials

Piezoelectric materials generate an electric potential in response to applied mechanical stress, called the direct piezoelectric effect. Because this effect is reversible, piezoelectric actuators can be used in both sensor and actuator applications. A common piezoelectric material is Lead Zirconate Titanate (PZT). This material has randomly distributed dipoles within a poly-crystalline structure. Poling the material is done by creating a large through-the-thickness electric field, which orients all dipoles in that direction. Figure 2.4 schematically shows the poling process as well as the direct piezoelectric effect on a crystalline level.
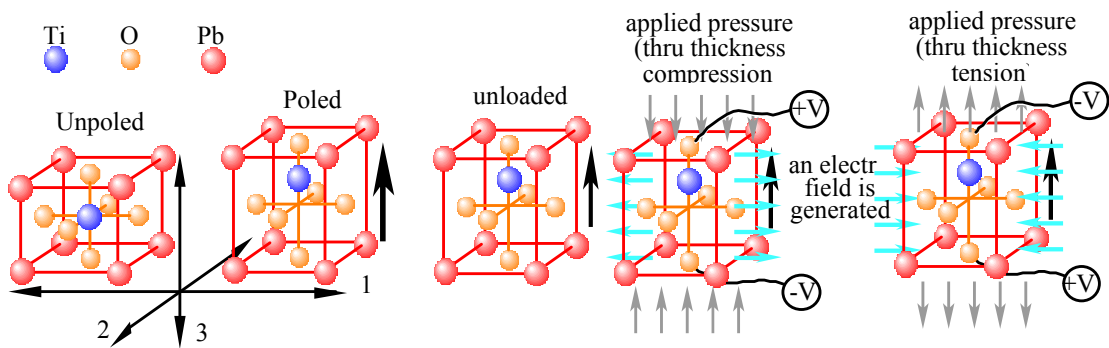
Figure 2.4   Poling PZT and the Direct Piezoelectric Effect (copied from Ref. 5)

Piezoelectric materials have been used for many years in applications such as pressure trans-ducers and smoke detectors. Actuator applications include fuel injectors and valve lifters [18]. The first applications of piezoelectric actuators in flight control systems appeared in the early 1990s relying on directionally attached piezoelectric torque plates. These torque plates were demonstrated in missile fins, subsonic and supersonic twist-active wings, and twist-active rotor blades [19-21]. Figure 2.5 schematically shows the concept of a twist-active wing based on an internal torque plate with directionally attached piezoelectric elements.
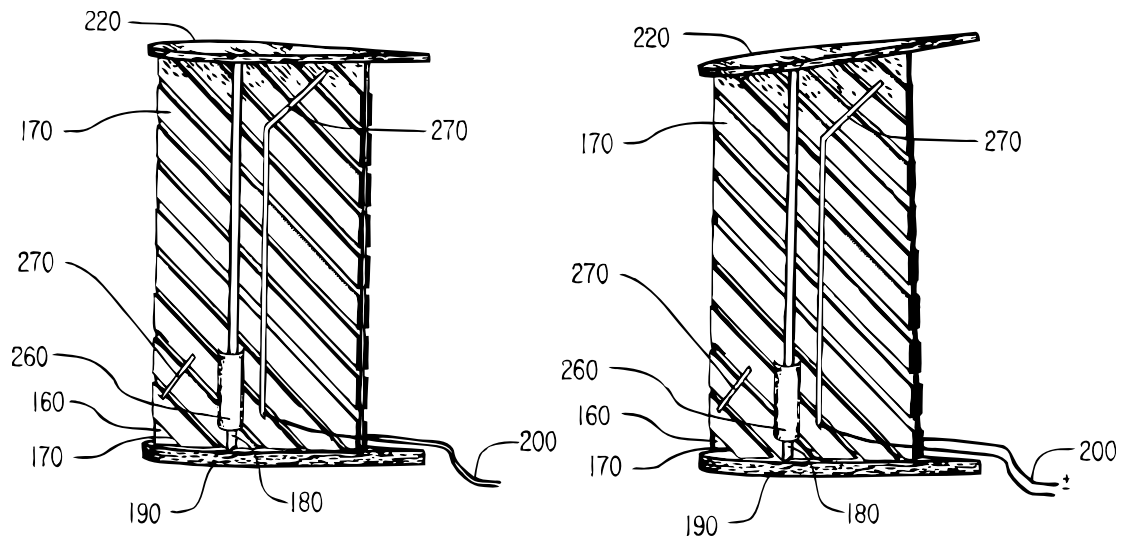
Figure 2.5   Directionally Attached PZT (nr. 170) in Twist Active Wing [20]

Over the past two decades piezoelectric actuator elements have been demonstrated to reduce overall flight-control-system weight on miniature UAVs. By integrating piezoelectric bender elements into the control surfaces themselves, power consumption and complexity could be greatly reduced while a much higher actuation bandwidth could be achieved. An example of such an embedded actuator is the Flexspar concept, shown in Figure 2.6.
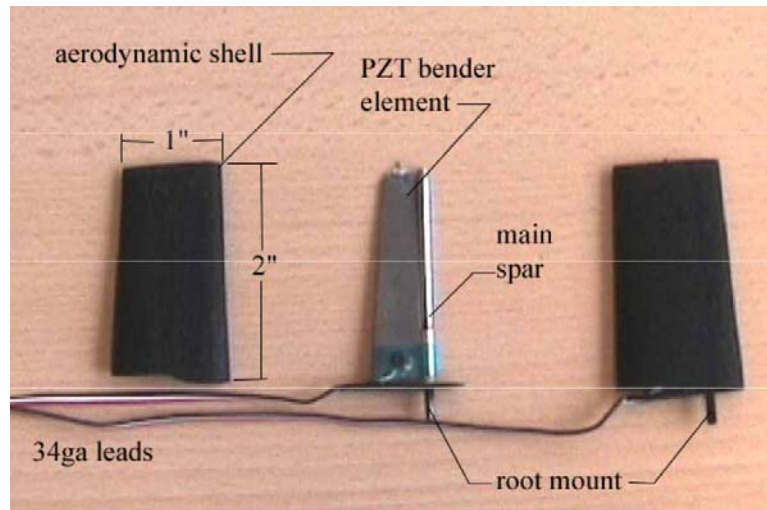
Figure 2.6   Example of Piezoelectric Flight Control Actuator System for Miniature UAVs [22]

Flight control based on these type of actuator elements was demonstrated on Mothra, the first aircraft to rely solely on adaptive materials for flight control (see Figure 2.7). Eventually, these Flexspar actuators were integrated in a VTOL miniature UAV outperforming conventional electromechanical actuators in terms of weight, power consumption, and bandwidth [23].

Figure 2.7   Mothra, the First Aircraft to Fly Using Piezoelectric Flexspar Actuators for All Flight Control [24]

Piezoelectric materials have a lower single-stroke work density than SMAs and generally a limited stroke and force capability. However, recent advances in actuator design have led to a more robust and competitive actuator which has successfully been used in uninhabited aerospace applications ranging from subsonic through supersonic [25-27]. This new class of actuators relied on an additional axial load to decrease the effective inherent stiffness of the actuator element. This axial force was conveniently introduced by an elastic band and increased the peak–to-peak deflection of the Flexspar actuator with more than 100%, doubling the work output, while maintaining the high actuation bandwidth [28]. The improved Flexspar-based flight-control surface is schematically shown in Figure 2.8. This new class of actuators was termed Post-Buckled Precompressed (PBP) and was also demonstrated in a transonic missile fin and a morphing wing concept [27, 29].
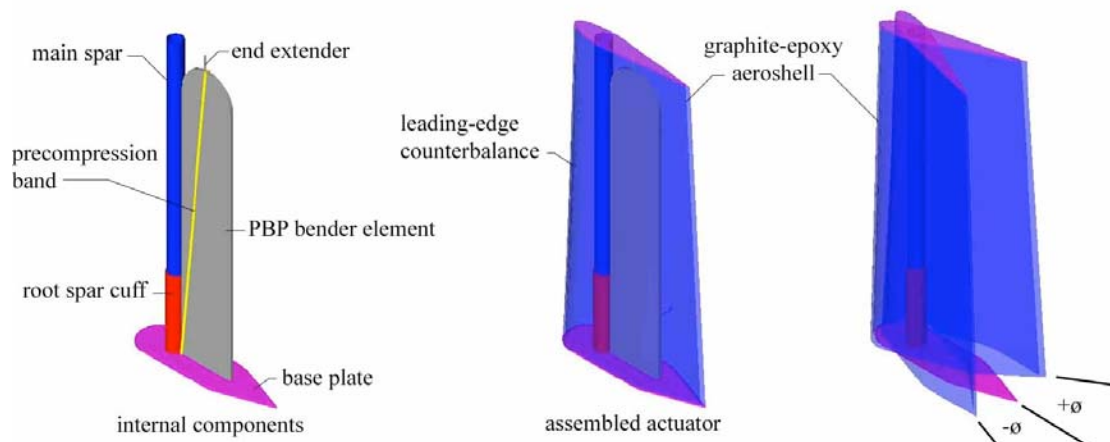
Figure 2.8   Typical Arrangement of Flexspar Stabilator with Elastic-Enabled PBP Actuator (copied from Ref. 28)

2.1.3 Comparison of Adaptive Actuator Technology

Comparing adaptive materials can be done based on their mechanical, electrical, and/or chemical properties. One of the most important properties for aircraft applications is the specific energy density, or the amount of mechanical work that can be performed by a single gram of adaptive material. The coupling efficiency, κ^2, at which input energy is converted into mechanical work is another important parameter because it relates to the amount of energy that is required to induce mechanical work. In Table 2.1 an overview of a variety of adaptive materials is presented along with their most important intrinsic characteristics. The data in this table has been copied from Ref. 30, which also states that the data is based on preliminary data and that it pertains to active material mass only. In addition, it is stated that practical values of energy density might be 10 to 100 times lower than presented.

Table 2.1   Comparison of Actuator Technologies (copied from Ref. 31)

Actuator Type (specific example)	Maximum Strain, ε (%)	Maximum Pressure, σ (MPa)	Specific Elastic Energy Density, E_m (J/g)	Elastic Energy Density, E_v (J/cm³)	Transfer Efficiency, η (%)	Maximum Efficiency (%)	Specific Density, ρ (g/cm³)	Relative Speed (full cycle)
Electroactive Polymer Artificial Muscle								
Acrylic	215	7.2	3.4	3.4	~60	60–80	1	Medium
Silicone (CF19-2186)	63	3.0	0.75	0.75	63	90	1	Fast
Electrostrictor Polymer								
P(VDF-TrFE)	4	15	0.17	0.3	5.5	–	1.8	Fast
Electrostatic Devices								
(Integrated Force Array)	50	0.03	0.0015	0.0015	~50	> 90	1	Fast
Electromagnetic								
(Voice Coil)	50	0.10	0.003	0.025	n/a	> 90	8	Fast
Piezoelectric								
Ceramic (PZT)	0.2	110	0.013	0.10	52	>90	7.7	Fast
Single Crystal (PZN-PT)	1.7	131	.13	1.0	81	90	7.7	Fast
Polymer(PVDF)	0.1	4.8	0.0013	0.0024	7	n/a	1.8	Fast
Shape Memory Alloy (TiNi)	> 5	> 200	> 15	> 100	5	< 10	6.5	Slow
Shape Memory Polymer	100	4	2	2	–	< 10	1	Slow
Thermal (Expansion)	1	78	0.15	0.4	–	< 10	2.7	Slow
Electrochemo-mechanical Conducting Polymer	10	450	23	23	< 1	< 1%	~1	Slow
Mechano-chemical Polymer/Gels (polyelectrolyte)	> 40	0.3	0.06	0.06	–	30	~1	Slow
Magnetostrictive (Terfenol-D, Etrema Products)	0.2	70	0.0027	0.025	–	60	9	Fast
Natural Muscle (Human Skeletal)	> 40	0.35	0.07	0.07	n/a	> 35	1	Medium

From the data in this table it can be observed that the conducting polymer has the highest mass-specific energy density (23J/g), closely followed by SMA (15J/g). Although their energy densities are high, their low transfer efficiency requires a relatively large amount of energy to actuate these materials. In addition, the actuators are relatively slow. Piezoelectric materials can have much higher transfer efficiencies. The ceramics (which are often considered for aircraft application) have a transfer efficiency of $\eta = 52\%$ and are relatively fast. However,

their energy density is three orders of magnitude lower than that of SMA. Other well-performing adaptive materials are the electroactive polymers. The acrylic artificial muscle, for example, has mass-specific energy density of 3.4J/g, a transfer efficiency around 60%, and is relatively fast.

2.1.4 Application in Aerospace Industry

Even though adaptive materials have been successfully applied in uninhabited aerospace vehicles for almost three decades, they remain excluded from primary and secondary structure of inhabited air vehicles due to the fact that no FAA or MIL-STD certification database exists or is even planned. Since certification of a material for use on inhabited, commercial aircraft can take more than twenty years [32] the use of adaptive materials is not anticipated in the short term. However, that does not mean that adaptive structures have to remain abandoned from certified aircraft. If the previous definition of an adaptive structure is broadened such that it encompasses all materials, the opportunity arises to build an adaptive structure based on certified materials. A more suitable definition of an adaptive structure would therefore be: *A structure which undergoes a change in mechanical, thermal, optical, chemical, electrical, or magnetic properties as a function of a given stimulus.* If this definition is used to describe adaptive structures, then more examples of aerostructures qualify as being adaptive.

2.2 <u>Variable Geometry Wings</u>

To satisfy the disparate design requirements of a high $C_{L_{max}}$ at landing and a high L/D at cruise, typically an aircraft relies on high lift devices. High lift devices change the geometry of the wing considerably. However, they typically do so in a discontinuous way, requiring hinges or tracks to rotate and displace individual wing components. A result is that systems of high lift devices are complex, heavy and often maintenance intensive [2]. An alternative to using traditional high lift devices is to rely on continuously deforming wing sections for optimal performance both in the low speed realm and during cruise. This requires a dedicated structural arrangement of the wing that allows for shape deformations without losing structural integrity. Wings that possess the ability to change their shape are often termed 'adaptive' or 'morphing' wings. This section gives an overview of past and present efforts to tailor wing geometry to fulfill different mission requirements and expand the flight envelope. It

also qualitatively details what geometries are desired to be obtained under various flight conditions.

Historically, wing morphing has played an important role in aircraft design. It were the Wright brothers that introduced the concept to aircraft structures.They had observed soaring birds and believed they could obtain roll control by warping a portion of the wing. In 1900 they demonstrated this on their 17ft span glider. They used cables to deform the wing tips such that the local incidence angle changed. This technique found its way on the first pilot-controlled powered aircraft, the Wright Flyer II (see Figure 2.9). However, in subsequent years, aircraft designers abandoned this concept in favor of hinged control surfaces which required less force to deflect.

HOW THE WINGS WERE WARPED

RIGHT   LEFT

CRADLE

→ →→ CABLES ATTACHED TO CRADLE — SLIDING CRADLE TO LEFT
OF MACHINE PULLS TRAILING EDGE OF RIGHT WING DOWNWARD

→ → → CABLE (NOT ATTACHED TO CRADLE) IS MOVED
AUTOMATICALLY BY DOWNWARD MOVEMENT OF RIGHT WING
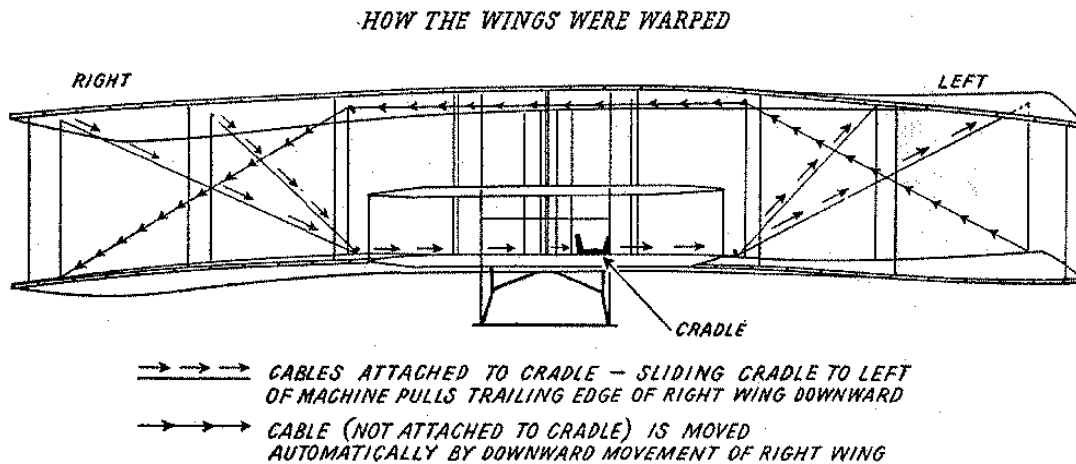
Figure 2.9   The Wright Brothers' Wing Warping Scheme [33]

In the following decades an array of morphing concepts were conceived, ranging from variable camber airfoils to telescopic wings and from variable incidence wings to swing wings. Ref. 34 gives an overview of all of these concepts and discusses their application. The most successful wing morphing application (excluding flaps/slats) is arguably the swing wing. Conceived in the 1940's and extensively used on military aircraft such as the F-111, the F-14, and the B-1. By varying the wing sweep, the swing wing allowed these aircraft to take-off and land at relatively low speeds and dash at supersonic speeds [34].

Description:	Aircraft:	Airfoil:	$c_{l_{max}}^*$	L/D^*	c_{d0}^*
Transonic Airfoil	Boeing 737	BAC 442	1.3	90	.0082
Subsonic Airfoil	Saab 2000, Let 610	MS(1)-0 313	1.6	80	.0089
High Lift Airfoil	Sailplanes	FX74-CL5-140	2.4	130	n/a
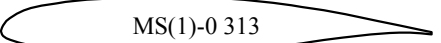
* All values based on Xfoil calculations for $M = 0.3$, $Re = 1 \cdot 10^6$, and $\tilde{n} = 9$

Figure 2.10   Examples of Airfoil Geometries and Their Characteristics [35-37]

The geometry of the airfoil determines, for a large part, the maximum lift coefficient of a wing. Looking at Figure 2.10, it can be observed that camber, leading edge shape and thickness distribution are distinct parameters that determine the maximum lift coefficient of the airfoil. Another important parameter is the Reynolds number:

$$Re = \frac{\rho V c}{\mu} \qquad (1.1)$$

Considering V, velocity, ρ, density, μ, viscosity, and c, the characteristic chord length.

In general (as can be seen from Figure 2.11) the maximum lift coefficient increases with Reynolds number. However, for high-lift airfoils there is an unusual tendency for a decrease in $c_{l\,max}$ with Reynolds number. This is attributed to "fast trailing edge stall," which is caused by a fast moving transition in connection with a continuously high-loaded turbulent boundary layer [37]. Note also the large difference in $c_{l\,max}$ between the conventional airfoils and the high lift airfoils.
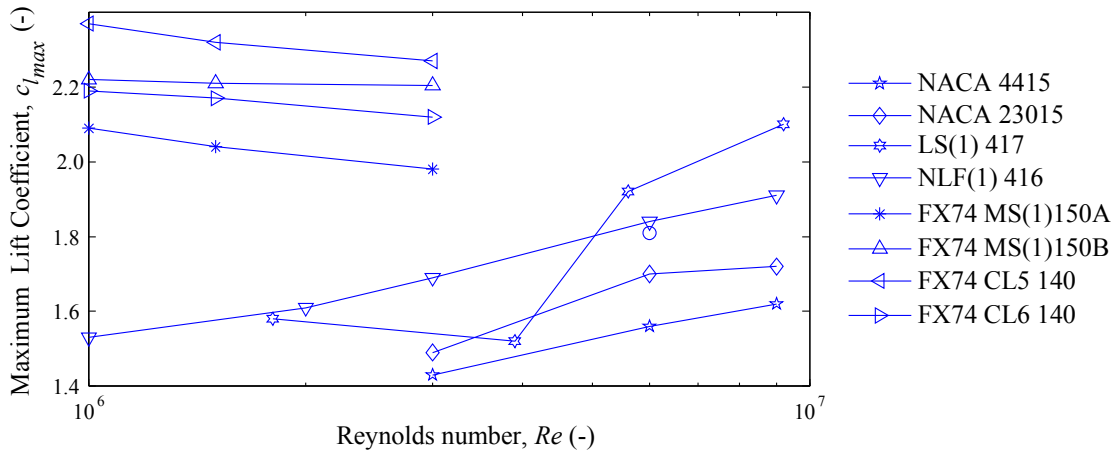
Figure 2.11   Influence of Reynolds Number on Maximum Lift Coefficient [37, 38]

In the most general terms, the maximum lift coefficient ($c_{l\,max}$) occurs at an angle of attack, $\alpha_{c_{l\,max}}$, such that as the angle of attack is increased even further, the airfoil enters a stall. This stall can be gradual (trailing-edge stall) or abrupt (leading-edge stall or thin-airfoil stall) depending on the geometry of the airfoil [39]. During a stall, the boundary layer cannot cope with the large adverse pressure gradient and detaches from the airfoil surface, leaving a turbulent flow wake. This causes the lift to drop and the drag to increase. In the past, a number of efforts have been made to produce high lift airfoils for various Reynolds numbers. Ref. 40 gives an overview of these airfoils, their performance and their (potential) applications.

2.2.1 Discrete High Lift Devices

During the last decades, the ratio between cruise speed and landing speed has increased for commercial passenger aircraft. Sweeping the wing backwards to increase the drag divergence Mach number has had an adverse effect on the low-speed lifting capability of the wing. To account for the high C_L conditions during take-off and landing, wings are generally equipped with high lift devices (flaps and/or slats). Figure 2.12 demonstrates how the wing lift coefficient is influenced by high-lift devices. In Ref. 2 a comprehensive overview is given of contemporary high lift devices, their mechanics, and their impact on the performance, cost, and complexity of the aircraft. The more exotic flap systems that also have fully aft-translating capabilty are generally only found on high subsonic aircraft with swept wings. Low-subsonic aircraft such as light sport aircraft (LSA) do not require such a complicated high-lift system because the cruise-to-landing speed ratio is lower and the wings are generally

unswept. In addition, LSAs are highly cost sensitive, which makes the addition of a complicated high-lift device less attractive. These aircraft therefore employ simple flap systems such as a split or plain flap. Leading-edge high-lift devices are not found on low-subsonic aircraft.

Basic transonic airfoil, $C_{L_{max}}$ =1.6

Plain flap, $C_{L_{max}}$ = 2.0

Leading edge flap, $C_{L_{max}}$ = 1.8

Split flap, $C_{L_{max}}$ = 2.4

Slat, $C_{L_{max}}$ = 1.8

30% Fowler Flap, $C_{L_{max}}$ = 3.2

$C_{L_{max}}$ = 3.4

Double Slotted, $C_{L_{max}}$ = 2.8

$C_{L_{max}}$ = 3.0

Single Slotted, $C_{L_{max}}$ = 2.5

$C_{L_{max}}$ = 2.5
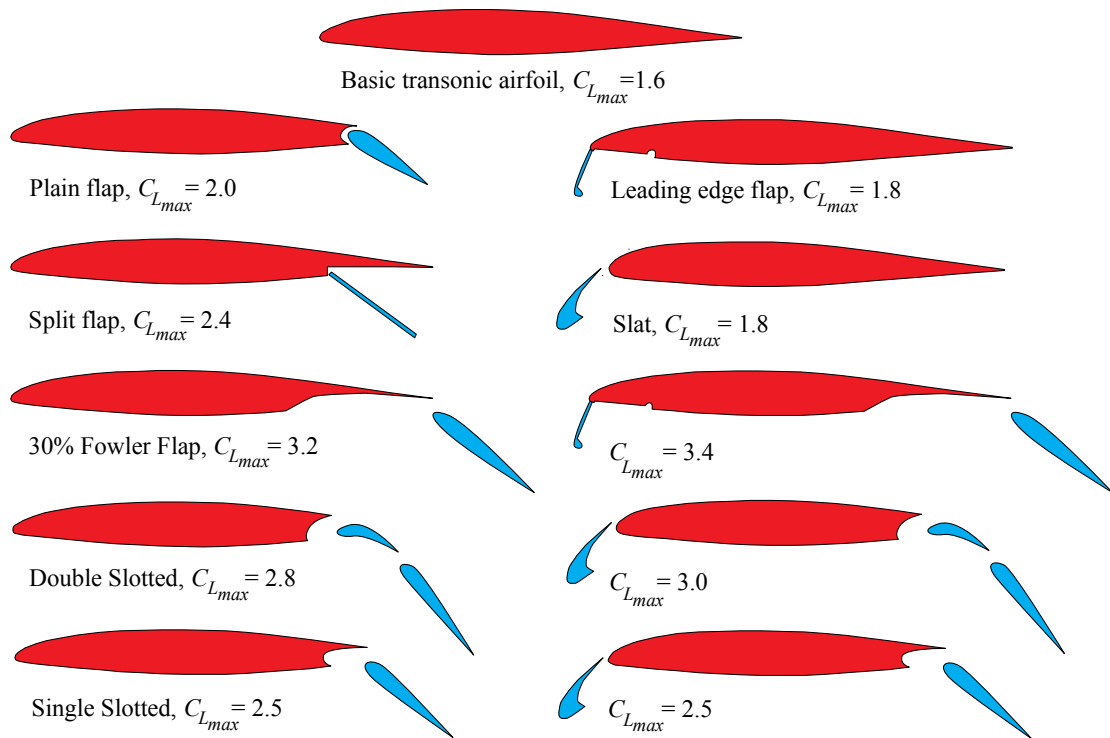
Figure 2.12   Effect of Flap Type on Maximum Wing Lift Coefficient for an Unswept, A=6 Wing (Reproduced from p. 206 in Ref. 41)

Modern transonic transport aircraft use these high lift devices during take-off and landing to increase their lift capabilities. Table 2.2 (page 22) gives details for a selection of modern transport aircraft. By using the approach speed, V_{apr}, in combination with the maximum landing weight (W_{ML}) of each the aircraft the approach lift coefficient can be calculated (assuming ISA conditions). Noting that all the aircraft studied herein can be considered as long-coupled aircraft, the wing lift coefficient is found by adding 5% to the approach lift coefficient (accounting for the horizontal tail down force [42]). Assuming the stall speed is 1.3 times the approach speed (according to FAA regulations [1]) the maximum wing lift coefficient can be obtained:

$$C_{Lmax} = 1.05 \cdot (1.3)^2 \frac{2W_{ML}}{\rho SV_{apr}^2} \tag{2.2}$$

Accounting for the wing sweep angle, Λ, and following the approach of Ref. 43 the average section lift coefficient can be approximated from:

$$c_{lmax} = \frac{C_{Lmax}}{0.9 \cdot cos\Lambda_{c/4}} \tag{2.3}$$

It is pointed out to the reader that Equation 2.3 is an averaged approximation of the typical section lift coefficient of the wing. Although rough, it gives a good first order estimate of the two-dimensional lift capabilities of an airfoil employing high lift devices. Furthermore, the reader is asked to note that apart from the Fokker 70 all aircraft employ both leading and trailing edge high lift devices (see Table 2.2).

The maximum wing and section lift coefficients of the aircraft from Table 2.2 are presented in Figure 2.13. Ranging from 3.0 to 4.26, it is shown that high lift devices can produce significantly higher section lift coefficients than were presented in Figure 2.12. The fully aft translating single slotted flap combined with a slotted forward translating slat of the A340-600 proves to produce the highest lift coefficient. This demonstrates that careful aerodynamic design can make the complexity of a multi-slotted flap obsolete while still achieving excellent lift characteristics. Another explanation for the higher lift coefficient is the fact that the A340, A330 and A380 use trailing edge high lift devices over the full span of the wing as they employ 10° drooped ailerons. In contrast to the larger Boeing aircraft (747, 767, 777, 787) the Airbus aircraft do not have an inboard aileron (or flaperon) so they employ their single slotted flaps over a larger part of the span. Thirdly, while the Airbus aircraft used supercritical airfoil sections, the older Boeing designs (737, 747, 767) used modified airfoils from previous designs with some form of supercritical technology [44]. In practice, the supercritical airfoils proved to yield higher maximum lift coefficients resulting in more lift capabilities during take-off and landing.
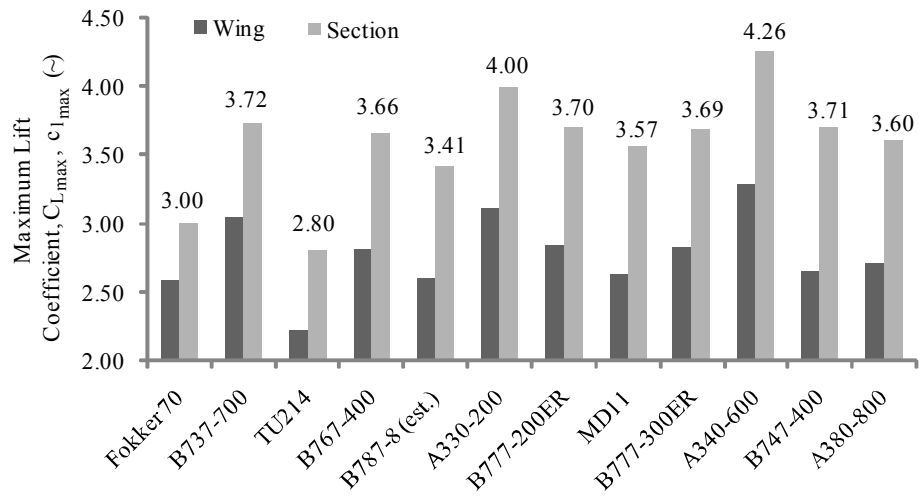
Figure 2.13   Maximum Lift Coefficients for Modern Jet Transport Aircraft (obtained from Data of Table 2.2 and Eqs. 2.2 and 2.3)

Although effective, the aerodynamic advantages of a high-lift system come at a price. At the leading edge, movable flaps or slats are the highest- (aerodynamically) loaded parts of the wing. This requires extremely stiff and strong components within the extend/retract mechanism, which generally results in a significant weight penalty. An example of a complex leading edge flap is shown in Figure 2.14. The flap system complicates the wing's trailing edge structure and introduces electrical systems in relatively thin parts of the wing. For aft translating flaps, flap tracks are required that penetrate the airflow during cruise and increase wing drag (see Figure 2.15 and Figure 2.16). Furthermore, the system adds weight to the wing and increases the cost of manufacturing. However, the performance improvements are historically considered to outweigh these penalties [43].
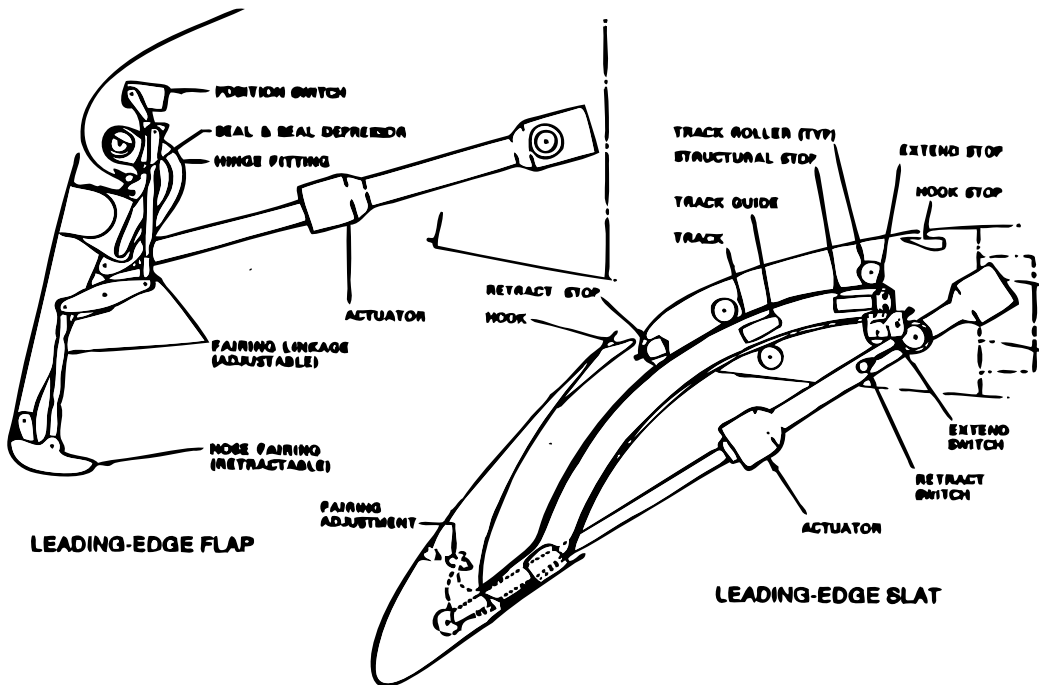
Figure 2.14   Example of Leading-Egde High-Lift Devices (B727-200) [2]
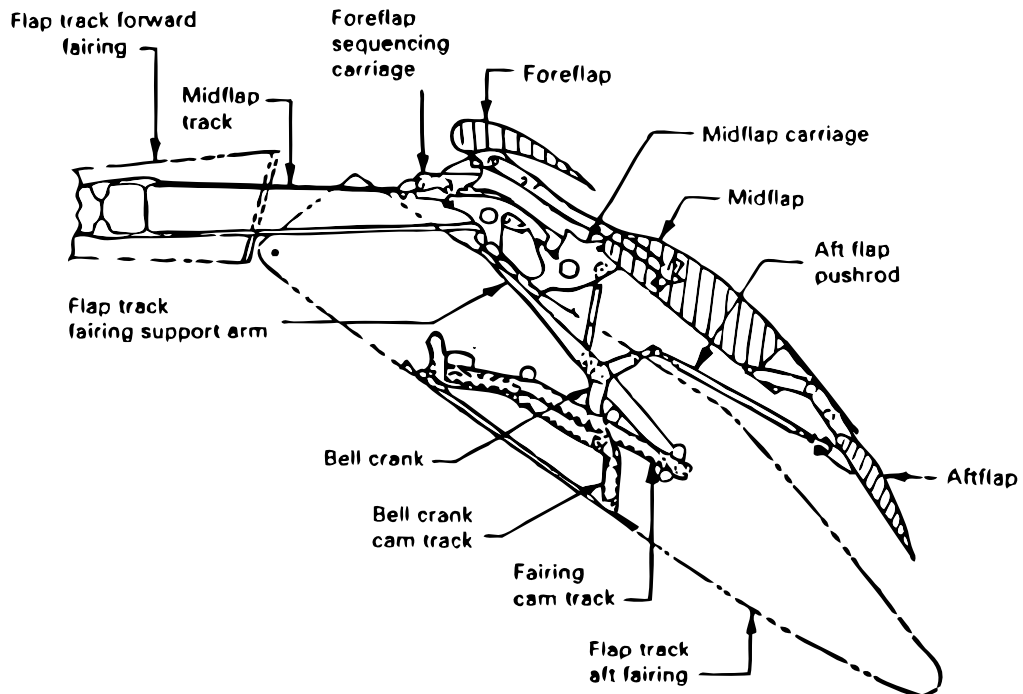
Figure 2.15   Trailing-Edge High-Lift Device (B737 Triple-Slotted Fowler Flap) [2]

Table 2.2 Details for a Selection of Modern Transonic Transport Aircraft [43, 45, 46]

Item	Symbol	Units	Fokker 70	B737-700	TU214	B767-400	B787-8 (est.)	A330-200	B777-200ER	MD11	B777-300ER	A340-600	B747-400	A380-800
Passengers	PAX	(-)	79	162	210	245	223	253	301	293	365	378	420	555
Wing span	b	(m²)	28.0	35.7	40.9	51.9	60.0	60.3	60.9	51.6	65.0	63.5	64.4	79.8
Aspect ratio	A	(-)	8.39	9.45	9.07	9.27	11.07	10.06	8.67	7.85	9.88	9.16	7.98	7.54
Wing Area	S	(-)	93.5	134.9	184.2	290.7	325.3	361.6	427.8	339.0	427.8	439.4	520.3	845.0
Sweep	Λ	deg	17.0	25.0	28.0	31.5	32.2	30.0	31.6	35.0	31.6	31.1	37.5	33.5
flaps		(-)	d.s	d.s.	d.s	d.s./s.s	s.s	s.s	d.s/s.s	d.s.	d.s/s.s	s.s	t.s.	s.s
l.e. device		(-)	-	Kr./sl.	sl.	sl.	sl.	sl.	Kr./sl.	sl.	Kr./sl.	sl.	Kr./sl.	sl.
MTOW	W_{MTO}	(10⁵ kg)	0.38	0.71	1.10	2.04	2.19	2.30	2.60	2.73	3.40	3.52	3.63	5.60
MLW	W_{ML}	(10⁵ kg)	0.34	0.59	0.93	1.59	1.64	1.82	2.05	1.95	2.51	2.65	2.60	3.86
Cruise Mach	M_{cr}	(-)	0.77	0.79	0.80	0.80	0.85	0.82	0.84	0.82	0.84	0.83	0.85	0.85
Approach Speed	V_{apr}	(m/s)	64.8	65.3	82.3	76.1	76.1	69.4	71.0	80.8	78.7	74.1	75.1	71.0
Cruise Altitude	h_{cr}	(m)	10670	11430	12100	10668	13106	10668	11156	10668	10607	10668	12500	10668

Note: s.s. = single slotted, d.s.= double slotted, t.s = triple slotted, Kr. = Kruger flap, sl. = slat

22
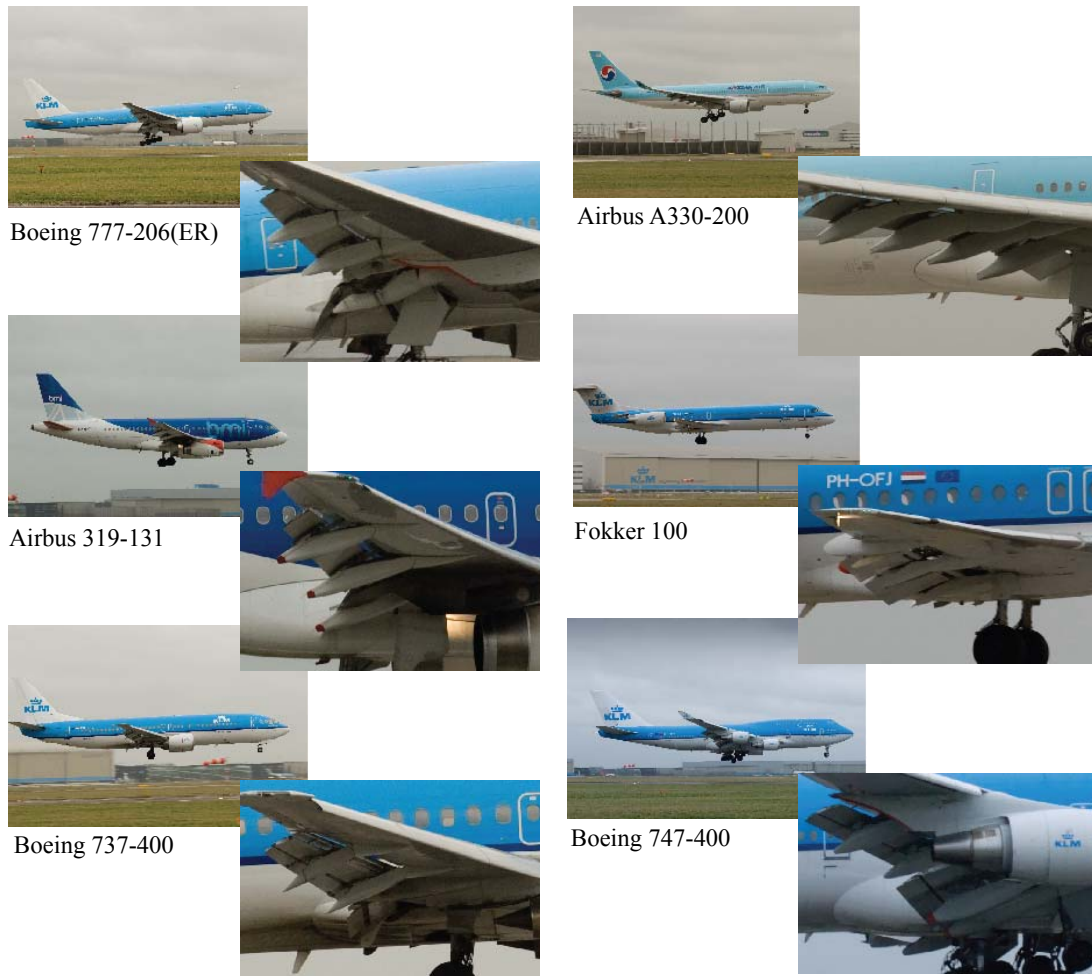
Figure 2.16   Example of High Lift Augmentation Systems on Current Jet Transport Aircraft (Photo Credit: Sander Wever)

2.2.2 Variable Thickness Ratio

The thickness ratio of an airfoil is its maximum thickness (measured perpendicular to the chord line) divided by the chord of the airfoil. The thickness ratio is one of the parameters that determine the maximum lift an airfoil can generate. It also has an influence on the post-stall behavior of the airfoil.

A basic example of the influence of thickness on the pressure distribution is demonstrated in Figure 2.17 where 6% and 18% thick airfoils of otherwise similar geometry are compared. The pressure peak (in a negative sense) at the leading edge of the thin airfoil is much higher than for the thick airfoil. Consequently, the pressure gradient, dp/dx, for this airfoil is much

steeper. The steep slope of the pressure gradient is an indication that the boundary layer will separate at a lower angle of attack than for the thick airfoil, giving rise to an abrupt drop in lift. A simple two-dimensional Euler code (Xfoil, see Section 4.6) predicts a maximum lift coefficient of 1.0 for the NACA 0006 and 1.8 for the NACA 0018. The stall for a NACA 0006 results in an abrupt loss in lift while the NACA 0018 shows a more gradual decay. Furthermore, for the NACA 0018 $c_{l\,max}$ occurs at $\alpha = 20$. while for the NACA 0006 this is at $\alpha = 9$.
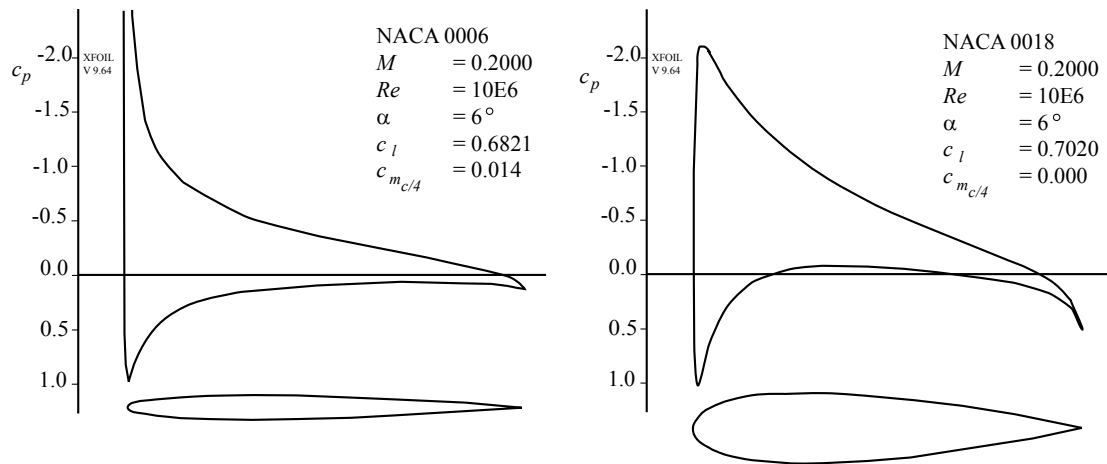
Figure 2.17   Effect of Thickness Ratio on Pressure Gradient

Figure 2.18 shows the maximum lift coefficients for a series of airfoils as a function of their thickness. Note in these graphs how $c_{l\,max}$ is strongly influenced by the Reynolds number. Comparing Figures (a) and (b) shows the difference in maximum lift due to camber. The MS(1) airfoil shows distinctly better high lift characteristics than all the other airfoils but is much more susceptible to a change in Reynolds number (see Figure 2.10 for geometry).

24

(a) Symmetric Airfoils   **(b) Cambered Airfoils**
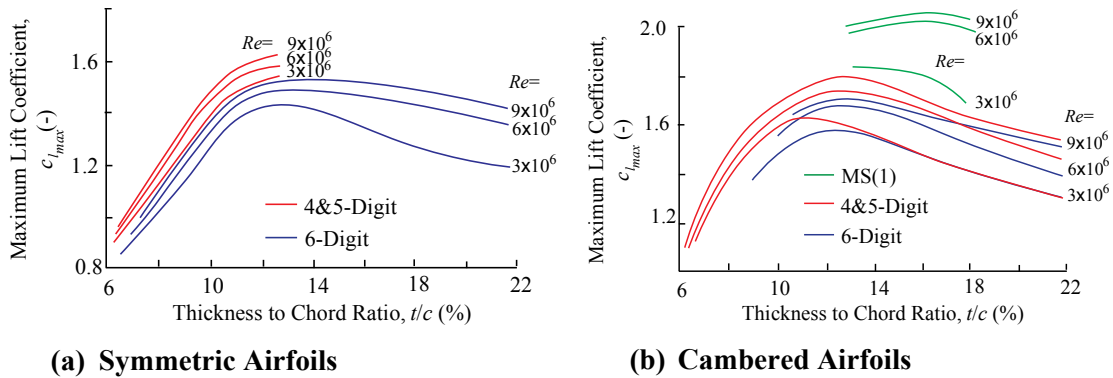
Figure 2.18   Effect of Thickness Ratio and Reynolds Number on NACA Airfoil Maximum Lift coefficient (Reproduced from p. 363 in Ref. 38)

The influence of airfoil thickness and camber on the maximum lift coefficient was investigated in the 1950s using NACA 4- 5- and 6-digit series airfoils. The results of this investigation are found in Ref 47. For each of these airfoils two cases were considered: clean $c_{l\,max}$ and $c_{l\,max}$ with a split flap deflected over 60°. It was found that maximum lift coefficient occurred at a thickness ratio of 12% for plain airfoils (which is in agreement with the graphs in Figure 2.18), while for airfoils having a split flap this optimum laid at 18%.

The combination of airfoil thickness and flap type was shown to be instrumental in the maximum lift capabilities of an airfoil, as can be seen in Figure 2.19. This graph displays the change in maximum lift coefficient for a relative flap chord of 25% and standard flap deflection angles. Deviating from these standard angles generally results in lower $\Delta c_{l\,max}$ [38]. Figure 2.19 shows that flap deflection is more effective on thick airfoils than on thin airfoils. Using advanced flap mechanisms (double slotted) in combination with a 19% thick airfoil can change the maximum lift coefficient as much as 1.9. A simple single slotted flap mechanism combined with a 18% thick airfoil results in $\Delta c_{l\,max} = 1.8$.
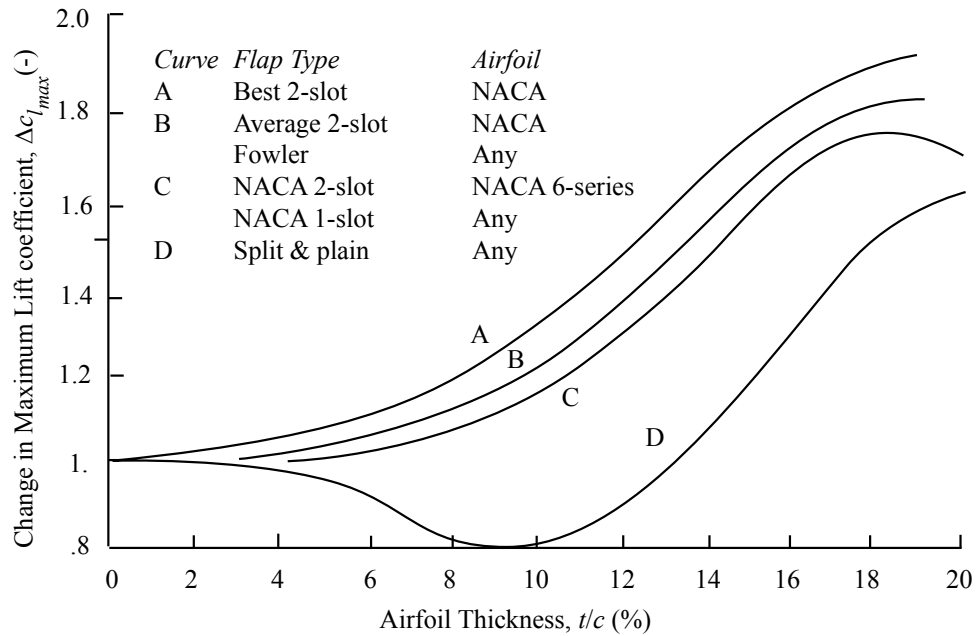
Figure 2.19   Basic Airfoil Maximum Lift Increment due to Trailing Edge Flaps, Given for a Flap Chord to Airfoil Chord Ratio of 25% and Reference Flap Deflections: Fowler = 40º, 1 Slot = 45 º, 2 Slot = 50 º and Split and Plain=60º (Reproduced from p. 240 of Ref. 38)

Even though it is apparent that changing the airfoil thickness during flight can be beneficial for high-lift capability, there are few examples in the literature of morphing wings that employed this feature. In 1929, Otto Lientz from Meriden, Kansas filed for a patent on a variable-thickness wing where the top and bottom skin could be pushed outwards by a linkage mechanism (see Figure 2.20). Vought Corporation patented a variable thickness airfoil that would allow airfoils to sustain supersonic cruise as well as to provide good low-speed performance (see Figure 2.21). Northrop patented an adjustable airfoil that relied on inflation of the area between the top surface of the torque box and the skin of the airfoil (see Figure 2.22). This airfoil has conventional leading and trailing edge flaps but relies on the bulging of the skin for a smooth transition between the high-lift devices and the main body of the wing.
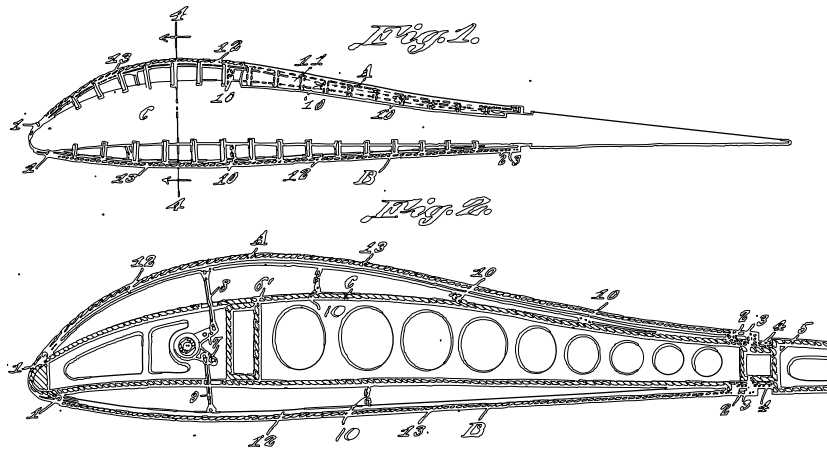
Figure 2.20 Variable Thickness Airfoil and Mechanism (copied from Ref. 48)
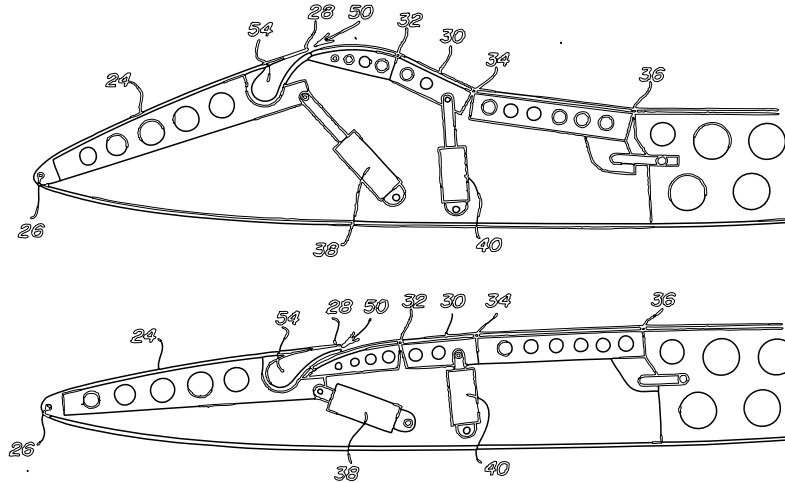
Figure 2.21 Change in Airfoil Thickness to Accommodate Supersonic Cruise and Good Low-Speed Performance (copied from Ref. 49)
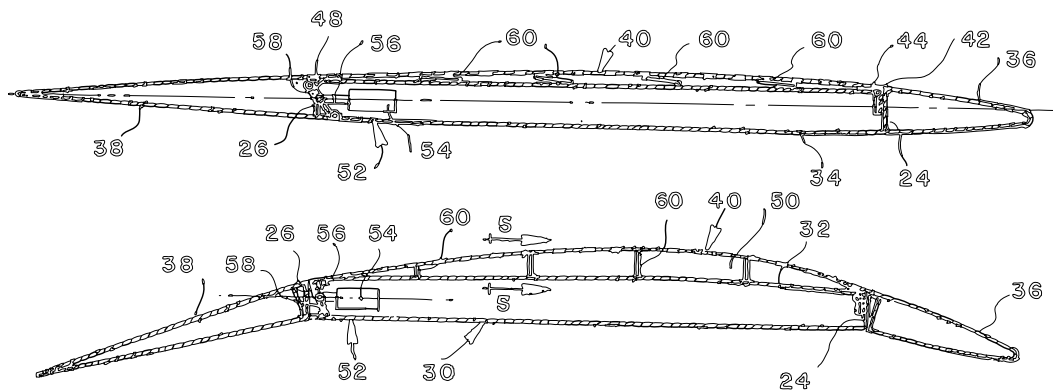
Figure 2.22 Airfoil having Adjustable Thickness Ratio (copied from Ref. 50)

27

2.2.3 Variable Camber

A second characteristic of the wing section geometry that is important in determining its maximum lift capability is its camber. As was already clear from Figure 2.18, the more positive camber is present, the higher the lift that can be generated. On conventional transonic wings, the deployment of high lift devices increases the effective camber of the airfoil (see Figure 2.12). High-lift airfoils usually exhibit a large amount of camber to achieve a large value of $c_{l\,max}$.

Apart from the amount of camber in an airfoil, the chordwise position of maximum camber is of importance to the maximum lift. Another parameter that influences the maximum lift is the change in local thickness, Δy, of the airfoil between 0.15% and 6% chord. It was shown that when $\Delta y > 0.03c$ the effect of camber on maximum lift coefficient becomes negligible [51, 52]. Furthermore, it was demonstrated that by increasing the camber to 6% of the airfoil chord and locating the point of maximum camber at 30% chord, the increase in $c_{l\,max}$ with respect to a baseline symmetric airfoil was as much as $\Delta c_{l\,max} = 0.65$, provided that $\Delta y = 0.015c$. Figure 2.23 shows how the maximum lift coefficient is influenced by camber position and amount of camber.
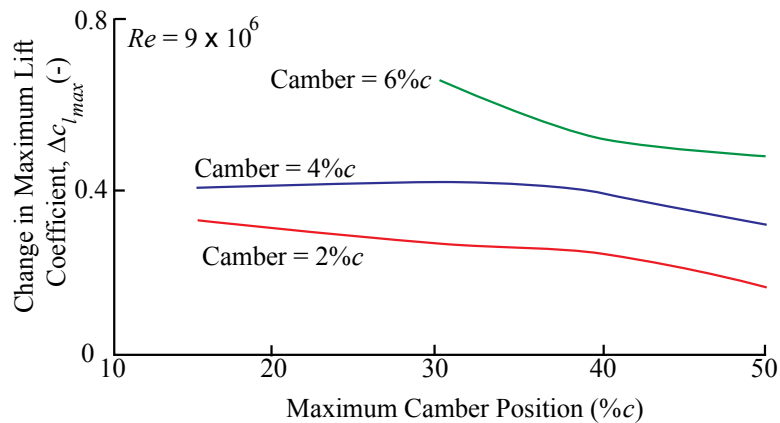
Figure 2.23   Effect of Maximum Camber Position on Change in Maximum Lift Coefficient, Plotted for Optimum Δy [38, 51]

In the 1920s a morphing wing concept for a triplane was conceived [53]. The middle wing relied on the local angle of attack to change its camber and consequently its maximum lift capability (see Figure 2.24). This simple concept of passive wing morphing did not require

pilot input but relied on a balance between the external aerodynamic forces and the internal spring force that dictated the shape of the airfoil. An example of active wing cambering is displayed in Figure 2.25 where a hydraulically powered mechanism is employed to increase the camber of the wing while the spars remain in a fixed position. According to the patent document that this figure was extracted from, the skin of the airfoil could be manufactured from flexible aluminum. Even though the mechanism could work well, the structure lacks an integral torque box that is essential to provide appropriate levels of torsional stiffness.

Low Speed Shape

Maximum Speed Shape
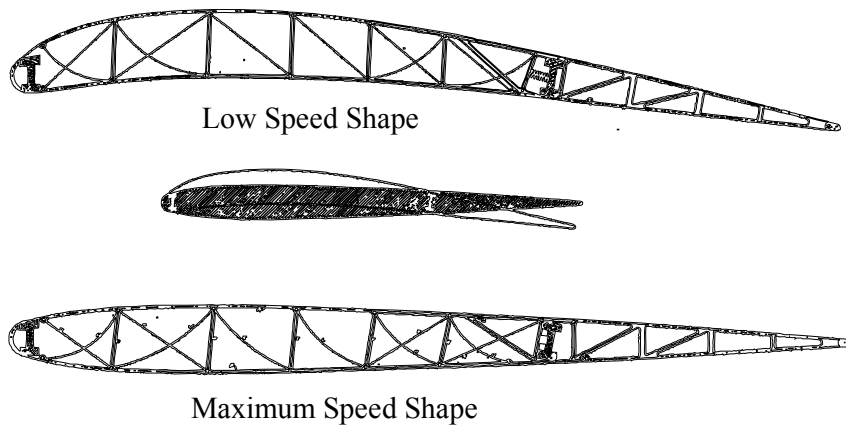
Figure 2.24   The Parker Variable Camber Wing [53]
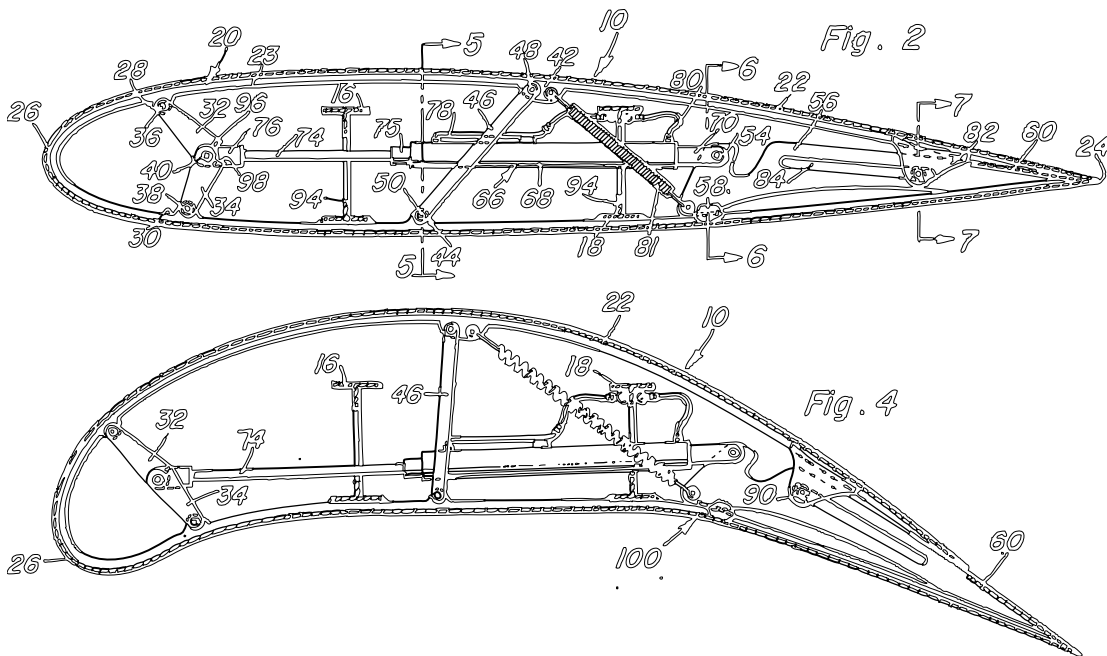
Figure 2.25   Variable Camber Airfoil and Mechanism (copied from Ref. 54)

Over the past three decades a renewed interest in wing morphing has sparked various re-search programs [55]. Among these programs was the Mission Adaptive Wing (MAW) re-search program that investigated the effectiveness of variable leading and trailing edge camb-er on an F-111 aircraft (see Figure 2.26). This wing had an internal mechanism to flex the outer wing skin and produce a symmetrical section for supersonic speeds, a supercritical sec-tion for transonic speeds, and a high-camber section for subsonic speeds. Flight tests demon-strated that an improvement in lift-to-drag ratio of 20% could be obtained in large parts of the flight envelope while some parts even showed an increase of 100% [56-59]. Even though the flight tests (Figure 2.27) demonstrated advantages of the wing morphing, there were signifi-cant drawbacks to the way the morphing was achieved. Bulky, heavy hydraulic screw jacks were employed to induce the deformation in the wing. In addition, internal mechanisms em-ploying multiple linkages ensured the desired kinematics of the mechanism. This resulted in a relatively heavy and complex actuation system.
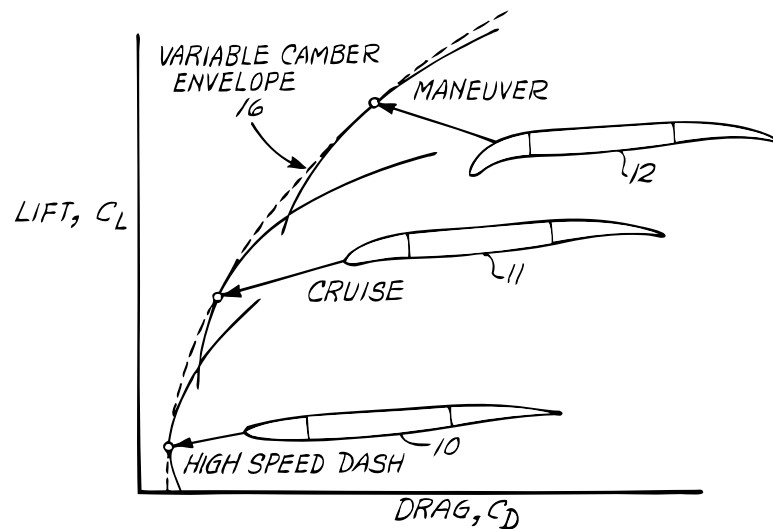
Figure 2.26   Mission Adaptive Wing Variable Leading and Trailing Edge Camber [58]

30
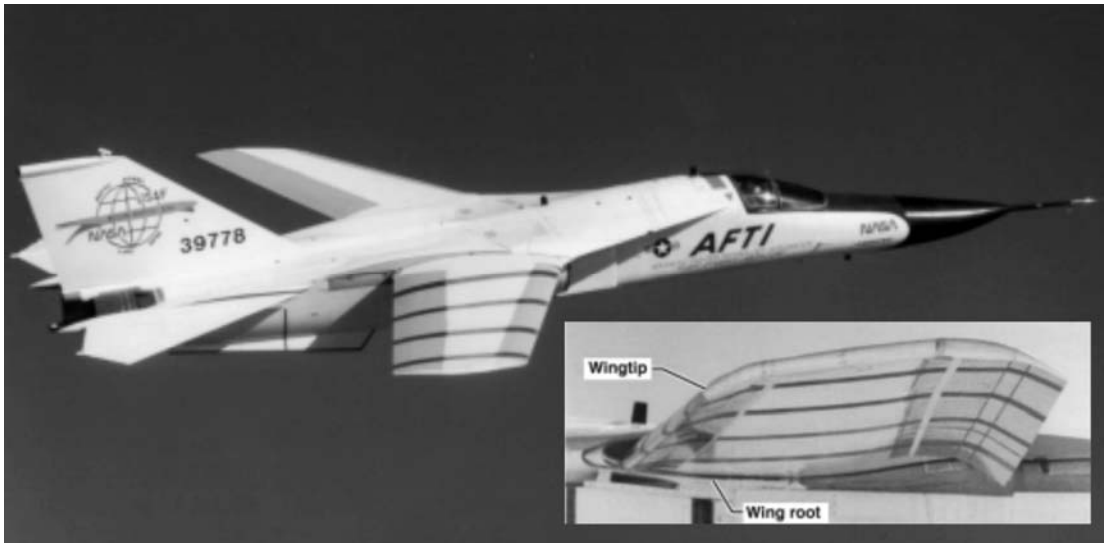
Figure 2.27   F-111 Mission Adaptive Wing [59]

It has been recognized that wing morphing on stiff aircraft structures requires dedicated structural mechanisms and often compliant wing skins (such as in the MAW) that allow for these shape deformations. As a result, compliant mechanisms [60-62] and compliant materials [62-64] have been conceived that can be used in morphing wings. Although effective in providing significant wing deformations and smooth transitions, compliant mechanisms are often much more complicated than the control surfaces they are replacing.

2.2.4 Variable Leading Edge Geometry

The shape of the leading edge is a third parameter that influences the maximum lift capabilities of an airfoil. As was mentioned in the previous section, to achieve a maximum $\Delta c_{l\,max}$ due to change in camber, there exists an optimum Δy. For symmetric airfoils (no camber), Figure 2.28 shows how the leading edge shape triggers the type of stall that occurs and its influence on the maximum lift coefficient. It shows that relatively sharp leading edges suffer from leading edge stall and have a low $c_{l\,max}$, while with incrementally more blunt airfoils, stall starts at the trailing edge and leads to higher lift coefficients. The (recirculation) "bubble" that is mentioned in this graph refers to the laminar separation bubble. This bubble occurs when the laminar boundary layer cannot follow the curvature of the airfoil, separates from it, becomes turbulent, and re-attaches to the airfoil again further downstream. At a cer-

tain angle of attack, the bubble bursts, no re-attachment occurs, and a sudden drop in lift results.
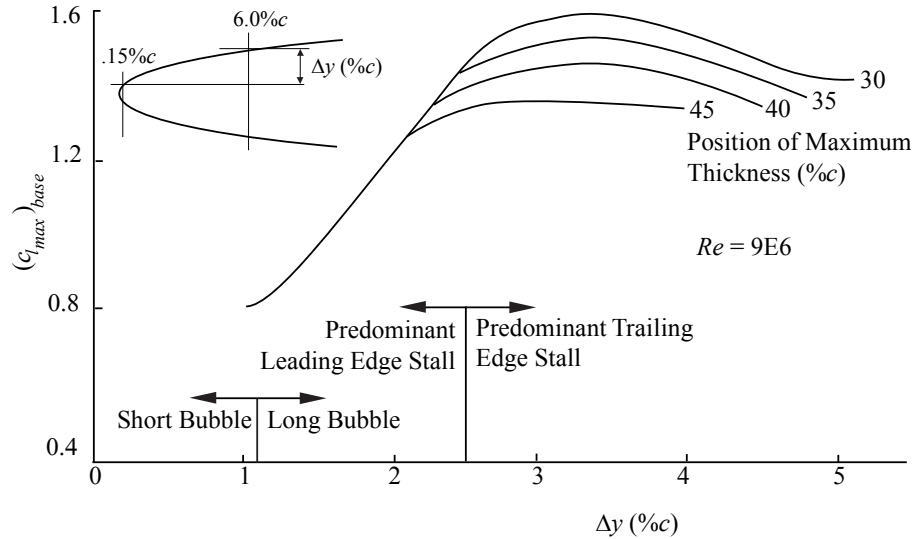
Figure 2.28   Basic Airfoil Maximum Lift Coefficient for Uncambered airfoils (Reproduced from p. 219 of Ref. 38)

It was already shown in the 1950s that modification of the nose of a 35º swept wing could result in significant changes in maximum lift coefficient. Demele and Sutton demonstrated that by adding body to the bottom side of a NACA 64A-010 over the first 20% of the chord resulted in an increase in $c_{l\,max}$ of 35% (at a Reynolds number of 11×10^6) [52].
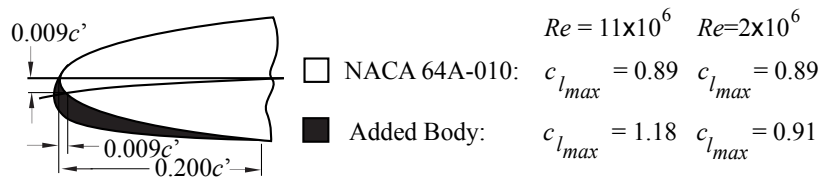
Figure 2.29   Example of Leading Edge Modification to Increase Maximum Lift Coefficient on a 35º Swept Wing (Reproduced from Ref. 52)

Closely related to the leading edge shape parameter, Δy, is the leading edge radius, R. Figure 2.30 shows an example of how the radius influences the maximum lift coefficient. A NACA 64A-010 has a maximum lift coefficient of 1.07. Increasing leading edge droop resulted in an increase in maximum lift coefficient of 0.37. Increasing the radius from 1.10%c to 1.50%c

32

yielded an additional increase in $c_{l\,max}$ from 1.44 to 1.65 bringing the total increase to 0.58 or roughly 50% of the original maximum lift [65]. Efforts to increase the maximum lift coefficient on a NACA 63012 airfoil yielded similar results. A larger nose radius (increased from 1.09%c to 3.5%c) was introduced. In addition, keeping the nose radius tangent to the upper surface contour of the basic airfoil resulted in an increase in leading edge droop. These combined measures resulted in a $\Delta c_{l\,max} = 0.35$ [66].

Basic Airfoil: NACA 64A-010, $Re=4\times10^6$

.0112c .0123c .0123c

0.075c 0.15c 0.15c

$R = .011c$ $R = .011c$ $R = .015c$
$c_{l_{max}} = 1.36$ $c_{l_{max}} = 1.44$ $c_{l_{max}} = 1.65$
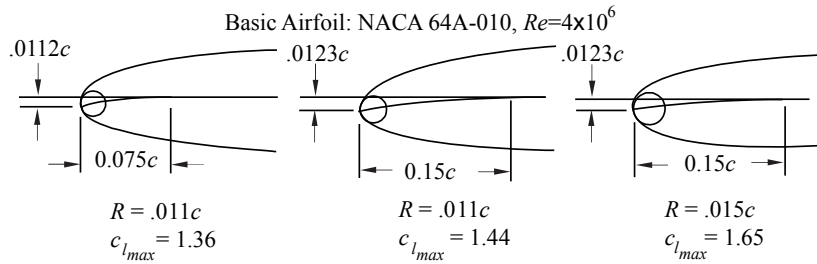
Figure 2.30   Nose radius Effect on Maximum Lift Coefficient (Reproduced from Ref. 65)

Increasing the nose radius reduces the local curvature of the airfoil which in turn lowers the leading edge pressure peak (see Figure 2.17 for comparison of sharp and blunt airfoils). Accordingly, the boundary layer is less likely to separate, which means a postponement of leading edge stall. All measures that are described above essentially aim to reduce the local over speeds at the leading edge. Apart from increasing the nose radius and adding body on the bottom side of the airfoil, other measures, such as adding body on the top side of the airfoil, also proved to be effective on other airfoils [67]. It depends on the contour of the basic airfoil which measure proves to be most effective in increasing the maximum lift coefficient.

Examples of leading edge morphing are often found in conjunction with thickness and camber adaptivity as shown in Figure 2.21 and Figure 2.25. This means that by changing the thickness or camber the leading edge geometry is also altered in a favorable manner. Research has been done on helicopter blades to ensure attached flow on the retreating blade at high angles of attack (see Figure 2.31). It was shown that by using a compliant mechanism inside the blade leading edge, the leading edge geometry could be altered on a 3-ft-span full-scale chord blade at a rate of 6Hz. Figure 2.32 shows patent drawings from the Boeing Company. An adaptive leading edge, similar to a drooped nose, was designed where the top skin curved continuously when the nose deflected downwards.
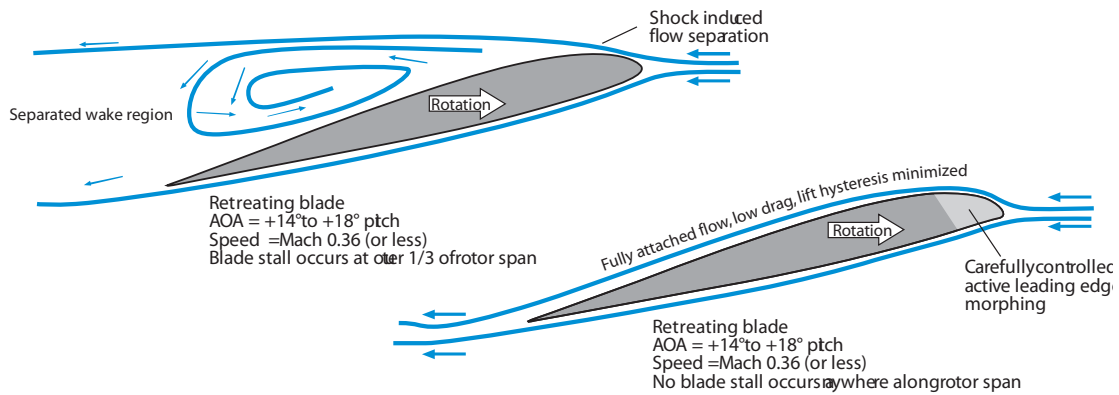
Figure 2.31   Leading Edge Morphing Avoids Flow Separation on the Retreating Helicopter Blade (modified from Ref. 68)
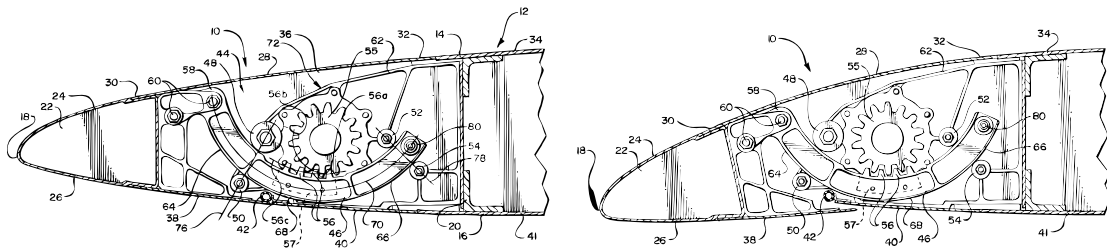
Figure 2.32   Adaptive Leading Edge Mechanism (copied from Ref. 69)

2.2.5 Variable Trailing Edge Geometry

Significant effort has been conducted in the realm of morphing flaps or ailerons. The benefit of continuously deforming flap is that there are no gaps or seams between individual wing components. This is beneficial during cruise operations because it decreases friction drag. Because adaptive flaps are integrally attached to the main wing, they do not benefit from the jet effect that exists when a flap is slotted. In addition, they lack any Fowler motion. Therefore, it is expected that maximum lift capability of an adaptive flap is not as high as that of any of the slotted or Fowler flaps of Figure 2.12. However, the smooth transition between main wing and adaptive flap, makes it an excellent candidate for an adaptive control surface such as an adaptive aileron.

The concept of an adaptive aileron has been explored by various researchers. The DARPA smart wing program encompassed the design and wind tunnel testing of a continuously deforming trailing edge [8, 9, 70]. A silicone skin was used to allow for the continuous morphing of the trailing edge control surface (see Figure 2.33). On a smaller scale, adaptive ailerons

that relied on postbuckled precompressed (PBP) piezoelectric actuators were applied on a subscale UAV to demonstrate flight control. This concept also relied on a highly compliant rubber skin for smooth geometry changes (see Figure 2.34). On even smaller UAVs that rely on membrane wings trailing edge morphing has been shown work very well [71]. Membrane wings, however, do not have the torsional and bending stiffness that is required for larger UAVs and manned aircraft and the morphing techniques pioneered on these small aircraft can therefore often not be extrapolated to larger aircraft.
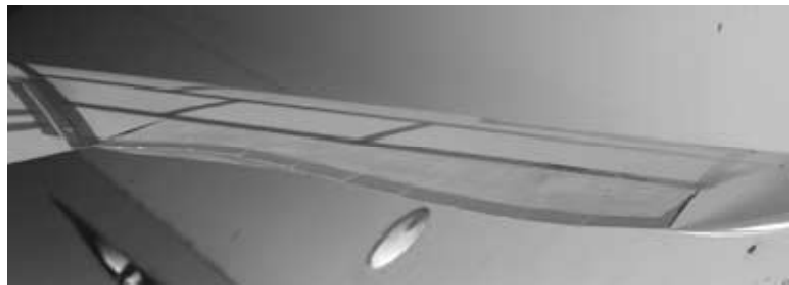
Figure 2.33   Geometry of Smoothly Contoured Control Surface [70]
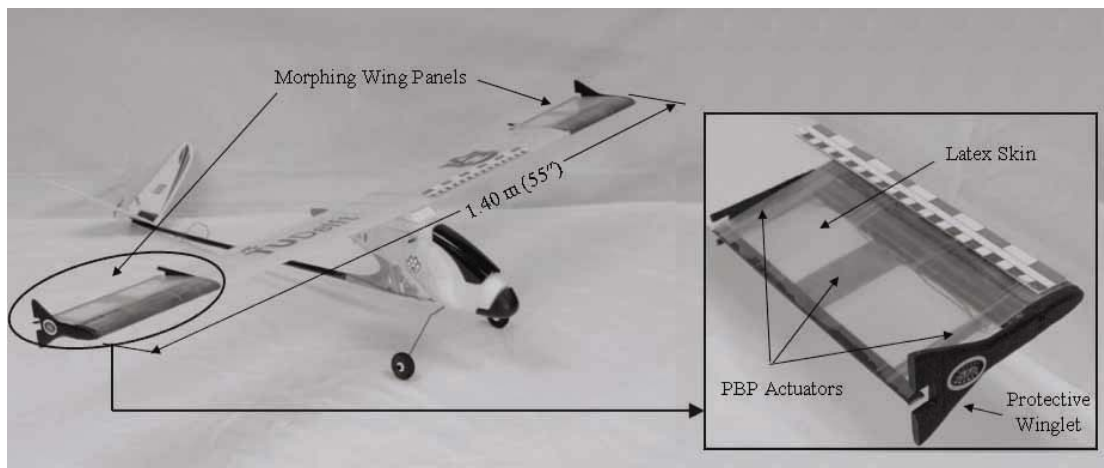
Figure 2.34   UAV employing PBP Actuated Morphing Wing for Roll Control [27]

One particularly interesting concept with respect to the topic of this dissertation is the use of a nastic structure to flex the aft part of an inflatable wing. A nastic structure is a biomimetic device whereby materials are activated in order to generate large strains while still performing a structural function. The narstic structure that was used on the inflatable wing consisted of a series of small pouches at the top and bottom skin of the wing (see Figure 2.35). By in-

flating or deflating the individual pouches a change in strain could be accomplished that induced a curvature over the aft part of the wing [72].

Airfoil Upper Surface -
Cells Deflated

Airfoil Lower Surface -
Cells Inflated
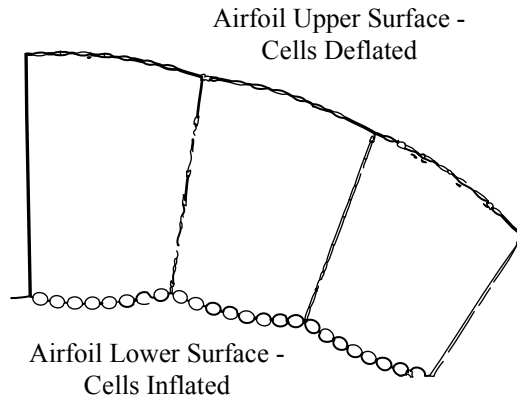
Figure 2.35   Nastic Structure to Deform Inflatable Wing Section (copied from Ref. 72)

2.2.6 Flow Control

To enhance maximum lift capabilities, aircraft can often benefit from passive or active flow control. A commonly used example of flow control is the use of vortex generators (VGs). VGs are local imperfections on a wing surface that induce streamwise vortices that give rise to mixing of the flow, energizing the boundary layer and thereby delaying separation [73]. They come in a variety of geometries (see for example Ref. 74) and their optimal placement, spacing and size largely depend on the flow characteristics and the type of flow problem [73]. VGs are often found in front of the ailerons to keep the flow attached at high angles of attack and to ensure lateral control. The most common use of vortex generators has been to postpone stall and increase the maximum lift coefficient. This can be achieved by placing VGs on the main wing, on the flaps, or on both [73]. Because they penetrate the flow, a disadvantage of the VGs is the increase in profile drag during cruise. To counteract this problem smart vortex generators (SVGs) can be used that only penetrate the flow when a high maximum lift coefficient is required (see Figure 2.36). SVGs using shape memory alloy actuators were demonstrated to increase the maximum lift coefficient of a NACA 4415 wing section with 14% [75].
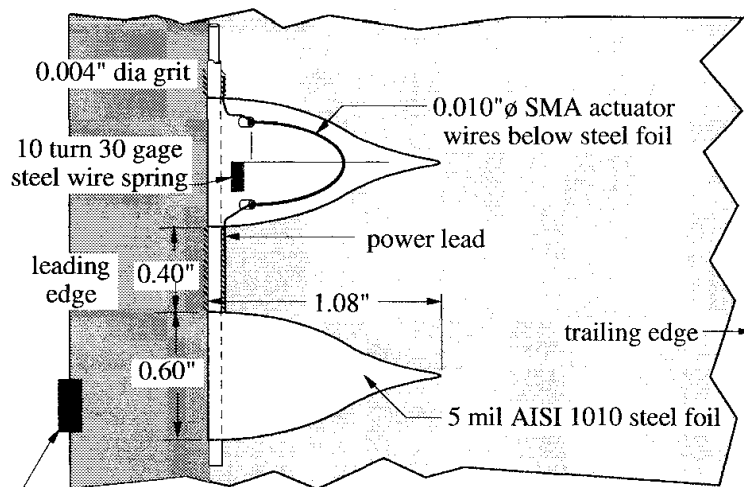
Figure 2.36   Ramp VG and SMA Actuator Filament Arrangement (Top View) [75]

Another way of increasing the maximum lift capability of a wing is to apply a Gurney flap at the trailing edge. A Gurney flap is small vertical tab (generally not larger than $5\%c$) that makes a right angle with the pressure surface at the trailing edge of the wing [40, 76]. It creates a local increase in pressure which gives rise to a higher lift coefficient. It also induces a significant increase in pitching moment because of high aft loading [77]. Different geometries of Gurney flaps have been investigated in terms of lift, drag and pitching moment characteristics [78, 79]. For example, a NACA 23012 airfoil at a Reynolds number of $1.95 \cdot 10^6$ experienced a maximum-lift increase of 49% (from 1.26 to 1.88) due to the application of a $5\%c$ straight Gurney flap [77]. Rather than applying the Gurney flap to the end of the airfoil, it can also be attached to the trailing edge of a flap. Application of a $1\%c$ Gurney flap on $30\%c$ Fowler flap resulted in an increase of 3% in $c_{l_{max}}$ at a flap angle of $39°$ [80]. A 5%c Gurney flap on a 2-element, single-slotted wing showed an increase in $c_{l_{max}}$ of 20% (from 1.70 to 2.05, see Ref. 81).

2.2.7 Variable Spanwise Twist

Another way of achieving wing deformation is by utilizing the aerodynamic loads that are already present. This can be beneficial because deformation of a wing structure generally requires considerable amounts of energy [82]. Extracting this energy from the airstream rather than from actuators reduces the size and consequently the weight of the wing-movable. Research into these so-called active aeroelastic wings (AAWs) has resulted in successful flight

tests of an F/A-18A (Figure 2.37) that employed a flexible wing that demonstrated spanwise twist as a result of small leading and trailing edge control surface deflection [83-86]. Although roll rates of the aircraft increased to 400 deg/s, a complex control mechanism was required to deflect the various control surfaces in order to obtain the required wing twist. In addition, the torsional rigidity of the wing was intentionally weakened which must have decreased the flutter and divergence clearance.

Other academic efforts that demonstrated the use of aeroelastic flight control include the use of adaptive internal structures. This concept relied on a change in wing stiffness to have the air loads induce wing twist [87-89]. Both internal and external mechanisms relied effectively on the twisting of the wing to induce roll control.

Figure 2.37   F-18 Employing Active Aeroelastic Wings [86]

Because aeroelastic active wings can be sensitive to adverse aeroelastic effects such as aileron reversal, static divergence, or flutter, research has been conducted to make morphing wings that rely on internal actuators for deformation. Driven by the knowledge that washout-adaptive wings can reduce induced drag as well as control the rolling motion, researchers have implemented a variety of twist active wings on (subscale) UAVs [90, 91]. An example is shown in Figure 2.38, where a UAV uses so-called twisterons that can be adjusted to decrease lift-induced drag during cruise. DARPA's smart materials and structures demonstration program explored the use of an SMA torque tube to twist the wing [70]. The main drawback of twist-active wings is that there is should always be a trade-off between torsional stiffness on the one hand and actuator sizing on the other hand. In general, powerful (heavy) actuators are required to torque a structure that is designed to be torsionally stiff. One concept

of active wing twist, however, relied on the warping of the skin to induce the torsional change. Because the skin warping was done by using a jack-screw, the torsional rigidity was not compromised and relatively light-weight actuators were required [92].

Figure 2.38   Experimental Aircraft with Operational Twisterons (3.2m span) [93]

2.2.8 Variable Wing Sweep, Aspect Ratio, and Surface Area

For a given airfoil (2D) shape, the thickness ratio (t/c) is often the most important parameter that influences the drag divergence Mach number. Figure 2.39 shows how for supercritical and NACA airfoils the thickness ratio influences the drag-divergence Mach number. According to this graph, for supercritical airfoils, the drag-divergence Mach number decreases linearly according to $M_{DD} = 0.92 - 1.16\left(^t/_c\right)$. For example, decreasing the thickness of a 10% thick airfoil down to 8% increases the drag-divergence Mach number from 0.80 to 0.83.
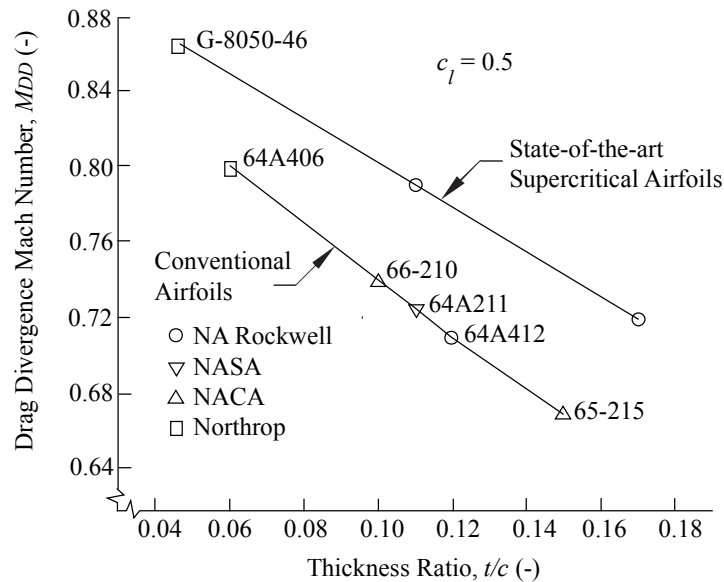
Figure 2.39   Effect of Thickness Ratio Drag Divergence Mach Number for NACA and supercritical Airfoils (Reproduced from p. 151 in Ref. 42)

The drag divergence Mach number of a wing is typically a function of both the sweep of the wing and the thickness of the airfoil. The critical Mach number, M^*, is the Mach number at the onset of supersonic flow locally on the wing. The critical Mach number and the drag divergence Mach number can be roughly correlated according to $M_{DD} = M^* + 0.1$ [42]. By decreasing the airfoil thickness, the critical Mach number and hence the drag-divergence Mach number is decreased. Figure 2.40 shows how the critical Mach number varies with thickness and sweep angle for a wing of aspect ratio larger than 6 and a lift coefficient of 0.4. From this graph it can be seen that in order to decrease the critical Mach number (and hence the drag-divergence Mach number) a trade off needs to be made between airfoil thickness and sweep angle. The influence of the sweep angle on the maximum lift coefficient is evident from Equation 2.3. It is therefore desired to keep the wing sweep as low as possible to maximize low-speed performance. Other disadvantages include (a) the added structural weight that is required to bear the torque load that is introduced by sweeping the wing, (b) reduced flap effectiveness , and (c) a spanwise drift over the wing that increases boundary layer thickness and leads to increased drag and reduced aileron effectiveness [43]. Because of these disadvantages, decreasing airfoil thickness would be a beneficial solution. However, this leads to other inconveniences like added structural weight to bear the bending moment of the wing

and less volume for fuel storage. Furthermore, in Section 2.2.2 it was shown that thin airfoils generally have worse high-lift characteristics than thick airfoils, which require higher take-off and landing speeds.
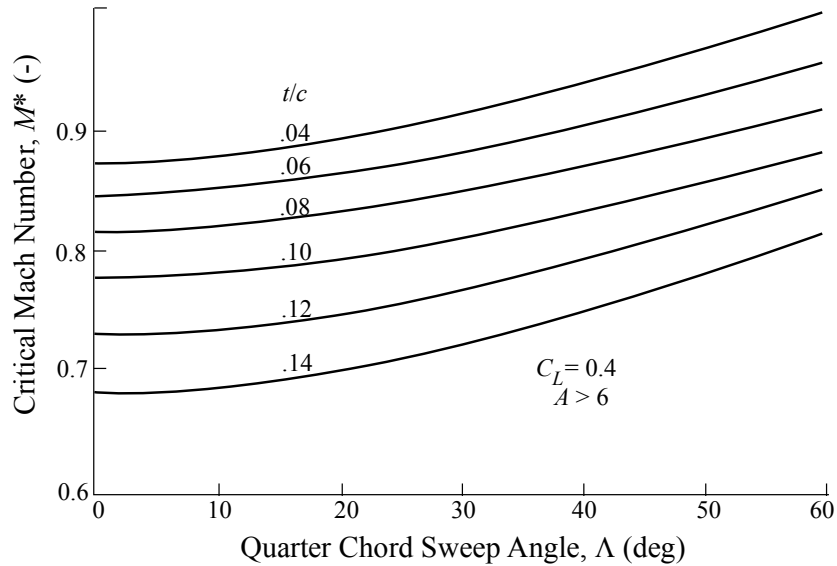
Figure 2.40   Effect of Thickness Ratio and Sweep Angle on Critical Mach Number (Reproduced from p. 151 of Ref. 42)

The drag-divergence Mach number of a swept wing can be related to the drag divergence Mach number of the same wing without sweep according to [43]:

$$M_{DD-swept} = M_{DD-unswept}/\cos \Lambda_{c/4} \tag{2.4}$$

Since transonic aircraft cruise close to the drag-divergence Mach number ($M_{DD} \cong M_{cr}$) an example of the relation between sweep angle and Mach number for the aircraft of Table 2.2 is presented in Figure 2.41. The direction of the arrow in this graph indicates that most efficient transonic wings both have low sweep angles and still cruise at relatively high Mach numbers. From this graph it becomes apparent that particularly the Fokker 70 employs a very efficient transonic wing design. Its wing is swept backwards over only 17 degrees and still its cruise Mach number is 0.77. Remember that this aircraft does not have any leading-edge high-lift devices to increase its maximum lift coefficient at take-off and landing, which demonstrates that the lack of sweep makes for better low-speed wing performance. An explanation for these performance characteristics is the relatively thin wing which measures only 12.3% at

the root and 9.6% at the tip. For comparison, the wing of a B767-400 has a thickness of 15.7% at the root, 28% more than the Fokker 70 [35].
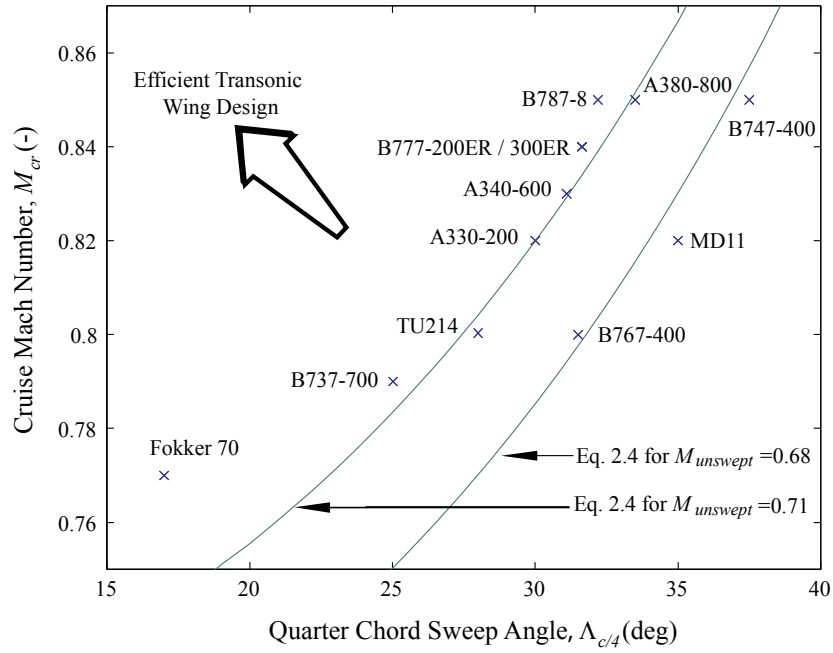
Figure 2.41   Wing Sweepback Angle versus Cruise Mach Number (Data from Table 2.2)

Planform morphing is yet another form of wing shape deformation that allows an aircraft to expand its flight envelope and fly efficiently in both the high speed and low speed realm. An example of planform morphing was successfully demonstrated in 2006 on both a wind-tunnel model and a scaled prototype [94, 95]. Using a scissor-type mechanism this wing was capable of changing its span, planform area, aspect ratio and sweep angle. An elastic skin ensured a smooth wing surface at each stage of wing morphing. Figure 2.42 shows the prototype and two details of the wing structure. Even though the effectiveness of this wing was excellent, penalties in terms of complexity and the impossibility to store fuel become clear from the two details in Figure 2.42. In addition, the complex wing structure in combination with the re-quirement of powerful actuators led to a very high weight penalty.

Figure 2.42   Example of Planform Morphing Wing and Details of Wing Structure [96]

Another approach to planform morphing used a hinged segmented wing that could fold partly against its fuselage, thereby decreasing the wing surface area and increasing the effective sweep angle [97, 98]. This concept is schematically shown in Figure 2.43. The design of this folding wing concept incorporated tailored seamless skins around the hinge points such that a smooth surface was ensured in all positions of the wing. By reducing the effective surface area when in folded position the intention was to reduce drag and be able to fly efficiently in the high speed realm. Wind tunnel tests successfully demonstrated the morphing mechanism, but were inconclusive about the expected drag reduction at transonic and supersonic speeds [99]. It might be expected that interference-drag penalties occurring in folded position negate the drag reduction due to increased effective sweep and decreased wing area.
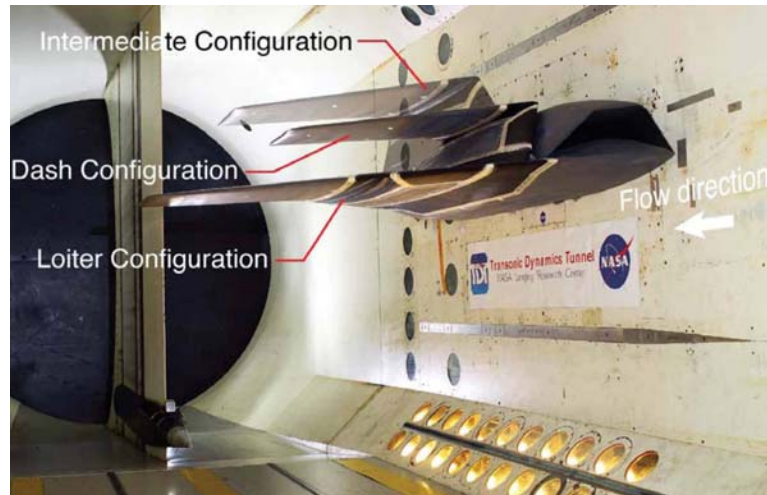
Figure 2.43   Folding Wing Concept [99]

Continued efforts are being made to conceive new morphing concepts that could potentially be used in future aircraft designs. These efforts include research into new compliant mechan-

isms, adaptive materials, and aircraft configurations that enable morphing flight control. The majority of the research is tailored towards novel UAV designs and is often still in the conceptual stage of the design. An overview of these investigations can be found in Ref. 55.

2.2.9 Lessons Learned and Applicability to Passenger Aircraft

The overview of morphing projects in the past decades has been primarily targeted towards military applications, particularly UAVs. Passenger aircraft have to comply with strict rules and regulations (FARs) in terms of structures and materials. Therefore, morphing structures have been limited to the high lift devices such as flaps and slats. An example of wing morphing on passenger aircraft can be found on the (cancelled) Boeing 2707 supersonic transport (SST), which was proposed in 1964 in response to the European Concorde. A swing-wing configuration similar to that of the F-111 (and later F-14) was used to change the wing sweep between subsonic and supersonic speeds. However, due to insurmountable weight problems associated with the swing-wing mechanism Boeing discarded this morphing concept in favor of a fixed delta wing [100]. The project was cancelled before one prototype was built due to heavy opposition by (among others) environmentalists [101].

Figure 2.44   Artist's impression of the Boeing 2707 SST, version 1967 [102]

Since contemporary passenger aircraft rely on their efficiency in order to be cost effective, changes in structural arrangement are only justified when direct operating cost (DOC) is decreased and the structural integrity is not compromised. The morphing wing concepts which

were conceived for military applications (e.g. F-111, F-14 and F-18 AAW) are therefore un-suitable for commercial applications. The Mission Adaptive Wing [57], the tendon actuated structure [13], and the variable planform wing [95] are examples of complex internal struc-tures that require large numbers of parts, hinges and actuators to work properly. Maintaining such structures can be costly and is, therefore, unattractive for commercial airliners. Other disadvantages such as the limited ability to store fuel in the wings or a complex control sys-tem have prevented morphing technology from transferring from the experimental military aircraft to modern transport aircraft. As was mentioned before, because adaptive materials have not been certified for use in primary or secondary aircraft structures, applying them on commercial aircraft is still impossible.

Commercial applications of morphing structures can only be viable if certifiable systems (in-cluding certifiable materials) are used, direct operating costs are decreased, and structural integrity is maintained. To satisfy these disparate requirements, a radically different approach is required. The following chapters present a new morphing wing concept that relies on solid state actuators to deform the wing to provide high lift during take-off and landing and low drag during cruise made from certified materials. To be competitive with conventional high lift devices on modern jet transports this morphing wing should produce values of $C_{L_{max}}$ that are comparable to those presented Figure 2.13. Furthermore, there is the objective to keep the number of parts, number of actuators and system complexity as low as possible. This enables a reduction in both manufacturing and maintenance cost. Finally, no weight, aerodynamic or aeroelastic penalties may arise as a result of the morphing concept. In summary, this novel morphing wing concept is relatively simple to manufacture and maintain, only contains certi-fied materials and is competitive with contemporary conventional wings in terms of aerody-namic efficiency during cruise and high lift performance during take-off and landing.

2.3   The Standard and Non-Standard Atmosphere

The journey of a typical jet transport aircraft imposes different atmospheric conditions on the aircraft. Most jet transports cruise at altitudes between 10 and 13 kilometers (see for example Table 2.2 on page 22), which means lower temperature, density, and pressure than at take-off and landing conditions. This section shows the temperature, pressure and density distribution

in terms of latitude and altitude of the Earth's atmosphere in standard and deviated conditions.

2.3.1 International Standard Atmosphere

The international standard atmosphere (ISA) is a reference atmosphere which represents globally averaged values of (among others) temperature, pressure, and density with altitude. Many books (for example Ref. 1 and Ref. 103) list the reference atmosphere as an appendix and refer to it for aircraft performance calculations. To capture pressure and temperature properties of the atmosphere at various altitudes, appropriate models have been developed. In the troposphere, change in temperature with altitude (or lapse rate) has been established at $c = -6.5°C/km$. The temperature varies linearly with altitude, h, according to:

$$T = T_0 + ch \tag{2.5}$$

The ambient pressure can then be calculated according to Ref. 1:

$$p_a = p_0 \left(1 + c\frac{h}{T_0}\right)^{-g_0/cR} \tag{2.6}$$

Notice that for ISA conditions the following values apply: $p_0 = 101325$ Pa, $T_0 = 288$ K, and $g_0 = 9.81$ m/s^2. Furthermore, R is the perfect gas constant for air and amounts to 287.15 J/kg/K.

2.3.2 Seasonal Deviations from ISA

In reality the atmosphere is never constant and standard atmospheric conditions are rarely encountered. The influence of seasons provides the first deviation from standard conditions. A second deviation comes from the position on Earth in terms of latitude. Figure 2.45 shows how the mean temperature varies with altitude and latitude. Data was taken from Ref. 104 which presents measurements that were taken between -10˚S and 75˚N latitude and were averaged over the circles of constant latitude (see Appendix A for a clear outline of Earth latitudes). The difference between the isotherms in (a) and (b) shows that during winter the temperature distribution is more dependent on latitude than during summer. An aircraft flying over the tip of Greenland (60˚N latitude) at an altitude of 10km would therefore experience a temperature of 217K during winter and 226K during summer (on average). Furthermore, at

the tropics there is hardly any seasonal influence on the temperature distribution. The data presented in this section were taken from Ref. 104 and were compared to the reference atmospheres for aerospace use, given in Ref. 105, resulting in almost an exact match.

(a) **Winter Temperature, T (K)**   (b) **Summer Temperature, T (K)**
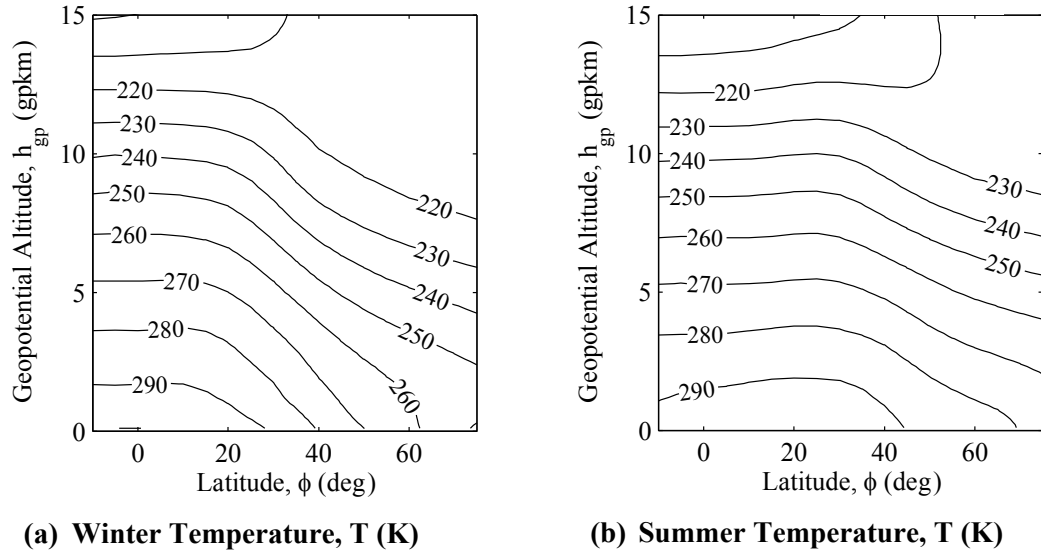
Figure 2.45   Isotherms for Mean Winter and Summer Atmospheric Conditions [104]

In contrast to the global temperature distribution, Figure 2.46 demonstrates that the mean global pressure distribution is only mildly dependent on latitudinal and seasonal changes. The upper layers of the troposphere show a somewhat higher variability while near sea level the variations are almost negligible.

(a) **Winter Pressure, p_a (hPa)**   (b) **Summer Pressure, p_a (hPa)**
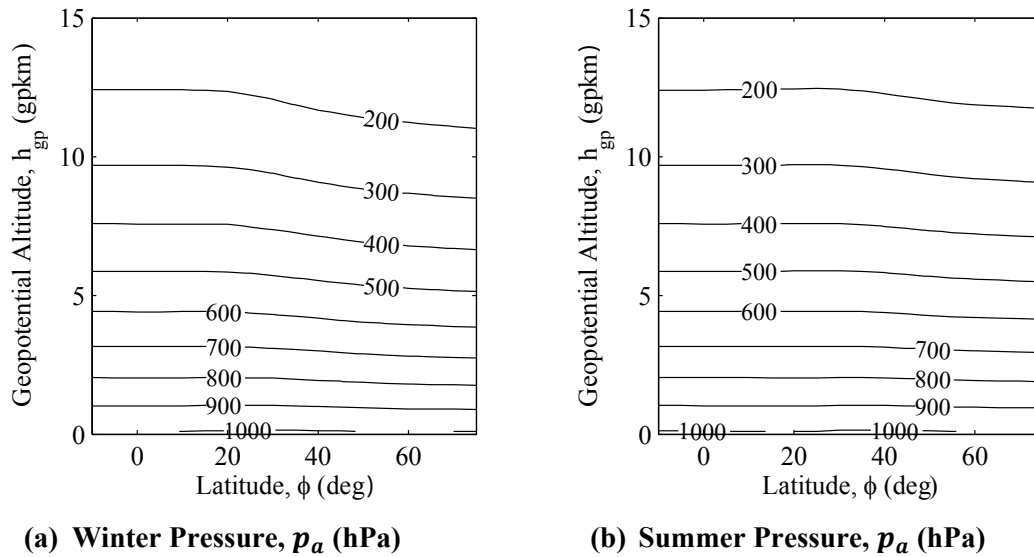
Figure 2.46   Isobars for Mean Winter and Summer Atmospheric Conditions [104]

By using the mean temperatures and pressures and assuming that air behaves as a perfect gas the global density distribution can be calculated (using the perfect gas law, $p = \rho R T$, and $R = 287$ J/kg/K). The density distribution, which is presented in Figure 2.47, demonstrates that near the surface the mean density in both winter and summer is dependent on latitude, while at higher altitudes the isochors show little latitudinal or seasonal variation. The isochors of Figure 2.47 are important for aircraft cruise and airfield performance because they directly relate to the amount of lift the wings can generate. The temperature on the other hand only plays a role in the cruise condition because it determines the local speed of sound, $a = \sqrt{\gamma R T}$ ($\gamma = 1.4$), and therefore the cruise velocity of the aircraft. The small seasonal and latitudinal variability in mean densities at altitudes between 10 and 15km indicate that the cruise altitude for aircraft is fairly independent of place and time.

Contrary to cruise performance, airfield performance *is* dependent on the latitudinal position and seasonal time of the year. Figure 2.47 demonstrates that near sea level mean air densities increase with latitude and are higher in winter than in summer. A statistical relationship seems to exist between temperature and density. Lower densities imply that aircraft need longer take-off distances, not only because of less lift capability but also because of reduced engine thrust [1].

(a) Winter Density, ρ (kg/m³) **(b) Summer Density, ρ (kg/m³)**
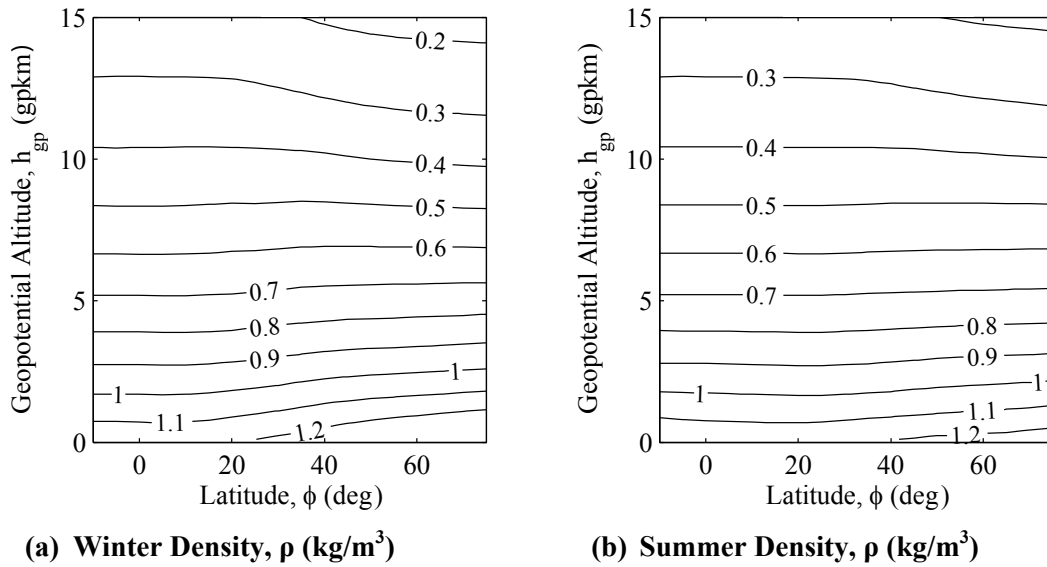
Figure 2.47   Isochors for Mean Winter and Summer Atmospheric Conditions

From the data presented in Figure 2.45 to Figure 2.47 the relation between temperature and density was investigated up to altitudes of 3gpkm. This relation is shown in Figure 2.48 for mean winter conditions. Investigating summer conditions resulted in a close match with the winter data, only over a smaller range of temperatures and was, therefore, not drawn in. The seasonal influence was negligible and data from latitudes between 10˚S and 75˚N was used. For this reason, it was anticipated that the temperature-density relation as presented in Figure 2.48 was representative for global atmospheric conditions. Isobars were drawn to show the pressure-temperature relation according to the perfect gas law. It can be seen that at low altitudes (up to 1gpkm) the density-temperature relation followed the shape of the isobars closely, resulting in good predictability of aircraft thrust and lift as a function of temperature only.
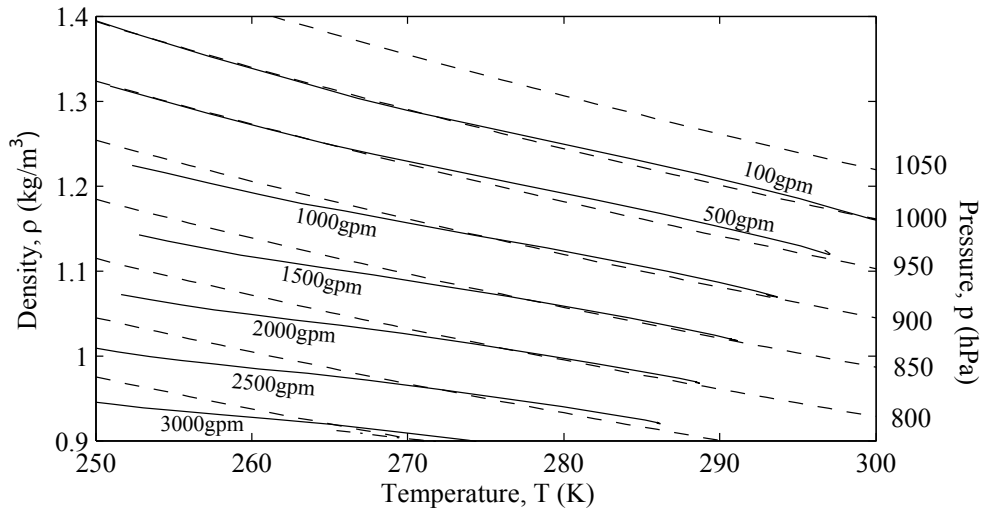
Figure 2.48   Winter Temperature and Density Relation at Low to Moderate Altitudes

2.3.3 Latitudinal Deviations from Standard Atmosphere

The previous section discussed mean atmospheric conditions during winter and summer. Assuming a normal distribution, Ref. 104 also listed the variation (VAR) in geopotential altitude and temperature. From the variation the standard deviation could be calculated according to:

$$\sigma = \sqrt{VAR(X)} \tag{2.7}$$

Extreme conditions during winter and summer were found at 2 times the standard deviation, which accounted for 5% of winter or summer days (see p. 122 of Ref. 106). Acknowledging that during winter only the cold extremes were of interest and during summer only the warm extremes resulted in extremes which only occurred 2.5% of the time during winter or summer. This translated into 2-3 extreme temperature days per season.

Analogous to Figure 2.45, Figure 2.49(a) represents the two or three coldest days of the year while (b) shows the two-or three warmest days in the year. A distinct difference between the isotherms of (a) and (b) can be seen. Not only is the latitudinal variation during the extreme winter days much higher than during the extreme summer days, the temperature difference between the two at a particular location can be as high as 50K. An aircraft cruising at an altitude of 10km and latitude of 40N experiences a 30K difference between a hot summer day (240K) and a cold winter day (210K).

50

(a) Winter Low Temperature, T (K)   **(b) Summer High Temperature, T (K)**
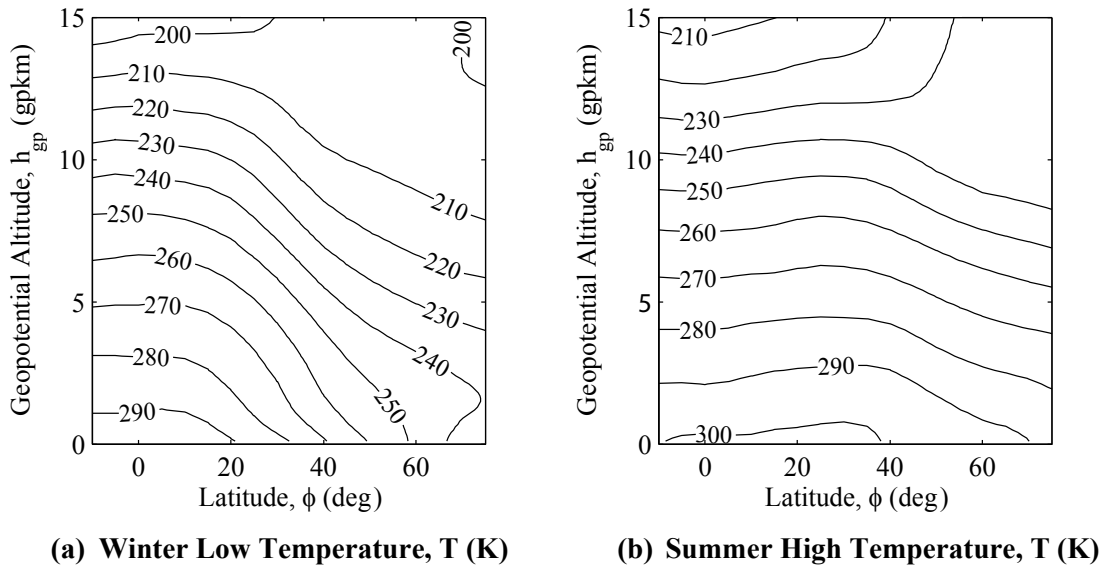
Figure 2.49   High and Low Extreme Values of Isotherms [104]

In addition to the standard deviation in temperature, the deviation in pressure was also inves-
tigated. Due to the fact that the pressure extremes during winter and summer were virtually
the same as the average pressure distribution as shown in Figure 2.46 it is not presented in a
separate figure. Due to the minimal pressure deviation, the extreme density was assumed to
be a function of temperature only. The relationship between temperature and density on ex-
tremely cold days is shown in Figure 2.50. As can be seen in Figure 2.50, near sea level the
density-temperature relation followed the isobars closely, while at higher altitudes the devia-
tion was larger, although a higher correlation with isobars was present than for the mean win-
ter temperatures. The same trends between density and temperature hold on extremely cold
days as well as on extremely hot days throughout the range of latitudes shown in Figure 2.49.
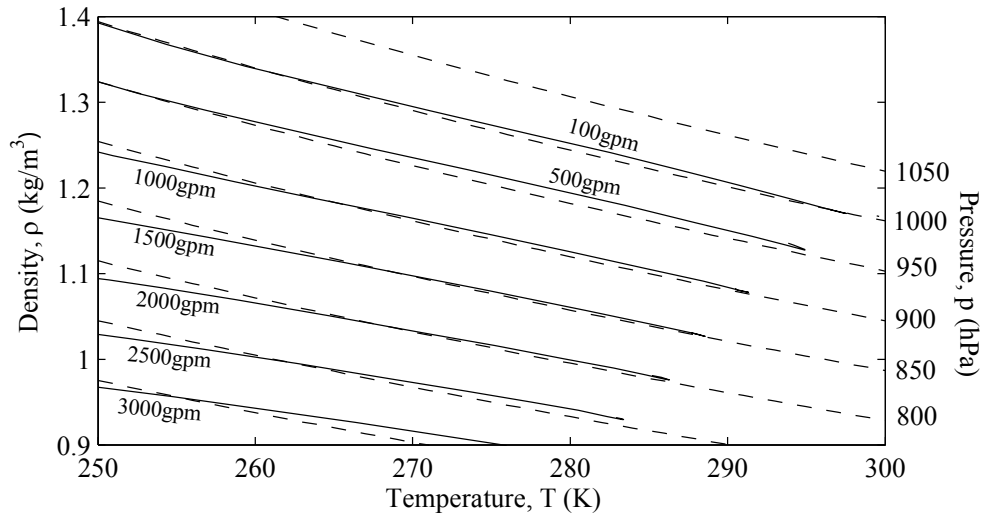
Figure 2.50   Temperature Density Relation at Extreme Cold Days

The fact that near sea-level the density can be predicted over a wide range of latitudes as a function of temperature is important if the ambient temperature is used as a stimulus to induce a structural wing deformation to increase the wing lift capability. Near sea level, for instance, this would mean that at lower temperatures this shape change would be less profound, meaning less high-lift capability. However, this could be compensated by the higher local density. At airports which are situated at higher altitudes (e.g. El Alto International Airport, Bolivia, $h = 4016$m) the colder temperatures would reduce the maximum lift capability due to the limiting deployment of the temperature-active structure, while the lower density would amplify this effect due to a decrease in lifting capability. In other words, at places where high lift capability is most vital, it would be least available.

Pressure-induced deformation, on the other hand, would be a much more reliable throughout seasons and latitudes. In the next chapter a qualitative analysis is presented that demonstrates how the lowering of the atmospheric pressure can be utilized as a reliable and powerful stimulus for wing deformation.

CHAPTER 3   PRESSURE INDUCED MORPHING AND ITS ENVI-SIONED APPLICATIONS

Based on the general outline of desired morphing properties, past efforts in wing morphing, and possible atmospheric stimuli, this chapter presents a novel aircraft morphing concept. For actuation, this concept can rely on the atmospheric pressure difference that exists between take-off and cruise altitudes or commanded pressure changes from within. A solid state compliant structure based on ordinary honeycomb cells is used to enhance structural deformation. Section 3.1 lays out the fundamentals of this concepts and explains why this is a feasible option to further benefit aircraft. In addition, Section 3.2 presents possible applications of this new technology. Finally, Section 3.3 describes the sources that are available to actuate this adaptive structure.

3.1   Fundamentals of Pressure Adaptive Honeycomb

In Chapter 1 it was hypothesized that an adaptive structure could be developed that had low part count, complexity and that would be manufactured from conventional aerospace materials. Pressure adaptive honeycomb is such a structure. It can be made from aluminum and nylon pouches at relatively low cost, does not comprise of many parts, and can be easily integrated in conventional aerospace structures. To the best of the author's knowledge, pressurized honeycomb has not been used in previous adaptive structures. Conventional inflatable structures have been around for several decades and have proven their applicability in aerospace structures [72, 107-112]. Partial inflation of individual cells on inflatable wings has been shown to alter airfoil geometry and change the aerodynamic characteristics [113]. The only pneumatic actuator that could be qualified as an adaptive structure is a pneumatic artificial muscle that was designed to actuate a flap system [114]. The load-bearing capacity of honeycomb was shown for a rigidified inflatable structure. It was shown that three-dimensional honeycomb blocks could be inflated and subsequently rigidified to form walls for residential buildings. It was shown that these structures yielded low material usage, a short manufacture time, and the ability to easily build complex structures [115]. Other applications of (non-pressurized) honeycomb have included energy absorption under in-plane compressive loading (see for example Ref. 116). Adaptive honeycomb has also been investigated where honeycombs made from SMA were used to enhance the energy absorption capability of honeycomb [117]. Even though all these research efforts have similarities to the

present invention, they all differ substantially from the fundamental concept that is the topic of this dissertation.

3.1.1 Why use Pressure Adaptive Honeycomb?

If atmospheric stimuli are used to control morphing properties on an aircraft, the predictability of these stimuli is important to the performance of the aircraft. In Section 2.3, it was shown that temperature varies considerably with seasons and latitudes. If an adaptive structure is built that relies on the temperature difference between take-off and cruise altitude these global and seasonal temperature variations should be accounted for. Tailored structures that rely on a particular transition temperature might work very well, as was demonstrated in Refs. 15, 16, 118. However, since these structures rely on specific uncertified shape memory alloys they cannot be used in aircraft primary or secondary structure. Adaptive laminates that rely on the difference in coefficient of thermal expansion (CTE) between individual lamina (e.g. an aluminum carbon fiber laminate), in turn, require a consistent temperature range to function properly. In addition to the varying ambient temperature it should also be noted that aerodynamic heating during transonic conditions might offset part of the temperature decrease that is encountered as aircraft climb to higher altitudes. In conclusion, temperature induced morphing would not be feasible to install on modern transonic jet transports.

Pressure, on the other hand, does show consistent values throughout seasons and latitudes. Pressure differences between take-off and cruise altitude can be as much 80kPa. Utilizing this pressure difference properly could result in solid stated pneumatic actuator elements producing large strains and relatively high forces. In addition, conventional, certified aerospace materials could be used to make up a comparatively uncomplicated adaptive structure.

One of the most compliant and widely used structural elements in aerospace structures are honeycombs. Generally, they are used as a low density core material in sandwich structures. Other applications of honeycombs are found in impact absorbing structures [119-121]. The ability of honeycombs to exhibit considerable strains without any plastic deformation was explored with the objective of constructing reinforced adaptive wing skins [122, 123]. Several types of honeycomb are used (Figure 3.1), of which the standard type is most common. The auxetic type can exhibit comparatively large strains in all directions, while the hybrid honeycomb exhibits no lateral contraction upon deformation in horizontal direction.

54

| Standard Honeycomb | Auxetic Honeycomb | Hybrid Honeycomb |
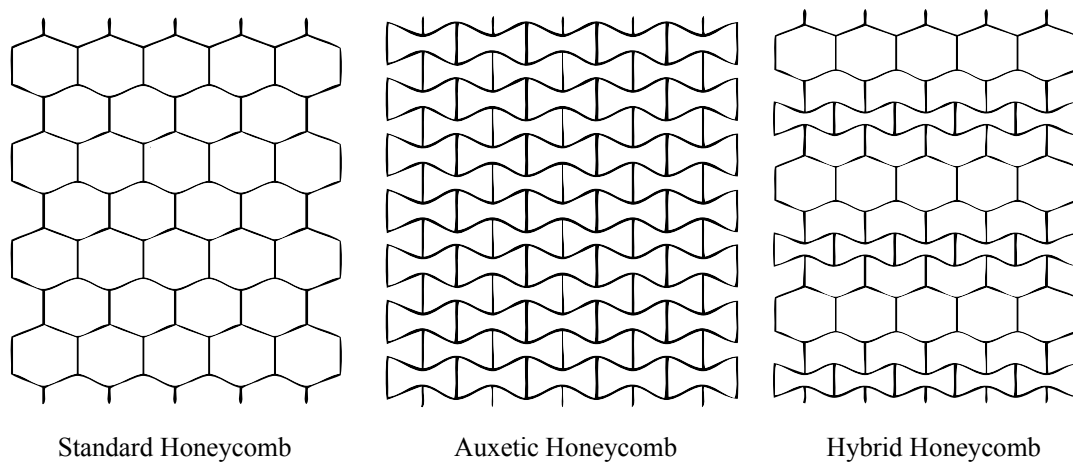
Figure 3.1   Types of Honeycomb used in Aerospace Applications [122]

A pressure adaptive structure based on honeycomb cells can be realized by sealing off the ends of each of the honeycomb cells at a particular geometry. When there is a fixed amount of air in each of the cells, the pressure between the inside and outside can control the shape of the honeycomb. By pressurizing the honeycomb it tries to assume a shape close to a perfect hexagon. Strained honeycomb therefore tries to go back to a perfect hexagonal shape when the pressure in the cell exceeds the ambient pressure. Consequently, airtight honeycomb could be used as a pressure adaptive structure, exhibiting comparatively large strains and high forces. It therefore qualifies as a narstic structure.

3.1.2 Strain and Curvature Induced by Pressure Adaptive Honeycomb

When the pressure difference between the cell and its surroundings is increased, the pressure stiffness increases accordingly. This pressure difference is generally referred to as the CDP (cell differential pressure): $CDP = p - p_a$, where p is the pressure in the cell and p_a the ambient pressure. Whether using the powered approach (controlling p) or relying on the change in ambient pressure (p_a), the geometric properties of the honeycomb pose some physical limits on the amount of shape deformation that can be achieved. Linear deformation of honeycombs is quite straightforward. Whether using the auxetic, regular or hybrid honeycomb, the longitudinal strain is independent on the number of cells that are stacked. The absolute change in geometry is linearly related to the strain of one cell. Figure 3.2 gives an impression

of how the lateral strain exceeds 60% compared to its inflated geometry when a CDP is applied to the pouches. This is one of the possible applications.

| Deflated Pouches | Inflated Pouches |
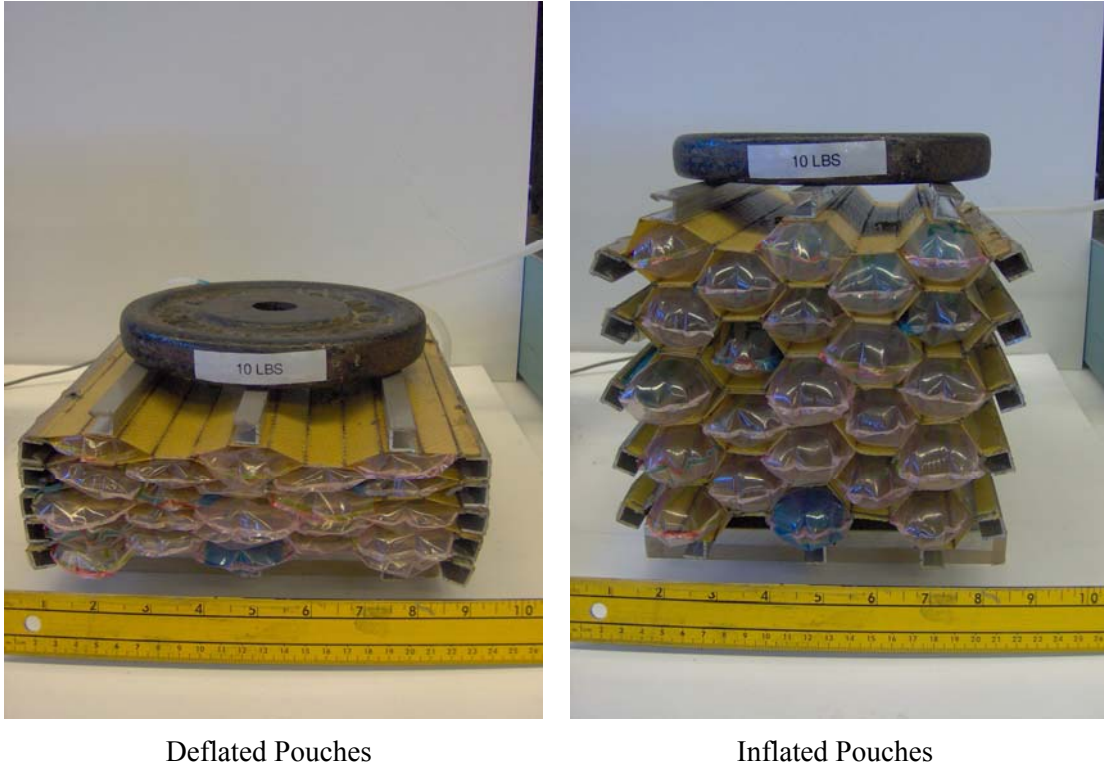
Figure 3.2   Proof-of-Concept Pressure adaptive Honeycomb Structure

In Table 3.1 three possible deformation schemes are presented. In the first column the deployed shape of the honeycomb is displayed. This is the shape the honeycomb cells would ideally take when no CDP (p) is applied. In the second column the perfect hexagon is shown. This is the shape the hexagon takes when an infinite CDP is applied. Next to that are the maximum strains in horizontal (x) and vertical (y) direction. With strains being defined as:

$$\varepsilon_x = \frac{x_0 - x_1}{x_0} \qquad\qquad \varepsilon_y = \frac{y_0 - y_1}{y_0} \qquad\qquad (2.1)$$

Those are the maximum strains that the honeycomb experiences during its transformation between the two shapes. The strain is measured with respect to dimensions of the honeycomb when its cells form perfect hexagons (as in the second column). The final column displays the change in honeycomb angle that is required. The honeycomb angle is the angle measured between the diagonal member and the horizontal and is denoted with θ. This parameter is a

good indication for the amount of bending that the walls of the honeycomb cells need to sustain in order to deform between the two given shapes.

Table 3.1   Geometric Properties of Pressure adaptive Honeycomb

$CDP = 0$	$CDP \to \infty$	$(\varepsilon_x)_{max}$	$(\varepsilon_y)_{max}$	$\Delta\theta$ (rad)
		-67%	$\pm15\%$	$\pi/3$
		-33%	$+15\%$	$\pi/6$
		$+33\%$	-100%	$\pi/3$
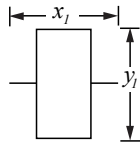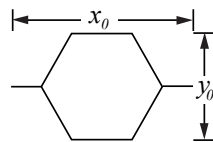
From the data of Table 3.1 it can be seen that the most linear displacement in x direction can be found when the honeycomb changes between the auxetic shape and the regular shape. A potential disadvantage for this shape is the fact that the strain in y direction changes sign during deformation. When a small amount of bending is required in the honeycomb (to prevent any plastic deformation, for example) it can be wise to limit the change in honeycomb angle and have a shape change between rectangular and hexagonal honeycomb. A deformation between those two shapes is also required in hybrid honeycomb if no net longitudinal strain is allowed. The deformation shown in the bottom row of Table 3.1 is similar to the one shown in Figure 3.2. There is a potential for very high lateral deformation.

Apart from linear deformation, pressurized honeycomb can be used to induce changes in curvature when it is bounded on one side to a plate. A schematic example of how this can be achieved is shown in Figure 3.3. Here, a rectangular honeycomb is used as the cell that borders the free boundary. This results in a convex shape of the curved plate. If the cells that borders the free boundary were flat in their default shape, the plate would display a concave curvature.

57
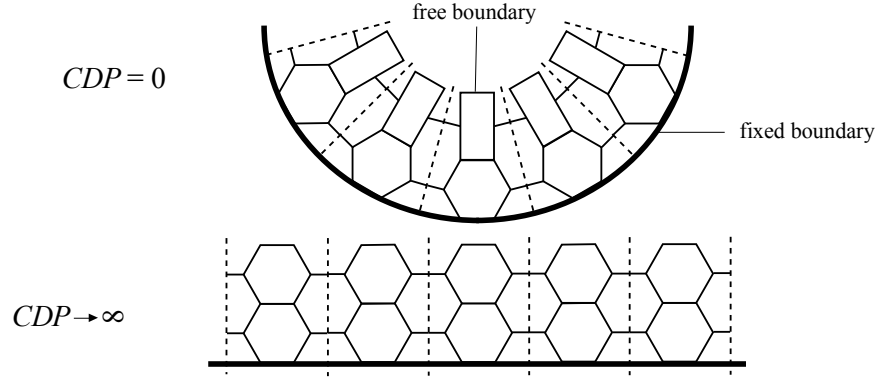
Figure 3.3   Example of a Curvature Change due to Pressure adaptive Honeycomb

The maximum curvature that can be achieved is based on the number (N) cells that are stacked atop each other and the characteristic length, l, of the honeycomb walls. It can be shown that given these inputs, the curvature, κ, of the plate is a function of the honeycomb angle of the cell touching the plate (θ_1) and the honeycomb angle of the cell at the free boundary (θ_N):

$$\kappa = \frac{1}{l(1+\cos\theta_1)} \times \frac{\cos\theta_N - \cos\theta_1}{\sin\theta_1 + \sin\theta_N - 2\sum_{j=1}^{N}\sin\theta_j} \tag{2.2}$$

The honeycomb angles of the cells that are in between the first and last cell are linearly distributed according to:

$$\theta_j = \frac{\theta_N - \theta_1}{N-1} \tag{2.3}$$

Equation 2.2 is plotted in Figure 3.4 for two different cases: $\theta_N = 90°$ and $\theta_N = 0°$. These cases correspond to a rectangular and a flat honeycomb cell at the free boundary, respectively (see also the two bottom rows of Table 3.1). In this case, it has been assumed that the cell that interfaces with the fixed boundary has a honeycomb angle of $\theta_1 = 60°$.

(a) Rectangular cell at free boundary **(b) Flat cell at free boundary**
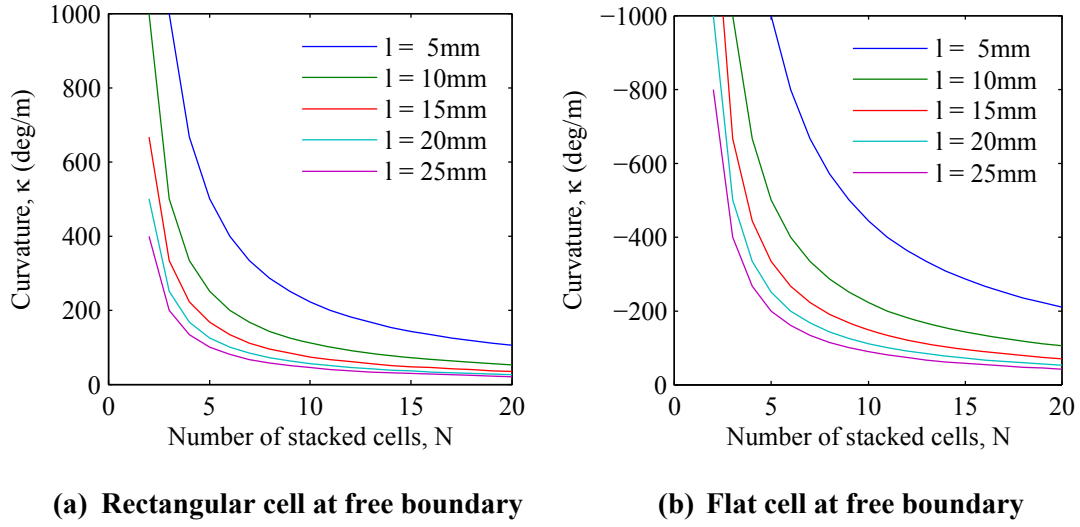
Figure 3.4   Change in Maximum Curvature with Stacked Cells

From the graphs above it can be seen, that by increasing the number of stacked cells, the maximum absolute curvature decreases. Also, with larger honeycomb face lengths this decrease is much steeper. Comparing both graphs, it can be observed that the change in curvature induced by the honeycomb having a flat cell at the free boundary is considerably larger than for the honeycomb with a rectangular cell at the boundary. This is due to the fact that the latter one does not display as much change in lateral strain (ε_y) during deformation as the first one. The total honeycomb thickness (measured between the fixed and the free boundary) is much smaller for the deployed honeycomb with a flat cell at the free boundary than it is for the deployed honeycomb with a rectangular cell at the free boundary. That said, the incremental thickness variation between deployed and retracted state can be calculated as follows:

$$\frac{\Delta t}{t_i} = \frac{2\sum_{j=1}^{N}\sin\theta_j}{2N\sin\theta_1} - 1 \tag{2.4}$$

Noting that the relative thickness change is independent of the wall length, Equation 2.4 is valid for any honeycomb size. When 20 cells are stacked atop each other, the relative change in thickness amounts to 45% for the case when a flat cell is at the free boundary and only 10.5% when a rectangular cell is at the free boundary.

3.2   Applications Utilizing Pressure Induced Morphing

Based on the fundamental principles of pressure induced morphing a variety of applications can be envisioned. This section lists some of these applications and demonstrates how aircraft could benefit from the addition of a pressure adaptive structure. The majority of the application are tailored to replace conventional high lift devices. Because of their complexity, part count and weight, replacing high lift devices with an adaptive structure of similar capability would be most beneficial. Ref. 2 gives a comprehensive overview of conventional high lift devices on subsonic commercial aircraft. It is shown that a 250klb aircraft employing double slotted flaps uses approximately 2430 individual parts, contributes over 4000lb to the OEW, and takes up 5% of the airplane manufacturing costs. In addition, translating slats add 2640lb, comprise of approximately 2700 parts and account for 3% of the manufacturing cost.

3.2.1   Pressure Adaptive Wing Section

The most profound application of pressure adaptive honeycomb is its integration into an entire wing section. The proposed airfoil profile of such a section is shown in Figure 3.5. A brief description about its features follows.
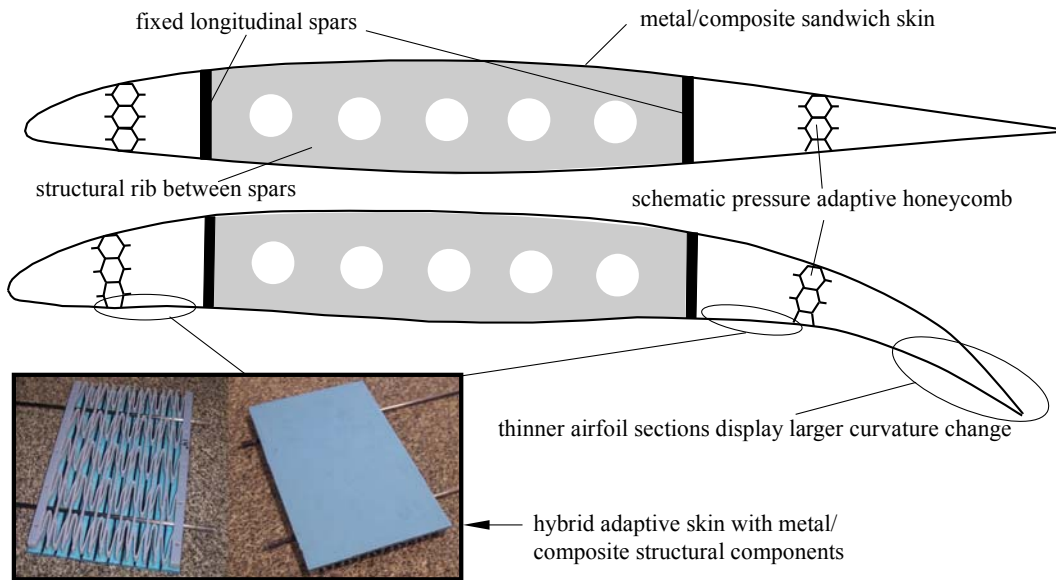
Figure 3.5   **Schematic of Morphing Airfoil Utilizing Pressure adaptive Honeycomb**

This proposed design features pressurized honeycomb over the entire section of the airfoil except for the torque box. To allow for the large induced curvatures the bottom skin needs to be flexible. In 2007 it was shown that a compliant skin can be manufactured that allows strains in excess of 30% and does not suffer from lateral contraction [62]. A picture of this hybrid adaptive skin is shown in Figure 3.5 in the lower left inset. The structural grid of this skin is similar to the workings of a hybrid honeycomb grid and can be manufactured out of metal or composite materials. The skin provides enough flexibility to allow for complete morphing and simultaneously is able to sustain the aerodynamic loads at the pressure side of the airfoil. In addition, the elasticity of the skin can be used as a restoring force for the honeycomb to enforce its cambered shape when no CDP exists.

The size of the pressure adaptive honeycomb should be determined at a later stage based on structural, manufacturing, and weight requirements. In Figure 3.5 it is merely shown as an indication of the workings of the pressure adaptive honeycomb in this concept. Notice how the honeycomb changes from a perfect hexagon close to the upper skin (which is the fixed boundary) to a rectangle close to the lower skin. This gradual transition induces a curvature in the upper skin and an increase in camber with respect to the baseline shape. At the same time, the total thickness of the wing increases as well.

From this conceptual sketch, the change in camber is difficult to predict. This is because the boundary conditions that are enforced by the spars might interfere greatly with the possible camber change. However, it is expected that the amount of camber can be changed substantially (in excess of $5\% c$). Based on the analysis in the previous section it can be deduced that at the thinner sections (e.g. near the trailing edge) the induced curvatures are larger than at the thicker parts of the section. This results in a highly curved trailing end of the wing.

There are multiple aerodynamic benefits that could be deduced from this morphing section. First of all, notice that there are no external actuators. There is no need for flap-track fairings or other external additions that increase interference drag. At the low speed realm there are more mutual benefits to be gained from this morphing airfoil. The camber of the wing can increase significantly which means added maximum lift capacity (see Figure 2.23). The nose becomes thicker, which means the relative change in thickness between the $0.15\% c$ and the $6\% c$ becomes larger. According to Figure 2.28 this also contributes to a higher maximum lift coefficient.

Naturally, the continuous flap contributes greatly to the increase in $c_{l_{max}}$. However, at this point it is still difficult to quantify each of these performance increases because the shape of the wing in low-speed and in cruise-speed configuration can still only be estimated. A detailed two-dimensional finite element analysis should be carried out to nail down the exact shapes in the two configurations. A two-dimensional panel code could be employed to calculate the aerodynamic coefficients at various angles of attack.

Structurally, the adaptive structure needs to be able to guide the distributed load from the skin panels via the spars to the fuselage of the aircraft. To that extent, this concept employs fixed spars that are connected chord-wise by fixed ribs. The spars form the backbone of the adaptive wing structure, as they do in a conventional wing.

The top skin is instrumental in keeping a proper shape both during cruise and the low speed realm of the mission profile. Since no shape ribs are available in front of and behind the torque box, it is proposed to make the skin slightly thicker than conventional wing skin such that it is stiffer and can provide the desired wing shape. By making a sandwich structure of two thin metal or composite plates with a foam or honeycomb core the thicker skin does not necessarily need to be much heavier. Since structural interconnection between the skins and the adaptive honeycomb needs to be done using adhesives rather than rivets (except for maybe at the spars), a sandwich skin does not significantly affect assembly.

The challenge in designing and manufacturing this structure is the large difference between the jig shape of the product and the shape during cruise. It would be most convenient to start from a desired supercritical wing section, apply the pressurized honeycomb, and calculate (using for example finite element software) the shape the section would take when no CDP would be applied. From a manufacturer's point of view it would then be straightforward to fabricate all the individual components according to the zero-gage-pressure shape. After assembly is complete the section should then be tested to see if the wing returns to its supercritical shape once the prescribed CDP is applied. When the ambient pressure is employed to deform the wing shape, this experiment requires a vacuum chamber that enables a lowering of the pressure surrounding the wing. If a pressurized approach is used, this test is easier to carry out by just pressurizing the honeycomb cells.

3.2.2 Pressure Adaptive Gurney Flap

As was described in section 2.2.6 a Gurney flap is a small trailing-edge tab that can increase high lift capabilities on airfoils and airfoils employing high lift devices. When properly designed, a Gurney flap can increase the lift-to-drag ratio and the maximum lift coefficient of the wing during take-off and landing conditions. However, during transonic conditions a Gurney flap can produce wave drag and flow separation resulting in a reduction in lift-to-drag ratio. An adaptive Gurney flap that retracts during cruise operations could therefore be beneficial. An example of a pressure adaptive Gurney flap is presented in Figure 3.6. In this example a double slotted flap system is used as the baseline wing section and a 5%c Gurney flap is considered. For an adaptive Gurney flap to be effective it should produce a higher lift to drag ratio when the flaps are in take-off configuration and a higher maximum lift coefficient when the flaps are in landing configuration.

cruise condition

take-off condtion

landing conditions

Pressure adaptive gurney flap
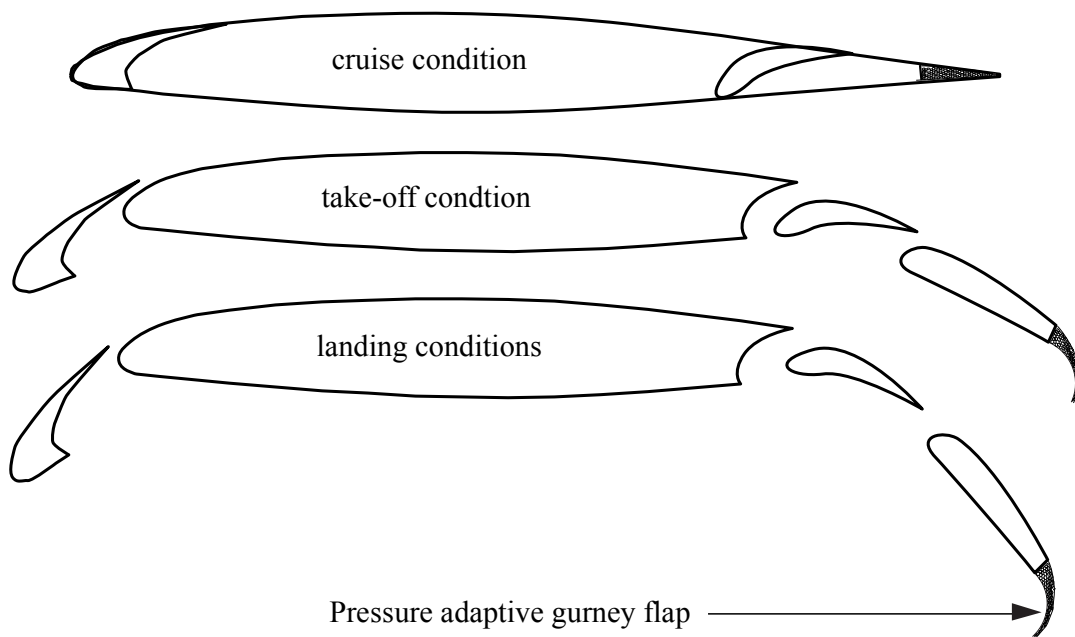
Figure 3.6   Sketch of Application of Pressure adaptive Honeycomb on a 5%c Gurney Flap

Similar to the solid state flap (Section 3.2.3) the pressure adaptive Gurney flap is based on regular honeycomb that in its unstrained configuration is strained and attached to a curved lower skin panel. The spring force in the honeycomb and the spring force in the curved lower skin provide a restoring force that deploys the solid state Gurney flap. When the relative pres-

sure in the pouches is increased, the strained honeycomb contracts and retracts the Gurney flap. The upper skin slides over the top of the honeycomb by means of a simple mechanism that needs to be developed. The honeycomb attaches to the rear spar of the flap and fills the entire trailing edge. It runs over the entire span of the flap.

To demonstrate the mechanism of a pressure adaptive Gurney flap a proof-of-concept model was built and tested. This model relied on 25µm stainless steel honeycomb cells with a face length of 10mm. Sealed pouches with a fixed amount of air enclosed were positioned in the strained hexagonal cells. The upper and lower skins were made from rolled 203µm stainless steel sheets. The span of this flap measured 15cm and its length, in retracted position, was 25cm. The structure was positioned upright in a sealed vacuum chamber. The air was evacuated by means of a vacuum pump and the resulting ambient pressure, , was measured by means of an analog pressure indicator. The result of this experiment is shown in Figure 3.7.

p_a = 100kPa, fully deployed flap p_a = 70kPa

p_a = 50kPa p_a = 20kPa, fully retracted flap
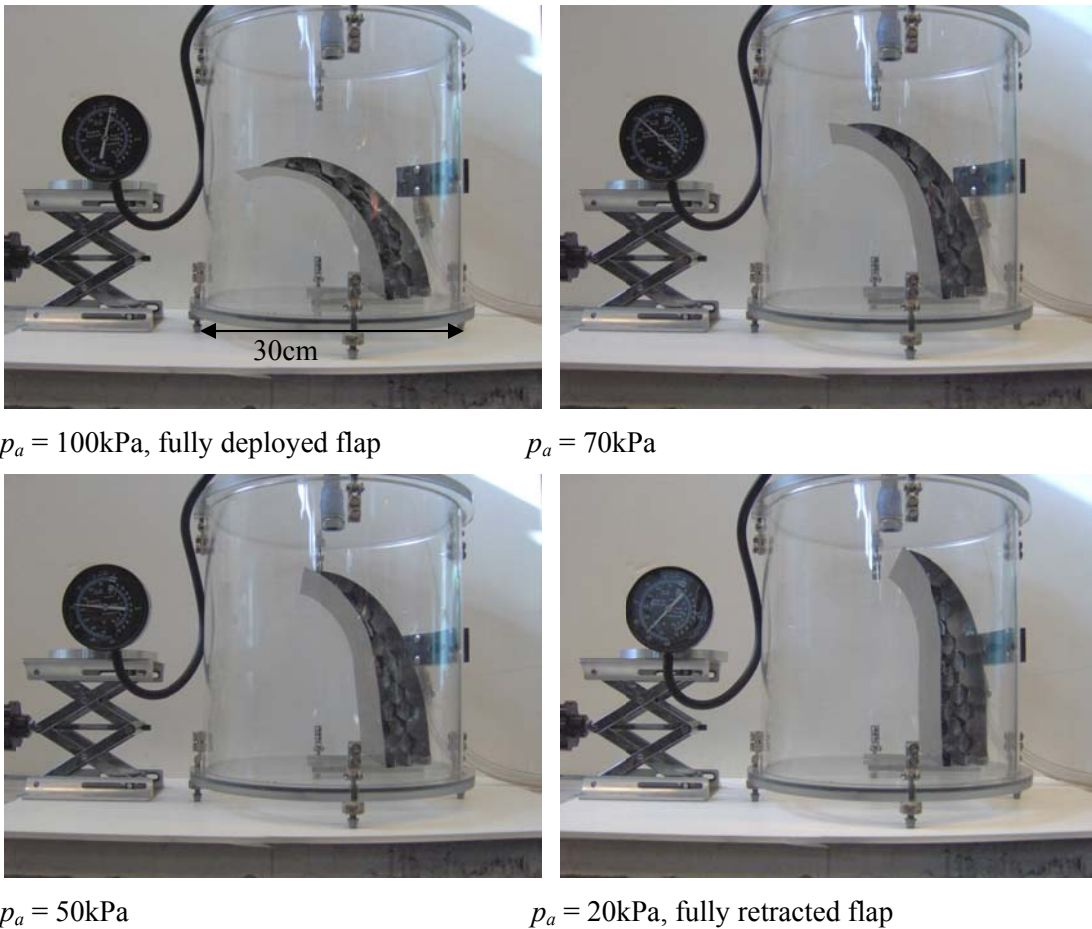
Figure 3.7   Proof-of-Concept Pressure adaptive Gurney Flap

Even though the demonstration article was not optimized in any way it performed extremely well. As can be seen from Figure 3.7 an 80kPa pressure difference over the pouches resulted in almost full retraction of the Gurney flap. Since the trailing edge of the flap was not reinforced with pressure adaptive honeycomb cells it did not straighten properly. The honeycomb in the test article proved to deform well since it did not show any plastic deformation. No bond line failures between the individual cells or the cells and the lower skin were observed showing that the pressurized pouches did not cause any detrimental peel forces.

3.2.3 Pressure Adaptive Solid State Flap

The pressure adaptive solid state flap that is proposed in this section is similar to a plain flap, only with a continuous shape change rather than being hinged about a pivot point. According to Figure 2.12 a plain flapped airfoil ($25\%c$) can have a lift coefficient of 2.0, adding about 0.4 to the baseline airfoil. Since the solid state flap does not translate nor display a slot, it does not benefit from an increase in chord or the jet effect. Therefore, lift coefficients are below the lift coefficients found on single slotted Fowler flaps. However, the solid state flap has other benefits including a low part count. It also does not require any flap tracks, which yields lower maintenance cost and a drag reduction. Since there are no hinges or sliding parts in this concept, the wear on the structure is minimal. In addition, no external actuators are required to deploy the solid state flap as it relies on the atmospheric pressure decrease with altitude.

Figure 3.8 shows a possible configuration of the solid state flap on a transonic airfoil. It can be seen how the honeycomb attaches to the bottom skin of the wing. The wing skin and honeycomb are in their default, unstrained configuration when the flap is deployed. When the structure is activated, the honeycomb contracts and retracts the flap to its cruise configuration. The size of the honeycomb that is shown in Figure 3.8 is merely to indicate where the honeycomb would go. Actual cell size and material sheet thicknesses can vary and should be determined as a function of the required restoring force and stiffness properties. The upper skin of the flap is not bonded to the honeycomb but slides over the upper surface of the cells. A simple sliding mechanism attaches the upper skin to the honeycomb.
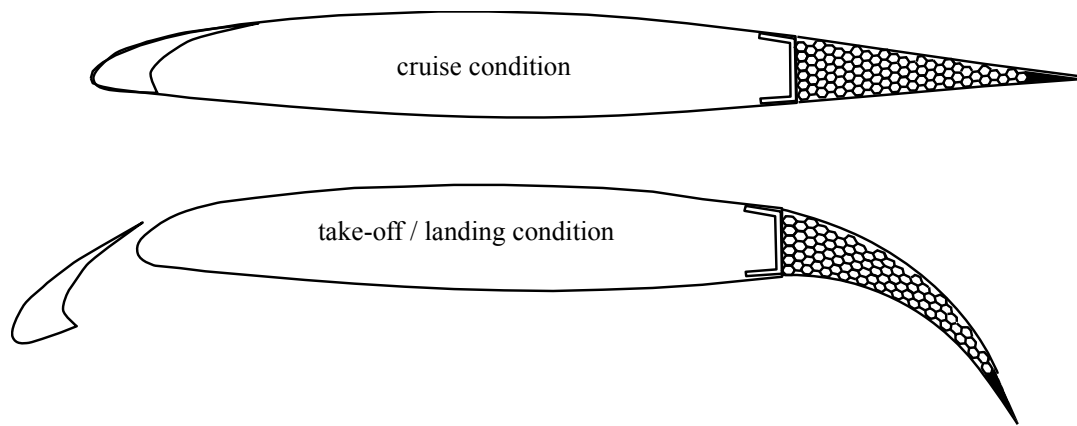
Figure 3.8   Sketch of Pressure adaptive Solid State Plain Flap

In addition, both the upper and lower skins are pre-curved metal or composite sheets. They provide a restoring force such that the flap is deployed at low altitudes. Naturally, the sheet thickness is limited by the yield strain of the material that is used for the lower and upper skins. One way to increase the total thickness of each of the skins is stacking two or more layers of sheet metal (composite) together with an elastomeric adhesive in between them. The elastomeric tape allows for the individual layers to slide with respect to each other. This lowers the strain that the material experiences in deployed position. Furthermore, the elastomeric adhesive also serves as a damper and can therefore limit excitations of the solid state flap during aerodynamically induced vibrations.

Another class of aircraft that could potentially benefit from this technology would be the light sport aircraft (LSA). Even though their operational ceiling is typically limited to 15,000ft (e.g. Jabiru J250 [124]), this could be enough pressure difference to induce the required strain in the pressure adaptive structure. By applying the pressure adaptive honeycomb over the last 25% of the chord and over the entire span of the wing (including the ailerons) the pressure adaptive honeycomb could be a low-weight replacement for mechanical plain flaps. No fuel storage space is compromised using this concept and there is no need for leverages that control the flap settings. An impression of such an LSA wing is presented in Figure 3.9. In this example, the engagement altitude is fixed at a 5,000ft and the full-pressurization altitude is set at 10,000ft. In between those altitudes the flap setting changes gradually between the two positions sketched in Figure 3.9.
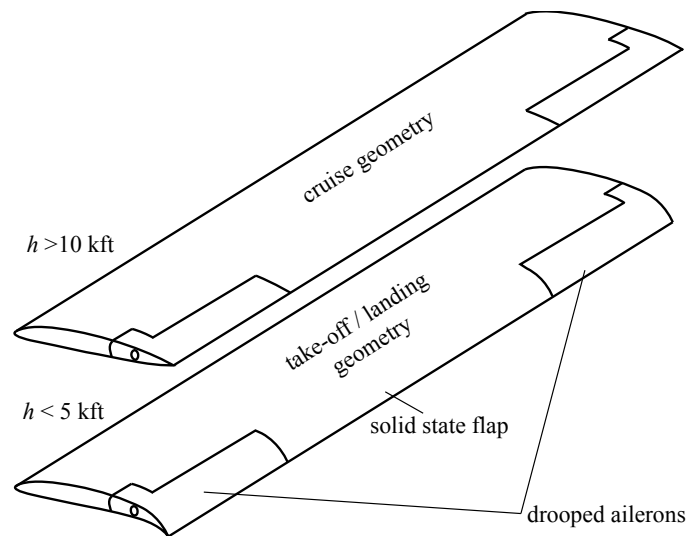
Figure 3.9   Potential Application of Pressure adaptive Honeycomb for LSA Wing

The hinged ailerons in this conceptual design work the same as conventional ailerons. However, their internal structure of ribs and stringers is replaced by the pressure adaptive honeycomb. The fact that both ailerons droop down creates a force balance on the control mechanism, which means no net hinge moments are created that need to be compensated by the pilot. The pilot is able to operate the ailerons in the same manner, whether they are drooped down or in cruise configuration.

3.2.4 Pressure Adaptive Engine Inlet

The shape of engine inlets is a compromise between an optimal shape at transonic velocities and an optimal shape at low subsonic velocities. The inside of the intake lip is shaped such that it allows for attached flow at high angles of attack and slip angles. On the other hand, the outside of the lip is designed to ensure attached flow during transonic conditions. The first condition requires a relatively blunt, well rounded lip, but the latter condition requires a sharper lip. To account for both conditions adaptive engine intakes have been designed (see for example Ref. 125). Adaptive inlets that rely on hinging and sliding components are susceptible to leaking and improper sealing resulting in pressure losses and consequent losses in efficiency. Other disadvantages include the increased part count, complexity and weight.

A solid state, pressure adaptive intake lip, based on a hybrid honeycomb internal structure could change the shape of the lip between the two before-mentioned flight conditions. Figure

3.10 shows how the thickness of the lip can be varied by using the pressure adaptivity of 25% of the honeycomb cells. The cells that induce the shape change are termed 'pressure adaptive' in Figure 3.10. These cells contain pouches while the other cells have no pouches and are therefore inactive. In the default position, when no pressure difference is present, the honeycomb cells are rectangular. When the pressure is increased, the structural deformation decreases the thickness of the lip with 15%, making it sharper and therefore more suitable to transonic conditions.
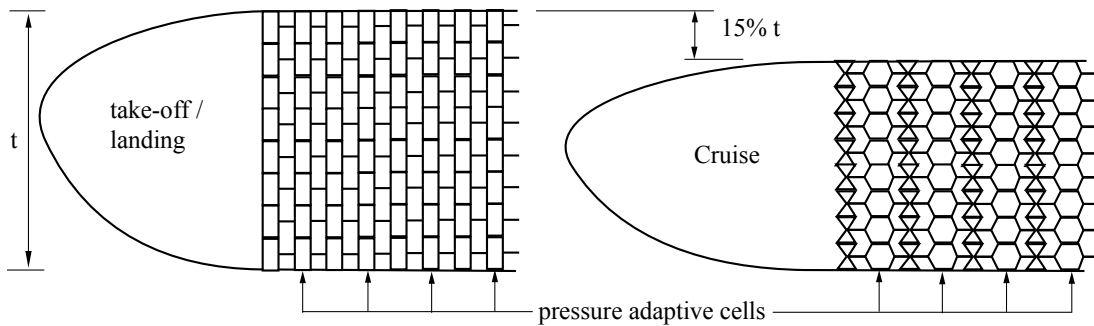
Figure 3.10   Sketch of Pressure adaptive Engine Intake Lip Based On Hybrid Honeycomb

The pressure difference required to switch between the two configurations can be acquired from the ambient pressure decrease with altitude. However, since this application relies on only 25% of all the available cells, and because it is located near the engine compressor, it is very suitable to be powered by pressurized bleed air from the compressor. Note that this would not decrease engine efficiency because there is no net flow of air in this pressure adaptive structure.

Advantages of this concept compared to other adaptive incentives include a relatively simple structural layout, a low part count, low wear and almost no power requirements. Manufacturing of the honeycomb structure requires an additional step, where each layer is bent such that the cells can revolve around the engine centerline. Properly filling the lip with hybrid honeycomb cells can be a design challenge, along with predicting the shape change when three-dimensional effects come into play. However, pursuing this concept might lead to more efficient engine intakes in both subsonic and transonic flight conditions.

3.2.5 Empennage Applications

During take-off and landing the flap settings on an aircraft generate a higher nose-down pitching moment than during cruise. When an ambient-pressure approach is used for pressure adaptive flaps, the flap setting gradually changes between take-off and landing. By trimming the horizontal stabilizer accordingly, a higher nose-up moment is generated by the empennage to compensate for the moment generated by the flaps. Alternatively, this moment could be generated by modifying the leading edge, such that it becomes blunter and gives the airfoil more camber. This section presents two conceptual designs on how to do this using pressure adaptive honeycomb.

The first design employs pressure adaptive honeycomb in the elevator control surface. As can be seen in Figure 3.11, this design combines the hinged control surface with the solid-state, pressure adaptive honeycomb. It is pointed out to the reader that the pressure adaptive honeycomb is solely used to change the aft airfoil shape. The hinged elevator works the same as in conventional empennages. However, the internal structure of ribs and stringers is replaced by the pressure adaptive honeycomb, similar to the drooped aileron in Section 3.2.3. The increased curvature of the elevator increases the overall camber of the airfoil which enhances the horizontal tail maximum lift coefficient, $C_{L_{max_h}}$ (see Figure 2.23). To balance the elevator hinge moment, this conceptual design incorporates a pressure adaptive trim tab. The increased camber of the elevator in combination with the trim tab results in an s-shape of the top and bottom skins. Therefore, a careful design does not require either of the two skins to show any strain which means no adaptive skin is needed to allow for the desired curvatures. In addition, the hinge moment derivatives, c_{h_α}, and c_{h_δ} should be close to zero [38].
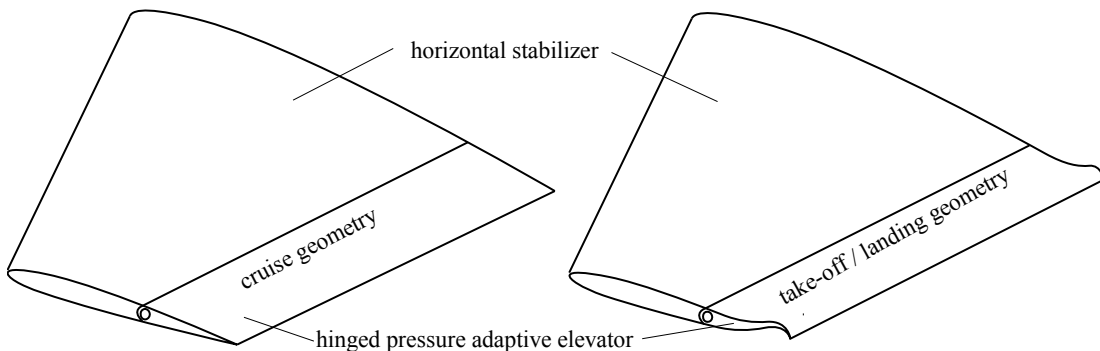
Figure 3.11   Sketch of Hinged Pressure adaptive Elevator for Enhanced Down Force

Rather than modifying the rear end of the stabilizer, the leading edge can also be altered to contribute to additional down-force during take-off and landing. Similar to the change in leading edge geometry in Section 3.2.1, this design relies on the adaptive skin on the pressure side (top) of the stabilizer along with a thickened skin on the suction side (bottom). A change in CDP droops the leading edge slightly upwards. Simultaneously, the nose becomes thicker. The resulting increase in camber and bluntness of the stabilizer increases its $C_{L_{max_h}}$ (see Figure 2.23 and Figure 2.28). A sketch of this concept is presented in Figure 3.12 for a swept and tapered horizontal stabilizer. It could just as well be used on straight horizontal stabilizers. Aircraft classes that could potentially benefit from this concept include LSA, business jets and commercial jet transports.
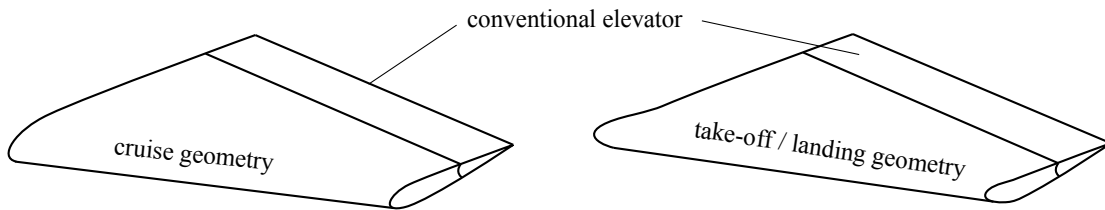
Figure 3.12   Sketch of Pressure adaptive Leading Edge on Horizontal Stabilizer

3.2.6 Pressure Adaptive Droop Nose

There has been considerable interest in an adaptive droop nose over the past several years (see Ref. 126). The desire to sustain laminar flow over a large part of the airfoil requires a drooped nose without any discontinuities such as seams between individual parts.

This can be achieved by applying pressure adaptive honeycomb in the nose of the wing. Figure 3.13 schematically demonstrates the mechanics behind this idea. The honeycomb would be attached to the inside of the top skin of the airfoil. In the default configuration, the pressure in the pouches would match the surrounding pressure and the nose would be drooped (as in the right-hand side of Figure 3.13). When increasing the CDP, the cells would expand and the top skin would lose some of its curvature. This brings the droop nose into the cruise geometry (as in the left-hand side of Figure 3.13). The sketches presented here are merely to give the reader an impression of the applicability of pressure adaptive honeycomb in a droop nose and are by no means an accurate depiction of what a real structure would look like.

| Cruise Configuration | Deployed Configuration |
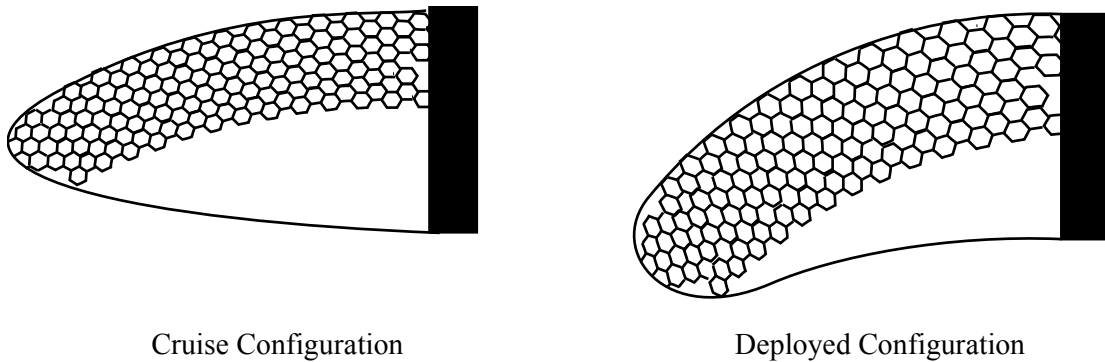
Figure 3.13   Sketch of Pressure adaptive Droop Nose (Cross Section)

Conventional hinged droop noses often suffer from small hinge radius that can induce flow separation at high angles of attack [44]. The present drooped nose does not suffer from this because it is based on the straining of the top skin. When appropriately designed, the present concept should not have a discontinuity in curvature over the top skin.

3.3   Actuation Sources

When pressurizing the pressure adaptive honeycomb there are essentially two approaches that can be taken. The first approach relies on the atmospheric pressure change with altitude which can induce a cell differential pressure, provided that the amount of enclosed mass in the honeycomb cell remains constant. The second approach relies on a pressure source within the aircraft. The next two subsections discuss these two alternatives.

3.3.1 Atmospherically Triggered Actuation

The initial objective of this adaptive structure is to induce deformation between take-off and cruise altitude. Take-off altitude can vary considerably between airfields around the world with altitudes as high as 4km (El Alto International Airport, see Ref. 127). If a pressure adaptive structure is used in any type of high lift device, it should be fully deployed at these high altitude airports. Airtight honeycomb cells would not suffice for this purpose. The difference in altitude between sea level and local airport altitude could already induce a significant change in structural geometry. In other words, a potential high lift device powered by such a pressure adaptive structure would already be partly retracted at these high altitude airports. By implementing separate air bladders (pouches) inside each of the honeycomb cells this is-

71

sue can be avoided. By carefully inflating the pouches with a fixed amount of gas at a known pressure and temperature it is possible to control the pressure differential at which the pouches pull taut, and start pushing against the honeycomb wall. During the initial altitude gain, the decreasing pressure does nothing else than expanding the gas in the pouches up until the pouch is constrained by the honeycomb structure. Then, as the pressure difference increases, the pouch attempts to reach its perfect circular shape, taking the honeycomb to a grid of near perfect hexagons (see Figure 3.2). A more thorough analysis of this process is detailed in Section 4.4.2.

To see how a pressure adaptive structure would be deployed, the reader is asked to consider the mission profile in Figure 3.14. This diagram is typical for a jet transport or business jet. It shows the engagement altitude, and full pressurization altitude. In between those two altitudes the pressure adaptive structure deforms between its two states. If the pressure adaptive structure is used to enhance high lift devices it is fully deployed between sea level and engagement altitude. Above full pressurization altitude it is completely retracted. This means that during the climb and decent phases of the flights, the structure continuously changes its shape between these two states without any pilot interference.
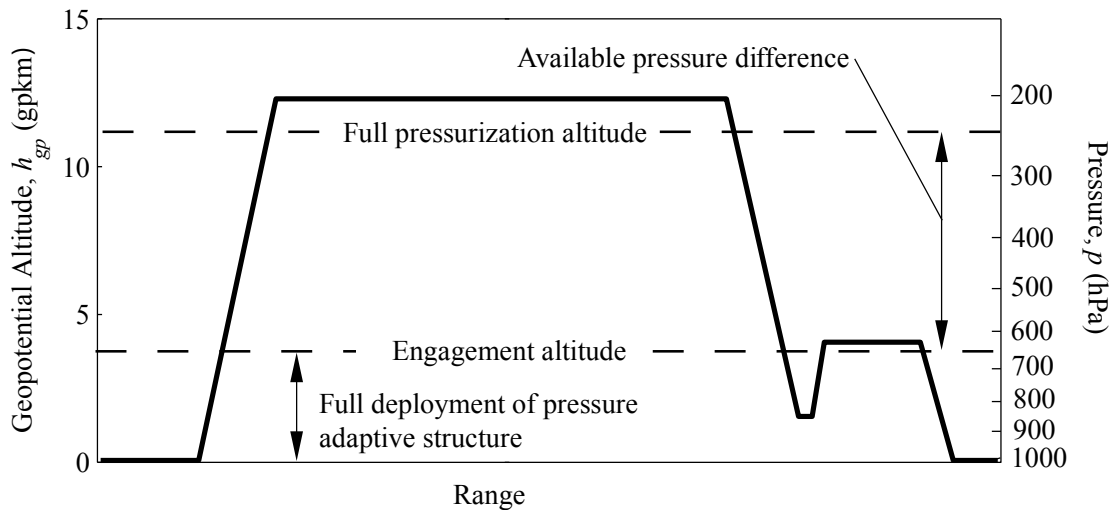
Figure 3.14 Notional Mission Profile with Outlined Engagement and Full Pressurization Altitude

On the right hand side of the diagram, the atmospheric pressure is indicated, based on the pressure distribution around the equator in the summer. Note that in this example the differ-

ence between engagement altitude and full pressurization altitude is around 400hPa. Now, based on the application of the pressure adaptive structure this may or may not be enough pressure to perform the specified task. By lowering the engagement altitude a significant increase in available pressure difference can be gained. However, the device is not fully deployed at airports that exceed the engagement altitude. A careful trade-off must be made for every application to come to a compromise between these two features.

One way to avoid a compromise between available pressure and serviceable airports is to make the pressure adaptive structure independent of the ambient pressure. By installing a tubing system that finds its origin at the compressor of the jet engine an aircraft-based source is found. This makes the deployment of the structure controllable and provides an exponential increase in available pressure. The pressurized bleed air that is taken from the engine should not degrade engine efficiency because there is no net flow of air since all the pouches are airtight. By interconnecting all pouches a relatively simple morphing structure can be constructed that can show significant force and stroke capability, all the while keeping energy requirements minimized.

One of the characteristics of the proposed pressure adaptive structure is that it is not antagonistic. In other words, it needs a restoring force, e.g. a spring, to return the structure to its initial position. When the pressure difference over the pouches is present, the structure overcomes this restoring force and changes into its retracted configuration. A careful balance should be found between the restoring force and the force generated by the structure. The restoring force can be embedded in the honeycomb structure by ensuring its initial configuration induces no strain on the structure. Whenever the structure deviates from its initial configuration the honeycomb structure provides a restoring force due to elastic straining of the cell walls.

A second characteristic of this structure is that its bandwidth is very low. It is not intended to replace any of the wing or empennage primary flight control surfaces. It is designed such as to adapt the aircraft configuration to take-off/landing and cruise conditions. If an adaptive actuation scheme based on ambient pressure is used then the rate of structural deformation keeps pace with the rate of descent or climb of the aircraft. If a powered approach is used the rate is limited by the maximum mass flow through the tubing system. Larger tubing allows for higher mass flow, but also increases weight and volume penalties.

The preceding discussion on aircraft applications silently assumed that pressure adaptive honeycomb would be used exclusively in jet transport aircraft that cruise at altitudes in excess of 10km. Indeed, this would be a suitable market for this new technology. A close relative, in terms of cruise altitude, would be the business jets. Since they cruise at altitudes close to that of jet transports, they could benefit from almost the same pressure difference. All aircraft classes that experience a significant pressure difference between their cruise and take-off altitude can potentially benefit from embedded pressure adaptive honeycomb. This includes military aircraft and light sport aircraft (LSA).

3.3.2 Internal Actuation Sources

Rather than relying on external sources for actuation, it is possible to use sources from within the aircraft to actuate the pressure adaptive honeycomb. Compared to the atmospherically triggered pressure adaptive honeycomb, the internally powered version is more controllable. The pilot can therefore determine exactly when the structure is pressurized. A second advantage is the fact that much higher CDPs can be achieved when the pressure is internally generated.

For aircraft that employ turbomachinery, pressure could be tapped from the compressor stages of the engine. Since pressure adaptive honeycomb essentially requires no continuous flow of air, this would not degenerate the pressure ratio of the engine. Consequently, the engine efficiency would not be influenced by the addition of pressure adaptive honeycomb. A controllable valve could be positioned between the pressure adaptive honeycomb and the compressor to regulate the CDP. Contemporary dual-shaft turbofans are capable of generating overall pressure ratios on the order of 40 [Pratt&Whitney PW4000: 35, Rolls-Royce Trent 900: 39, General Electric GE90-115B: 42, GE/PW GP7270: 44 (all data from www.wikipedia.org)]. When cruising at an altitude of 11km (~36kft) a cell differential pressure of 0.9MPa can be achieved, assuming ISA conditions.
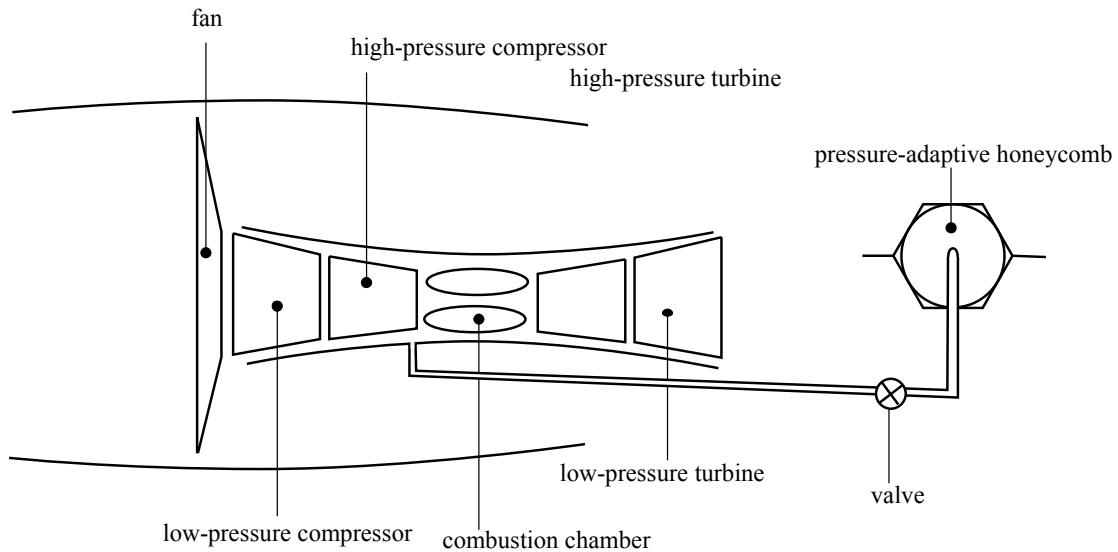
Figure 3.15   Pressurizing Adaptive Honeycomb from the High-Pressure Compressor

The generated CDP in the aircraft has an effect on the overall weight of the system. High CDPs ask for a dedicated infrastructure of tubes and hoses to connect to the pouches inside the honeycomb. For the envisioned applications a low actuation bandwidth is required. Relatively small diameter tubes could therefore be used in order to minimize added system weight. Another effect of high pressure is that the pouch material incurs a much higher circumferential stress level. In order to keep this stress level below the material yield stress either the thickness would need to be increased or the radius decreased. The first option, obviously has a negative effect on total weight. However, the latter option has a similar negative impact because it increases the cell density of the honeycomb and consequently the total weight of the system, for a given volume. Because of those possible negative effects on the total weight of the system, the designer is advised to carefully review the impact of a higher CDP on the total weight of the system. A measure for the effectiveness of the adaptive actuation system could be the specific energy density, where the total energy output is divided by the total weight of the system.

When internally generated pressure is used to power the pressure adaptive honeycomb, there should be a back-up system to supply power in case the engine fails. In that case a static pressure source such as a CO_2 cartridge could be used to provide pressure over a sufficient period of time, such that the aircraft can safely land. These cartridges are commonly used on subs-

cale UAVs with inflatable wings and can supply sufficient gage pressure for more than eight hours, providing that there is no significant leak [107, 128].

CHAPTER 4   MODELING PRESSURIZED HONEYCOMBS

If pressure adaptive honeycombs are used in aerospace structures, designers should have some tools they can use to predict the mechanical properties of the structure and its influence on the aerodynamics of the deforming part. This chapter introduces these tools. The main focus is on the mechanics of pressure adaptive honeycomb. A simple analytic model is proposed that gives the designer a first cut at stress-strain relationships based on the geometry of the honeycomb and the cell differential pressure. In addition, a finite-element-based model is presented that relies on linear elasticity with appropriate boundary conditions and pressure loading. To predict the gross aerodynamic performance of a flap deformed by pressure adaptive honeycomb, an off-the-shelf Euler code is used.

4.1   Cellular Material Theory for Honeycombs

4.1.1 Model Setup and Assumptions

A Newtonian approach is used to find the stress-strain relationships in honeycomb. Cellular material theory (CMT, see Ref. 129) has been shown to give good predictions of material stiffness up to strains of 20%, provided that the relative thickness of the material $t/l < 1/4$. Figure 4.1 schematically shows how a honeycomb cell deforms when subjected to pure longitudinal and transverse stresses. If this deformation is elastic it is assumed that the wall angle, θ_i, does not change throughout the process. Instead, the members between the corner points bend into an (inverse) s-shape.
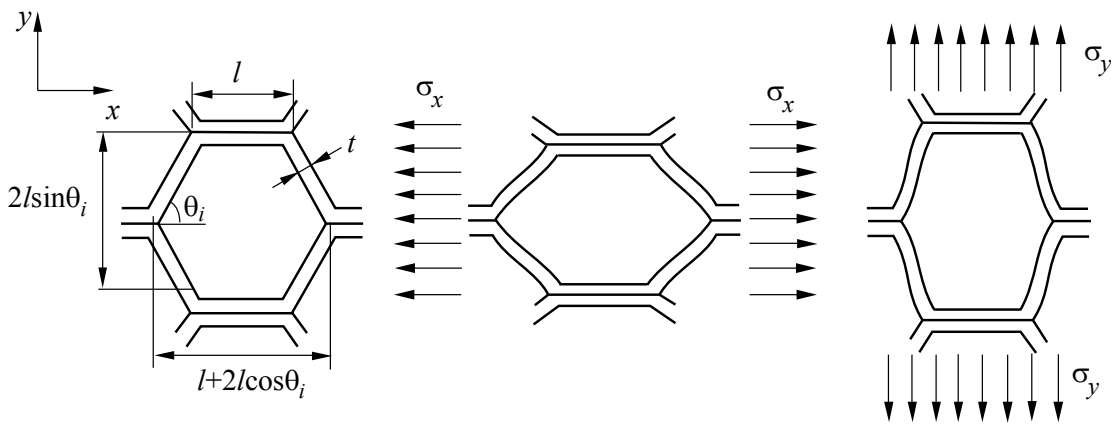
Figure 4.1   Cell Deformation due to Stresses in Principal Directions (After Ref. 129)

As shown in Figure 4.1 the honeycomb that is considered in this section is comprised of layers that are joined together. The reason behind this lies in the fact that the envisioned honeycomb is manufactured out of corrugated sheet metal or a composite material. Joining the corrugated sheets together is a relatively simple method for creating a honeycomb structure. For analysis purposes it is assumed that the bond thickness between the two sheets is negligible with respect to the wall thickness, t. Therefore, the thickness of the horizontal members in Figure 4.1 amounts to $2t$.

By following the analysis laid out in Ref. 129 the equivalent material properties of the honeycomb structure can be determined. To distinguish the material properties from the honeycomb structure properties, the latter one uses a '*'. For example, E would be the stiffness of the material of which the honeycomb consists, while E^* is the stiffness of the honeycomb structure itself. By doing so, the density ratio of a regular honeycomb structure can be found from:

$$\frac{\rho^*}{\rho} = \frac{2t/l}{(1+\cos\theta_i)\sin\theta_i} \tag{4.1}$$

4.1.2 In-Plane Deformation in Principal Directions

In this section it is assumed that the honeycomb structure is build from sheets of elastic material that are strip-glued together, as shown in Figure 4.1. The principal stresses on the honeycomb are redistributed throughout the structure in terms of forces and moments that induce bending in the single-thickness wall. A detail of the forces and moments acting on each of these walls is depicted in Figure 4.2.
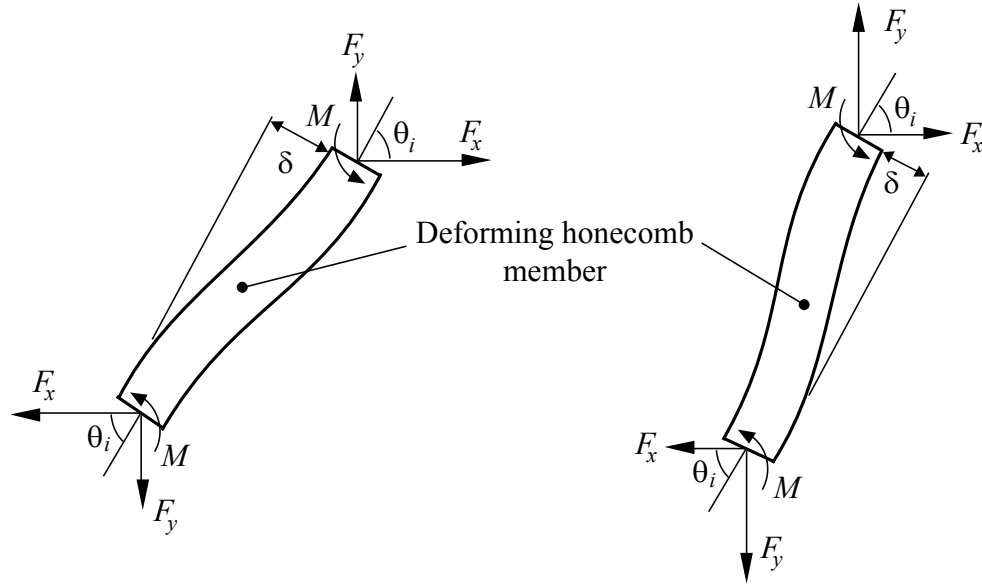
Figure 4.2   Wall Deformation due to Loads in Principal Directions (Reproduced from Ref. 129)

The deformation due to longitudinal stress, σ_x, is considered first. The force in x-direction is related to the longitudinal stress according to (assuming unit width):

$$F_x = \sigma_x l \sin \theta_i \tag{4.2}$$

Due to equilibrium, $F_y = 0$. Therefore, the moment, M, can be defined as:

$$M = \frac{F_x l \sin \theta_i}{2} \tag{4.3}$$

Using Euler-Bernoulli beam theory the beam deflection due to the loading is:

$$\delta = \frac{F_x l^3 \sin \theta_i}{12EI} \tag{4.4}$$

where I is the second moment of area of the cell wall ($I = t^3/12$ for a wall of uniform thickness and unit width). The strain parallel to the x-axis can be found as follows:

$$\varepsilon_x = \frac{\delta \sin \theta_i}{l(\cos \theta + 1)} = \frac{\sigma_x l^3 \sin^3 \theta_i}{12EI(\cos \theta_i + 1)} \tag{4.5}$$

Knowing that the equivalent material stiffness, $E_x^* = \sigma_x/\varepsilon_x$, the ratio of honeycomb stiffness to material stiffness is as follows:

$$\frac{E_x^*}{E} = \left(\frac{t}{l}\right)^3 \frac{\cos\theta_i + 1}{\sin^3\theta_i} \tag{4.6}$$

A similar analysis applies to the deformation due to a stress in y-direction. By equilibrium $F_x = 0$ and the resulting moment can be found from:

$$M = \frac{F_y l \cos\theta_i}{2} \tag{4.7}$$

where F_y is defined according to:

$$F_y = \sigma_y l \left(1 + \cos\theta_i\right) \tag{4.8}$$

The wall then deflects according to:

$$\delta = \frac{F_y l^3 \cos\theta_i}{12EI} \tag{4.9}$$

This results in the following expression for the strain in y-direction:

$$\varepsilon_y = \frac{\delta\cos\theta_i}{l\sin\theta_i} = \frac{\sigma_y l^3 (1+\cos\theta_i)\,\cos^2\theta_i}{12EI\sin\theta_i} \tag{4.10}$$

Again, the equivalent material stiffness in y-direction can be expressed as:

$$\frac{E_y^*}{E} = \left(\frac{t}{l}\right)^3 \frac{\sin\theta_i}{(1+\cos\theta_i)\,\cos^2\theta_i} \tag{4.11}$$

If $\theta_i = 60°$, then both Young's moduli reduce to the same value, yielding isotropic properties:

$$\frac{E_{x,\theta_i=60°}^*}{E} = \frac{E_{y,\theta_i=60°}^*}{E} = \frac{4}{\sqrt{3}}\left(\frac{t}{l}\right)^3 \tag{4.12}$$

By loading the honeycomb members, their s-shape essentially shortens the length of the member which is not accounted for in the model. In addition, the axial loads on the members magnify their deflection. In particular, when the axial load comes close to the buckling load of the member, this magnification becomes substantial. However, the linear-elastic model assumes this effect to be negligible.

The Poisson's ratios can be found by taking the ratio of strains caused by the applied stress in either x- or y-direction:

80

$$v_{xy}^* = -\frac{\varepsilon_y}{\varepsilon_x} = \frac{\cos\theta_i(\cos\theta_i + 1)}{\sin^2\theta_i} \qquad (4.13)$$

$$v_{yx}^* = -\frac{\varepsilon_x}{\varepsilon_y} = \frac{\sin^2\theta_i}{\cos\theta_i(\cos\theta_i + 1)} \qquad (4.14)$$

The Poisson's ratios that are defined above should be interpreted as global Poisson's ratios. In other words, their value changes with the reference angle, θ_i, of the honeycomb. The following identity is satisfied:

$$E_x v_{yx}^* = E_y v_{xy}^* = E\left(\frac{t}{l}\right)^3 \frac{2}{\sin 2\theta} \qquad (4.15)$$

4.1.3 In-Plane Shear Deformation

The shear deformation of honeycomb is less straightforward as the deformation in principal directions (shown in Figure 4.17). To verify the behavior in shear, a simple shear frame was constructed in which a regular honeycomb was positioned at an arbitrary honeycomb angle As can be seen in Figure 4.3, the shear frame was photographed at its initial position (left) and in its skewed position. Detailed analysis of 126 honeycomb cells confirmed that during shear deformation only the 'horizontal' members of the cell showed deformation. The angled members were rotated, but their relative position remained unchanged.

Figure 4.3   Simple Test Setup To Verify Honeycomb Cell Deformation During Shear Loading

The shear deformation in honeycomb cells is schematically shown in Figure 4.4. The shear stress, τ_{xy}, is redistributed as a set of discrete forces that act on the individual members. As was explained in the previous paragraph, there is no relative motion of points A, B, and C when the honeycomb is sheared. The shear deformation is entirely due to the rotation, ϕ, of the joint at point B and the deflection, δ, at point D. Forces resulting from shear stresses that run in horizontal direction, therefore, do not contribute to the shear deformation of the cells. Only forces resulting from the vertical components of the shear stress induce shear strain in the honeycomb cells.
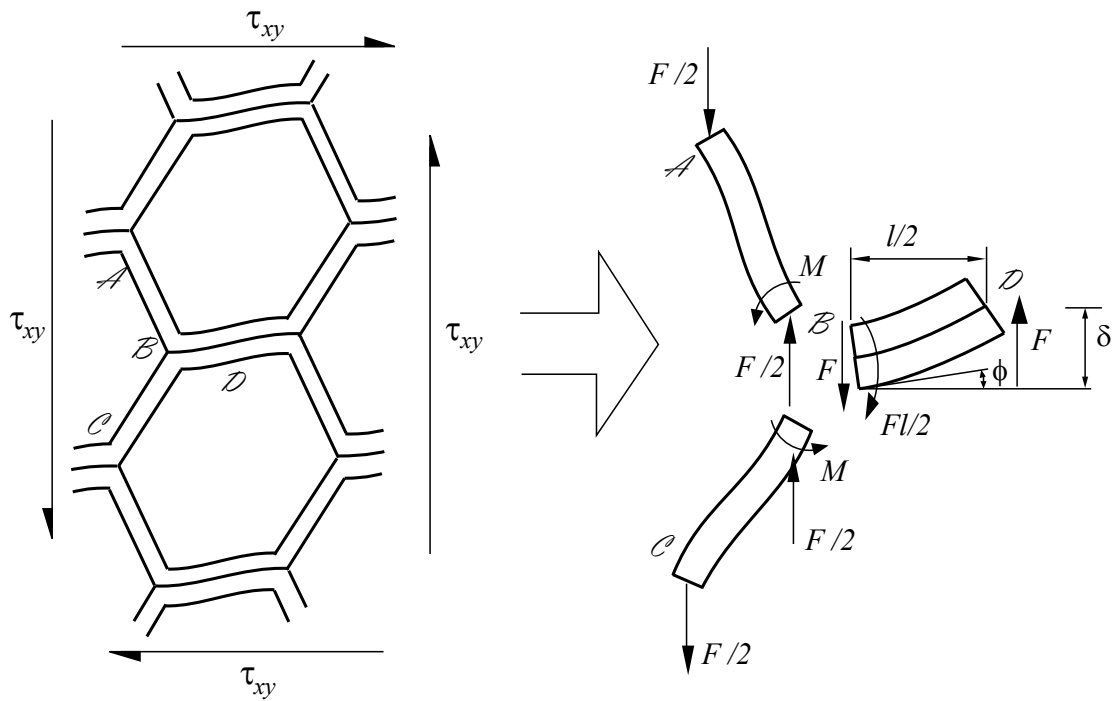
Figure 4.4   Shear Deformation of Honeycomb Cells (Reproduced from p. 80 of Ref. 129)

Following the nomenclature laid out in Figure 4.4, the moment applied to members AB and BC amounts to:

$$M = Fl/4 \tag{4.16}$$

The deflection due to the shear load at point D is:

$$\delta = \frac{1}{2}\phi l + \frac{F}{3EI_2}\left(\frac{l}{2}\right)^3 = \frac{Fl^3}{48EI_1} + \frac{Fl^3}{24EI_2} = \frac{5Fl^3}{16Et^3} \tag{4.17}$$

82

Where I_1 is the second moment of the cross-sectional area of the single-thickness walls and I_2 is the second moment of the cross-sectional area of the double-thickness walls. The shear strain, γ_{xy}, can be obtained as follows:

$$\gamma_{xy} = \frac{2\delta}{l(1+\cos\theta_i)} = \frac{5}{8(1+\cos\theta_i)}\frac{Fl^2}{Et^3} \tag{4.18}$$

The discrete force, F, relates to the shear stress according to:

$$\tau_{xy} = \frac{F}{2l\sin\theta_i} \tag{4.19}$$

Combining Equations 4.18 and 4.19 and substituting for the moment of inertia yields the shear stiffness:

$$\frac{G^*_{xy}}{E} = \frac{4}{5}\left(\frac{t}{l}\right)^3\frac{1+\cos\theta_i}{\sin\theta_i} \tag{4.20}$$

For regular honeycomb where $\theta_i = 60°$ this relation reduces to

$$\frac{G^*_{xy,\,\theta_i=60°}}{E} = \frac{12}{5\sqrt{3}}\left(\frac{t}{l}\right)^3 = 5\,E^*_{\theta_i=60°}/4E \tag{4.21}$$

4.2 Mechanics of Pressurized Rigid-Wall Honeycombs

This section lays out a simple model that characterizes pressurized honeycomb cells with rigid walls. The model can be used to predict honeycomb strains as a function of pressure, initial geometry, and applied stress.

4.2.1 Model Setup and Assumptions

It is assumed that the ratio between pouch volume and the volume occupied by the hexagonal cell is constant during deformation. This ratio is set to the ratio that is found when the pouch forms a perfect circle inside the hexagon and touches each of its flanges. This ratio is denoted with ζ, and amounts to $\zeta = \sqrt{3}\pi/6 \approx 0.91$. Furthermore, it is assumed that the honeycomb walls are rigid and connected by frictionless hinges. Therefore, no structural stiffness comes into play. In addition, the pouch is assumed to be totally inelastic. Its perimeter does not change during deformation.

The honeycomb angle, θ, changes continuously during deformation. Along with the honeycomb angle, the internal volume, V, of the pouch changes as well. When the pressurized honeycomb is to perform mechanical work, the pressure needs to overcome the inherent stiffness of the honeycomb and some sort of external stress, σ. In practice the external stress might originate from aerodynamic and/or structural loads. Figure 4.5 shows how a cell within the honeycomb grid would deform as a result of applied stresses. To model the relationship between the stress and the strain of the honeycomb an energy approach is considered.
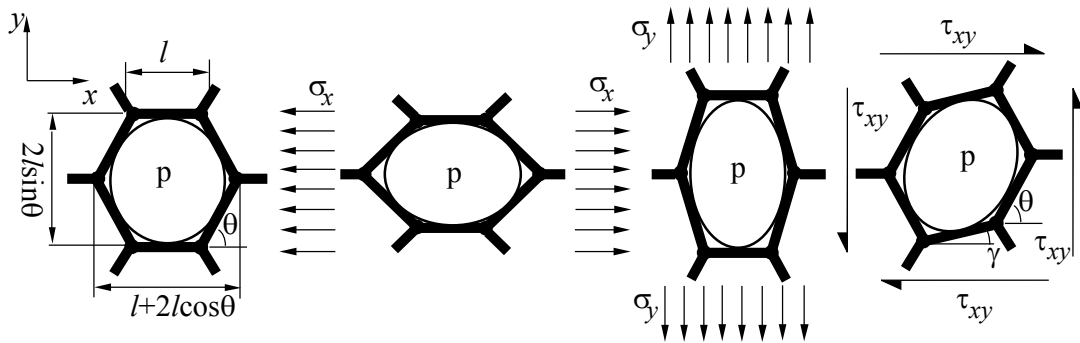
Figure 4.5   Definitions and Sketch of Principal and Shear Deformations

To model its bulk properties the honeycomb grid is broken down into smaller and smaller sections that still exhibit the same geometric and stiffness properties. This stepwise process is shown schematically in Figure 4.6. The smallest building block that still possesses the same properties as the bulk structure is depicted in Figure 4.6(d).

(a) Full honeycomb grid

(b) Rectangular section with symmetry lines

(c) Section with hinged members

(d) Incremental section; basis for model
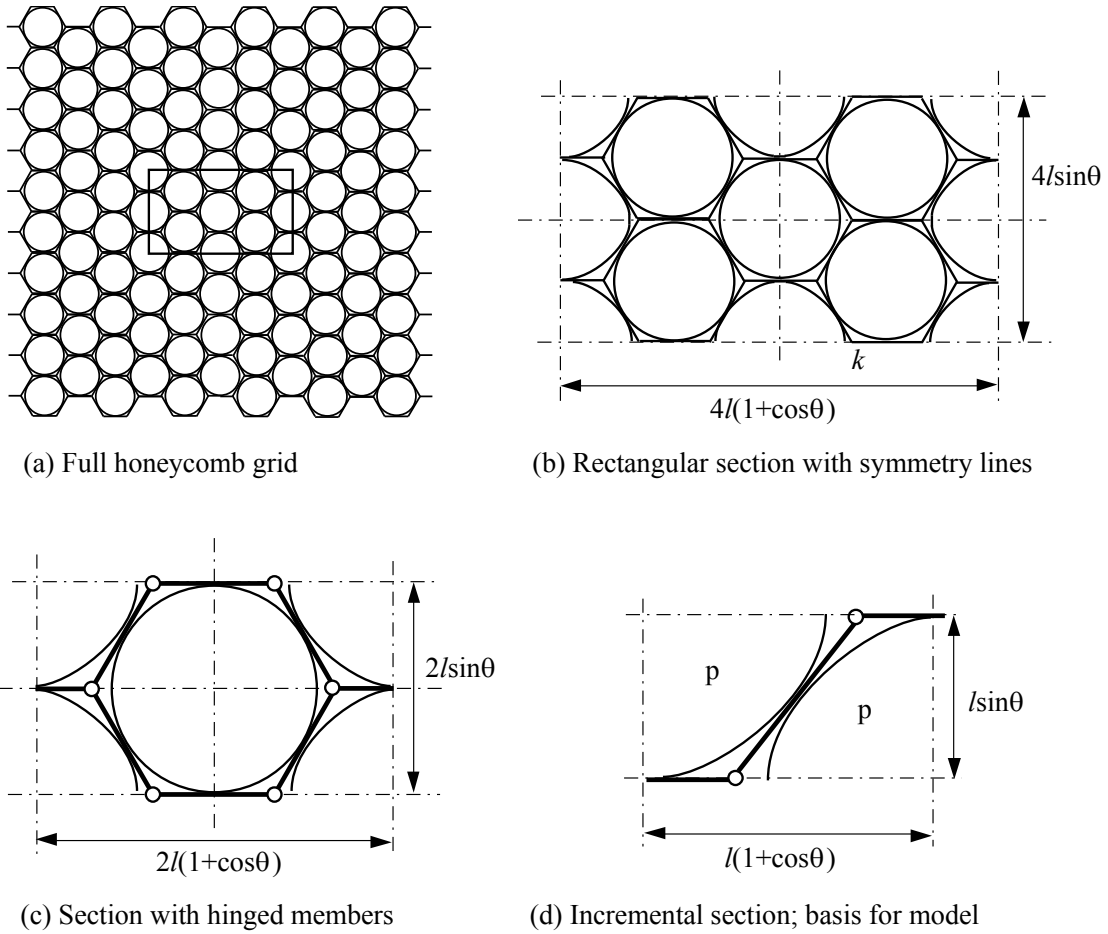
Figure 4.6   Breakdown of Honeycomb Grid into Basic Modeling Blocks

4.2.2 Force-Displacement Relation for Constrained Pressurized Volumes

To evaluate the relation between the internal volume and pressure, the perfect gas law [1] is employed, where R is the gas constant for air, T is the temperature, and m is the mass of air that is trapped in the pouch:

$$p = mRT/V \tag{4.22}$$

Following the approach laid out in Ref. 130 the useful work of a pressurized volume can be expressed as follows:

$$W_{use} = \int_{V_i}^{V} p\,dV - p_a(V - V_i) \tag{4.23}$$

85

In this equation, V_i is the initial volume of the system. The ambient pressure is the pressure is denoted with p_a. Two forms of applications can be envisioned for the pressurized honeycomb. One application would use sealed pouches that have a constant mass of air in them. In that case Equation 4.23 yields:

$$W_{use} = mRT\ln(V/V_i) - p_a(V - V_i) \tag{4.24}$$

Note that Equation 4.22 relates the change in pressure to the change of the inverse of the volume. When temperature and mass are independent of the displacement they are taken outside the integral.

Another application could rely on an outside pressure source to keep the pouches at a constant pressure. In that case p is constant and Equation 4.23 integrates to:

$$W_{use} = (p - p_a)(V - V_i) \tag{4.25}$$

The external work done by the force F can be found from:

$$W_{ex} = \int_s F \cdot ds \tag{4.26}$$

When the external work is balanced by the useful work done by the pressurized honeycomb a solution can be found for the external force, F. This force, in turn, can be related to principal and shear stresses as is pointed out in the next two sections.

4.2.3 In-Plane Deformation in Principal Directions

By loading a honeycomb grid with shear and normal stresses, discrete forces are introduced in the hinge points of the members. Figure 4.7(a) shows schematically how the stresses are introduced into the grid. Figure 4.7(b) demonstrates how an incremental section of the honeycomb would be loaded as a result of the stresses. The force that is introduced is related to the applied stresses and initial honeycomb angle, θ_i, as follows:

$$F = l\sqrt{\sigma_x{}^2 \sin^2 \theta_i + \sigma_y{}^2(1 + \cos \theta_i)^2} \tag{4.27}$$

$$\varphi = \tan^{-1}\left[\sigma_y(1 + \cos \theta_i)/\sigma_x \sin \theta_i\right] \tag{4.28}$$
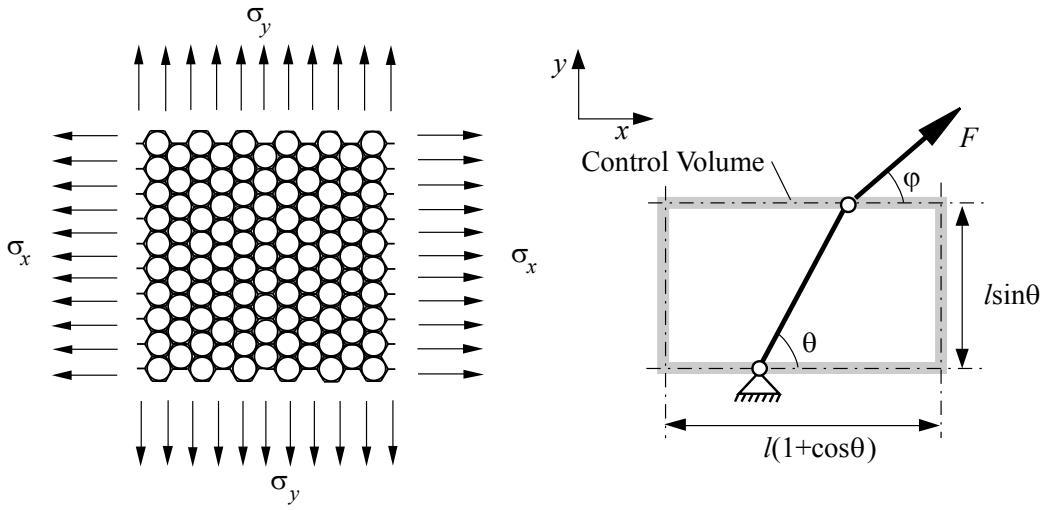
(a) Honeycomb grid loaded by Normal
Stresses

(b) Forces on Incremental Section Stemming
from Normal Stresses

Figure 4.7   Normal Stress on a Honeycomb Grid

Referring to Figure 4.7(b) for definitions, the relation between the pouch volume, V, and angle, θ, can be expressed as follows:

$$V = \zeta l^2 (1 + \cos\theta) \sin\theta \tag{4.29}$$

The incremental displacement in the direction of the applied force, ds, can be found from geometry:

$$ds = -l \sin(\theta - \varphi) d\theta \tag{4.30}$$

Integrating between θ_i and θ and taking the constant force out of the integral results in the following:

$$W_{ex} = Fl[\cos(\theta - \varphi) - \cos(\theta_i - \varphi)] \tag{4.31}$$

The external work balances the closed system work of Equations 4.25 and 4.24, respectively. For a constant mass, the force can be expressed as a function of the geometric and physical parameters according to:

$$F = \frac{1}{l} \frac{mRT\ln(V/V_i) - p_a(V - V_i)}{\cos(\theta - \varphi) - \cos(\theta_i - \varphi)} \tag{4.32}$$

In the case of a constant pouch pressure the force yields:

$$F = \frac{1}{l} \frac{(p-p_a)(V-V_i)}{\cos(\theta-\varphi)-\cos(\theta_i-\varphi)} \tag{4.33}$$

The relations of Equations 4.27 and 4.28 can be inverted to express the stresses as a function of the force as follows:

$$\sigma_x = \frac{F\cos\varphi}{l\sin\theta_i} \tag{4.34}$$

$$\sigma_y = \frac{F\sin\varphi}{l(1+\cos\theta_i)} \tag{4.35}$$

Equations 4.32 and 4.33 can be combined with Equations 4.34 and 4.35 to demonstrate relationships between stress and honeycomb angle for constant mass and constant pressure scenarios.

Two special cases are distinguished: pure longitudinal stress ($\varphi = 0$ or, equivalently, $\sigma_y = 0$) and pure lateral stress ($\varphi = \pi/2$ or, equivalently, $\sigma_x = 0$). For these two instances the relationship between stress and honeycomb angle can be determined for the case of constant mass and the case of constant pressure. These relations are presented below. Note that the volume terms should be substituted with the RHS of Equation 4.29, where V_i is found by substituting $\theta = \theta_i$.

Assume constant mass:

$$\sigma_y = 0 \qquad\qquad \sigma_x = \frac{1}{l^2\sin\theta_i} \frac{mRT\ln(V/V_i)-p_a(V-V_i)}{\cos\theta-\cos\theta_i} \tag{4.36}$$

$$\sigma_x = 0 \qquad\qquad \sigma_y = \frac{1}{l^2(1+\cos\theta_i)} \frac{mRT\ln(V/V_i)-p_a(V-V_i)}{\sin\theta-\sin\theta_i} \tag{4.37}$$

Assume constant pressure:

$$\sigma_y = 0 \qquad\qquad \sigma_x = \frac{1}{l^2\sin\theta_i} \frac{(p-p_a)(V-V_i)}{\cos\theta-\cos\theta_i} \tag{4.38}$$

$$\sigma_x = 0 \qquad\qquad \sigma_y = \frac{1}{l^2(1+\cos\theta_i)} \frac{(p-p_a)(V-V_i)}{\sin\theta-\sin\theta_i} \tag{4.39}$$

If the honeycomb is modeled with rigid members connected by hinges, the angle θ is related to the strain of the honeycomb according to:

$$\varepsilon_x = \frac{\cos\theta - \cos\theta_i}{1 + \cos\theta_i} \tag{4.40}$$

$$\varepsilon_y = \frac{\sin\theta - \sin\theta_i}{\sin\theta_i} \tag{4.41}$$

Both stress and strain are defined in terms of the honeycomb angle, θ. A comparison is made between the constant-mass and constant-pressure models in pure longitudinal and lateral stress, respectively. These stress-strain relations are displayed in Figure 4.8, where the following conditions apply: $\theta_i = 60°$, $R = 287\text{kJ/kg/K}$, $T = 288\text{K}$, and $\rho = 1.225\text{kg/m}^3$. In addition, the mass is calculated according to $m = \rho V_i$ and the pressure is calculated using the perfect gas law (Eq. 4.22).
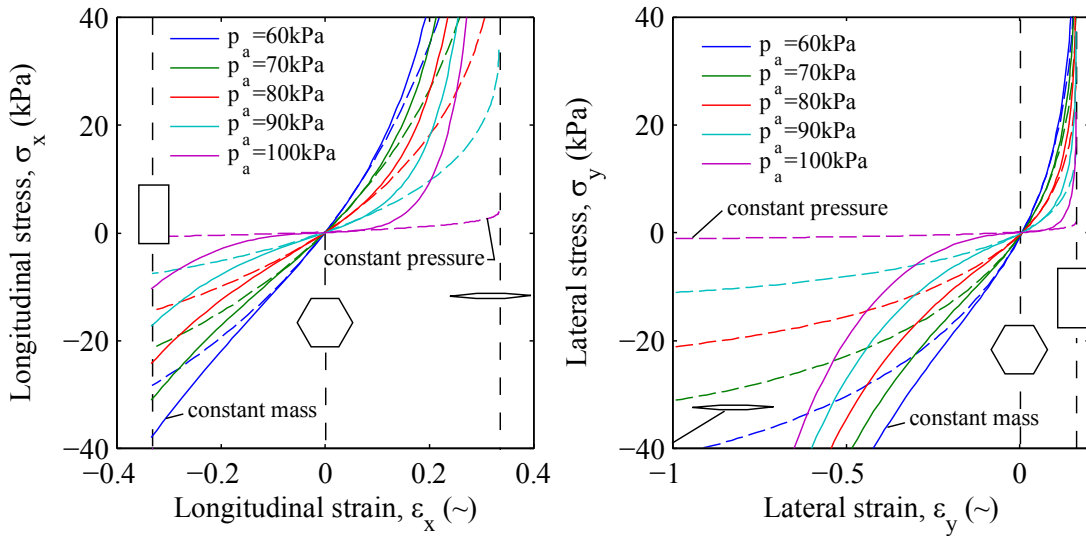
Figure 4.8   Comparing Results between Constant Mass and Constant Pressure Models in Pure Longitudinal Stress (left) and Pure Lateral Stress (right)

From the graphs above it can be seen that both models predict non-linear stress-strain behavior. Both models align around the zero-stress point. The constant-mass model shows more resistance against deformation than the constant-pressure model, especially at large positive longitudinal strains and large negative lateral strains. Note, that these two strain situations

correspond to the same volumetric change. At negative longitudinal strains and positive lateral strains both models follow each other much more closely.

In addition, the stress-strain relations for high-gage-pressure honeycomb are shown in Figure 4.9. Notice that the scale on the vertical axis in these graphs show stresses an order of magnitude greater than those presented in Figure 4.8. Apart from the scaling, the lines show similar behavior to those in the graphs above. The stress strain graphs for high-gage-pressure honeycomb are useful for determining the performance of externally pressurized honeycomb.
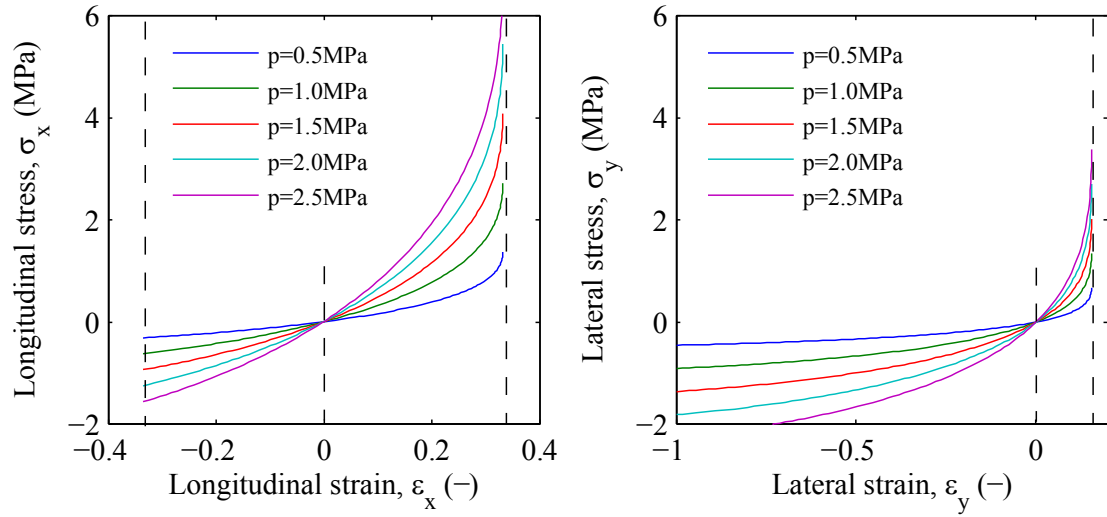
Figure 4.9   **Stress Strain Relations at Elevated Constant CDPs**

The Poisson's ratio is highly nonlinear because of the kinematics of the honeycomb structure. The Poisson's ratio is related to the angle θ according to:

$$v_{xy} = -\frac{\varepsilon_y}{\varepsilon_x} = -\frac{1+\cos\theta_i}{\sin\theta_i}\frac{\sin\theta-\sin\theta_i}{\cos\theta-\cos\theta_i} \tag{4.42}$$

$$v_{yx} = -\frac{\varepsilon_x}{\varepsilon_y} = -\frac{\sin\theta_i}{1+\cos\theta_i}\frac{\cos\theta-\cos\theta_i}{\sin\theta-\sin\theta_i} \tag{4.43}$$

Via the honeycomb angle, θ, the relation between the longitudinal and lateral strain, as well as the relation between the longitudinal strain and the Poisson's ratio can be plotted. Equations 4.40 through 4.43 are graphed in Figure 4.10 for $\theta_i = 60°$. From the figure below it can be seen that at the initial position ($\theta = \theta_i$) the Poisson's ratios equal unity.
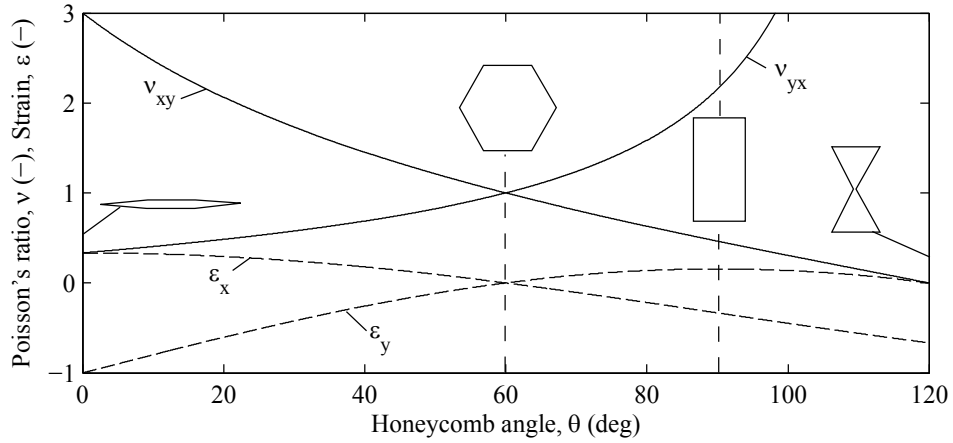
Figure 4.10   Poisson's Ratio and Strain Plotted Against Honeycomb Angle

Because the relationship between stress and strain is highly nonlinear the stiffness induced by the pressure is not constant. The stiffness changes throughout the deformation of the honeycomb. To explore the variation in longitudinal and lateral stiffness, respectively, the slopes of the local tangents to the stress strain curves are found:

$$E_x = \frac{d\sigma_x}{d\varepsilon_x} = \frac{d\sigma_x}{d\theta}\frac{d\theta}{d\varepsilon_x} \tag{4.44}$$

$$E_y = \frac{d\sigma_y}{d\varepsilon_y} = \frac{d\sigma_y}{d\theta}\frac{d\theta}{d\varepsilon_y} \tag{4.45}$$

If the derivatives in these relations are solved an expression for the stiffness as a function of the honeycomb angle, θ, is found. This process is detailed in Appendix B. Equations 4.44 and 4.45 are graphically shown as a function of strain in Figure 4.11 for the cases of constant mass (solid lines) and constant pressure (dashed lines). In addition, Figure 4.12 demonstrates the change in pressure stiffness for honeycombs at higher constant CDPs.

91
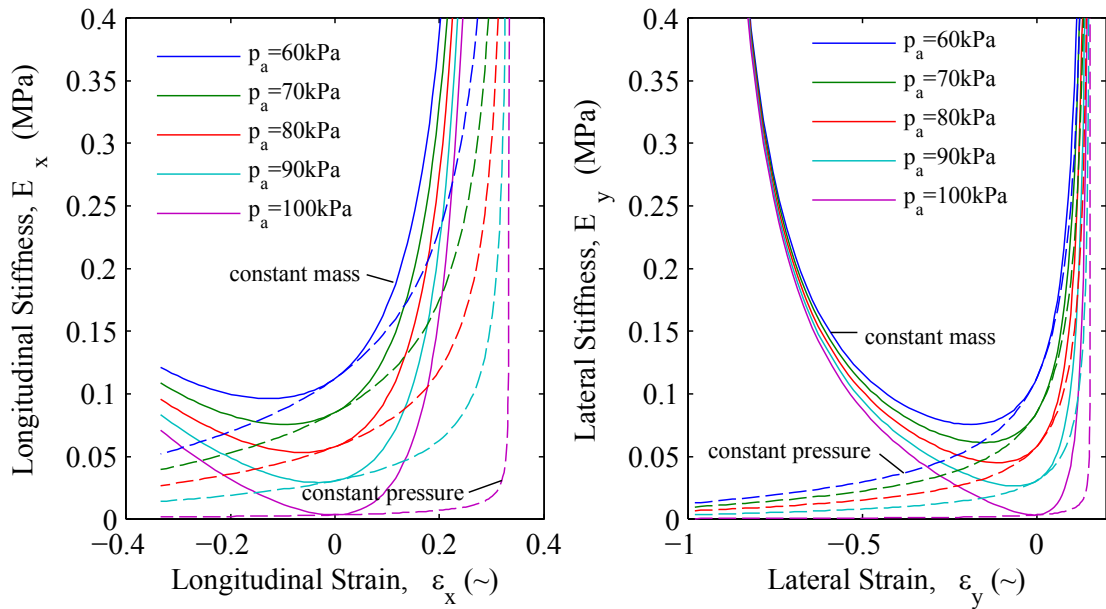
Figure 4.11   Stiffness Variation with Strain for $p = 101.3\text{kPa}$
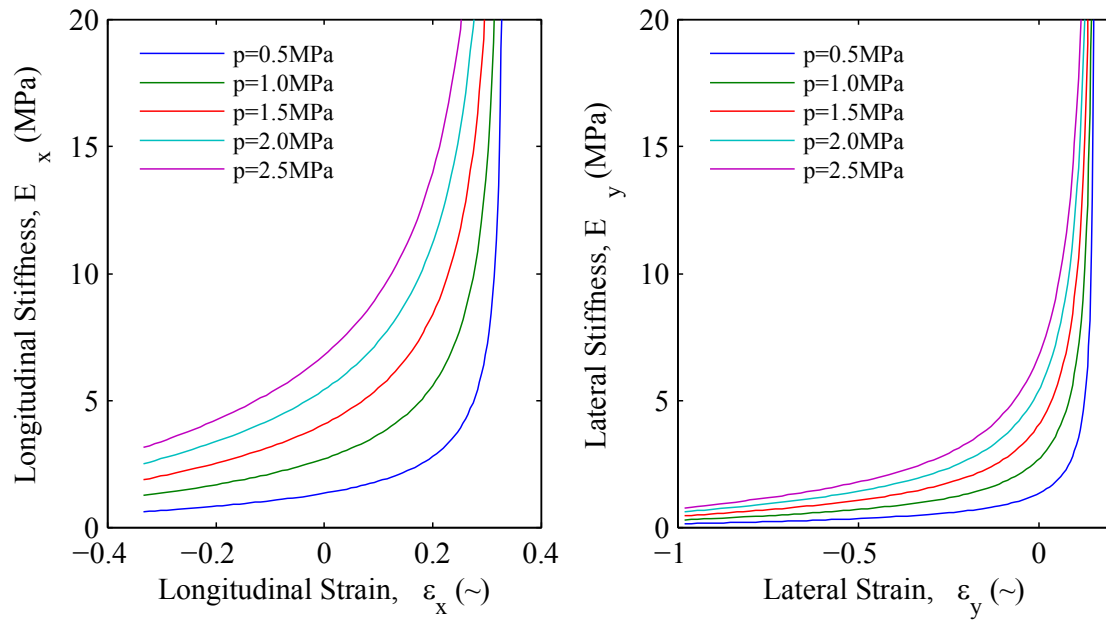
Figure 4.12   Stiffness Variation with Strain at Elevated CDPs ($p_a = 0$)

From the figures above some statements can be made about the pressure induced stiffness in the honeycomb. First of all, for both cases (constant mass and constant pressure) the stiffness

in principal directions is highly nonlinear. Furthermore, when there is no strain, the constant-mass and constant-pressure lines have the same value and the same slope. Moreover, at this point the stiffness in longitudinal direction equals the stiffness in lateral direction, yielding isotropic material properties. This is an important feature because once the pressure difference becomes high enough the honeycomb assumes a shape very close to where there are no effective strains. In this state, the honeycomb has isotropic in-plane stiffness properties which are well understood. Substituting $\theta = \theta_i = 60°$ in Equations 4.44 or 4.45 results in the appropriate value for the isotropic in-plane stiffness of the honeycomb.

4.2.4 In-Plane Shear Deformation

The shear deformation cannot be captured if the incremental section of Figure 4.7 with its constraints is considered. However, the proposed model of rigid members and frictionless hinges *is* capable of capturing the shear modulus of the pressurized honeycomb. Figure 4.13 shows how the incremental section in the honeycomb deforms as a result of forces stemming from shear stresses. Because of symmetry there is no relative motion of the diagonal member. Therefore, in this setup it is fixed between two hinge points. Similar to deformation of the honeycomb structure in Figure 4.3, all the shear deformation comes from rotation of the horizontal members. Therefore, the diagonal member in Figure 4.13 is shown with two fixed hinge points, preventing it from rotation.

(a) Honeycomb Grid Loaded by Shear
Stresses

(b) Forces on Incremental Section Stemming
from Shear Stresses
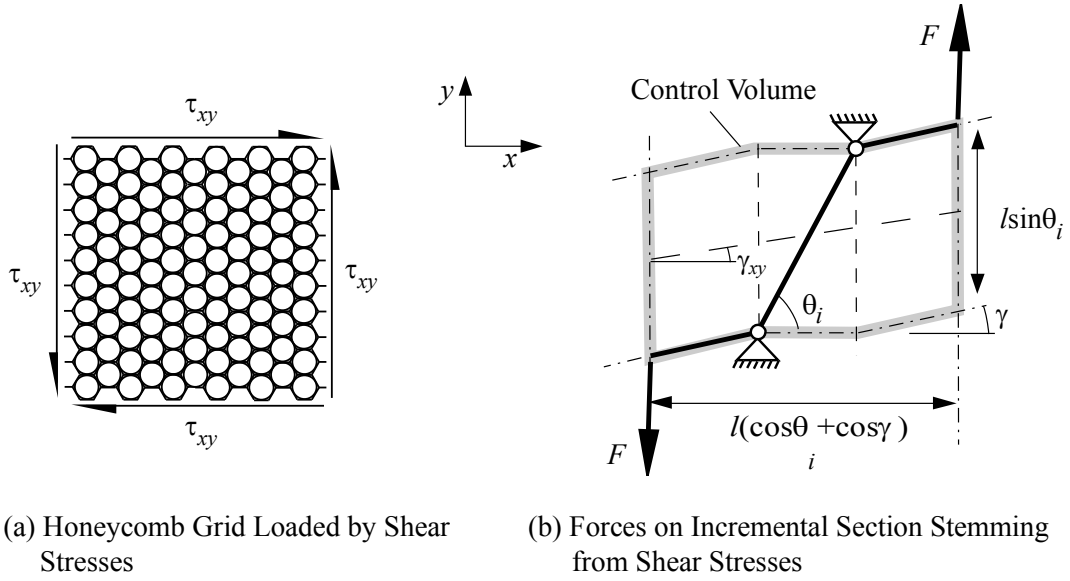
Figure 4.13   Shear Stresses on Honeycomb Grid

The shear strain, γ_{xy}, is related to the angular rotation, γ, of the horizontal member according

to:

$$\gamma_{xy} = \tan^{-1} \frac{\sin \gamma}{\cos \theta_i + \cos \gamma} \tag{4.46}$$

The force that stems from the shear stresses can be easily solved for:

$$F = \tau_{xy} l \sin \theta_i \tag{4.47}$$

To relate the shear stress to the shear strain, the same approach is used as in Section 4.1.3.
The control volume is a function of the shear strain according to:

$$V = \zeta l^2 \sin \theta_i \left(\cos \theta_i + \cos \gamma \right) \tag{4.48}$$

Equations 4.22 through 4.25 can be employed to find the work done by the pressurized vo-
lume for the case of constant mass and the case of constant pressure. The displacements of
the top right corner and the bottom left corner in the direction of the force add up to:

$$ds = 2l \cos \gamma \, d\gamma \tag{4.49}$$

94

Substituting ds in Equation 4.26 and integrating between 0 and γ results in the external work applied to the structure. Balancing the external work with the work done by the pressurized volume results in an expression for the force, F. In the case of a constant mass the shear stress is:

$$\tau_{xy} = \frac{1}{l^2 \sin \theta_i} \frac{mRT\ln(V/V_i) - p_a(V - V_i)}{2\sin \gamma} \tag{4.50}$$

When the pressure is held constant this relation changes to:

$$\tau_{xy} = \frac{1}{l^2 \sin \theta_i} \frac{(p - p_a)(V - V_i)}{2\sin \gamma} \tag{4.51}$$

Figure 4.14 shows how the shear stress and shear strain are related for when the honeycomb has perfectly hexagonal cells. In the case of constant mass, the structure shows a higher stiffness than in the case of constant pressure. Note that the graphs in this figure are only for positive shear strain.

(a) Const. Mass and Const. Pressure   (b) Constant Pressure
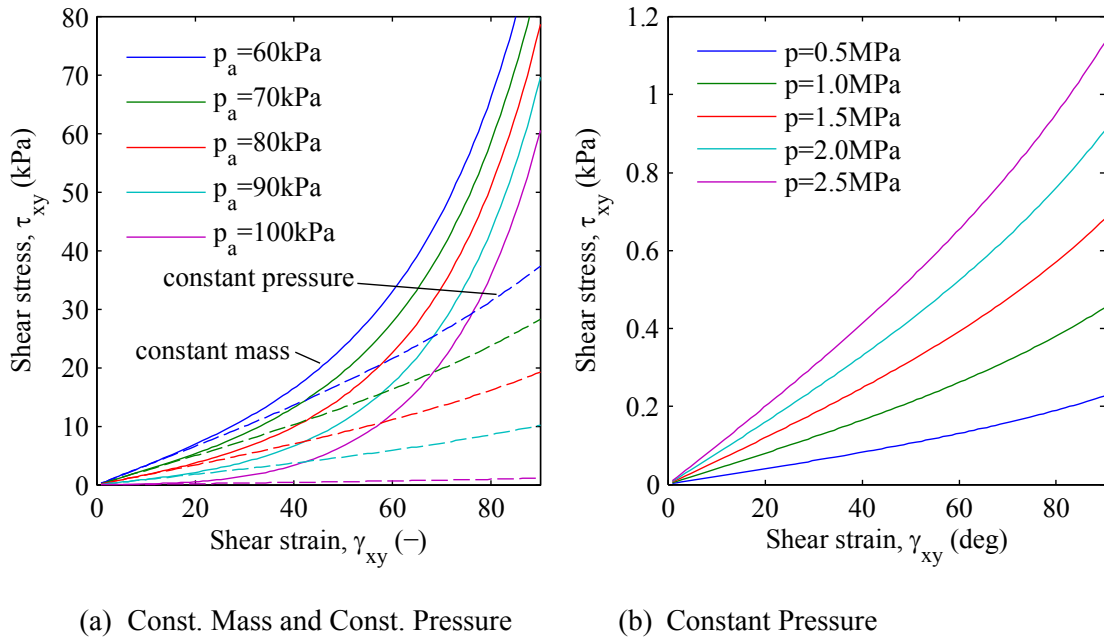
Figure 4.14   Shear Stress-Strain Relation for $\theta_i = 60°$; Comparing Results between Constant Mass and Constant Pressure Models in Shear Stress (left) and Elevated CDP (right)

The in-plane shear stiffness, G_{xy}, can be calculated according to:

$$G_{xy} = \frac{d\tau_{xy}}{d\gamma} \frac{d\gamma}{d\gamma_{xy}}$$ (4.52)

The derivatives in Equation 4.52 are elaborated in Appendix B. The variation in shear stiffness with shear strain is depicted in Figure 4.15. It is clear from this figure that the shear stiffness is highly non-linear with shear strain in case of constant mass. This non-linearity is less profound in the case of a constant pressure. Therefore, for relatively small shear strains, this could be very well approximated with a constant value, e.g. the value found when $\gamma = 0$.

(a) Const. Mass and Const. Pressure   (b) Constant Pressure at elevated CDP
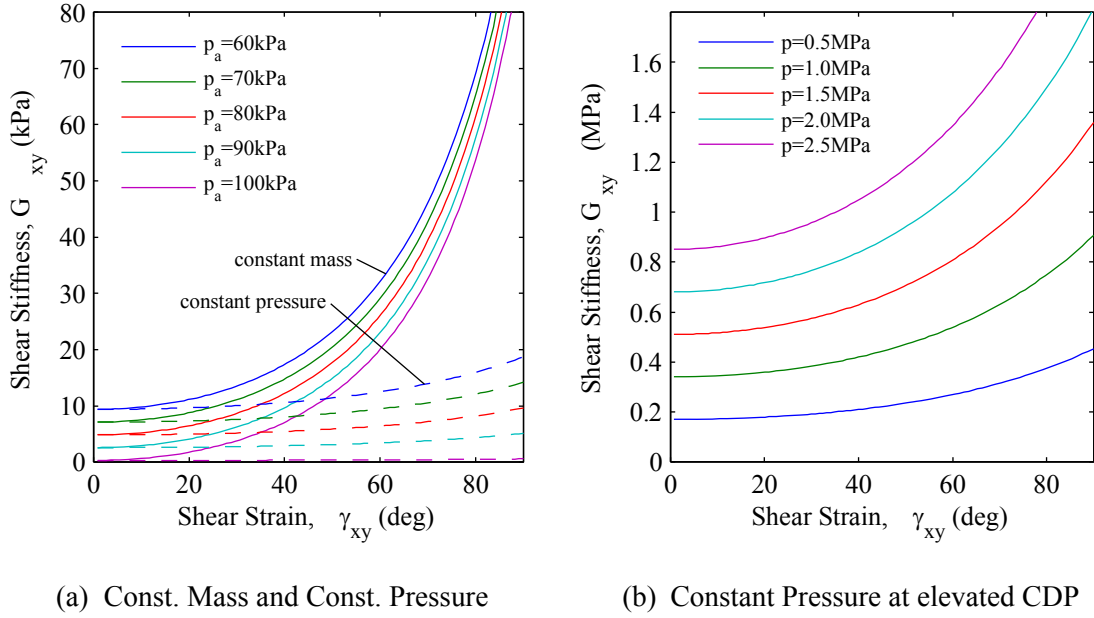
Figure 4.15   Shear Stiffness Variation with Shear Strain

4.2.5 Linearized Stress-Strain Relations

The stress-strain relations that have been presented in the previous sections are highly nolinear. In an effort to simplify the analysis of pressurized honeycomb, these relations can be linearized around a particular honeycomb angle. In this section the linearization of these relations is done around the honeycomb angle where $\varepsilon_x = \varepsilon_y = 0$. The slope of the line tangent to the stress-strain curve at zero strain is found by evaluating the stiffness (Equations 4.44, 4.45, and 4.52) at $\theta = \theta_i = 60°$. Since direct substitution does not result in a finite value for the stiffness, the limit for $\theta \to \theta_i$ needs to be evaluated. In the case of constant mass, taking

this limit results in the following values for the longitudinal, lateral and shear stiffnesses, respectively:

$$\lim_{\theta \to \theta_i} E_x = 3\zeta \left(\frac{mRT}{V_i} - p_a \right) \tag{4.53}$$

$$\lim_{\theta \to \theta_i} E_y = 3\zeta \left(\frac{mRT}{V_i} - p_a \right) \tag{4.54}$$

$$\lim_{\theta \to \theta_i} G_{xy} = \frac{3\zeta}{8} \left(\frac{mRT}{V_i} - p_a \right) \tag{4.55}$$

For the case of a constant pressure inside honeycomb pouches, these limits can be shown to evaluate to:

$$\lim_{\theta \to \theta_i} E_x = 3\zeta (p - p_a) \tag{4.56}$$

$$\lim_{\theta \to \theta_i} E_y = 3\zeta (p - p_a) \tag{4.57}$$

$$\lim_{\theta \to \theta_i} G_{xy} = \frac{3\zeta}{8} (p - p_a) \tag{4.58}$$

4.2.6 Stiffness Variation due to Varying Volume Ratio

In the previous sections the ratio between pouch and honeycomb volume has been denoted with the constant ζ. It can be shown that the assigned value of $\zeta = \sqrt{3}\pi/6$, is in reality a lower limit of this parameter and that its value increases when the honeycomb angle is altered. In addition, its maximum value is geometrically limited to one. Therefore, there is a possible 10% increase in this value. In this section the influence of a variable volume ratio is investigated by doing a sensitivity analysis on the stress and stiffness expressions.

The stiffness is linearly related to the first derivative of the stress to the honeycomb angle (see Equations 4.40, 4.45, and 4.52). The stress in the honeycomb is a function of the volume and consequently of the volume ratio, ζ. To see how the stress is related to the volume ratio, consider Equations 4.36 through 4.39. Substituting for the constant mass:

$$m = \rho_i V_i \tag{4.59}$$

By substituting Equation 4.29 into the expressions in 4.36 through 4.39 and extracting the volume ratio, the following can be deduced:

$$\bar{\sigma} = \zeta \cdot \bar{f}(\theta, \gamma) \qquad (4.60)$$

where $\bar{\sigma}$ is the stress vector and $\bar{f}(\theta, \gamma)$ is a vector containing the functions that relate stress to honeycomb and shear angles. The linear relationship between stress, $\bar{\sigma}$, and ζ is obvious from the above equation. To find the stiffness vector, the components of the stress vector are differentiated one-by-one with respect to their corresponding components in the strain vector:

$$\bar{E} = \frac{d\bar{\sigma}}{d\bar{\varepsilon}} = \zeta \cdot \bar{g}(\theta, \gamma) \qquad (4.61)$$

Where $\bar{g}$ is the vector that contains the functions that relate the stiffness to the honeycomb and shear angles. The linear relationship between the stiffness components and the volume ratio is still intact because the strain is independent of the volume ratio. Given the fact that the theoretical variation in ζ is +10% with respect to the baseline value of $\zeta = \sqrt{3}\pi/6$, the model under-predicts the stiffness by a maximum of 10%.

An alternative approach could include the volume ratio as a variable dependent on the honeycomb angle. This approach was not chosen because it makes the model more complicated without significantly increasing its accuracy.

4.3 Mechanics of Pressure Adaptive Honeycombs

The previous sections have introduced two models. The first one is a simple analytic model for the principal stiffnesses of honeycomb made from isotropic material. The second one is an analytic model of pressurized honeycomb under the assumption of rigid members that are hinged together. In this section it is proposed to fuse these two models into one single model under the assumption that the stiffness predicted by either model is independent of the other.

4.3.1 Model Setup and Assumptions

Before presenting this model it is important to describe the most important limitations and its use for engineers. Similar to the analytic model for honeycomb (Ref. 129 and Sec.4.1) this present model is only applicable to honeycombs that are loaded in one principal direction and are free expand/contract in the direction perpendicular to this direction. Figure 4.16 demon-

strates schematically which boundary conditions can be in place when the honeycomb model is used and which boundary conditions cannot be used. Examination of the sketches in this figure shows that when too many boundary conditions are applied, the honeycomb becomes essentially fixed. In that case, the honeycomb members become loaded in pure tension/compression. The material stiffness (E) is then the dominant property when it comes to deformation, while the stiffness of the honeycomb (E_x, E_y) becomes negligible. In a real application of pressure adaptive honeycomb this is not an appropriate way to constrain the honeycomb because it cannot be used as an actuator. In that sense, the proposed model can still be used for realistic applications.
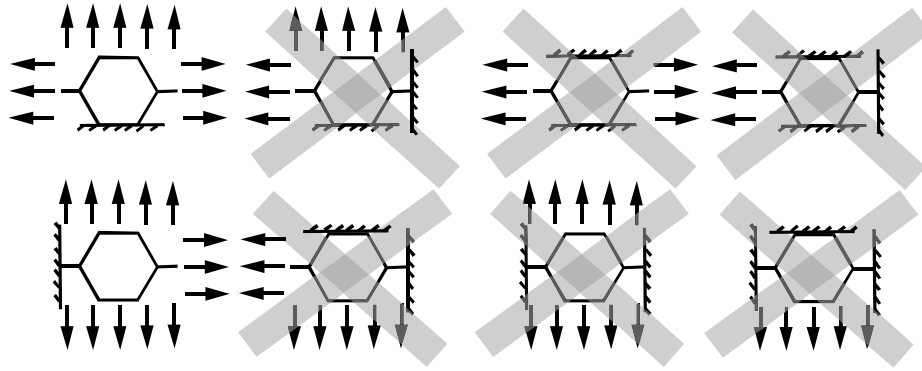
Figure 4.16   Schematic Representations of the Boundary Conditions that Can /Cannot be in Place when using the Analytic Model for Pressurized Honeycomb

Figure 4.17 schematically shows how a honeycomb structure would contract and expand (depending on the loading condition) when two opposite sides of the honeycomb would be cantilevered. This behavior is shown for regular and auxetic honeycomb in Ref 131. It is assumed that pressurized honeycomb shows the same global behavior as ordinary honeycomb, even though deformation stresses are much higher when pressure is applied to the pouches inside the honeycomb cells.

The boundary conditions have a profound effect on the cells neighboring the clamps. However, further away from the bounds their influence diminishes. In this area the structure is more-or-less free to expand or contract perpendicular to the loading direction. If it is assumed that the honeycomb cells far away from the boundaries can be modeled as being unconstrained in the direction opposite to the loading, the model presented in the this section can be used to predict the deformation as a function of the applied stress.
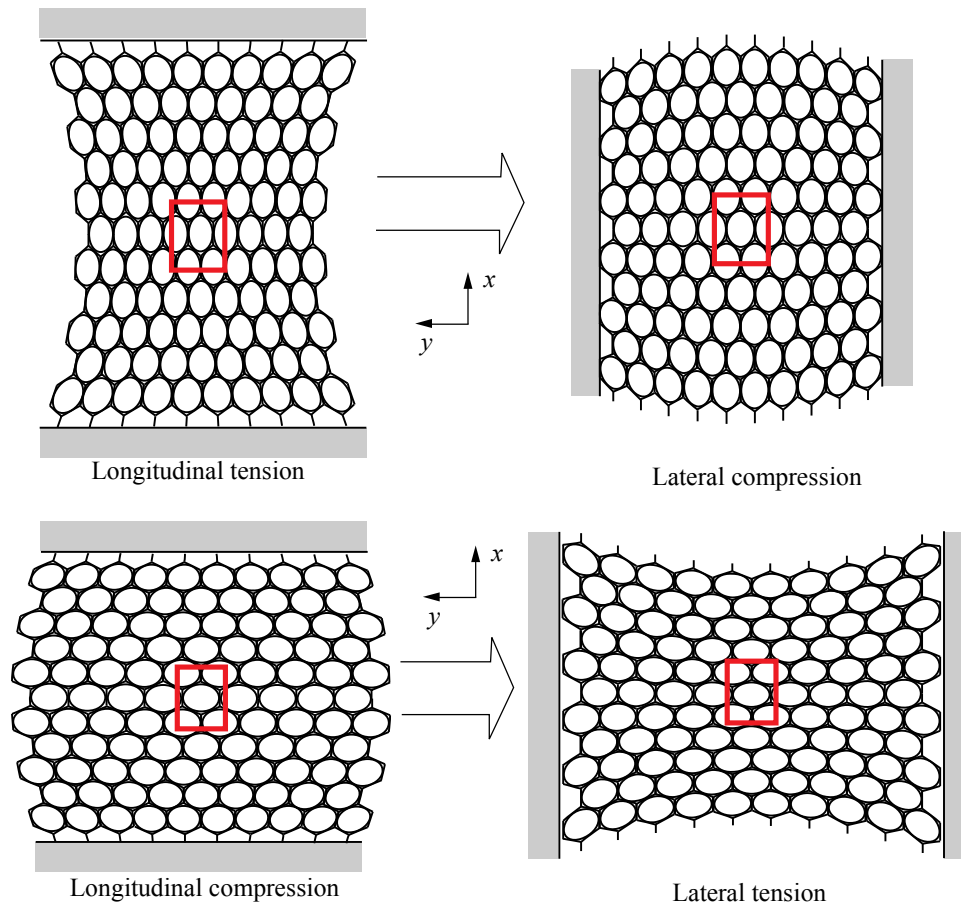
Figure 4.17   Schematic Representation of Honeycomb Deformation during Straining

In addition to the unconstrained deformation of the honeycomb cells away from the boundaries, there is another feature of the pressurized honeycomb that is pointed out in Figure 4.17. Longitudinal tension and lateral compression result in the same deformation of the cells and the contained pouches away from the boundaries. The same holds for longitudinal compression and lateral tension. In other words, the pressure stiffness introduced in these cells is identical in both cases.

Apart from the boundary conditions, the other assumptions that applied to the two original models also apply to the proposed model for pressure adaptive honeycomb. This includes a maximum strain range of +/-15%, the use of isotropic material, and a constant pouch-to-cell volume ratio.

4.3.2 In-Plane and Shear Stress-Strain Relations of Pressurized honeycombs

When pressurized honeycomb deforms, the stress field is balanced by the overall strain times the overall stiffness. The stiffness is induced by the honeycomb material and the pressure inside the pouches. The stiffness induced by the honeycomb material has been presented in Eqs. 4.6, 4.11, and 4.20. The pressure induced stiffness has been presented in Eqs. 4.44, 4.45, and 4.52. To establish the stress-strain relationships, these principal and shear stiffnesses are added resulting in the following analytic model:

$$\sigma_x = [E_x(\varepsilon_x, \theta_i) + E_x^*(t/l, E, \theta_i)]\varepsilon_x \tag{4.62}$$

$$\sigma_y = [E_y(\varepsilon_y, \theta_i) + E_y^*(t/l, E, \theta_i)]\varepsilon_y \tag{4.63}$$

$$\tau_{xy} = [G_{xy}(\gamma_{xy}, \theta_i) + G_{xy}^*(t/l, E, \theta_i)]\gamma_{xy} \tag{4.64}$$

The proposed nonlinear Poisson's ratios are the same as for the rigid-wall honeycomb (Eqs. 4.42 and 4.43), where it is added here that $\theta = \theta(\varepsilon_x)$ or $\theta = \theta(\varepsilon_y)$. This yields:

$$v_{xy} = v_{xy}(\varepsilon_x, \theta_i) \tag{4.65}$$

$$v_{yx} = v_{yx}(\varepsilon_y, \theta_i) \tag{4.66}$$

Equations 4.62 through 4.66 together form the analytic model that predicts the stresses and geometry as a function of honeycomb angle, thickness-to-length ratio, material stiffness, and strain.

4.3.3 Linearized Stress-Strain Relations of Pressurized Honeycombs

To simplify the stress-strain relations and Poisson ratios (Eq. 4.62-4.66) the linearization scheme of Section 4.2.5 can be applied. This linearization removes the dependency of the pressure stiffness (E_x, E_y, G_{xy}) on the overall strains, ε_x, ε_y and γ_{xy}. A linear relationship between stress and strain consequently results and the stiffness becomes a constant dependent on the CDP and the honeycomb geometry, material, and dimensions. The stress-strain relations, accordingly degenerate to:

$$\sigma_x^{lin} = [E_x^{lin}(\theta_i) + E_x^*(t/l, E, \theta_i)]\varepsilon_x \tag{4.67}$$

$$\sigma_y^{lin} = \left[E_y^{lin}(\theta_i) + E_y^*(t/l, E, \theta_i)\right]\varepsilon_y \tag{4.68}$$

$$\tau_{xy}^{lin} = \left[G_{xy}^{lin}(\theta_i) + G_{xy}^*(t/l, E, \theta_i)\right]\gamma_{xy} \tag{4.69}$$

Of course, this also implies the effect of deformation on θ_i is "small", generally in line with an infinitesimal strain assumption. The Poisson ratios are consequently only dependent on the honeycomb angle:

$$v_{xy} = v_{xy}(\theta_i) = \frac{\cos\theta_i(\cos\theta_i+1)}{\sin^2\theta_i} \tag{4.70}$$

$$v_{yx} = v_{yx}(\theta_i) = \frac{\sin^2\theta_i}{\cos\theta_i(\cos\theta_i+1)} \tag{4.71}$$

The values of E_x^{lin}, E_y^{lin}, and G_{xy}^{lin} can be quite easily obtained by substituting the appropriate honeycomb angle, θ_i, into Equations 4.44, 4.45, and 4.52, respectively. These equations are expanded in Appendix B and the resulting components can be easily assembled at the MAT-LAB level.

An intuitive example of a linearized model of pressure adaptive honeycomb is given here for the case when $\theta = \theta_i = 60°$. In that case the Equations 4.53 through 4.58 can be inserted for E_x^{lin}, E_y^{lin}, and G_{xy}^{lin}. In the case of a constant mass in the cell, this results in the following explicit stress-strain relationship:

$$\sigma_{x,\,\theta_i=60°}^{lin} = \left[3\zeta\left(\frac{mRT}{V_i} - p_a\right) + \frac{4E}{\sqrt{3}}\left(\frac{t}{l}\right)^3\right]\varepsilon_x \tag{4.72}$$

$$\sigma_{y,\,\theta_i=60°}^{lin} = \left[3\zeta\left(\frac{mRT}{V_i} - p_a\right) + \frac{4E}{\sqrt{3}}\left(\frac{t}{l}\right)^3\right]\varepsilon_y \tag{4.73}$$

$$\tau_{xy,\,\theta_i=60°}^{lin} = \left[\frac{3\zeta}{8}\left(\frac{mRT}{V_i} - p_a\right) + \frac{12E}{5\sqrt{3}}\left(\frac{t}{l}\right)^3\right]\gamma_{xy} \tag{4.74}$$

A comparison between the linear and nonlinear stress-strain relationships for the case of a constant mass is shown in Figure 4.18. The solid lines in the top two plots show the predicted nonlinear relation between the principal stresses and principal strains, while the dashed lines show the linearization about $\theta = 60°$. The corresponding equations are also referred to in the plots. In addition, the bottom two plots show the relative deviation of the linearized model

with respect to the original nonlinear model. In those plots a band is drawn that demonstrates where the linearized approximation deviates less than 5% from the nonlinear approximation. For a particular combination of ambient pressure, p_a, and strain, ε, a corresponding deviation in stress can be found from these two bottom plots. When this deviation is beyond 5% the linearized model might be considered invalid. This bounds the maximum strain range for which the linearized model can be employed. These bounds are denoted with a '+' mark in the bottom plots of Figure 4.18.
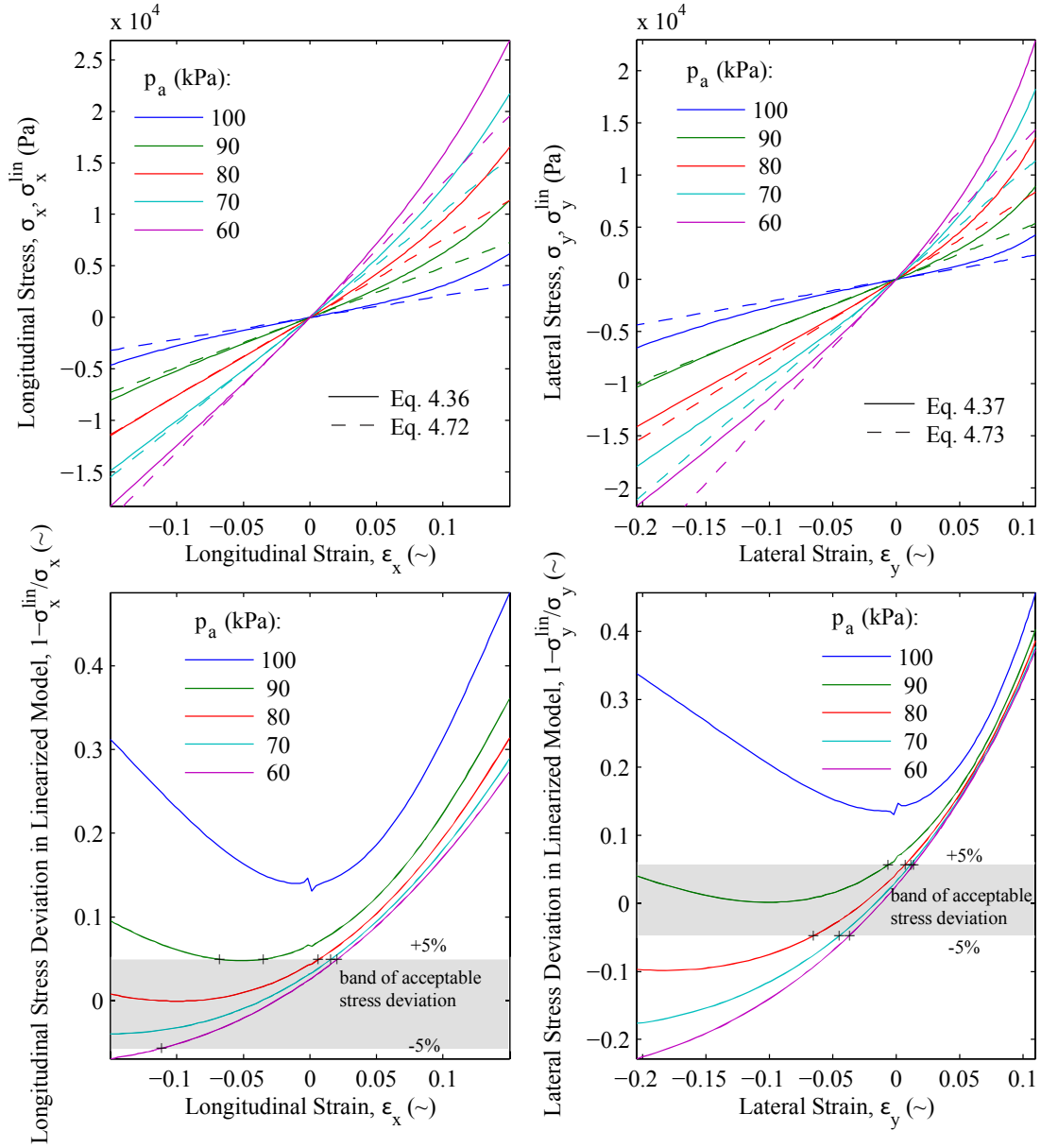
Figure 4.18 **Comparison between Principal Stresses as Predicted by Analylical Model and Linearized Model for the Case of Constant Mass ($mRT/V_i = 100$kPa)**

In the case of a constant pressure in the cell, the linear stress-strain relationship degenerates to:

$$\sigma^{lin}_{x,\,\theta_i=60°} = \left[3\zeta(p - p_a) + \frac{4E}{\sqrt{3}}\left(\frac{t}{l}\right)^3\right]\varepsilon_x \qquad (4.75)$$

$$\sigma^{lin}_{y,\,\theta_i=60°} = \left[3\zeta(p - p_a) + \frac{4E}{\sqrt{3}}\left(\frac{t}{l}\right)^3\right]\varepsilon_y \tag{4.76}$$

$$\tau^{lin}_{xy,\,\theta_i=60°} = \left[\frac{3\zeta}{8}(p - p_a) + \frac{12E}{5\sqrt{3}}\left(\frac{t}{l}\right)^3\right]\gamma_{xy} \tag{4.77}$$

The difference between the linearized model and the nonlinear analytic model is shown in Figure 4.19. The dashed lines in the two top plots show the stress-strain relationship for the linearized model, while the solid line shows the original nonlinear prediction. The corresponding equations are also denoted. In the two lower plots the relative deviation between the linearized model and the nonlinear analytic model is demonstrated. Similar to Figure 4.18, a band is shown where the principal stresses that are predicted by the linearized model do not deviate more than 5% from the stresses predicted by the nonlinear model. The '+' marks denote the minimum and maximum strains between which the linear model is perceived to be valid. It can be seen that these bounds tend to converge for higher values of CDP. At 40kPa the linear model is valid for: $-4.5\% < \varepsilon_x < 4.5\%$, and $-2.5\% < \varepsilon_y < 2\%$. At lower CDP this validity range becomes larger as can be seen in Figure 4.19.
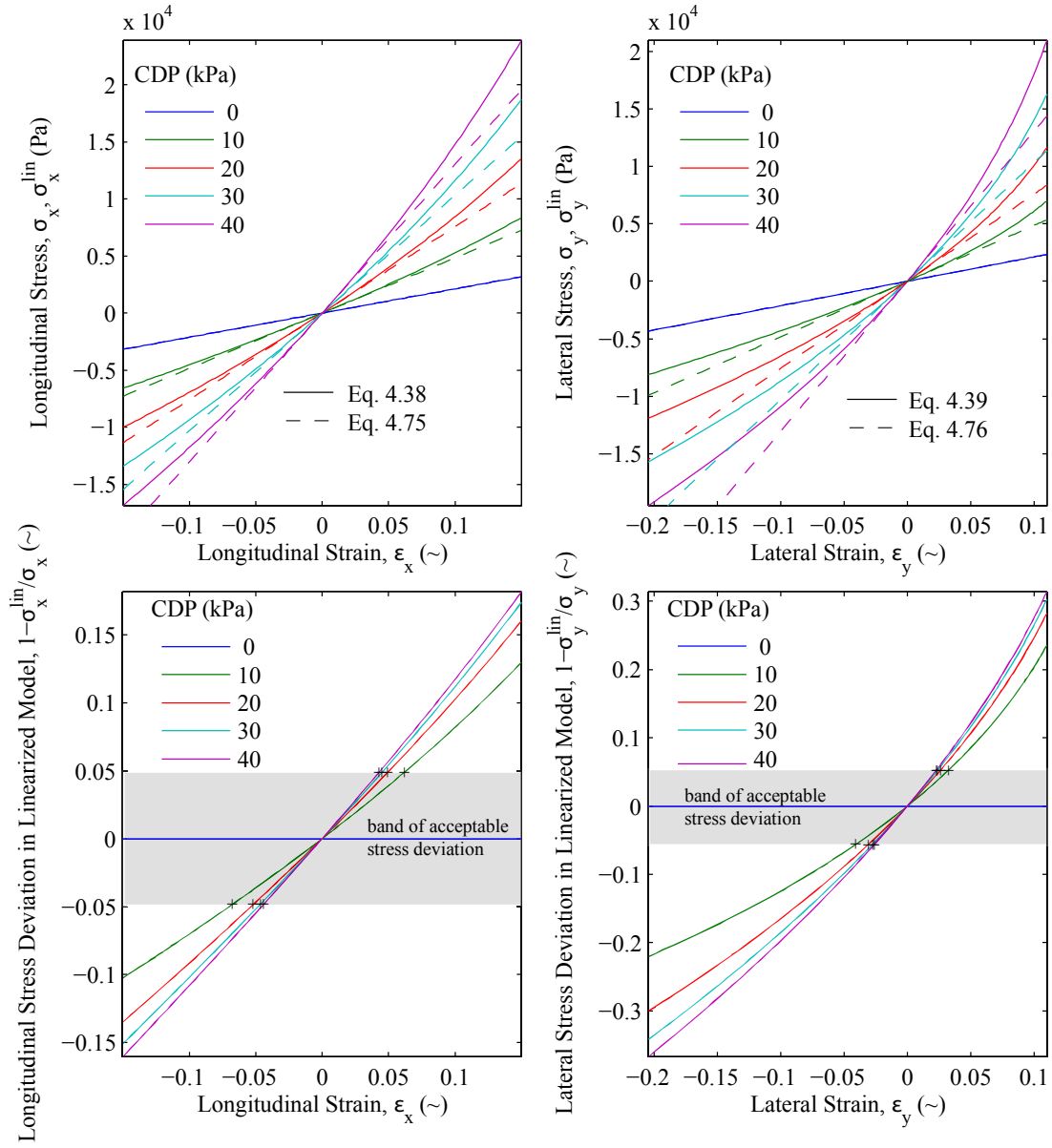
Figure 4.19   **Comparison between Principal Stresses as Predicted by Analylical Model and Linearized Model for the Case of Constant Pressure**

This linear model leads to the concept of equivalent stiffness, where the honeycomb material is artificially stiffened by the fact that there is a pressure acting on the ligaments. If the vector of combined linear stiffnesses is denoted with $\widehat{\boldsymbol{E}}$, then the following is implied:

$$\widehat{\boldsymbol{E}} = \boldsymbol{E}^{\text{lin}}(\theta_i) + \boldsymbol{E}^*(t/l, E, \theta_i) \tag{4.78}$$

This stiffness could be equated to the stiffness of honeycomb structure of identical geometry and dimensions but with no pressurized cells. In that case, the equivalent <u>material</u> stiffness, E_{eq}, can be extracted by using CMT. Equations 4.6, 4.11, and 4.20 can be inversed as follows to find the equivalent stiffness:

$$\frac{E_{eq}}{\hat{E}_x} = \left(\frac{l}{t}\right)^3 \frac{\sin^3 \theta_i}{\cos \theta_i + 1} \tag{4.79}$$

$$\frac{E_{eq}}{\hat{E}_y} = \left(\frac{l}{t}\right)^3 \frac{(1+\cos \theta_i)\ \cos^2 \theta_i}{\sin \theta_i} \tag{4.80}$$

$$\frac{E_{eq}}{\hat{G}_{xy}} = \frac{4}{5}\left(\frac{l}{t}\right)^3 \frac{\sin \theta_i}{1+\cos \theta_i} \tag{4.81}$$

From these equations it can be observed that only one component of $\hat{\boldsymbol{E}}$ needs to be known in order to calculate E_{eq}. The equivalent stiffness could potentially be used in a finite element analysis of a honeycomb grid. This would simplify the analysis considerably because external loading due to a CDP would already be implied in the material stiffness of the honeycomb.

4.4   Pressurized Honeycomb as Adaptive Actuator

The previous section introduced an analytic model for pressure adaptive honeycomb. This section shows how this model can be employed if pressure adaptive honeycomb is to be used as actuator. First the presence of a restoring force is discussed. While it is evident how to actuate pressure adaptive honeycomb when the pressure can be controlled, it is less obvious how to do this when the pouches are sealed and only a fixed amount of air is present in them. In 4.4.2 it is shown how to determine the amount of mass inside the pouches, such that they start actuating once a pre-determined atmospheric pressure is reached. This section closes with an example of altitude adaptive honeycomb.

4.4.1 Bidirectional Actuation

The application of pressurized honeycomb for actuation purposes can be various. As was presented in Chapter 3, small tabs, like vortex generators or Gurney flaps, could be deployed, or larger sectional variations in wing or flap geometry could be induced. Independent of the application, though, there are two basic means of providing pressure to the honeycomb pouches.

The first option relies on bleed air from the engine compressor in combination with a system of hoses, pipes, and valves. This could yield very high pressures in the pouches, while there would essentially be no mass flow, implying no pressure loss. The second option employs a sealed pouch that holds a fixed amount of air and relies on the change in ambient pressure to create a pressure differential. This last option would be particularly advantageous to high-subsonic aircraft that encounter a 60kPa pressure difference between take-off and cruise altitude. This system would require no control mechanism, hoses or valves. The stiffness of the structure would adapt to its surroundings and would therefore make this an entirely new type of adaptive structure.

Using either principle, the pressurized honeycomb is not per definition an actuator. One can imagine starting with a honeycomb that, at zero CDP, consists of perfect hexagons. Increasing the CDP leads to a stiffening of the honeycomb, but no deformation takes place. In other words, no mechanical work is performed. This illustrates that if the pressurized honeycomb needs to act as an adaptive actuator, it requires some kind of force that induces a deformation in the honeycomb when no CDP exists. This restoring force can come from elastic forces residing within the honeycomb structure. For any initial honeycomb angle, other than $\theta_i = 60$, these elastic forces exist and can be used to restore the structure to an initial shape.

Schematically, the superposition of the pressurized honeycomb and the elastic honeycomb is presented in Figure 4.20. The stiffness induced by the CDP is represented as a spring with a settling length of $2l$. The stiffness induced by the elasticity of the honeycomb is represented by a spring of stiffness k_s and has a settling length of $2l + s_s$. Since the pouches are physically in the honeycomb structure, the end point of both springs is identical. The settling length of the superimposed springs lies therefore between those of the individual springs: $0 < s < s_s$. As was shown in Section 4.1, the elastic stiffness is constant, meaning that the changing pressure stiffness (due do a change in CDP) directly influences the settling length of the superimposed springs. When the CDP approaches infinity the settling length equals $2l$, while when the CDP is zero, the settling length equals $2l + s_s$.
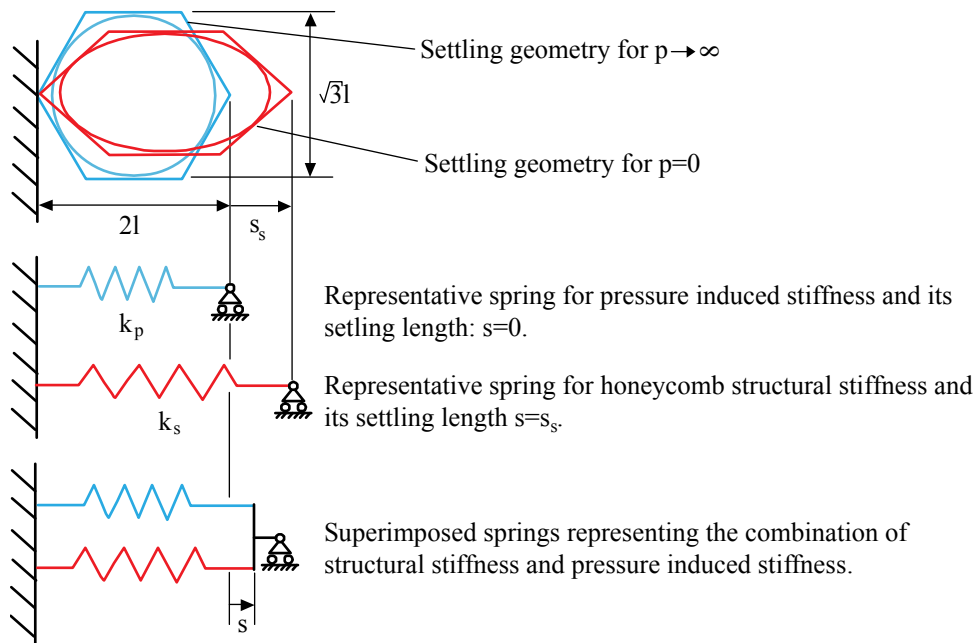
Figure 4.20   Superimposing Pressure Stiffness to Structural Stiffness

In addition to the elastic forces that are present in honeycomb, external (elastic) forces can be applied to assist in bringing back the structure to its original shape. Figure 4.21 schematically shows such an external restoring force to the pressurized honeycomb. Physically, such a force could arise from elastic components of the structure that surround the honeycomb. In the proof-of-concept Gurney flap that was presented in Section 3.2.2 this restoring spring force was introduced by a pre-curved steel sheet. When no CDP existed, the curved sheet assumed its original shape. However, when the CDP was increased and the stiffness of the pressurized honeycomb increased with it, the sheet assumed a much straighter shape.

Settling geometry for p→∞   Displacement for $0 < p < \infty$
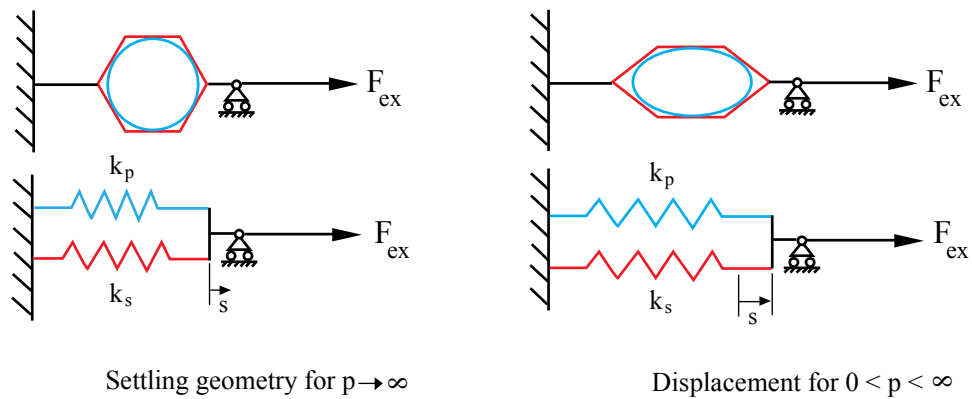
Figure 4.21   External Spring to Restore Pressurized Honeycomb to Initial Position

109

Note that the settling position of the system of springs and external force does not coincide with the settling position of the spring that represents the honeycomb material stiffness. Moreover, it is beneficial if an external force would pull the honeycomb spring beyond its settling length and into tension. The reason for this lies in the fact that, for a given strain, the maximum absolute curvature that is introduced in the diagonal honeycomb walls decreases when the wall is forced to bend in both directions. Therefore, it is less likely that any plastic deformation is encountered during the bending of these walls. An example of such a structure could consist of a honeycomb cells with a wall angle of $\theta_i = 75°$ and an external spring that would force the cells to bend to $\theta = 90°$ when no CDP is exists. Now, increasing the CDP would yield a structure for which $\theta \rightarrow 60°$. In other words, a 30° range of honeycomb angles would be achieved while the honeycomb wall would only see a maximum change of 15°.

4.4.2 Engagement of Pressure Stiffness

When an external pressure source is used to regulate the CDP in the pressurized honeycomb, the stiffness can be controlled quite easily. However, when the more adaptive variant is used, where a constant mass is present in the pouches, controlling the stiffness can only be done by ascending or descending of the aircraft. As was briefly shown in Figure 3.14, one thing that can be controlled is the altitude at which the stiffening starts. This altitude is referred to as the 'engagement altitude' and can be anywhere between the take-off and cruise altitude. In general, however, it would be wise to set this altitude to where the aircraft can serve for example 95% of all major worldwide airports with the adaptive honeycomb structure fully deployed. In the next paragraphs it is shown that a trade-off needs to be made between the elevation of the engagement altitude and the amount of mass that is available in the pouches. Remembering that the mass in the pouches has a positive correlation with the pressure stiffness (see Appendix B) it is generally desired to optimize the amount of mass inside the pouches.

When a particular pressure engagement altitude (ea) is desired the mass inside the pouch is:

$$m < \rho_0 V_{ea} \tag{4.82}$$

This results in a partly inflated pouch with a fixed amount of air at a pressure, p (see Figure 4.22). Decreasing the ambient pressure results in an expansion of the gas inside the pouch (Equation 4.22) until the perimeter pulls taut. When the ambient pressure decreases further,

the pouch tries to form a perfect circle, such as to minimize its circumferential strain energy. By doing so it forces the strained honeycomb cell into a perfect hexagon. The ambient at which the pouch pulls taut and starts to do work on the structure is termed the engagement pressure. It corresponds to a unique altitude in the international standard atmosphere.

Pouch unengaged Pouch engagement Perfect hexagon
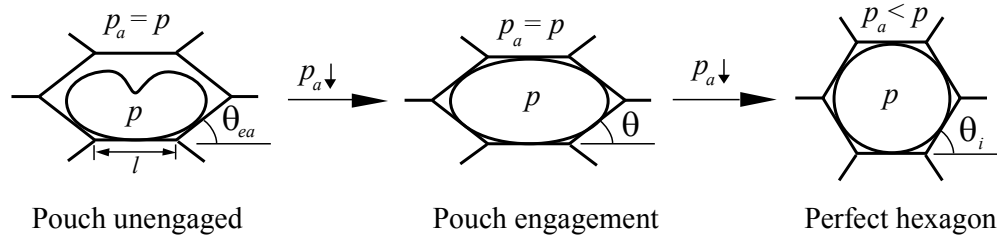
Figure 4.22 Sketch of Honeycomb Deformation with Pressure Assuming Constant Mass

To find the engagement altitude, a honeycomb cell is considered with a honeycomb angle of $\theta_{ea} \neq 60°$. At this angle, Equation 4.29 can be employed to find the volume, V_{ea}, at which engagement occurs. In that case Equation 2.6 can be equated to Equation 4.22 and the altitude at which engagement occurs can be extracted. Conversely, if an altitude of engagement is desired it is possible to determine the mass of trapped air that is required to have this happen. If the pouch is filled at sea level the mass of air that is put in can be correlated to the zero-altitude volume, V_0, according to:

$$m = \rho_0 V_0 \tag{4.83}$$

Combining these equations and noting that the temperature and pressure in the pouch change with pressure height according to Equation 2.5 and 2.6, respectively, the following can be deduced:

$$V_0 = V_{ea}\left(1 + c\frac{h}{T_0}\right)^{-\left(\frac{g_0}{cR}+1\right)} \tag{4.84}$$

where V_{ea} is the volume at which engagement occurs and is a function of the geometry of the hexagon only (Equation 4.29). By using Equation 4.84 the zero-altitude pouch volume can be found as a function of the engagement altitude, h. This is an important parameter because it is required when the sealed pouches are manufactured.

4.4.3 Example of Altitude Adaptive Honeycomb

All the tools to analyze the pressure adaptive honeycomb have been presented in the preceding sections. In this section an example is presented of how all this theory can be applied to make a simple pressure adaptive actuator that is controlled by aircraft altitude. In this example, no physical boundary conditions are enforced and all the assumptions mentioned in the preceding sections apply.

Consider an aluminum honeycomb grid with a characteristic cell wall length of $l = 5$mm, a wall thickness of $t = 25$µm, and an initial honeycomb angle of $\theta_s = 75°$. Assume the engagement altitude needs to be $h = 3$km and that the honeycomb angle beneath this position needs to be $\theta_{ea} = 90°$. This way, a maximum strain of $\varepsilon_x = 33\%$ can be achieved in longitudinal direction when the CDP approaches infinity. The longitudinal stiffness, E_x^*, introduced by the material properties of the honeycomb structure can be calculated using Equation 4.6. When no CDP exists, an external stress in the longitudinal direction forces the honeycomb to assume a shape where $\theta_{ea} = 90°$. This stress can be calculated according to:

$$\sigma_x = -E_x^* \frac{\cos\theta_s - \cos\theta_{ea}}{1 + \cos\theta_s}$$

If the linearized stress-strain relations are used, the pressure-induced stiffness can be easily calculated over the entire range of ambient pressures by employing Equations 4.53 and 2.6. If this stiffness is denoted with E_x^m, and the reference honeycomb angle $\theta_i = 60°$, the honeycomb angle at which all stresses are balanced can now be calculated according to:

$$\theta = \cos^{-1}\left[\frac{(1 + \cos\theta_s)(1 + \cos\theta_i)}{E_x^*(1 + \cos\theta_i) + E_x^m(1 + \cos\theta_s)}\left(-\sigma_x + E_x^* \frac{\cos\theta_s}{1 + \cos\theta_s} + E_x^m \frac{\cos\theta_i}{1 + \cos\theta_i}\right)\right]$$

The strain with respect to the perfect hexagonal shape of the honeycomb can be found subsequently:

$$\varepsilon_x = \frac{\cos\theta - \cos\theta_i}{\cos\theta_i}$$

The result is a closed-form relationship between altitude, h, and longitudinal strain, ε_x. This relationship is shown in Figure 4.23.
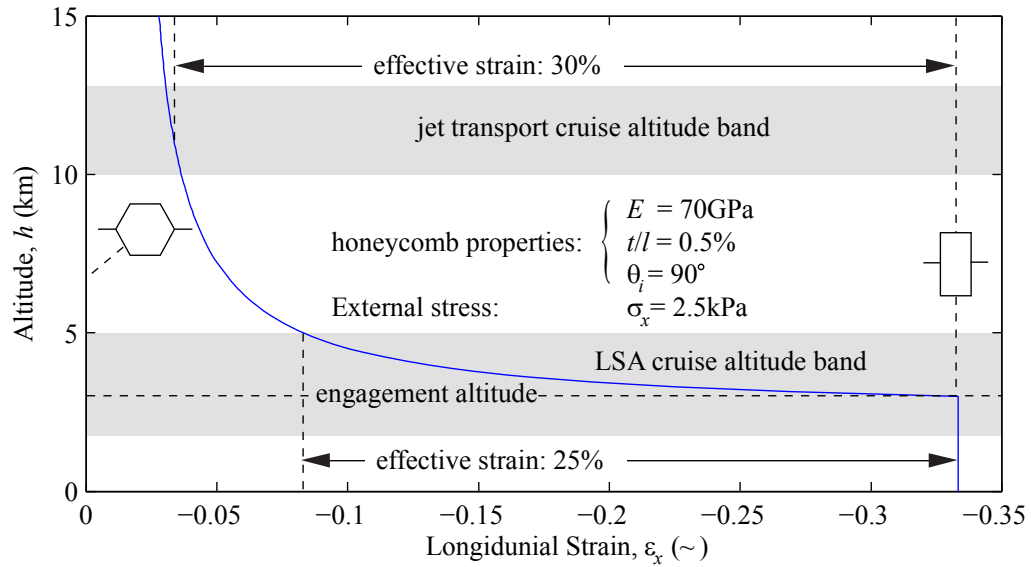
Figure 4.23 **Strain-Altitude Relation for Prescribed Engagement Altitude and Constant External Loading**

From Figure 4.23 it can be seen that a highly non-linear relationship exists between strain and altitude. As long as the aircraft stays beneath the 3km engagement altitude, the honeycomb stays in its deployed state with $\theta_{ea} = 90°$. Above this altitude the element starts to deform towards the perfect hexagon state. A 30% strain difference exists between the honeycomb at engagement altitude and the cruise altitude of jet transports. If measured in the frame of reference of the initial shape, the strain even amounts to 45%.

For light sport aircraft that cruise close to 5km, the ambient-induced strain amounts to 25%, which is less than for the transport aircraft but still significant. Given the fact that this example uses an engagement altitude of 3km, the cruise altitude and engagement altitude are quite close. However, it might be more convenient to lower the engagement altitude for LSA aircraft to for example 2km. This would imply that the aircraft would encounter a larger pressure gradient upon engagement which would induce a larger strain.

4.4.4 Comparison to Adaptive Materials

In Section 2.1.3 the state-of-the-art adaptive materials were compared based on their mechanical properties. In this section it is explored how pressure adaptive honeycomb compares to those materials in terms of energy density, specific energy density, and coupling efficiency.

The distinction is made between atmospherically-triggered pressure adaptive honeycomb and high-pressure adaptive honeycomb. For both cases a typical honeycomb structure is assumed that is detailed in the subsequent paragraphs. The mechanical properties of the honeycomb are based on the honeycomb model that was presented in Section 4.2. The dimensional and material characteristics are based on the envisioned feasible manufacturing procedures and the experience of the author in producing honeycomb test articles.

The exemplary honeycomb that is considered for this experiment has the following characteristics:

- Material: Aluminum, density: $\rho = 2700\text{kg/m}^3$

- Characteristic face length: $l = 10\text{mm}$

- Characteristic face thickness: $t = 75\mu\text{m}$

Using these characteristics, the density of the material is calculated according to Eq. 4.1, assuming a 20% addition of mass due to adhesives and pouches and a reference honeycomb angle of 60°. This results in a structural density of approximately 25kg/m^3.

The maximum strain that the honeycomb can utilize is another parameter that needs to be set before the specific work can be calculated. In this paragraph these maxima are derived. Cellular material theory holds for strains up to ±20% in any direction (see Section 4.1.1). Given a hexagonal honeycomb cell, 20% strain induces the largest change in average honeycomb angle when it is directed outwards (tension) in the x-direction. The resulting change in honeycomb angle amounts to 24°. This implies that a change in average honeycomb angle of 24° does not induce any plastic deformation in the faces of the honeycomb cells (given the assumptions of Section 4.1.1). This allows the designer to choose a minimum honeycomb angle that is two times 24° away from the default angle of 60°, with the unstrained geometry exactly in between those two angles. This yields two possibilities. The first possibility relies on a honeycomb that has a default honeycomb angle of $60 - 24 = 46°$ and an external load that induces elastic equilibrium at $60 - 2 \cdot 24 = 12°$. This results in a maximum horizontal strain of $\varepsilon_x = 32\%$ and $\varepsilon_y = -76\%$. The other option uses a honeycomb grid that exhibits a default honeycomb angle of $60 + 24 = 84°$ and an external load that induces elastic equilibrium at $60 + 2 \cdot 24 = 108°$. This option results in a maximum horizontal strain of $\varepsilon_x =$

-54% and maximum vertical strain of $\varepsilon_y = 15\%$. The extreme geometry changes are schematically shown in Figure 4.24.

pressure-induced geometry   manufactured geometry (default)   external-load-induced geometry   maximum strains:

$$60°\qquad 84°\qquad 108°\qquad \varepsilon_x = -54\%$$

$$60°\qquad 36°\qquad 12°\quad \varepsilon_y = -76\%$$

$$CDP \rightarrow \infty \qquad 0 < CDP < \infty \qquad CDP = 0$$
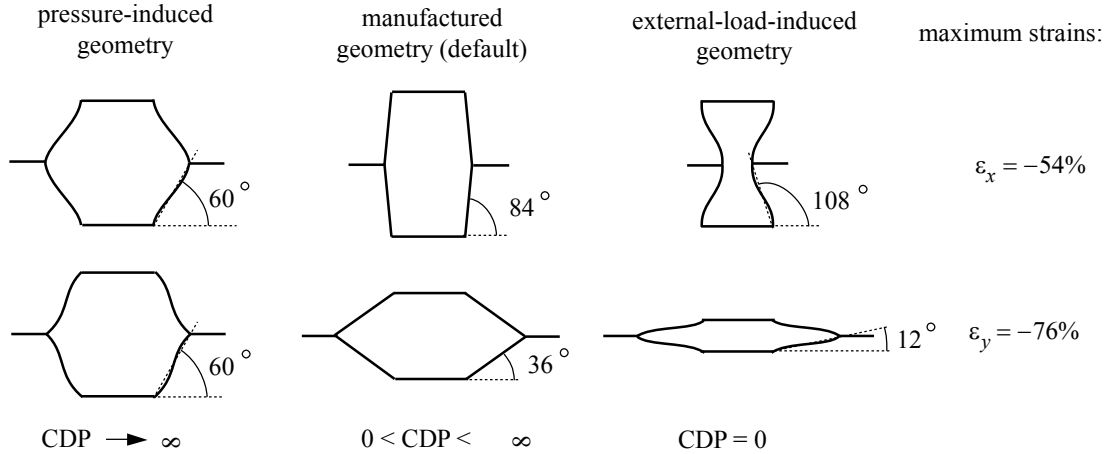
Figure 4.24   Maximum Deformations of Pressure adaptive Honeycomb

With these maximum values of strains it is possible to make an estimate of the amount of mechanical work that can be performed by each of them. To that extent, first the distinction is made between the atmospherically-triggered and the high-pressure adaptive honeycomb. For the first one an atmospheric induced pressure differential of 40KPa, is assumed to be a realistic upper bound. With the formulae of Section 4.2.3 and knowing that mechanical work per unit volume can be calculated according to $\int_0^{\varepsilon_{max}} \sigma\, d\varepsilon$, the maximum work density in x-direction amounts to $E_v = 16\text{mJ/cm}^3$, while the maximum work in y-direction totals $E_v = 27\text{mJ/cm}^3$. Dividing those numbers by the structural density of the pressure adaptive honeycomb results in a specific energy density of $E_m = 0.64\text{J/g}$ in x-direction and approximately $E_m = 1.1\text{J/g}$ in y-direction.

For the high-pressure adaptive honeycomb, an upper bound for the cell differential pressure is provided by the maximum pressure that can be generated on the aircraft. It was shown in Section 3.3.2 that turbomachinery on contemporary gas turbines can generate cell differential pressures on the order of 0.9MPa. Combining this with the previously quoted maximum strains in x- and y-direction, this results in a specific density (E_m) of 8.8J/g and 12J/g, in the respective directions.

Figure 4.25 demonstrates how the atmospherically-triggered and high-pressure adaptive honeycombs compare to other adaptive actuators in terms of maximum stress and strain. On the diagonals the energy density of each of the actuator is measured. In addition to the adaptive materials, a high-performance electromechanical servo is also charted based on data from Ref. 132. This servo is FAA-approved and designed for aerospace applications. It has a low bandwidth (0.04Hz) and could be used in similar applications as the pressure adaptive honeycomb (e.g. actuating high-lift devices). It can be seen that the high–pressure adaptive honeycomb has virtually the same energy density as the electromechanical servo. Furthermore, it can be seen that the pressure adaptive honeycomb exhibits a relatively large maximum strain being third behind the acrylic artificial muscle and the shape memory polymer.
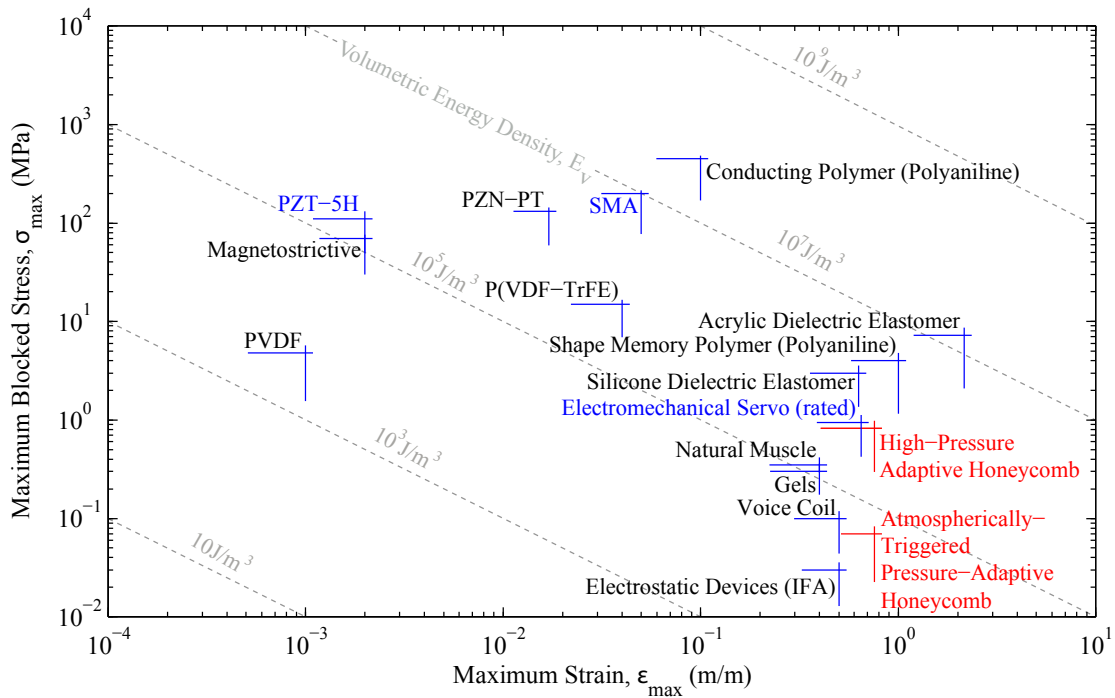
Figure 4.25   Maximum Stress-Strain for Various Adaptive Actuators (Data from Table 2.1)

The final characteristic of interest when comparing the present adaptive honeycomb to other aerospace structures is the coupling efficiency, κ^2, which relates the mechanical work output to the energy put into the actuator. For the atmospherically-triggered pressure adaptive honeycomb this parameter must equal 1 because there is no net energy extracted from the aircraft. For the high-pressure adaptive honeycomb the coupling efficiency can only be deter-

mined once the system is integrated into a deforming wing structure. However, it is expected that losses in energy are low. A possible cause for energy dissipation could lie in pressure losses in the tubing to the pouches. Because those losses are expected to be minor, the coupling efficiency is estimated to be larger than 95%. Figure 4.26 charts the coupling efficiency and the specific energy density of various adaptive actuators.
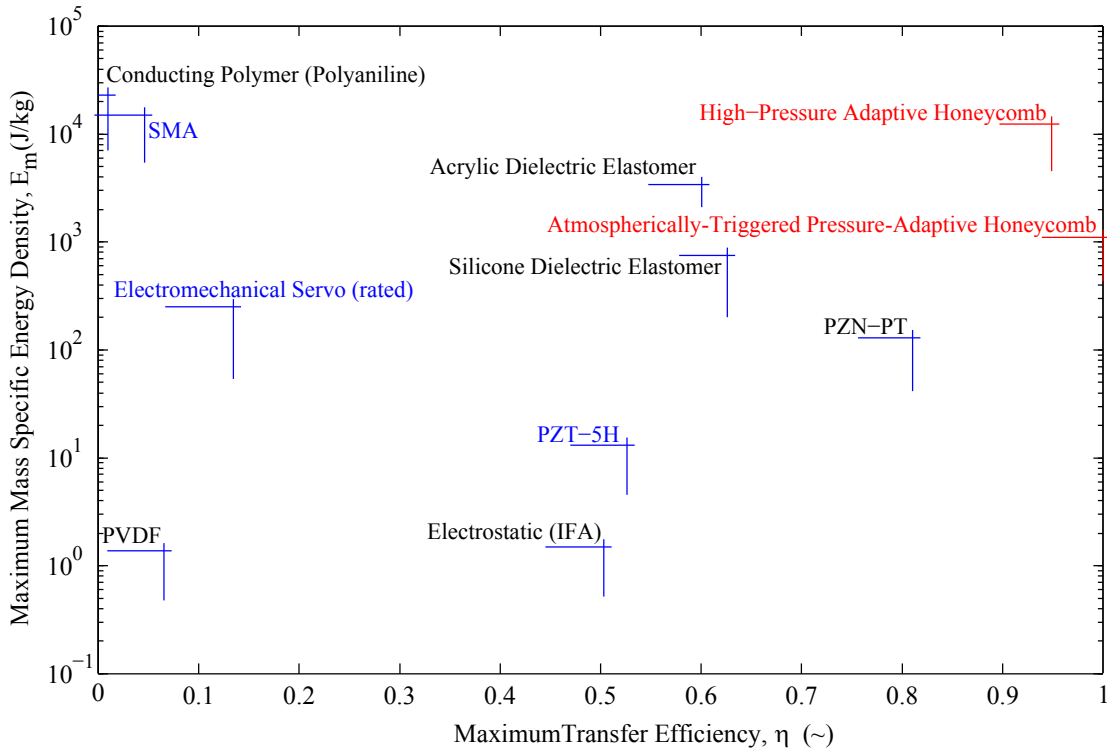
Figure 4.26   Transfer Efficiency versus Specific Energy Density for Various Adaptive Actuators (Data from Table 2.1)

From Figure 4.26 it can be seen that pressure adaptive honeycomb has quite good characteristics compared to the alternative adaptive materials. Its coupling efficiency is the highest of all actuators and the high-pressure adaptive honeycomb rivals SMA in specific energy density. Notice also, that both the atmospherically-triggered and the high-pressure adaptive honeycomb have a higher specific energy density than the electromechanical servo. The relatively low density of pressure adaptive honeycomb compared to the adaptive materials result in relatively high energy value per unit mass, while the energy value per unit volume (as shown in Figure 4.25) is comparatively low. For aircraft applications this translates to having a high volume requirement to store the actuator, but a very low weight penalty.

The present comparison between adaptive materials and the pressure adaptive honeycomb is purely based on exemplary values from the literature (Ref. 30) and the model presented in Section 4.2, resp. Even though it is limited, it gives a good indication of the abilities of pressure adaptive honeycomb. The present analysis has shown that this can be a viable alternative to other adaptive materials. In conclusion, Table 4.1 sums up the properties of pressure adaptive honeycomb, similar to how other adaptive materials were compared in Table 2.1.

Table 4.1   Intrinsic Properties of Pressure adaptive Honeycomb

Actuator Type (specific example)	Maximum Strain, ε (%)	Maximum Pressure, σ (MPa)	Specific Elastic Energy Density, E_m (J/g)	Elastic Energy Density, E_v (J/cm^3)	Transfer Efficiency, η (%)	Maximum Efficiency (%)	Specific Density, ρ (g/cm^3)	Relative Speed (full cycle)
Pressure Adaptive Honeycomb								
Atmospherically-Triggered	76	0.07	1.1	0.027	100	n/a	0.025	slow
High-Pressure (0.9MPa)	76	0.82	12.4	0.31	~ 95	n/a	0.025	slow

4.5   Finite Element Approximations

The following sections describe the two separate FE analyses of the pressurized honeycomb and explain the physics and mathematics behind them. The software that was used to carry out both of the FE tasks is called FINESSE. FINESSE has been developed by Dr. Karan Surana at the Mechanical Engineering Department of The University of Kansas. The proceeding sections present the solid mechanics theory utilized in FINESSE. An extensive description of the approximation can be found in Ref. 133.

4.5.1 Model Problem and Variational Statement

In the current problem it is assumed that the material is linearly elastic, isotropic and homogeneous. In this section the description of the model is introduced as described in Ref. 134.

Consider the domain Ω in Figure 4.27 which contains a linearly elastic solid material. It has boundary $\partial\Omega$ that contains the portions of the boundary, Γ_u and Γ_t, on which displacements

and tractions are specified, respectively. The body is subjected to a distributed body force, $\boldsymbol{f}$, and surface tractions, $\boldsymbol{t}$.
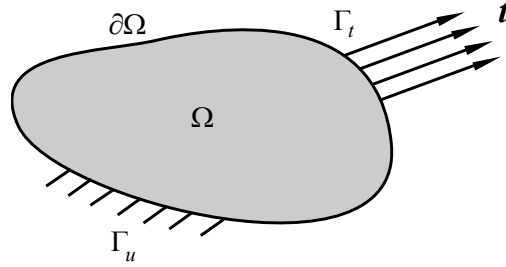
Figure 4.27 The Model Problem and Variational Formulation

The displacement vector field within this body are denoted $\boldsymbol{u}$ and its spatial gradient is denoted $\nabla\boldsymbol{u}$. The divergence of a vector or tensor, $\boldsymbol{x}$, is denoted $\nabla \cdot \boldsymbol{x}$. The Cauchy stress tensor, $\boldsymbol{\sigma}$, can then be written as a function of the fourth order elasticity tensor, $\boldsymbol{E} = \boldsymbol{E}(\boldsymbol{x})$, and the strain tensor, $\boldsymbol{\varepsilon}$:

$$\boldsymbol{\sigma} = \boldsymbol{E}\,\boldsymbol{\varepsilon} \tag{4.85}$$

The coefficients in the elasticity tensor satisfy the following symmetry conditions:

$$E_{ijkl}(\boldsymbol{x}) = E_{jikl}(\boldsymbol{x}) = E_{ijlk}(\boldsymbol{x}) = E_{klij}(\boldsymbol{x}) \tag{4.86}$$

It is assumed that the displacements are small and therefore the strain-displacement relationships are linear:

$$\boldsymbol{\varepsilon} = \frac{1}{2}(\nabla\boldsymbol{u} + (\nabla\boldsymbol{u})^T) \tag{4.87}$$

This results in the linear elastostatics problem that can be formulated as a boundary value problem as follows (see Ref. 134):

Find $\boldsymbol{u}$ such that

$$-\nabla \cdot (\boldsymbol{E}\nabla\boldsymbol{u}) = \boldsymbol{f}, \text{ in } \Omega$$

$$\boldsymbol{E}\nabla\boldsymbol{u} \cdot \boldsymbol{n} = \boldsymbol{t}, \text{ on } \Gamma_t \tag{4.88}$$

$$\boldsymbol{u} = 0, \text{ on } \Gamma_u$$

119

Equation 4.88 can generally not be solved analytically. Therefore, a finite element analysis (FEA) is used where Eq. 4.88 is solved numerically. Because the differential operator in Eq. 4.88, is self-adjoint and variationally consistent, formulation is possible using the Galerkin method with Weak Form. The space of test functions is defined as:

$$V = \left\{ v : \int_\Omega E \nabla u : \nabla v \, dx < \infty, \ v_{\Gamma_u} = 0 \right\} \tag{4.89}$$

Multiplying both sides of Eq. 4.88 with a test function v and integrating using Green's identity results in the variational form:

$$\text{Find } u \text{ such that}$$

$$B(u, v) = F(v), \quad \forall v \in V, \tag{4.90}$$

where,

$$B(u, v) = \int_\Omega E \nabla u : \nabla v \, dx, \tag{4.91}$$

$$F(v) = \int_\Omega f \cdot v \, dx + \int_{\Gamma_t} t \cdot v \, ds. \tag{4.92}$$

4.5.2 Finite Element Approximation

In the finite element representation an approximate solution u^h and an assumed test function v^h are considerd. This results in the following approximation:

$$B(u^h, v^h) = F(v^h) \quad \forall v^h \in V \tag{4.93}$$

The approximated solution and test function are expressed in a series as follows:

$$u^h(x) = \sum_{j=1}^N u_j^h \, \psi_j(x) \tag{4.94}$$

$$v^h(x) = \sum_{i=1}^N v_j^h \, \psi_i(x) \tag{4.95}$$

where ψ_i is a basis function. Substitution in Eq. 4.93 results in the following:

$$\bar{\bar{B}}\left(\sum_{j=1}^N u_j^h \, \psi_j, \sum_{i=1}^N v_i^h \, \psi_i \right) = F\left(\sum_{i=1}^N v_i^h \, \psi_i \right) \quad \forall v_i^h \in V \tag{4.96}$$

Rewriting this yields:

$$\sum_{j=1}^{N} \sum_{i=1}^{N} B\left(u_j^h \psi_j, v_i^h \psi_i\right) = \sum_{i=1}^{N} F\left(v_i^h \psi_i\right) \quad \forall\, v_i^h \in V \tag{4.97}$$

This can be rewritten as:

$$\sum_{i=1}^{N} v_i^h \left\{ \sum_{j=1}^{N} B(\psi_j, \psi_i) u_j^h - F(\psi_i) \right\} = 0 \quad \forall\, v_i^h \in V \tag{4.98}$$

If it is considered that $v_i^h \neq 0 \;\; \forall\, v_i^h \in V$ the following relation is obtained:

$$\sum_{j=1}^{N} B(\psi_j, \psi_i) u_j^h = F(\psi_i) \quad \text{for} \quad i = 1, \dots, N \tag{4.99}$$

In matrix form this results in the following matrix equation:

$$\bar{\bar{B}} \boldsymbol{u}^h = \bar{F} \tag{4.100}$$

This can be expanded according to:

$$\begin{bmatrix} B_{11} & \cdots & B_{1N} \\ \vdots & \ddots & \vdots \\ B_{N1} & \cdots & B_{NN} \end{bmatrix} \begin{Bmatrix} u_1^h \\ \vdots \\ u_N^h \end{Bmatrix} = \begin{Bmatrix} F_1 \\ \vdots \\ F_N \end{Bmatrix} \tag{4.101}$$

Accordingly, each element in matrix $\bar{\bar{B}}$ and vector $\boldsymbol{F}$ can be represented as follows:

$$B_{ij} = B(\psi_i, \psi_j) \tag{4.102}$$

$$F_i = F(\psi_i) \tag{4.103}$$

This system of linear equations is solved using FINESSE.

4.5.3 Meshing of Honeycomb Structure

The repeating element in the honeycomb was previously identified as a z-element (see Figure 4.7). This z-element forms the basis of the FE analysis discussed in this section. Previously the z-element was defined with sharp corners. In the finite-element model this would result in discontinuities in the stresses. In accordance with a realistic metal fold, the corners were therefore modeled as an arc section between the individual faces of the honeycomb. As is shown in Figure 4.28, the z-element could be divided in 5 individual element sets. To define a mesh over the z-element each element set had its own coordinate system as shown in Figure 4.28. The arc sections that connected the individual faces of the honeycomb were convenient-

ly defined in a circular coordinate system while the other elements were defined in Cartesian coordinates.
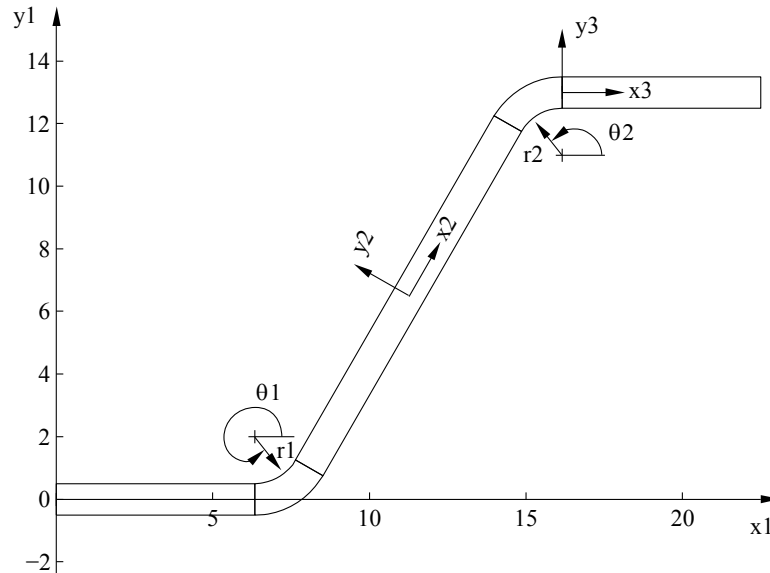
Figure 4.28   Definition of individual element sets and their local coordinate systems

A Matlab code was developed that could write an input file for Finesse with appropriate node distribution, boundary conditions and pressure loading. It used the following input parameters from the user:

- N_x, the number of z-sections in x-direction

- N_y, the number of z-sections in y-direction

- θ_i, the honeycomb angle

- N, half the number of elements in a ligament

- M, the number of through-the-thickness elements

- L, the number of elements in the corner

Based on these parameters the code generated the element numbering, node numbering and nodal coordinates. The elements that were used were quadrics and each element consisted of 9 nodes, 8 at the boundaries and one in the center. Furthermore, the polynomials that were used to describe the displacement within each element were of the sixth degree and a first

order continuity was prescribed between the polynomials at the interfaces of the elements, such that strains varied linearly over the element boundaries.
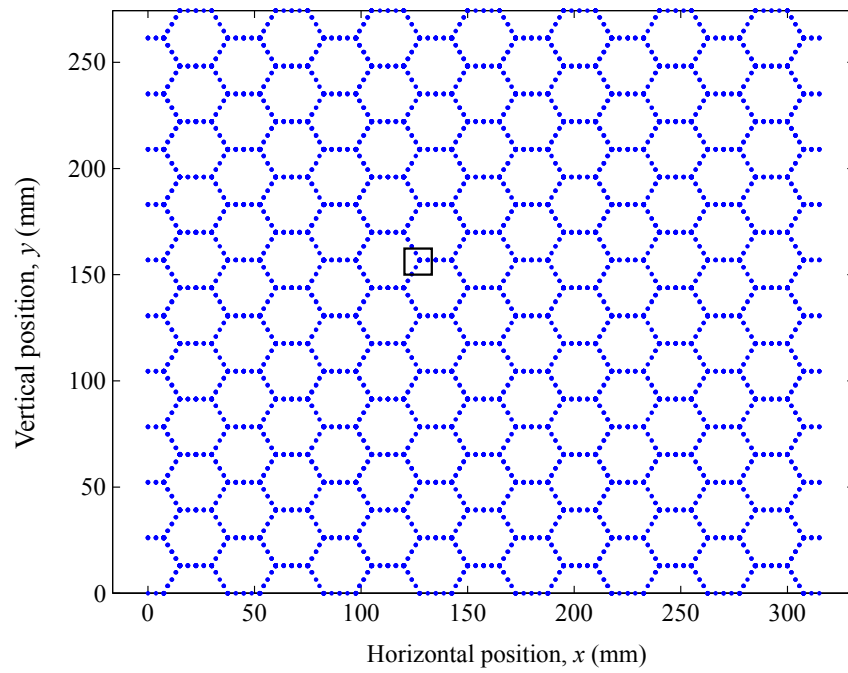
Figure 4.29   Birds-Eye View of Mesh for Rectangular honeycomb for N_x=14, N_y=21
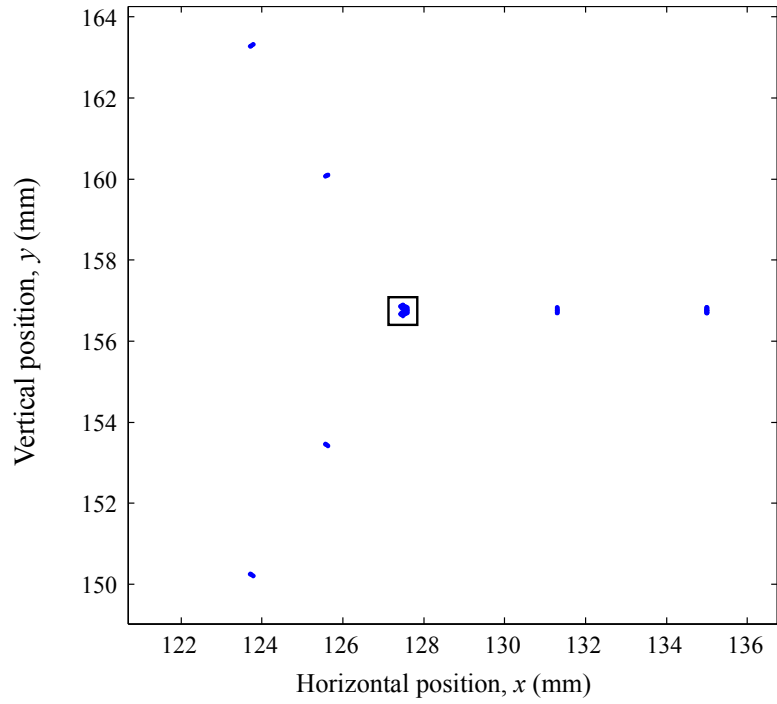
Figure 4.30   Closer View of Honeycomb Mesh for N=1, M=1, and L=2
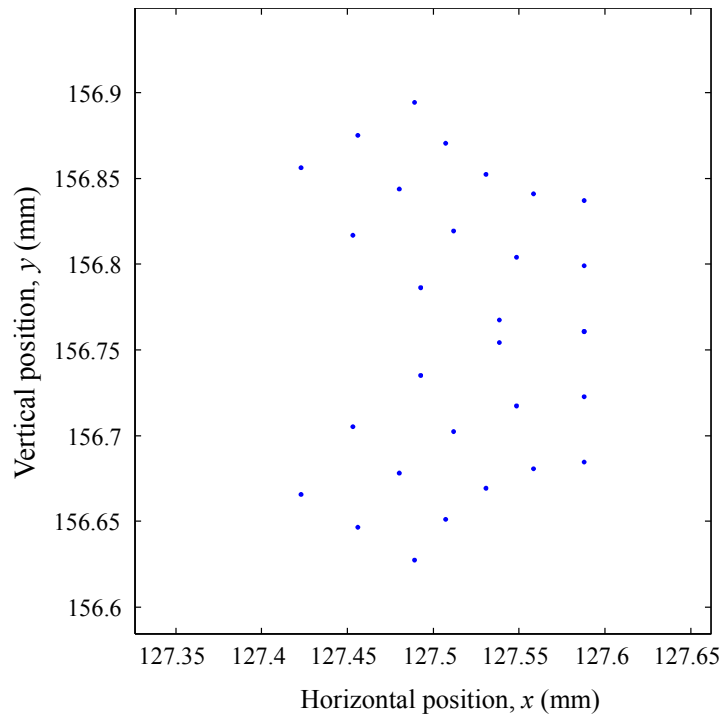
Figure 4.31   Detail of Meshed Corners for N=1, M=1, and L=2

4.5.4 Boundary Conditions and Applied Pressure Loading

In accordance with the experiments that were carried out (see Section 5.3.3), three sets of numerical simulations were conducted: lateral compression (up to 15% compressive strain in y-direction), longitudinal tension (up to 4% strain in x-direction), and longitudinal compression(up to 12% compressive strain in x-direction). In agreement with the test setup, the simulated test article was free to expand and contract in the direction perpendicular to the principal loading direction. This meant that two boundaries were prescribed (either top and bottom or left and right, depending on the test).

In Figure 4.32 the constraints for loading in the y-direction are schematically presented. The nodes that bordered the boundary were constrained in the y-direction: $v = 0$. To restrict rigid-body motion (and hence introduce a singularity) one single node was constrained in the both x and y-direction. In addition, the distributed loads on the top horizontal faces of the honeycomb are also shown in Figure 4.32. The value of the distributed load was calculated by dividing the load that was introduced during the experiment (see Section 5.4) by the total area of the top honeycomb faces.

■ constrained in y-direction
■ loaded in y-direction

■ constrained in x-direction
■ loaded in x-direction
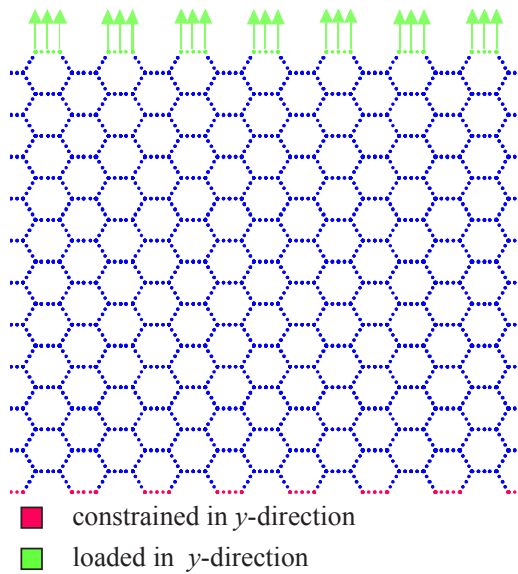
Figure 4.32   Constrains for Lateral Loading
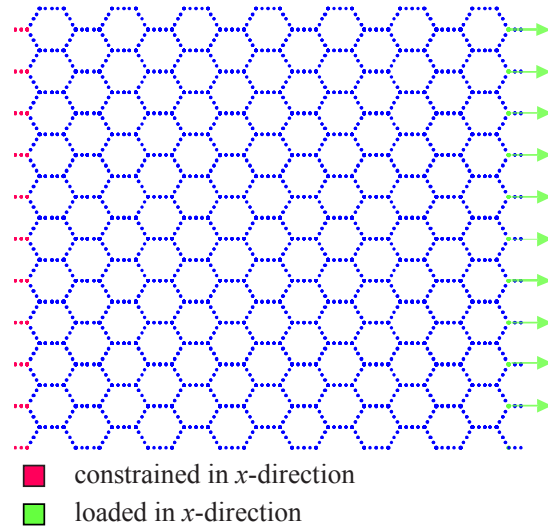
Figure 4.33   Constraints for Longitudinal Loading

Figure 4.33 schematically demonstrates the constrained nodes in the case of longitudinal loading (in the x-direction). In order to prevent buckling of the left extreme ligaments under

compressive loading, it is shown in Section 5.4.4 (p. 155) that the faces of the members were stiffened by using 3mm thick aluminum angle. It is assumed here that the compressive force on the aluminum angle was transferred to the honeycomb by means of pure shear loading. The nodes of the elements that bordered the angle on the left-hand side were therefore all constrained in the x-direction. This prevented buckling of these ligaments when compressive loading was applied. For the same reason, the external loading was applied at the intersection of diagonal ligaments at the right hand side. As can be seen from Figure 4.33, the force is not applied at the outer most element faces but rather at the left face of the last horizontal ligament.

During the experiments, pressure was applied to pouches that resided in each of the honeycomb cells. The pouches were not attached to the honeycomb in any way but stayed in place due to friction between the cell face and the pouch wall. However, a separate pouch in each of the cells was not included in the FE model due to the higher level of complexity this would imply. Instead, the pressure was applied directly to the cell walls, as if there were no pouches. Early FE runs demonstrated that applying pressure to the interior cell walls did not change the overall stiffness of the honeycomb structure as it had done during experiments. Therefore, the model was adjusted such that the material stiffness was artificially altered as a function of the pressure. The equivalent stiffness based on the analytic model (as derived in Section 4.3.3) could be used to specify the new material stiffness of the honeycomb. Alternatively, the equivalent stiffness could be determined from baseline experiments. Either method ultimately resulted in a homogenized model of pressure adaptive honeycomb.

4.5.5 Influence of Element Density on Deformation

A simple investigation was carried out to see the result of having more elements within the ligaments and in the corners on the deformation geometry of a simple z-section. The input parameters to create the mesh for a single z-element were:

- θ_i, the honeycomb angle

- N, half the number of elements in a ligament

- M, the number of through-the-thickness elements

- L, the number of elements in the corner

The thickness-to-length ratio of the honeycomb ligaments was assumed to be very small for the envisioned applications. For a minimum number of elements in a single z-section, this resulted in elements which had a large aspect ratio (close to $l/2t$).

The single z-element was subjected to a vertical displacement of the upper horizontal member. As a result of this displacement, the diagonal member deformed while the lower horizontal member was constrained from moving. This behavior was thought to be very close to what a typical z-section inside a honeycomb specimen would experience. Two sets of meshes were prescribed. The first one had the minimum number of elements (8), while the latter one had 184 elements. Both were subjected to the same displacement field and their deformed shape can be seen in Figure 4.34. The shapes here are plotted with intermediate points in between the nodes such that the reader could observe a more continuous shape deformation. The intermediate points were prescribed by the polynomial approximation of the displacement field within each element. As can be readily observed, the course mesh gives as good a prediction for deformation as the fine mesh. It was therefore decided to use the course mesh to discretize the honeycomb geometry.
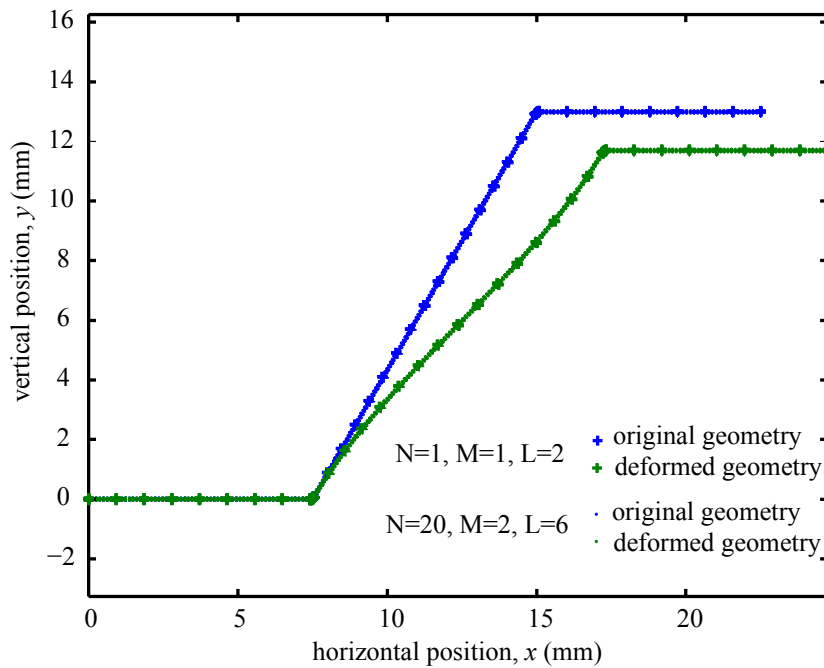
Figure 4.34   Comparison of Course and Fine Grid for a p-level of 4

4.6   Aerodynamic Model of Adaptive Flap

In close correspondence with wind tunnel experiments, a simple off-the-shelf numerical simulation model has been used to compare the experimental results to. The code is called Xfoil and was developed in the 1980s by Mark Drela and Michael Giles at the Massachusetts Institute of Technology. Xfoil is a program that is designed to predict pressure distributions and friction distributions about airfoils (two-dimensional). The origins of this code lie in solving the Euler equations in quasi one-dimensional streamtubes. Xfoil treats the flow as a set of stream tubes that are coupled through the position of the stream lines and the pressure at the streamline interfaces. If the viscous option in Xfoil is selected, the code relies on an interacted viscous-inviscid zonal approach. This means that the Euler equations are used everywhere in the flow where viscosity can be neglected and that boundary-layer equations are employed close to the airfoil boundary and in the wake. This code only employs boundary layer equations and can therefore only capture mildly separated flow. No appropriate wake equations have been implemented. The following sections give a description of the aerodynamic model, the approximation that is used and how the resulting set of equations is solved.

4.6.1 Inviscid Euler Formulation and Boundary Conditions

The inviscid zone of the flow is governed by the two-dimensional steady Euler equations. To allow for proper discretization, these equations are presented here in conservation form [135]:

$$\oint_{\partial V} \rho(\boldsymbol{V} \cdot \boldsymbol{n})\, \mathrm{d}l = 0 \tag{4.104}$$

$$\oint_{\partial V} [\rho(\boldsymbol{V} \cdot \boldsymbol{n})\,\boldsymbol{V} + p\boldsymbol{n}]\mathrm{d}l = 0 \tag{4.105}$$

$$\oint_{\partial V} \rho(\boldsymbol{V} \cdot \boldsymbol{n})\, h_0 \mathrm{d}l = 0 \tag{4.106}$$

These are the continuity equation, momentum equations (2), and energy equation, respectively. This total of four equations has five unknowns: pressure (p), the velocity components (u, v), density (ρ), and internal energy, e (remember that total enthalpy is defined as: $h_0 = e + p/\rho + V^2/2$). These equations are closed by the equation of state and the expression the relation between internal energy and temperature via the specific heat constant at constant volume (c_v):

$$p = \rho R T \qquad (4.107)$$

$$e = c_v T \qquad (4.108)$$

This yields a total of six equations with six unknowns. At this point it is important to list the assumptions that were made such that the original Navier-Stokes equations were reduced to the present set of equations:

1. The fluid is a continuum

2. The flow is steady

3. Viscous forces are neglected (inviscid)

4. The flow is non-conducting

5. There is no heat transfer (adiabatic)

6. Body forces are neglected

The last assumption is strictly speaking not applicable to the Euler equations, but is often added because it simplifies the set of equations even further. The most important body force that acts on a fluid particle is gravity. Its effect can generally be neglected for a low-density fluid like air.

The boundary conditions for the Euler flow are schematically displayed in Figure 4.35. The flow domain in which the Euler equations are solved is divided into two regions. Streamlines 1 through j_∞ make out the top region, while streamlines $j_\infty + 1$ through J form the bottom region. Upstream of the body, the stagnation streamlines 1 and J coincide. At the solid boundary the position of the adjacent streamline needs to be specified. Because of the viscous boundary layer, this streamline is displaced normal to the wall by a distance equal to the local displacement thickness, δ^*. The body that is drawn in Figure 4.35 should therefore be interpreted as the physical body plus the displacement thickness. It is shown that the streamline lies on this body ($\Delta n = 0$) and that there is no pressure jump ($\Delta \Pi = 0$) across the trailing edge between the two stream lines (Kutta condition). Upstream of the body, the two dividing streamlines lie on top of each other with no pressure discontinuity across them ($\Delta n = 0$ and $\Delta \Pi = 0$, resp.). At this boundary, the pressure is a result of the calculation. At the outer most streamlines, the pressure is specified corresponding to a uniform free stream plus a compress-

ible vortex, source and doublet (see Section 3.3 in Ref 136 for detailed far-field boundary conditions). In addition, at the inlet and outlet faces the local angle of the streamline is specified. At the inlet the stagnation density also needs to be specified. The compressible vortex strength is derived from the Kutta condition. The strength of the source component is derived from the far-field viscous wake. The two doublet components are determined by minimizing the deviation of the discrete streamlines from the direction of $\nabla\Phi$, with Φ denoting the analytic velocity potential of the freestream, vortex, source, and doublet combination [137].
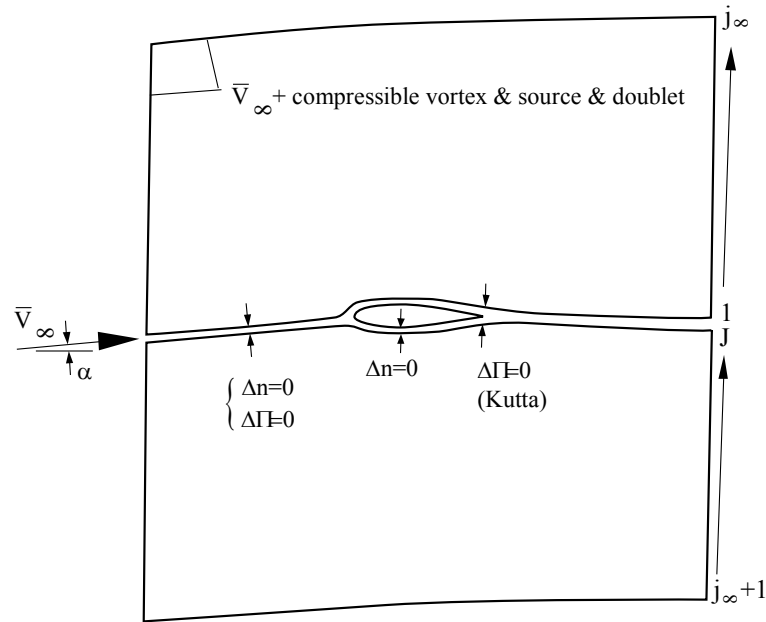
Figure 4.35   Isolated Airfoil Boundary Conditions (Modified From Ref. 137)

The steady Euler equations are solved over a finite volume. The total two-dimensional volume is subdivided into an intrinsic grid where one family of gridlines corresponds to streamlines. A typical conservation cell is depicted in Figure 4.36. In this figure, the nodes are denoted with x_i, y_i, the nodal pressure is denoted with Π, while the streamtube velocity vectors are denoted with s_i. The streamtube contour lengths are represented with the area vectors B^-, B^+ (bottom and top lengths), and A_1, A_2 (inlet and outlet faces). The density, pressure and speed are defined at the inlet and outlet of the conservation cell.

130
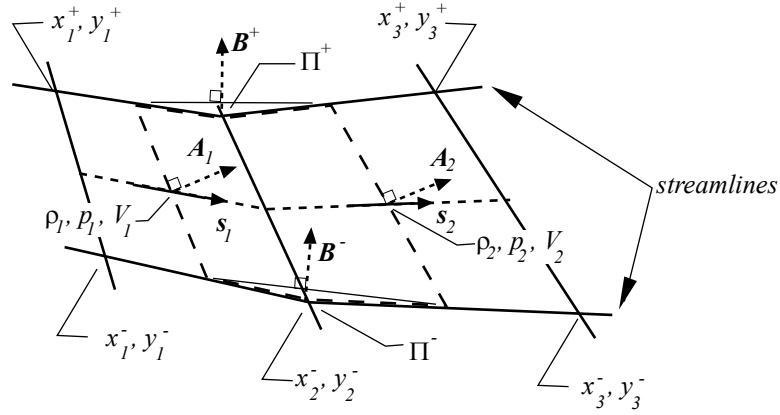
Figure 4.36   State Variables, Grid Coordinates, and Unit Velocity ($\hat{s}$) Vectors (modified from Figure 2.4 in Ref. 136)

Based on this finite volume element, the mass equation reduces to a statement that the flux along a streamtube is constant:

$$m = \rho_1 \mathbf{V}_1 \cdot \mathbf{A}_1 = \rho_2 \mathbf{V}_2 \cdot \mathbf{A}_2 \tag{4.109}$$

Similarly, the energy equation can be reduced to the statement that total enthalpy is constant along a streamtube:

$$h_0 = \frac{\gamma}{\gamma-1}\frac{p_1}{\rho_1} + 1/2\, V_1^2 = \frac{\gamma}{\gamma-1}\frac{p_2}{\rho_2} + 1/2\, V_2^2 \tag{4.110}$$

Because the streamlines do not allow any mass flow across their faces, the momentum equation is reduced to:

$$p_1 \mathbf{A}_1 + m\mathbf{V}_1 + \Pi^- \mathbf{B}^- = p_2 \mathbf{A}_2 + m\mathbf{V}_2 + \Pi^+ \mathbf{B}^+ \tag{4.111}$$

To close this set of equation the following additional equation is required:

$$p_1 + p_2 = \Pi^- + \Pi^+ \tag{4.112}$$

At this point two new vectors, $\mathbf{S}$ and $\mathbf{N}$, are defined that are the averages of the $\mathbf{A}$ and $\mathbf{B}$ vectors, respectively. The momentum equation can consequently be decomposed in the directions $\mathbf{S}$ and $\mathbf{N}$, resulting an S- and N-momentum equation. Since Xfoil is designed to be used in transonic conditions, artificial viscosity is added analogous to bulk viscosity to stabilize the solutions and ensure a well-posed problem in the supersonic realm. The explicit formulations of the resulting momentum equations can be found in Chapter 2 of Ref. 136. In the present

131

dissertation, Eq. 4.111 is deemed sufficient to describe to the reader how the momentum equation is discretized on the streamline grid.

4.6.2 Boundary Layer Coupling

An accurate description of the boundary formulation can be found in Ref 137. In this section a more qualitative description is presented. Xfoil employs a two-equation integral formulation in both the laminar and turbulent part of the boundary layer. Before going into the details of the description a few parameters need to be defined:

$$\text{Dissipation coefficient:} \quad C_D = 1/\rho_e u_e^3 \int \tau(\partial u/\partial \eta)\, d\eta \tag{4.113}$$

$$\text{Skin friction coefficient:} \quad C_f = 2\tau_{wall}/\rho_e u_e^2 \tag{4.114}$$

$$\text{Displacement thickness:} \quad \delta^* = \int[1 - \rho u/\rho_e u_e]\, d\eta \tag{4.115}$$

$$\text{Density thickness:} \quad \delta^{**} = \int(u/u_e)[1 - \rho/\rho_e]\, d\eta \tag{4.116}$$

$$\text{Momentum thickness:} \quad \theta = \int(\rho u/\rho_e u_e)[1 - u/u_e]\, d\eta \tag{4.117}$$

$$\text{Kinetic energy thickness:} \quad \theta^* = \int(\rho u/\rho_e u_e)[1 - (u/u_e)^2]\, d\eta \tag{4.118}$$

where u is the velocity in the ξ-direction, ρ is the density and superscript e denotes "edge." Notice that a $\xi\eta$-coordinate system is used, where the ξ direction is parallel to the flow, while the η direction is perpendicular to the flow direction. The implicit assumption is made that that the velocity-component in the η direction is zero. Based on the definitions of Eqs. 4.113 through 4.118, the following shape parameters are defined:

$$\text{Shape parameter:} \quad H = \delta^*/\theta \tag{4.119}$$

$$\text{Kinetic energy shape parameter:} \quad H^* = \theta^*/\theta \tag{4.120}$$

$$\text{Density shape parameter:} \quad H^{**} = \delta^*/\theta \tag{4.121}$$

$$\text{Kinematic shape parameter:} \quad H_k = \frac{\int[1-u/u_e]d\eta}{\int(u/u_e)[1-u/u_e]d\eta} \tag{4.122}$$

The derivation of the boundary layer equations used in this code starts with Prandtl's equations (see for example Ref. 138):

$$\text{Continuity: } \frac{\partial \rho u}{\partial \xi} + \frac{\partial \rho v}{\partial \eta} = 0 \tag{4.123}$$

$$\text{Momentum: } \rho u \frac{\partial u}{\partial \xi} + \rho v \frac{\partial v}{\partial \eta} = \rho_e u_e \frac{d u_e}{d \xi} + \frac{\partial}{\partial \eta}\left(\mu \frac{\partial u}{\partial \eta} - \rho \overline{u'v'}\right) \tag{4.124}$$

$$\text{Energy: } \rho u \frac{\partial h_t}{\partial \xi} + \rho v \frac{\partial h_t}{\partial \eta} = \frac{\partial}{\partial \eta}\left[\frac{\mu}{Pr} \frac{\partial h_t}{\partial \eta} + \mu\left(1 - \frac{1}{Pr}\right) u \frac{\partial u}{\partial \eta} - \rho \overline{h'v'}\right] \tag{4.125}$$

Here $-\rho\overline{u'v'}$ is the turbulent Reynolds stress and $-\rho\overline{h'v'}$ is the turbulent Reynolds heat flux, Pr the Prandtl number, and μ the viscosity of the fluid. It is assumed that the flow is adabatic and that the Prantdtl number is close to unity. This permits the enthalpy profile to be directly related to the velocity profile and the temperature recovery factor, reducing the energy equation to an analytic expression.

Integrating Eq. 4.123 over the thickness of the boundary layer, combining the result with Eq. 4.124 and integrating this over the thickness of the boundary layer results in the Von Karman integral formulation of the momentum equation:

$$\frac{d\theta}{d\xi} = \frac{C_f}{2} - \left(\frac{\delta^*}{\theta} + 2 - M_e^2\right) \frac{\theta}{u_e} \frac{d u_e}{d\xi} \tag{4.126}$$

Multiplying Eq. 4.124 by u and repeating the process results in:

$$\frac{d\theta^*}{d\xi} + \left[\frac{\delta^{**}}{\theta^*} + 3 - M_e^2\right] \frac{\theta^*}{u_e} \frac{d u_e}{d\xi} = 2C_D \tag{4.127}$$

Now, by substituting for the shape parameters, the following momentum and kinetic energy equations can be formulated, respectively:

$$\frac{d\theta}{d\xi} + (2 + H - M_e^2) \frac{\theta}{u_e} \frac{d u_e}{d\xi} = \frac{C_f}{2} \tag{4.128}$$

$$\theta \frac{dH^*}{d\xi} + [H^*(H-1) + H^{**}] \frac{\theta}{u_e} \frac{d u_e}{d\xi} = 2C_D - \frac{C_f}{2} H^* \tag{4.129}$$

This last equation is referred to as the kinetic energy thickness equation. Notice that both equations are solely differentiated with respect to ξ, which reduces the original PDEs to just ODEs, which are much easier to solve numerically. The flow in the boundary layer is thus

assumed to be steady and one-dimensional. If the expressions of Eq. 4.113 through 4.122 are substituted in the momentum and kinetic energy shape parameter equations (Eqs. 4.128 and 4.129) the reader can observe that there are three independent variables: u, ρ, and τ. To be able to solve for each of these variables an additional equation is required to close the current system of equations. In the laminar and turbulent parts of the boundary layer different equations are used for closure, both based on empirical data.

The closure equations in the laminar part of the boundary layer relate the momentum-thickness Reynolds number, Re_θ, to the kinematic shape parameter H_k, as well as the kinematic shape parameter, H_k to the shape parameter, H, and the edge Mach number, M_e. The turbulent closure is much more elaborate and is based on the velocity profiles of Swafford [139]. An extensive description of the closure formulas for the laminar and turbulent boundary layer equations can be found in Ref. 137.

Transition from a laminar to a turbulent boundary layer is based on the growth of the Tollmien-Schlichting waves in the laminar part of the boundary layer. It is assumed that the most unstable Tollmien-Schlichting wave has grown with some amplification factor, $\tilde{n}$, until it causes separation. This amplification factor is calculated by relating the disturbance growth in the boundary to the local boundary layer parameters. This is done by solving the Orr-Sommerfield equation. The Orr-Sommerfield equation is a linearized form of the Navier-Stokes equation and is essentially an eigenvalue problem. For a given shape factor, H, the resulting eigenvalue can be related to the amplification factor that causes the transition from laminar to turbulent flow. In Xfoil the Falkner-Skan family of velocity profiles (see for example Ref. 140) in the boundary layer is assumed and is used to substitute in the Orr-Sommerfield equation. The resulting amplification factor is related to a user-specified value. When the amplification factor equals this user-specified value, transition from laminar to turbulent closure is initiated. In the default configuration transition occurs when $\tilde{n} = 9$. This value can be increased or decreased by the user. The Xfoil manual [141] lists critical amplification factors for various environmental situations. These are reproduced in Table 4.2.

Table 4.2   Critical Amplification Factors for Various situations [141]

Situation	$\tilde{n}_{crit}$
sailplane	12-14

Motor glider	11-13
Clean wind tunnel	10-12
Average wind tunnel	9
Dirty wind tunnel	4-8

The boundary layer equations can be rewritten in terms of three independent variables, namely θ, δ^*, and C_τ, where C_τ is the shear stress coefficient defined as:

$$C_\tau = \tau_{max}\, \rho_e / u_e^2 \tag{4.130}$$

In the laminar portion of the boundary layer, the flow is described by two ODEs (Eqs. 4.128 and 4.129) with a set of analytic closure equations. In addition, the amplification factor is determined from a separate ODE (not listed in the present dissertation). Therefore, there is a total of three ODEs that needs to be discretized. In the turbulent portion of the flow, the original two boundary layer ODEs (Eqs. 4.128 and 4.129) are closed by means of an additional ODE, such that there are also three ODEs to be discretized. These are discretized on a structured grid which is shown in Figure 4.37. Here, '1' denotes the stream wise location $i-1$ and '2' denotes the location 'i.' To solve these ODEs on the present grid, a central difference scheme (trapezoidal scheme) is employed where the solution at i depends on the solution at $i-1$ and $i+1$.
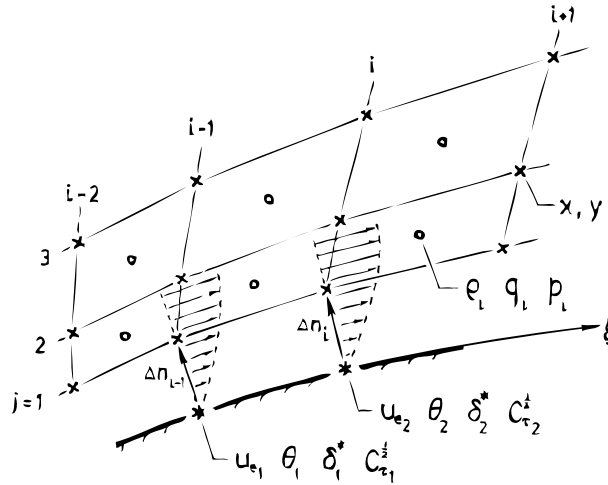
Figure 4.37   Boundary-Layer Variable Locations (Reproduced from Ref. 137)

4.6.3 Solution Procedure

The system of discretized Euler equations, boundary layer equations, and boundary conditions is solved by using the Newton method. The vector form of the Newton method is not much different from the scalar representation. For a problem of the form:

$$F(U) = 0 \tag{4.131}$$

the Newton solution procedure at some iteration level ν is:

$$F(U^{\nu+1}) \equiv F(U^\nu + \delta U^\nu) \cong F(U^\nu) + \left[\frac{\partial F}{\partial U}\right]^\nu \delta U^\nu = 0 \tag{4.132}$$

$$\left[\frac{\partial F}{\partial U}\right]^\nu \delta U^\nu = -F(U^\nu) \tag{4.133}$$

$$U^{\nu+1} = U^\nu + \delta U^\nu \tag{4.134}$$

Here U represents the vector with state variables and F is the vector with governing equations, boundary conditions, global constraints and boundary layer equations. The $[\partial F/\partial U]$ represents the Jacobian matrix which' (i, j) entry corresponds to the partial derivative of the i'th equation in F with respect to the j'th variable in U. At each iteration of the Newton procedure a linear system of equations (4.133) needs to be solved. With respect to the state variables S, N, s, V, and p the governing equations are linearized according to:

$$\delta F \cong \frac{\partial F}{\partial S} \delta S + \frac{\partial F}{\partial N} \delta N + \frac{\partial F}{\partial s} \delta s + \frac{\partial F}{\partial q} \delta V + \frac{\partial F}{\partial} \delta p \tag{4.135}$$

To minimize the number of unknowns in δU the momentum equations are rewritten such that two state variables remain: δn and $\delta \rho$. The first represents the nodal spacing perpendicular to the local streamline, while the latter is the change in density. To that extent the sensitivities are further elaborated using the chain rule such that the following symbolized expression results (Eq. 4.15 in Ref. 136):

$$\delta F \cong \left(\frac{\partial F}{\partial} \frac{\partial}{\partial \rho} + \ldots\right) \delta \rho + \left(\frac{\partial F}{\partial} \frac{\partial}{\partial n} + \ldots\right) \delta n \tag{4.136}$$

where the bracketed expressions represent a chain of partial differentials with respect to the individual state variables: S, N, A, s, V, x, y. These sensitivities are all grouped in the Jacobian matrix $[\partial F/\partial U]$ in Eq. 4.133.

The details of the linearization process of the Euler equations as well as the boundary condi-tions can be found in Ref. 136. In this dissertation it is deemed sufficient to mention that the resulting system of equations forms a block tri-diagonal coefficient matrix of bandwidth 69. This block tri-diagonal system is solved using a blockwise Gaussian elimination algorithm. This results in the values for δn and $\delta \rho$, which can be used to update the solution:

$$\rho_{i,j}^{v+1} = \rho_{i,j}^v + \delta \rho_{i,j}^v \tag{4.137}$$

$$n_{i,j}^{v+1} = n_{i,j}^v + \delta n_{i,j}^v \tag{4.138}$$

With these results and the sensitivities that were calculated and grouped in the Jacobian ma-trix, the state variables at each cell can be updated. This procedure is repeated until the up-dated solution shows little difference with respect to the previous solution (convergence) or until the maximum number of iterations is reached. In the latter case, Xfoil returns the mes-sage: 'not converged' to the user.

4.6.4 Description of Generating Results from Wind Tunnel Input

Xfoil is used to compare the experimental results to a theoretical approximation. In this sec-tion it is described how the airfoil geometry is generated from the wind tunnel experiments and how this is used in Xfoil. In the present analysis MATLAB 7 has been used to automatical-ly read experimental data, create input files for Xfoil, run Xfoil, and extract calculated pres-sure distributions and aerodynamic coefficients.

As can be read in Section 5.5, during the wind tunnel tests the flap geometry was recorded by taking a picture of the right-hand side. From this picture, five coordinate sets (x, y) were de-rived. One of these sets was the trailing edge position. The other four sets were two pairs of chordwise positions of the top and bottom skin. Through these coordinate sets a line was splined (using a cubic spline). The coordinate sets were chosen such that the splined lines accurately resembled the top and bottom skin positions during the wind tunnel experiments. Thus, from the wind tunnel experiment the flap geometry was obtained. Before inserting the coordinates into Xfoil, a coordinate re-distribution was applied using a cosine distribution. This allowed close coordinate spacing near the leading edge. Xfoil used these coordinates to generate the nodal distribution on the body according to a number of panels specified by the

user. Nodal spacing on the body was done according to a constant arc length between the individual nodes [136].

In addition to the geometry, other experimental parameters were necessary as input parameters for Xfoil. These included the free-stream velocity, angle of attack, and density. Instead of using those values directly, they were first corrected for wind tunnel wall effects as described in Section 6.6.1. After correction, these parameters were used in the input file along with the geometry of the airfoil. The angle of attack was measured with respect to the x-axis of the coordinate system [141]. This was important because with a deflected flap, the resulting chordline (the longest distance between two coordinates on the airfoil) was significantly tilted with respect to the x-axis.

Xfoil calculated the pressure distribution, momentum thickness, displacement thickness, along with the gross aerodynamic coefficients such as c_l, c_d, and c_m. All these results were stored in output files which are subsequently read by MATLAB. At each angle of attack, free-stream velocity, and cell differential pressure, this resulted in a plot that displayed the airfoil geometry (including the flap), the pressure distribution, and the gross aerodynamic coefficients (both for the experiment and for the numerical approximation). In addition, a table was created that compares the aerodynamic coefficients that were obtained experimentally and numerically.

CHAPTER 5   EXPERIMENTAL SETUP AND PROCEDURES

This chapter describes all the experiments that were carried out to learn about the mechanical properties of pressure adaptive honeycomb. Section 5.1 starts off with a simple experiment to determine the mechanical properties of a metallic honeycomb structure. Then, in the subsequent sections the mechanics of pressurized honeycomb are investigated. Section 5.2 starts off with experiments on a single-cell rigid-wall honeycomb specimen. In Section 5.3 this is expanded to a 23-cell rigid-wall test article. Section 5.4 culminates the structural experiments with a 130-cell and a 145-cell metallic pressurized honeycomb specimen. The experimental setup of a pressure adaptive flap is laid out in Section 5.5.

5.1   Metalic Honeycomb

A simple test was designed to validate the elasticity of a honeycomb structure and compare it to the linear-elastic theory of Chapter 4. Eight honeycomb specimen were constructed each comprising of 4 honeycomb cells. Variation in material stiffness, honeycomb angle (θ_i), and sheet thickness were made (see Table 5.1). From the manufacturer's data sheets it was found that the thickness of the sheet could vary up to 10% of the intended thickness [142, 143]. Two types of steel shim stock were used in this experiment: carbon steel (SAE 1010) and stainless steel (AISI 301). Each of the specimens was clamped in an Instron tension machine that could measure forces up to ±0.1N and displacements up to 1μm. An extension test was carried out to find the stress strain relation of each of the specimens (schematically shown in Figure 5.1).

Table 5.1   Properties of Tested Honeycomb Specimen [142, 143]

Specimen #	Thickness, t (μm)	Honeycomb angle, θ_i (deg)	Material	Stiffness, E (GPa)
1	12.7	74	AISI-301	190
2	25.4	74	AISI-301	190
3	25.4	96	AISI-301	190
4	25.4	78	SAE 1010	200
5	25.4	59	SAE 1010	200
6	38.1	85	AISI-301	190
7	50.8	83	AISI-301	190
8	50.8	85	AISI-301	190
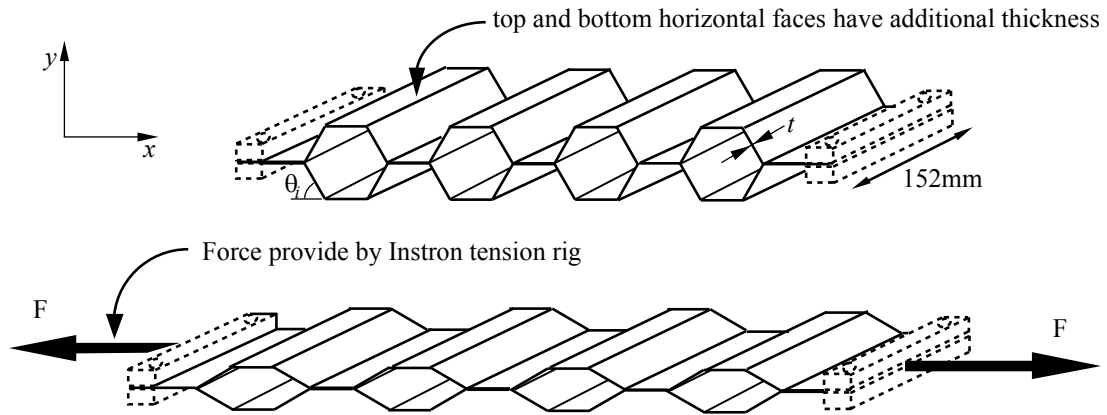
Figure 5.1   Schematic Representation of Straining of Four-Cell Honeycomb

5.2   Single-Cell Rigid-Member Pressurized Honeycomb

To verify the model presented in Section 4.2 a simple tension-compression test was constructed using an electromechanical tension/compression machine (Instron model nr. 3345). This section describes the experimental hardware and test procedures that were used.

5.2.1 Test Article and Experimental Hardware

A single honeycomb cell was constructed out of a 2-ply Kevlar pre-impregnated laminate. The hinges were introduced by local carbonization of the matrix structure which degraded the bending stiffness dramatically. The length of each hexagon face amounted to $l = 20$mm. Eight pouches were made with a diameter of approximately 34.5mm (perfect circle inside the hexagonal cell). Because of manufacturing inaccuracies it was decided to repeat the test with each of the pouches to get a spread of force readings at each cell differential pressure (CDP) and strain value. Two sets of tests were carried out. In the first test the force was aligned with the specimen's x-axis (longitudinal), while in the second test the force lined up with y-axis (lateral). In both tests the specimen was loaded through its center axis such that no shear loads were introduced.

The pressure in the pouch was kept constant during the experiment by using a variable pressure unit. The experiment was carried out in a quasi static way, meaning the top chuck displaced at a rate of 5mm/minute. Pressure, tensile force, and displacement were all sampled at

140

1Hz. A 5000N pressure transducer was used that could measure forces as small as 1mN. Displacements were recorded with an accuracy of 1μm. A strain-based pressure transducer was employed in combination with LabVIEW 8.5 to record the CDP. The pressure transducer was calibrated using a digital manometer that was accurate up to 0.1kPa. The single cell honeycomb element measured 29cm in depth. During the test, the displacement was controlled according to a triangular wave with time.

5.2.2 Longitudinal Compression-Tension Test

In the first test, the specimen was loaded along its longitudinal principal axis. A sketch of the experiment is shown in Figure 5.2 and a picture of the setup is found in Figure 5.4. From its original position, the specimen was put into a one-and-a-half loop such that any hysteresis in the process could be captured. In Figure 5.3 the input signal for the test is schematically shown. The realm of interest is displayed to show the reader in what realm the data was taken. Notice that this forms exactly one full hysteresis loop.
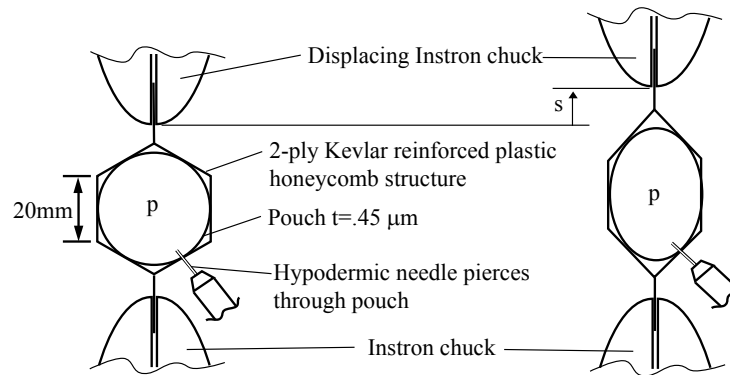
Figure 5.2   Sketch of Single Cell Longitudinal Compression/Tension Experiment
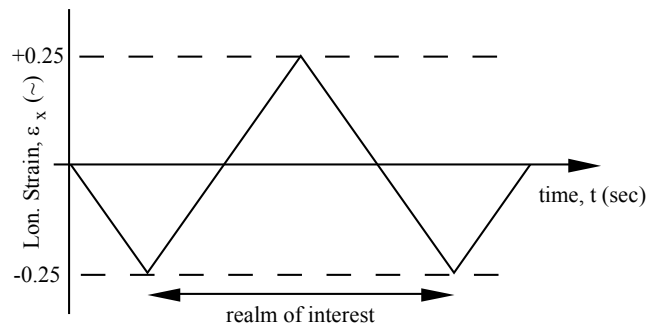
Figure 5.3   Input Wave Form for Longitudinal Compression-Tension Test
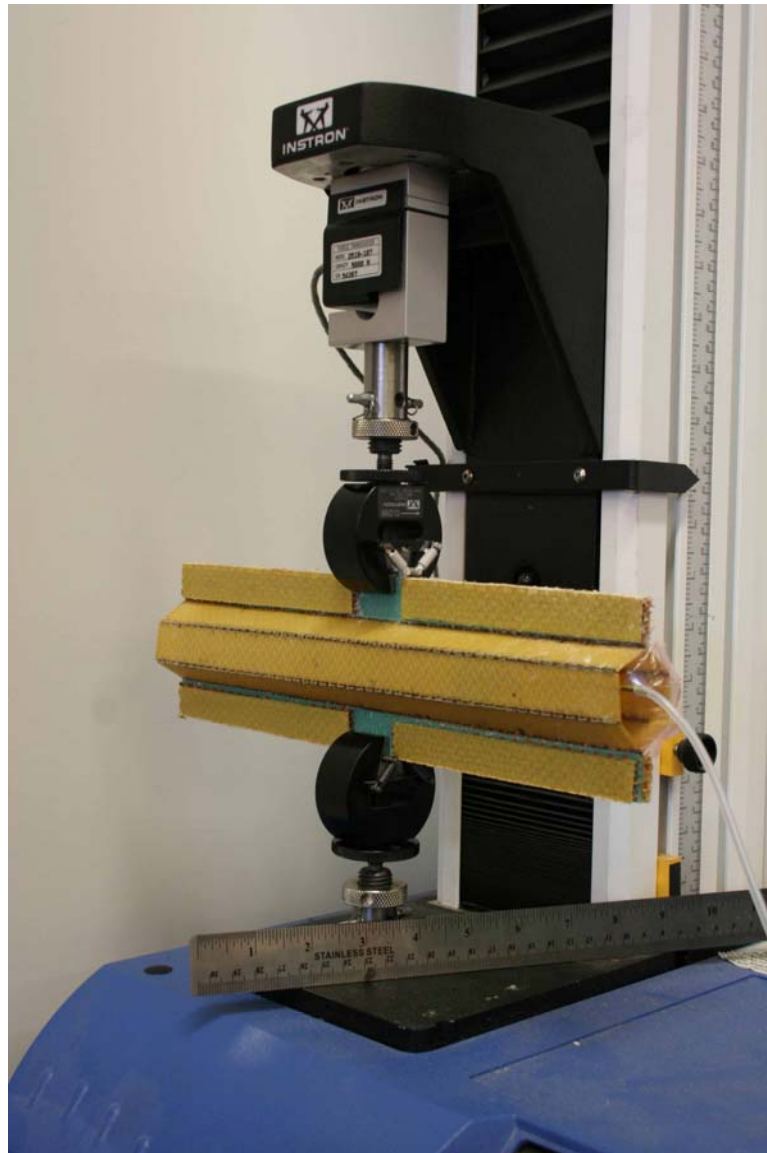
Figure 5.4   Experimental Setup of Single-Cell Rigid-Wall Longitudinal Test

5.2.3 Lateral Compression-Tension Test

The Kevlar test specimen needed to be modified slightly to perform the tension-compression test in the lateral direction. To enable the chucks of the Instron to grab the specimen, aluminum square stock was bonded to the top surface of the Kevlar specimen. Figure 5.5 displays a sketch of the experimental setup, while Figure 5.7 shows a photograph of the setup. Figure 5.6 shows the control input for the lateral tension-compression test. Notice that the realm of interest forms one full hysteresis loop.
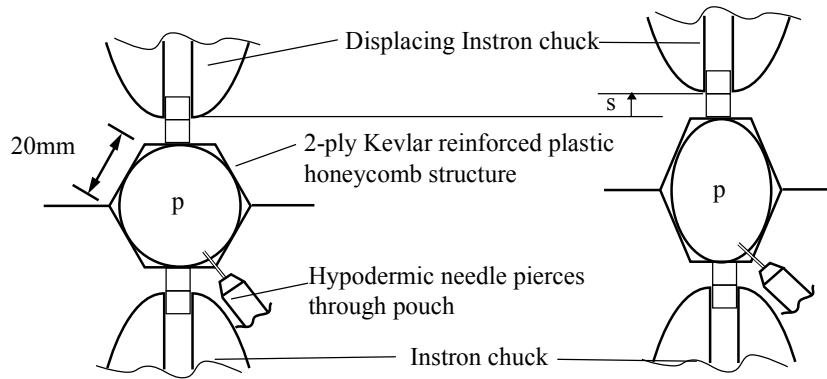
Figure 5.5   Sketch of Single Cell Lateral Compression/Tension Experiment
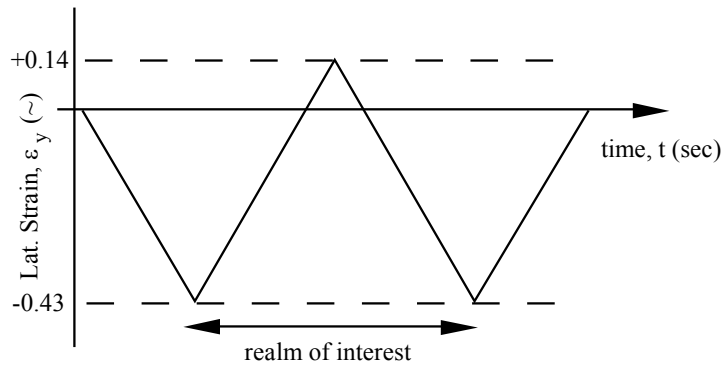
Figure 5.6   Input Wave Form for Lateral Compression-Tension Test

Figure 5.7   Single Cell Experimental Setup

5.3   Multi-Cell Rigid-Member Pressurized Honeycomb

To determine whether the results of the single-cell experiments could be extrapolated to a rigid-member honeycomb grid, a 23-cell honeycomb specimen was designed and built. The specimen was loaded in compression in longitudinal and lateral direction. At each position a series of compression tests was carried out. By testing at the two perpendicular principal orientations of the specimen the compressive pressure stiffness in both x (longitudinal) and y

(lateral) direction could be determined. The subsequent sections describe how this test article was tested in lateral and longitudinal compression, respectively.

5.3.1 Test Article and Experimental Hardware

Similar to the one-dimensional test article, this honeycomb grid was manufactured out of two-ply Kevlar laminates. All hinges were carbonized such as to minimize structural stiffness. This resulted in a structure with nearly frictionless hinges and approximately rigid walls, similar to the model presented in Section 4.2.1. In the plane of the honeycomb cells the outer dimensions in the x and y direction of the honeycomb grid were 180x173mm, respectively. The length of specimen in z-direction measured 290mm. To be able to distribute a point load over the length of all the cells, c-stiffeners were bonded to the specimen such that they spanned the length of the cells.

Each of the 23 cells inhibited a Mylar pouch. All the pouches were subsequently pierced with a hypodermic needle, which were, in turn, connected in series by a rubber tube. By attaching the rubber tube to a pressure variation apparatus on the one end and a pressure sensor on the other end the pressure in the tube could be controlled and monitored. The test specimen was positioned in an MTS858 Mini Bionix II servo hydraulic testing frame (see Figure 5.9 for details). This machine was equipped with two caul plates between which the specimen was sandwiched. To allow for free lateral contraction of the specimen all the c-stiffeners were coated with a layer of Teflease. In addition the caul plates were covered in a thin layer of petroleum jelly to ensure minimum friction between the specimen and the machine.

5.3.2 Lateral Compression Test

The first of the two tests was the lateral compression test. The specimen was positioned in the Mini Bionix such that a distributed load could be introduced in the y-direction (see Figure 5.8 and Figure 5.9). Notice in Figure 5.9 how the element was positioned between two horizontal plates. Greasing the plates ensured an almost free lateral contraction of the element during testing. Note also the continuous tube that ran from the pressurization apparatus on the left-hand side to the pressure sensor on the right-hand side. Hypodermic tubes pierced through the tube on one side and into the pouches on the other side. The pressure sensor connected to a data-acquisition unit that interfaced with Labview.
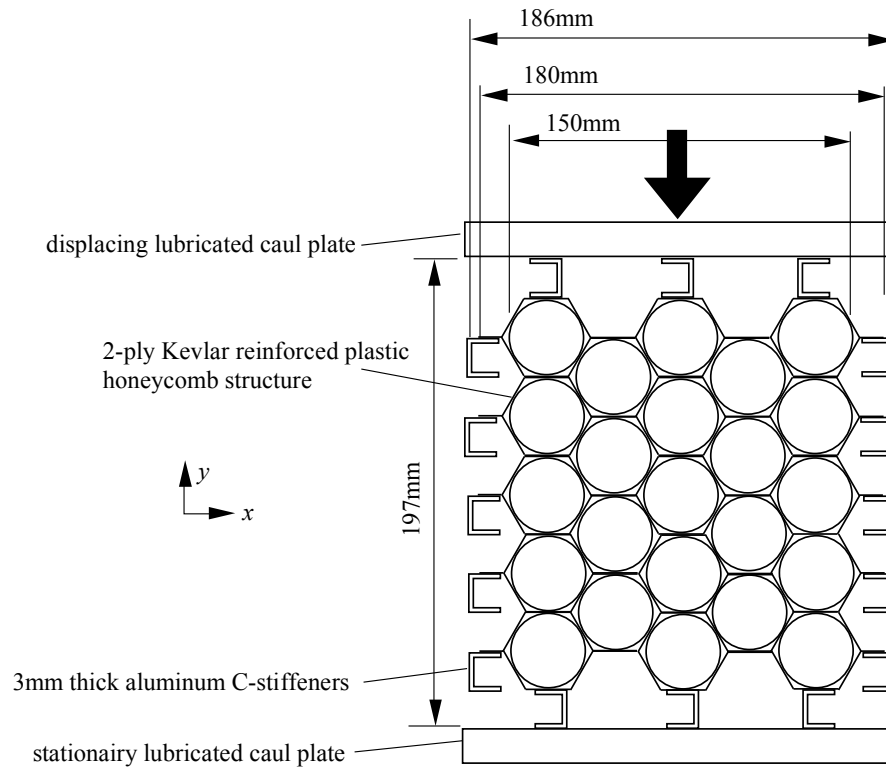
Figure 5.8   Sketch of Lateral Compression Test of 23-cell Rigid-Wall Pressurized Honeycomb

Starting at 5kPa, the pressure in the pouches (CDP) was increased in steps of 5kPa up to 50kPa. At each pressure a compression test was carried out where force and displacement were measured at a rate of 1Hz. Simultaneously, the CDP was measured using Labview at the same rate such that at each point in time the pressure, force and displacement were known. In Figure 5.10 a detail of the test setup can be seen.
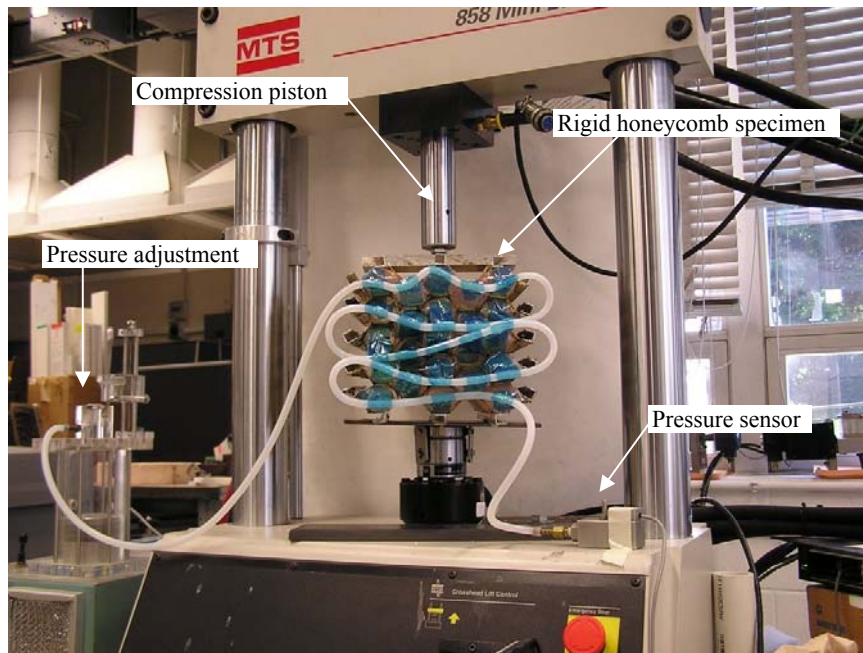
Figure 5.9   Multi-Cell Pressurized Honeycomb in Lateral Compression in the MTS Machine
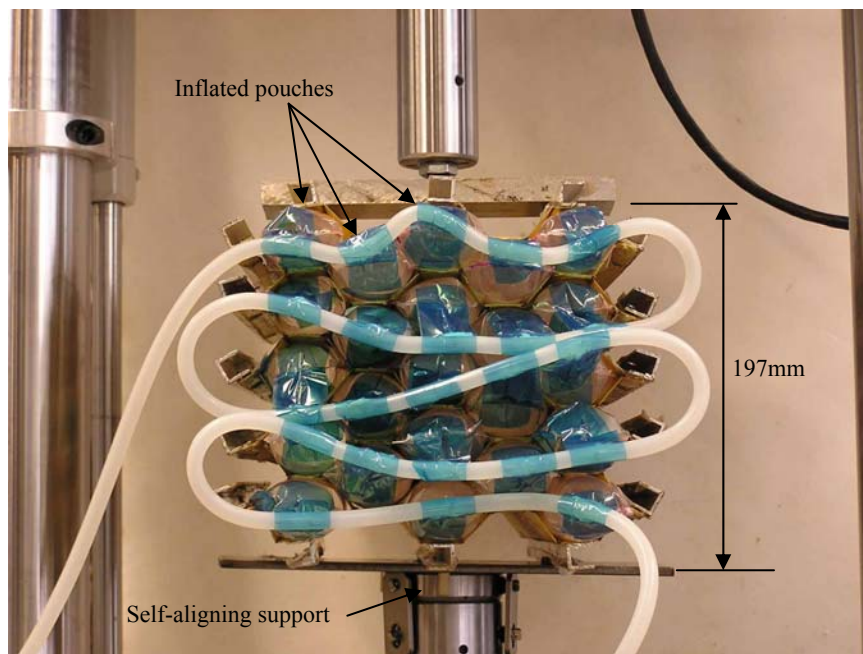
Figure 5.10   Detail of Multi-Cell Pressure adaptive Honeycomb Structure

5.3.3 Longitudinal Compression Test

The longitudinal compression test was carried out after the lateral compression test. The specimen was rotated ninety degrees and positioned between the caul plates as shown in Figure 5.11. The c-stiffeners that interfaced with the caul plate were covered with a layer of Teflease and were lubricated with petroleum jelly to allow for lateral contraction of the element. Similar to the lateral compression test, pressure, force, and displacement were recorded during this compression test at a rate of 1Hz. This test was carried out at 10 different CDPs, starting at 5kPa and ending at 50kPa in steps of 5kPa.
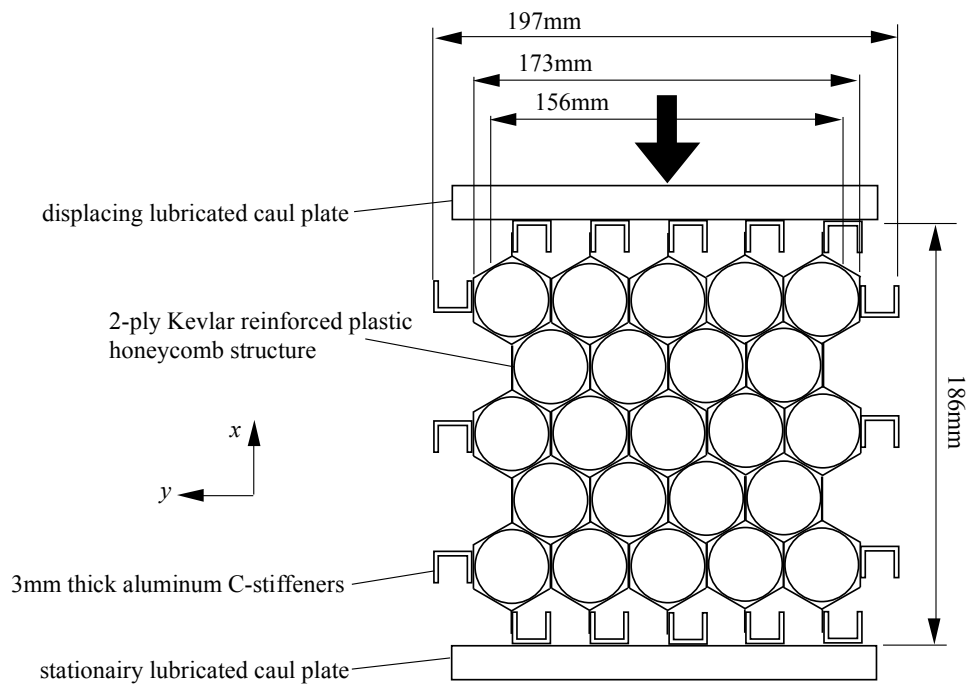
Figure 5.11   Sketch of Lateral Compression Test of 23-cell Rigid-Wall Pressurized Honeycomb

5.4   <u>Multi-Cell Pressurized Aluminum Honeycomb</u>

To investigate the structural properties of pressurized honeycomb, a 130-cell aluminum specimen was fabricated. This was the first test article that combined an aluminum honeycomb structure that could be pressurized such as to alter its stiffness. The tests on this specimen were conducted to see if the analytic model of Section 4.3 could be applied to predict the mechanics of pressurized honeycomb

5.4.1 Test Articles and Experimental Hardware

As a base material Aluminum 1145H19 was chosen with a thickness of 76μm. The reason for this option was that it had shown good manufacturability properties for the honeycomb in the sense that it allowed for straight folds to be induced by a press brake. In addition, it had relatively high yield strength, which was important because it needed to stay in the elastic realm while loaded. The aluminum sheets were cut, folded, and bonded together using Hysol 9412. Appendix D gives a more detailed description of the manufacturing procedure. The face length of a characteristic cell measured $l = 15$mm. The resulting aluminum honeycomb specimens can be seen in Figure 5.12 and Figure 5.13.
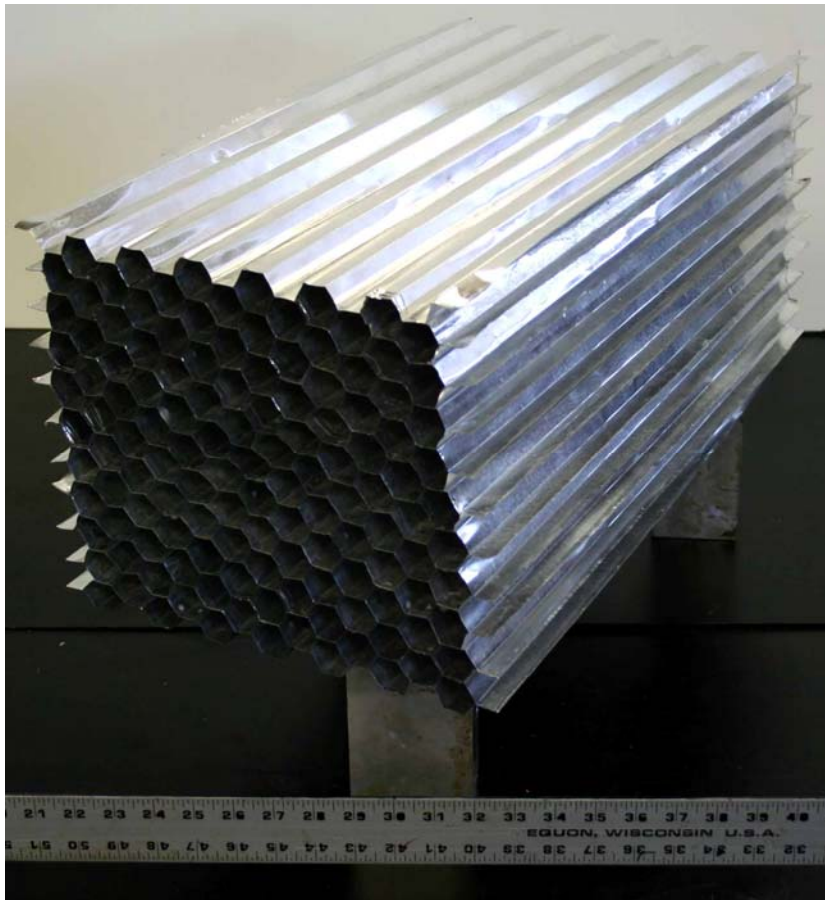
Figure 5.12   130-Cell Honeycomb Test Article
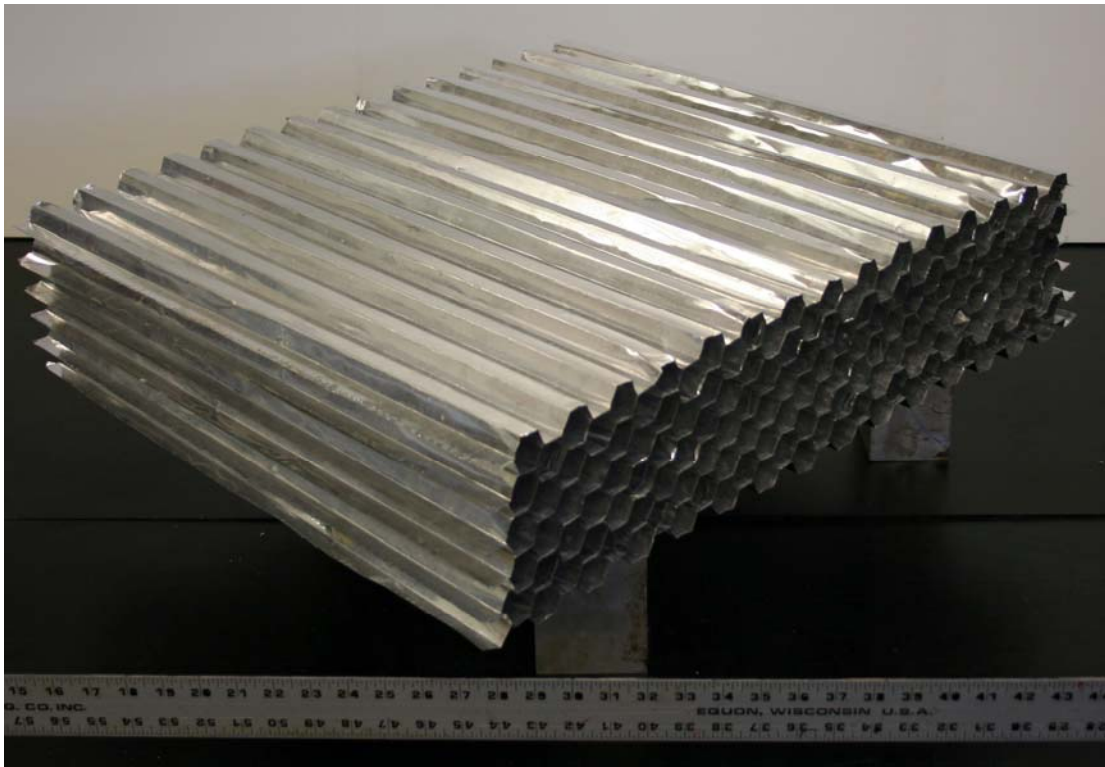
Figure 5.13   145-Cell Honeycomb Test Article

It proved challenging to properly align all the corrugated sheets on the rectangular (145-cell) specimen. The reader can understand that due to imperfect manufacturing techniques, not all the folds in the corrugated sheets were exactly parallel to one another. This resulted in slightly irregular sides in the plane of the honeycomb cells (Figure 5.14). Because of the high aspect ratio of the cells themselves, this was not perceived to have an adverse effect on any of the measurements that would be acquired by subjecting this test article to a load.
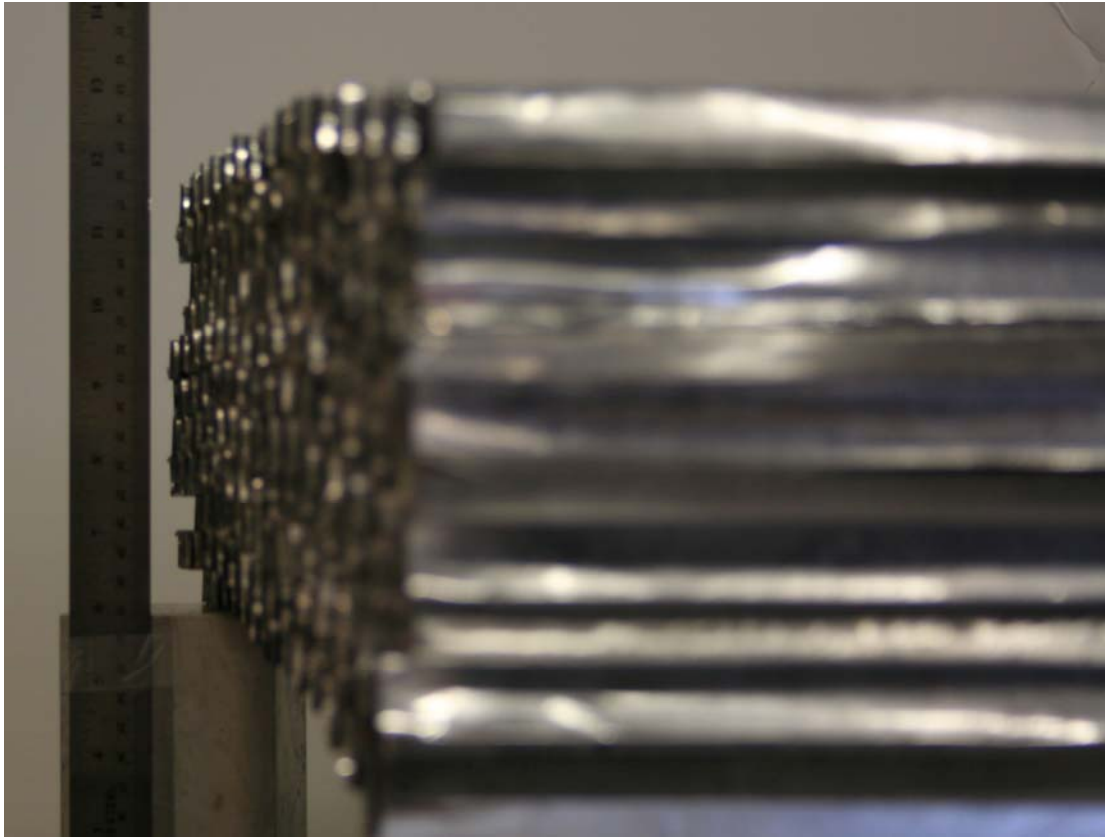
Figure 5.14   Misalignment in Corrugated Sheets

Similar as in previous experiments, each of the cells were subsequently filled with a plastic pouch. To inflate the plastic pouches they were connected to two plenum chambers by means of individual silicone tubes. To ensure good mass flow into the pouches each of them had a 3mm brass tube pierced through its surface that connected to the silicone tubes. The plenum chambers were made out of 51mm diameter copper tubing with fitting end caps. Each of the plenum chambers had 75 short (~1cm) brass tubes glued into it that connected to the other end of the silicone tubing. The plenum chambers were, in turn, connected to the pressure distribution apparatus that was also used for the previous experiments.

5.4.2 Lateral Compression Test

The lateral compression test was the first of three tests to be carried out. To be able to provide relatively constant distributed load over the top and bottom surface of the test article, two thick (~8cm) compression boards were fabricated. These boards were made as a sandwich

151

where a Styrofoam core was bonded to two stiff plastic plates on either side. The top board was connected to a 20mm thick aluminum plate, which in turn connected to the force transducer on the Instron machine via a swivel joint. The bottom board was connected to a 25mm thick aluminum plate, which was then bolted to the Instron machine. The test article was positioned in between the upper and lower boards. Petroleum jelly was applied between the surface of the test article and the board surface. This enabled the test article to expand perpendicular to the direction of applied load with minimum friction.

The Instron 3345 was slightly modified to geometrically allow for such a large test article. The arm between the thread rod inside the machine and the force transducer was made twice as long by means of an aluminum extension. Since the Instron 3345 was rated at a maximum load of 5kN, it was decided that due to the doubling of the moment arm, a new limit of 2500N needed to be enforced to ensure the integrity of the manchine. Figure 5.15 shows the entire experimental setup

The measurement and control of the Instron 3345 were carried out by using the software package Bluehill 2. The specimen was compressed at a rate of 0.1% strain per second. A maximum down stroke of 15% strain was prescribed such as to avoid plastic deformation in the aluminum ligaments (this was detected in an earlier test when the honeycomb specimen was strained in lateral compression up to 20%). During the experiment the force was measured at a rate of 1Hz. In addition, the pressure was controlled with the aforementioned pressure apparatus and was monitored in Labview by means of a pressure transducer. Pressure measurements were taken simultaneous with the force measurements at a rate of 1 Hz. To allow for hysteresis analysis, the test was carried out in a loop, where data was taken in the upstroke (0 to 15% strain) and downstroke (15% to 0 strain).

Four tests were carried out at target pressures of 10, 20, 30 and 40 kPa. Pressure, force and displacement were recorded. A post-processing code in Matlab was written that read the experimental results, translated the force/displacement measurements to average stress/strain measurements based on the geometry of the test article. In addition, the hysteresis was automatically calculated based on the enclosed area between the stress-strain curves of the upstroke and downstroke.
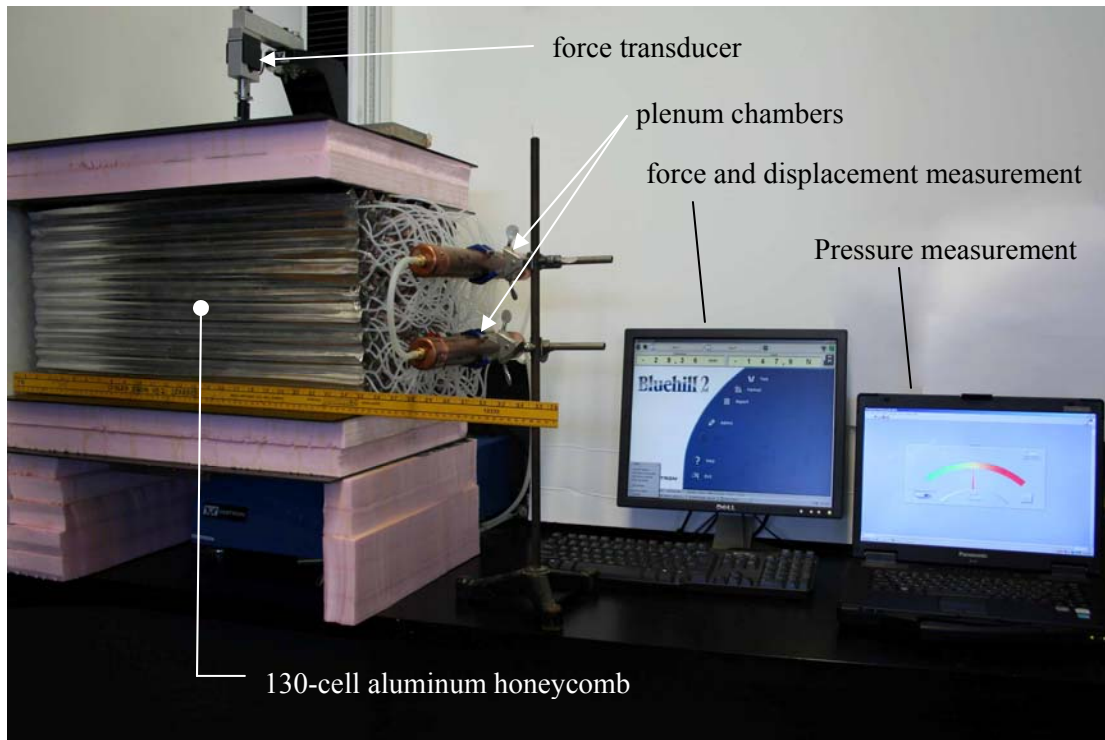
Figure 5.15   Lateral Compression Test on 130-Cell Honeycomb Specimen

5.4.3 Longitudinal Tension Test

In order to determine the stress-strain relation of the pressurized 130-cell honeycomb test article, a new test setup was created. The requirement for the test setup was to be able to pull on the specimen in longitudinal (x) direction, without constraining the article in lateral direction, such that it would be free to contract in that direction. To be able to do that, it was decided to suspend the test articles by means of multiple wires from a rigid frame. The frame was constructed such that in default position, each of the wires that connected to the test article was (close-to) vertical. The wires were relatively long (30cm) such that lateral contraction would not alter the force vector to any significant extent. For example, for a maximum lateral strain of 4%, the most lateral displacement amounted to 6mm. This changed the angle of the wire no more than 1.2º. The tensile test setup is displayed in Figure 5.16.
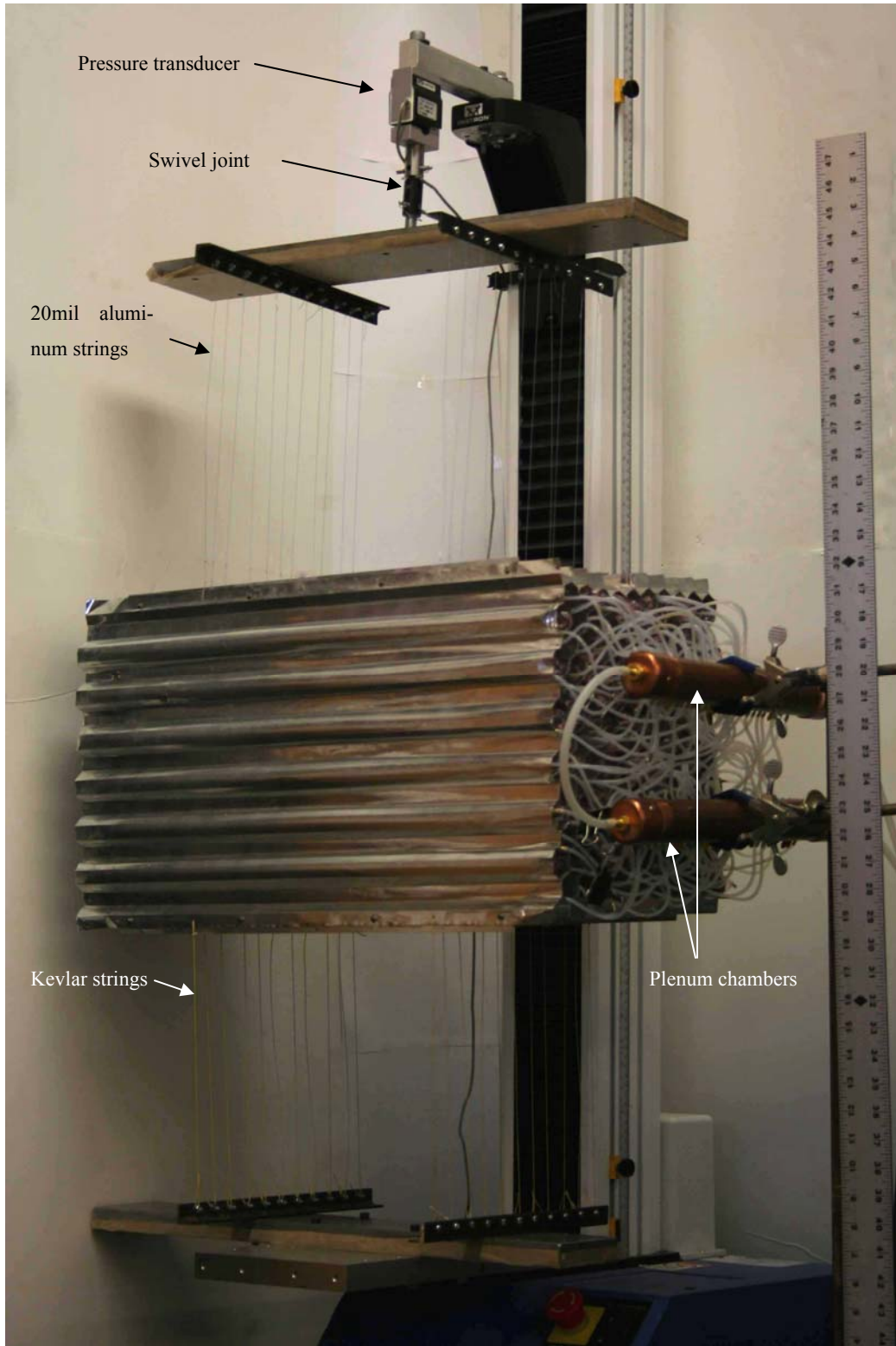
Figure 5.16   Experimental Setup for Tension Test on 130-Cell Pressurized Honeycomb

To perform the longitudinal tensile test, the test article was modified at its boundaries. Additional 0.62mm thick aluminum stiffeners were attached to the free outer flanges of the honeycomb to reinforce them and prevent tear due to the wire attachment. These aluminum stiffeners were bolted to the flanges and had double-sided tape on them. They were made such that they could be taken off again in order for the test article to be modified to do other tests. As might be noted from Figure 5.16, the upper wires that were used were made of aluminum while the lower wires were made of Kevlar. Both wires were adequate for the job and the choice for using either one was mainly based on the availability of both materials. The wires were tied to the test article and subsequently attached to the frame by clamping them between two washers in a simple bolt-nut assembly. Both upper and lower frame were constructed out of 3.2mm thick, 19mm square carbon steel angle. These were, in turn, connected to 20mm thick, 10cm wide aluminum plates. The entire frame contraption was perceived to be orders of magnitude stiffer than the pressurized honeycomb and therefore be an unlikely source of error in the measurements. A swivel joint was used between the force transducer and the frame, such as to automatically adjust for small misalignments that could occur during testing.

The testing was carried out in the Instron 3345 testing machine. With this particular test the tension on the honeycomb inadvertently created peal stresses inside the honeycomb structure. During initial testing it was therefore determined that maximum longitudinal strain could not exceed 4%. It was found that beyond this strain level the bonding layers between the individual corrugated sheets started to de-bond. Since this is a very undesirable condition, it would be recommended not to load a honeycomb structure that is manufactured like this in longitudinal direction. It would greatly limit the applicability of the material as a pressure adaptive actuator. The strains that were induced in lateral compression (Section 5.4.2) were far greater (up to 15%) and did not induce any adverse peel stresses. This loading condition would therefore be preferred over longitudinal tension.

5.4.4 Longitudinal Compression Test

To perform the longitudinal compression test, the test article needed to be modified appropriately. A pressure force would be introduced in the unsupported flanges of the honeycomb. To prevent these forces from buckling the flanges they needed to be reinforced. To that extent, aluminum angle pieces were bolted to the honeycomb flanges. In addition to a stiffening

effect, the angle pieces also provided the specimen with a much larger surface area to be pressed on by the Instron press. To ensure a close-to frictionless connection between the surface of the test article and the compression surface, the interface of the angle pieces were covered with a Teflon strip and subsequently lubricated with petroleum jelly.

Apart from the modified test article, the entire setup was identical to the lateral-compression experiment (see Section 5.4.2). An overview of the experimental setup is presented in Figure 5.17. The reader is asked to pay attention to the two rows of angle pieces bordering the compression plates. In Figure 5.18 the connection between the honeycomb material and the angle pieces is shown in even greater detail under compressive loading.
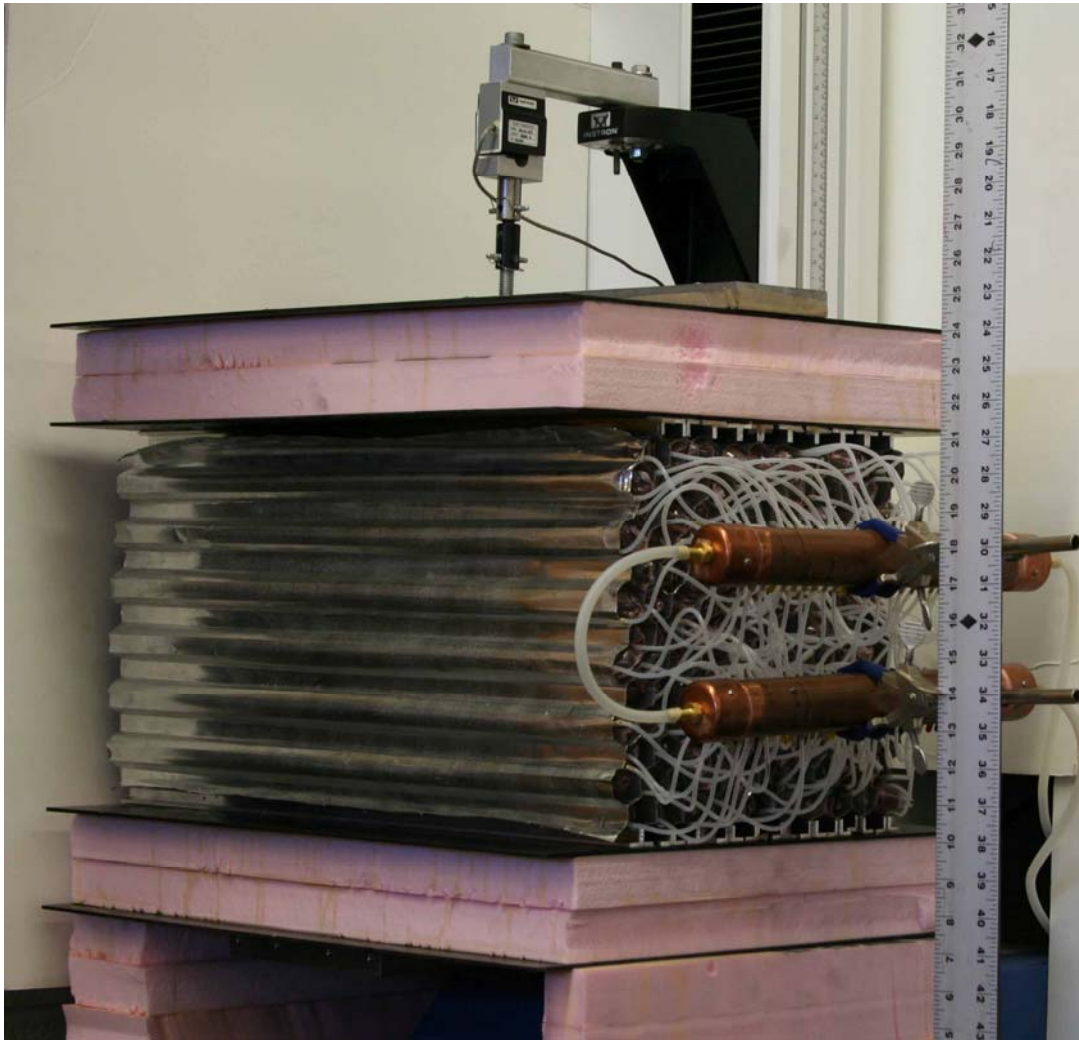
Figure 5.17   Experimental Setup for Longitudinal Compression Experiment on 130-Cell Honeycomb Test Article
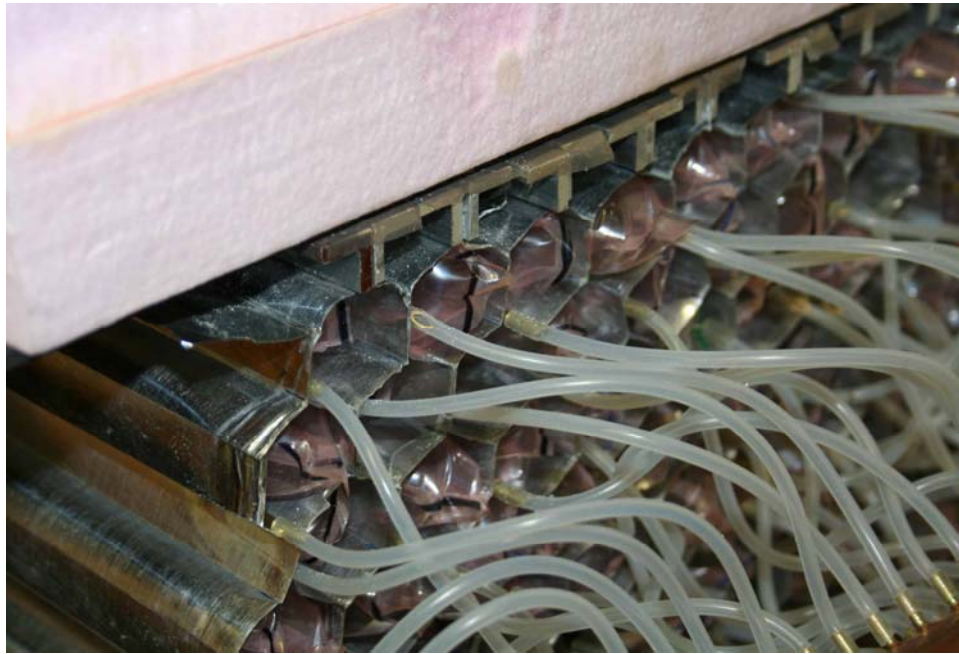
Figure 5.18   Detail of Cell Deformation during Compressive Loading

5.4.5 Three-Point Bend Test on Pressurized Honeycomb Beam

The previous described experiments were designed to capture the stress-strain behavior of pressure adaptive honeycomb. From the results of these tests an equivalent material stiffness could be deduced that could be used in the finite element analysis. To test if this method would result in accurate predictions for the mechanics of pressure adaptive honeycomb in an application, a three-point bend test was carried out. To that extend the 145-cell test article was employed. A schematic layout of the test can be seen in Figure 5.19.
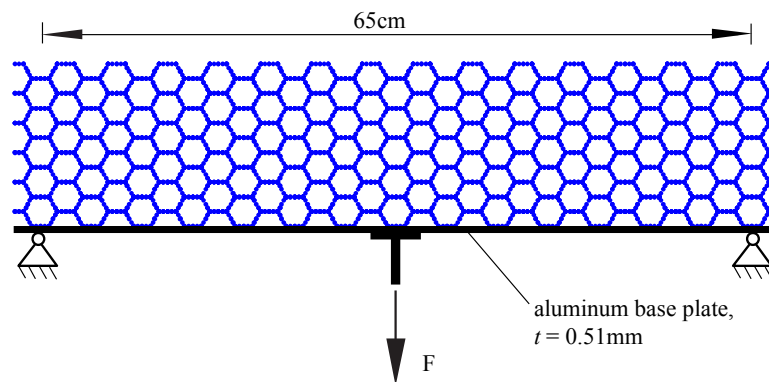
Figure 5.19   Schematic Representation of Three-Point Bend Test on 145-Cell Pressure adaptive Honeycomb

To accommodate this rather large test article, a frame was built that could be mounted to the base of the Instron Machine. It was anticipated that the forces in this test would not be as high as during the compressive and tensile tests on the 130-cell specimen. It was therefore decided to extend the arm of the instron out even further such that the force could be applied in the center of the test article. To simplify the test setup, the schematic setup of Figure 5.19 was built upside-down, such that the Instron could pull on the base plate and hence induce curvature in the beam. A wooden frame was built with two steel pins that provided the simply supported boundary conditions. The test frame was rigidly attached to the base of the Instron while the test article was hung from the Instron's force transducer. Figure 5.20 shows the experimental setup for this three-point bend test. By displacing the force transducer upwards bending was introduced in the test article.
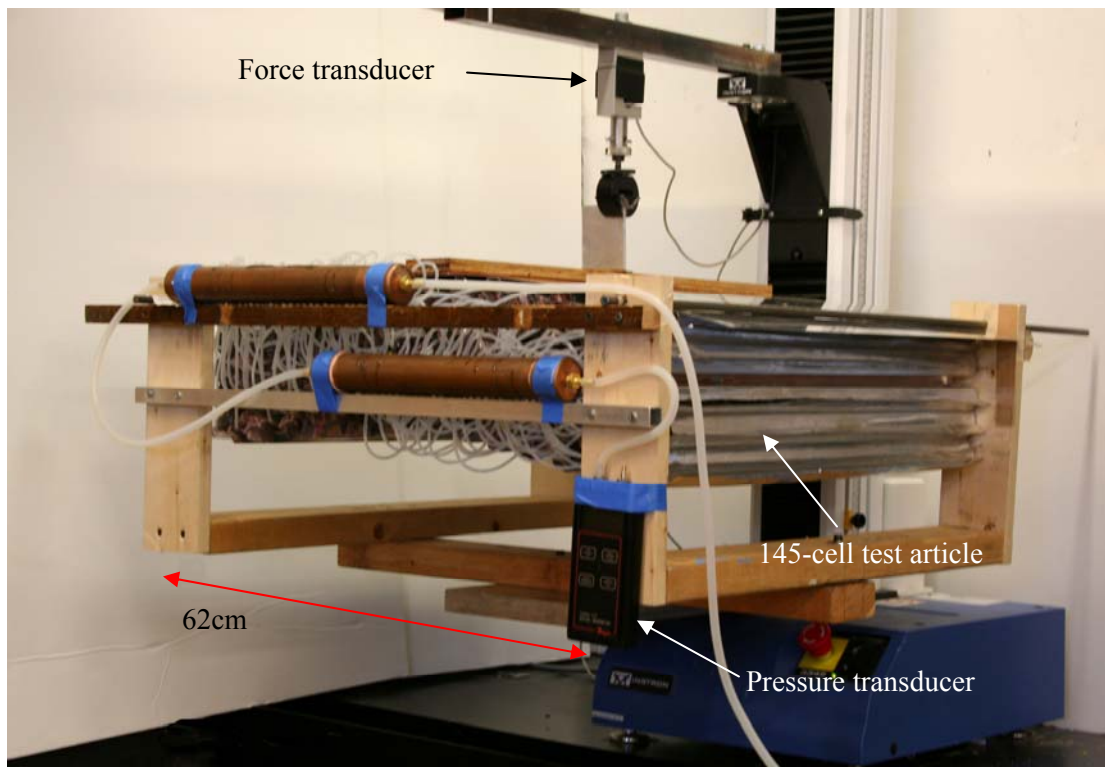
Figure 5.20   Experimental Setup for Three-Point Bend Test

5.5   Wind Tunnel Experiment with Pressure adaptive Flap

To demonstrate the workings of pressure adaptive honeycomb in an aerospace application, a wind tunnel model of a wing section with a pressure adaptive flap was constructed. Similar to

the explanation in Section 3.2.3, this flap increased the camber of the airfoil over the aft 30% of the wing chord. This section describes the details of the test article and the wind tunnel setup that was used to determine the aerodynamic properties of the wing section. It also pin-points similarities and differences between the current test article and a real wing that would rely on pressure adaptive honeycomb for flap actuation.

5.5.1 Wind Tunnel Model with Adaptive Flap

The honeycomb that was used in the pressure adaptive flap had the same cell dimensions as in previous experiments ($l = 15$mm). Compared to the flap size ($c_f = 28$cm), the cell was quite large. This implied that the total number of pressurized cells was limited to 13 and that the space between the upper and lower skin was not fully filled by the honeycomb. The main reason for not going to a smaller cell size lay in the manufacturing process. It was found that a honeycomb with a characteristic face length of 10mm required a higher level of accuracy to fabricate. Folding and bonding the honeycomb would lead to substantial misalignments that could be detrimental when pressurization was used. However, if manufacturing techniques were to improve, a smaller cell size compared to the flap dimension would be preferable. In that sense, the wind tunnel model deviated from a possible production model.

The entire wind tunnel model consisted of three main parts: a main body, an adaptive flap, and a stiffened trailing edge. Both the main body and the stiffened trailing edge were made from Styrofoam by using a wire-cutting technique. The cross-sectional shape that was chosen for this wing was a NACA 2412 section, which is also found on the Cessna 172. Two wooden templates were fabricated to use as a guide for cutting the foam to the correct shape. In a later stage, these templates were bonded to the foam such as to give the model a hard side surface to connect to. Small flaws in the surface of the foam model were filled in with glass putty. To give the foam model sufficient strength, it was covered in a single layer of fiber glass cloth, impregnated with Epoxy. The surface roughness of the fiberglass interface was reduced by applying glass putty over its surface and sanding it down with fine-grid sand paper. A grey primer sprayed on the surface to give the model an even smoother top layer. A thread rod with a diameter of 1.25cm was put through the entire model at chordwise position of $0.25c$ and on the local chord line. This provided the model with hinge fixture for the wind tunnel.

For the flap the same manufacturing techniques were used to produce the honeycomb as for the 130-cell honeycomb block. In addition, a top and bottom skin was fabricated out of Al110T3. The top skin measured 0.38mm in thickness and was rolled (cold-worked) such as to induce an initial curvature in the flap. The bottom skin was made from 0.25mm thick aluminum sheets. It was also rolled to an initial curvature. The honeycomb was attached to the top skin of the flap, while the bottom skin was free to translate with respect to the honeycomb. This can be seen in the two cross-sectional views in Figure 5.16. In these views, the flap is displayed in retracted position where the honeycomb cells form (close to) perfect hexagons. It can also be observed how the honeycomb is clamped between the main body of the model and the foam trailing edge. The honeycomb was therefore free to expand and contract in the direction perpendicular to the top skin of the flap.
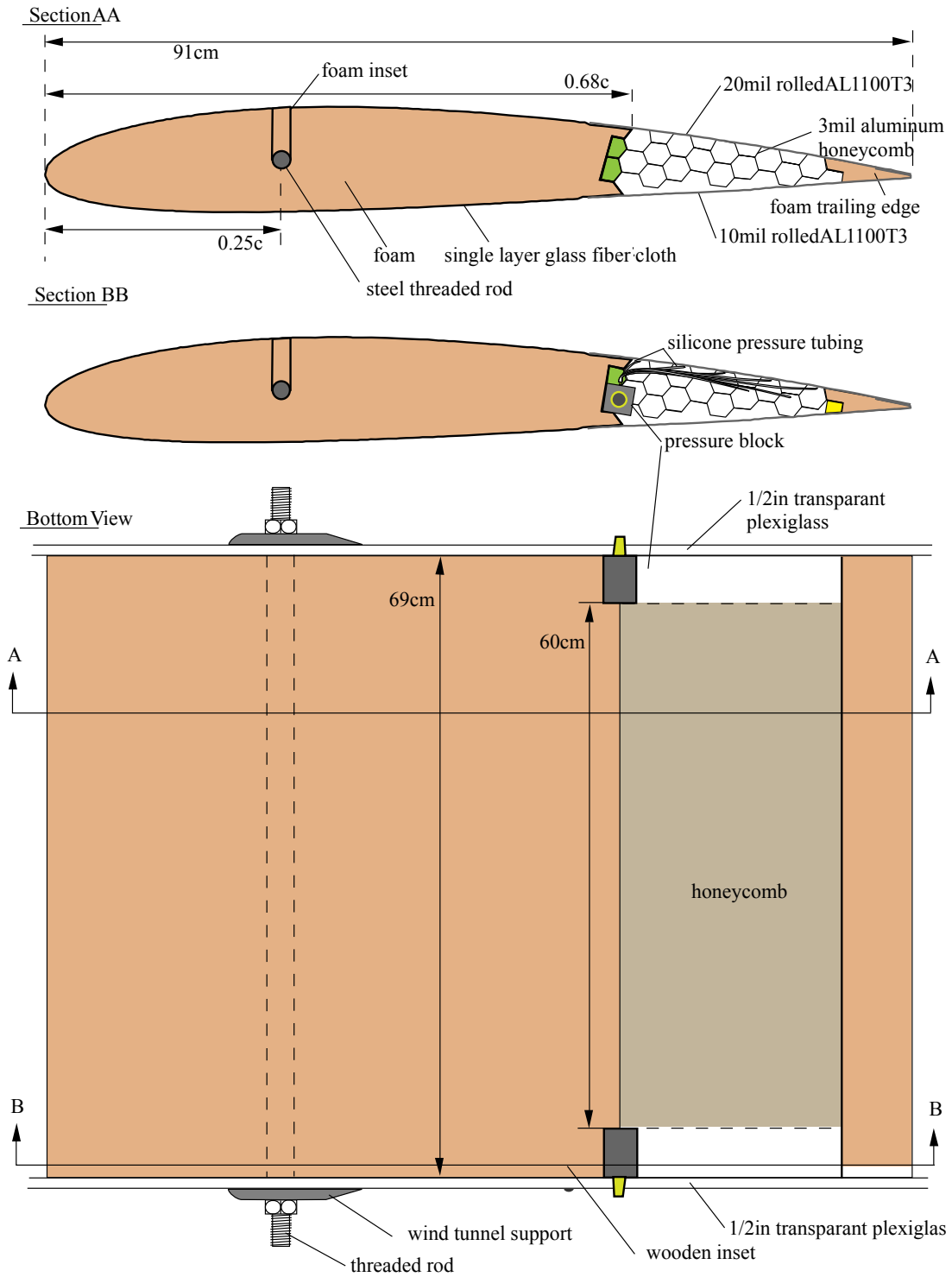
Figure 5.21   Bottom and Side View of Wind Tunnel Model with Pressure adaptive Flap
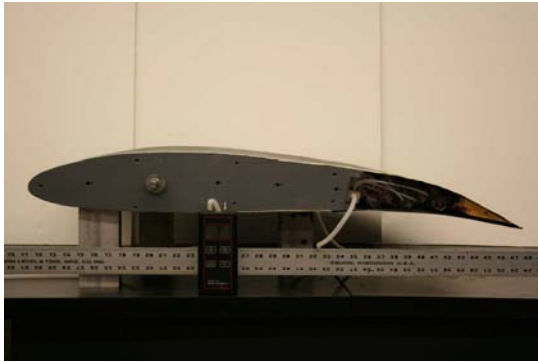
Figure 5.22   Side View of Wind Tunnel Model
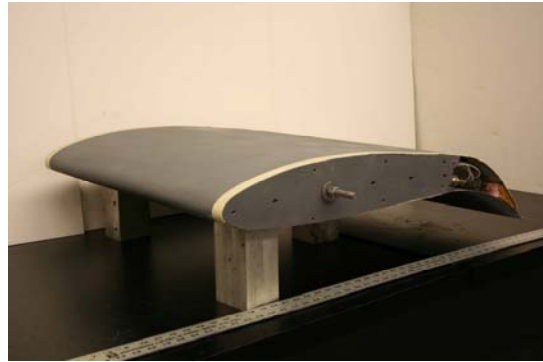
Figure 5.23   Isometric View of Wind Tunnel Model

Figure 5.24   Detail of Pressure adaptive Honeycomb

Figure 5.25   Detail of Sliding Trailing Edge

5.5.2 Low Speed Wind Tunnel

The experiment was carried out in the big low-speed wind tunnel of The University of Kansas. This tunnel is of closed-circuit type and has a test section measuring 92cm x 129cm (36" x 51") in cross section and 152cm (60") in length (see Figure 5.26). The tunnel has a maximum speed of 85m/s (165kts) and a contraction ratio of 9. According to wind tunnel documentation, the turbulence factor in the tunnel amounts to 1.1 which results in a turbulence level of < 0.1% according to Figure 6.7 in Ref. 144. The test section has two windows through which the model can be observed during testing.
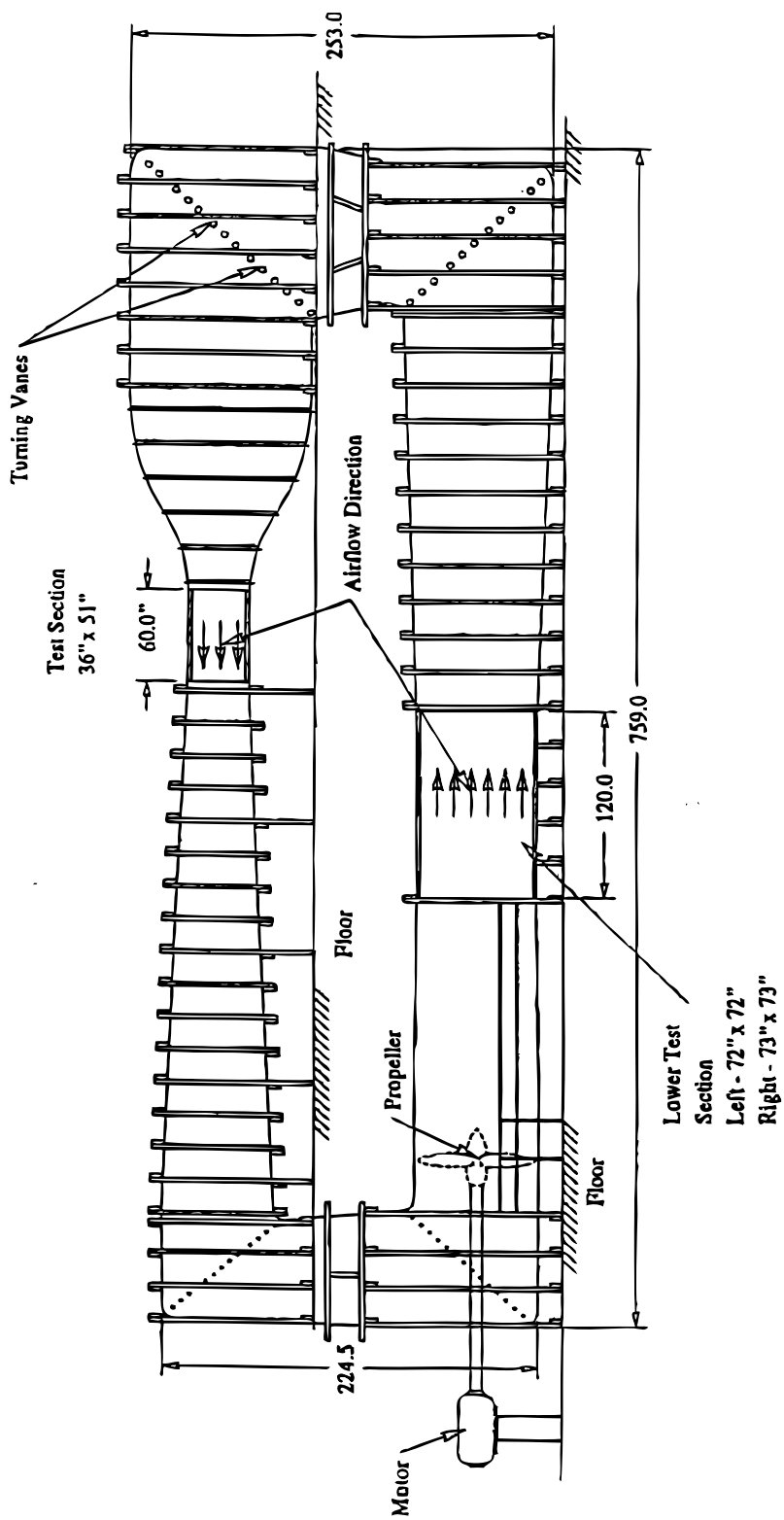
Figure 5.26   The Low Speed Wind Tunnel at The University of Kansas

163

The tunnel is equipped with a six-component strain-gage balance and a PC-based LabView data acquisition system. The maximum lift, drag, and pitching moments that can be obtained are 5400N, 2150N, and +/-2900Nm, respectively. The balance has been (re-)calibrated by using a $1/10^{th}$ scale model of a Cessna 210 and by verifying its aerodynamic coefficients against previously obtained data under the same conditions. This calibration was done for a model positioned 45cm above the center of the table.

5.5.3 Wind Tunnel Setup

The goal of the wind tunnel experiment was to see how the alteration of pressure in the pouches would change the aerodynamic coefficients of the airfoil. To ensure minimum influence of three-dimensional effects (especially flow around the edges) two endplates were constructed. This option was preferred over the option of clamping the model between the wind tunnel walls for two reasons. First of all, a thick boundary layer would be present on the wind tunnel wall which would not represent free-stream conditions. Secondly, clamping a model between the walls would induce a larger blockage effect which would adversely affect the accuracy of the wind tunnel measurements. The end plates were made of 0.64cm thick Plexiglas such that during the measurement the geometry of the flap could be observed. Figure 5.27 through Figure 5.30 shows the wind tunnel model between the two end plates and a few details. In Figure 5.28 it can be seen how tick marks were drawn on the transparent end plate at three chordwise locations. These tick marks were used to measure the coordinates of the top and bottom skin at two chordwise stations as well as the position of the trailing edge. It was found that by splining a line through these coordinates resulted in an accurate representation of the flap geometry (see Figure 5.31). This could then be used for CFD analysis to compare to the experiment.

Figure 5.27 Side View of Model with End Plates
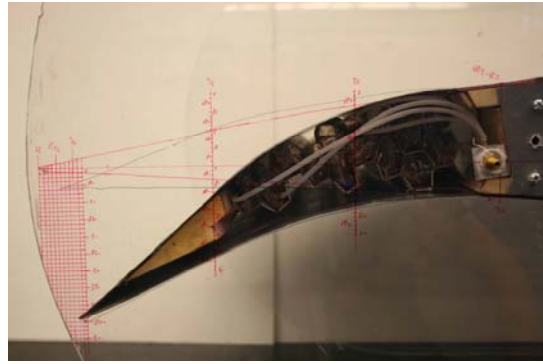
Figure 5.28 Detail of Flap with Tick Marks on End Plate

Figure 5.29 Detail of Angle-of-Attack Holes in End Plate
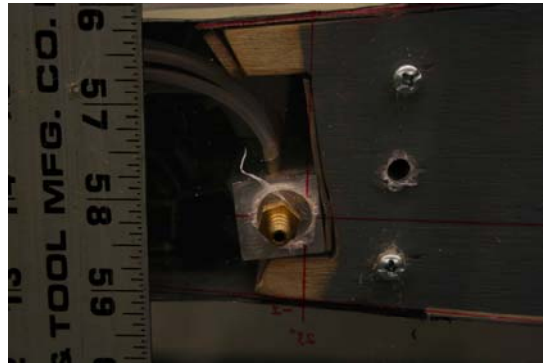
Figure 5.30 Pressure Tubing Pierces through End Plate
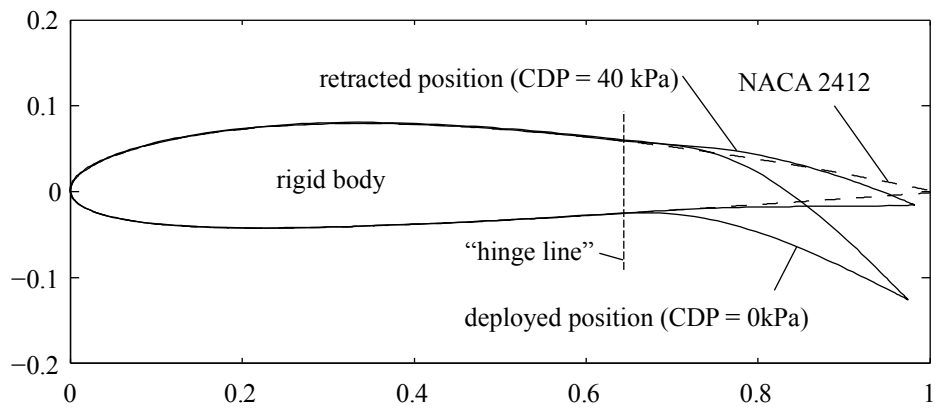
Figure 5.31 Normalized Geometry of Wind Tunnel Model With Adaptive Flap

After the model was sandwiched between the two plates, it was positioned in the wind tunnel. Two solid aluminum posts were used to mount the model onto the wind tunnel balance at an offset of 45cm from the balance table. To adjust the angle of attack, small holes had been drilled into the Plexiglas at a 32cm radius from the hinge point. This way 14 different angle-of-attack positions could be set between -6 and +20 degrees in steps of 2 degrees (see Figure 5.29). The aluminum posts were bolted onto the wind tunnel balance. A dimensional sketch of the proposed experimental setup is shown in Figure 5.32.
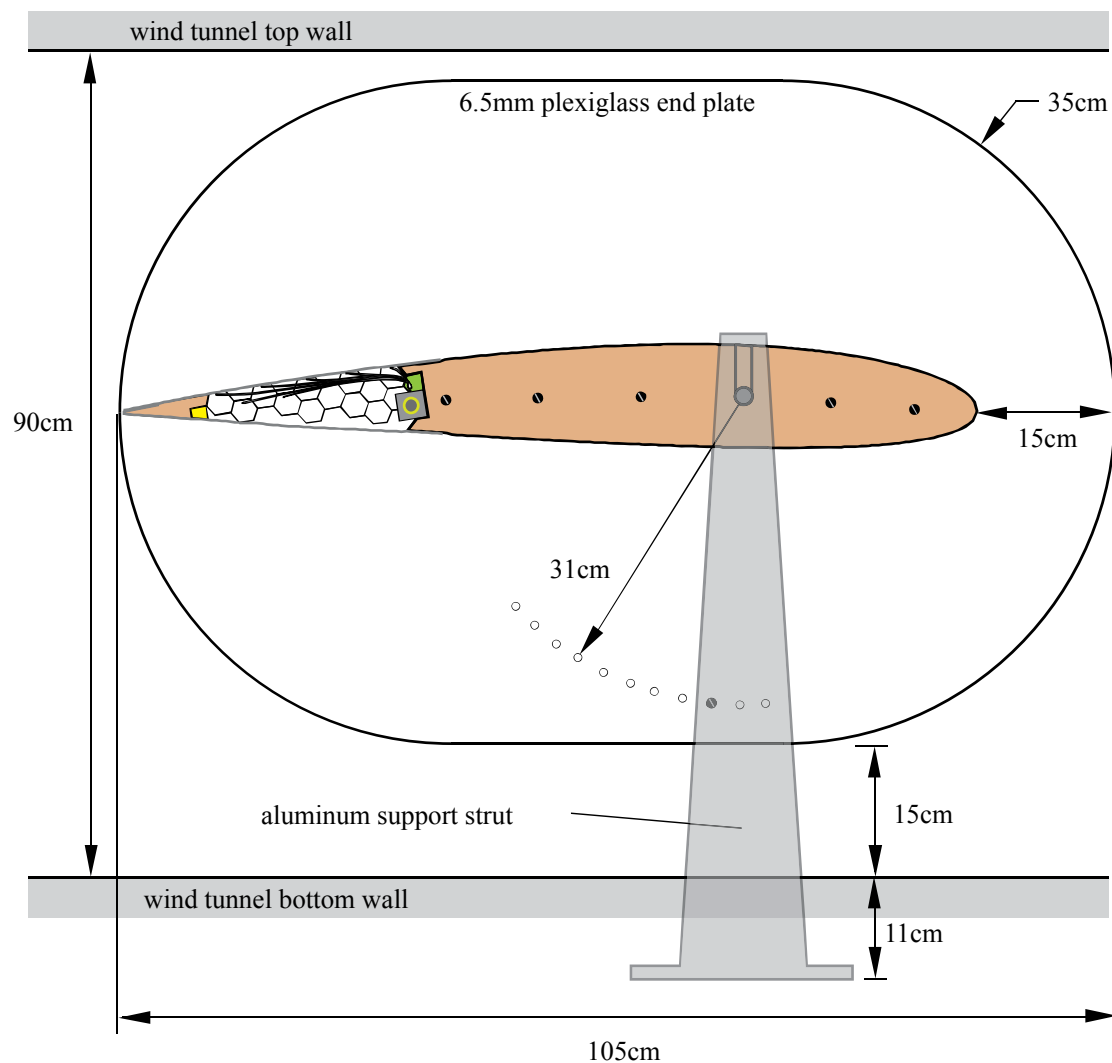
Figure 5.32   Sketch of Wind Tunnel Model in Wind Tunnel

During the experiment various parameters were measured or controlled. The controlled parameters were the geometric angle of attack, the free-stream wind speed, and the pressure in

the pouches. The measured parameters included all aerodynamic forces and moments as well as the Reynolds number, density, wind speed and cell differential pressure. The cell differential pressure was measured using a handheld manometer up to an accuracy of 0.1kPa. The pressure difference was measured between the pressure inside the pouches and the freestream static pressure. All the other measurements were recorded by Labview, which was connected to the wind tunnel balance sensors (forces and moments), the Pitot-static tube (velocity and static pressure) and a thermometer (static temperature). In addition, at each data point (i.e. a particular combination of the controlled parameters) a photograph was taken of the flap position. To that extent, extra lamps were added to ensure sufficient photo quality. A side view of the model in the wind tunnel is shown in Figure 5.33. The entire experimental setup can be seen in Figure 5.34. The latter figure shows the model at a geometric angle of attack of 18º, a measured wind speed of 61kts (31.3m/s), and a CDP of 40kPa.
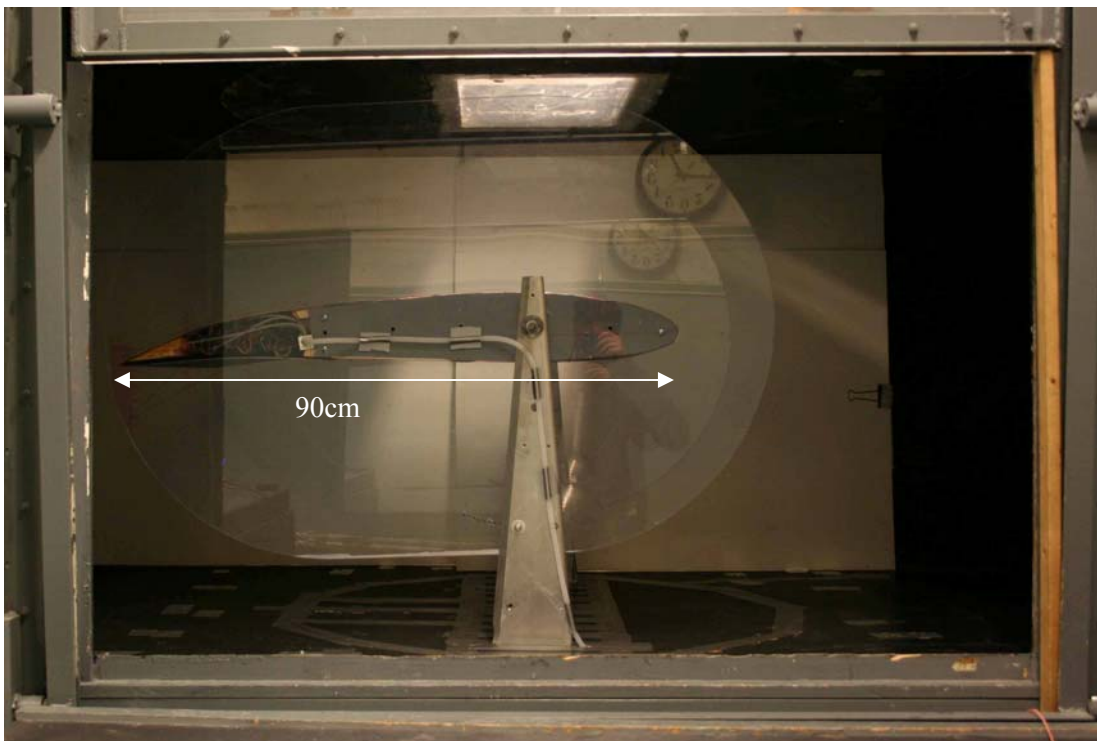
Figure 5.33   Side View of Model in Wind Tunnel with Stowed Flap

Photo camera

Model in wind tunnel

Lamps

Computer that controls wind speed and records aerodynamic forces

Pressure adjustment apparatus

Handheld manometer
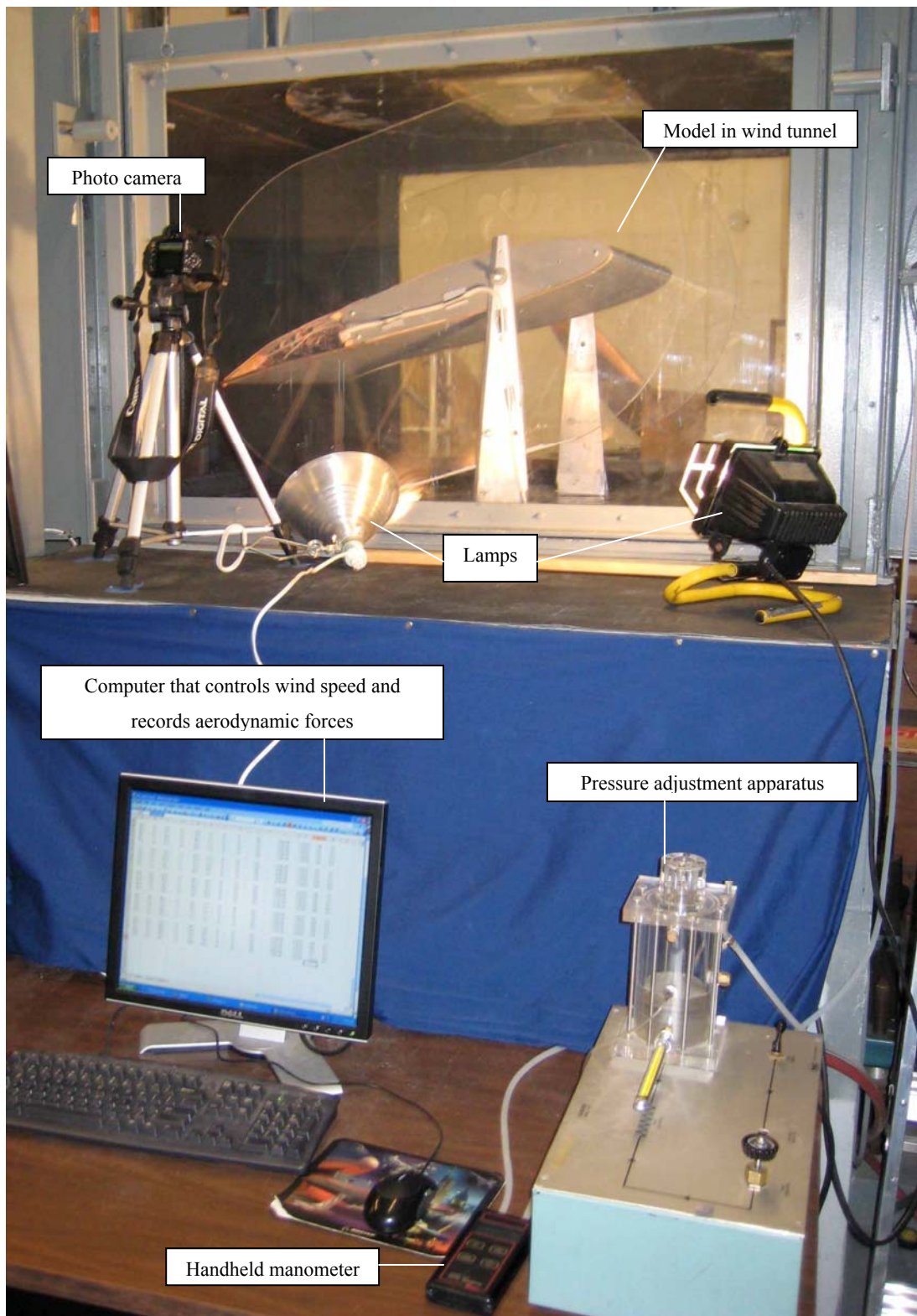
Figure 5.34   Overview of Experimental Setup in Wind Tunnel

CHAPTER 6   EXPERIMENTAL RESULTS, CORRELATION, AND DISCUSSION

This chapter presents an overview of the experiments that were done to validate the analytic models that were introduced in Chapter 4. The linear-elastic model that describes the honeycomb is checked against experimental data in Section 6.1. The non-linear model that describes the stress-strain relationship of rigid-member pressurized honeycomb is validated in the two subsequent sections. In addition, the hysteresis in the pressurized honeycomb is experimentally determined. An experimental validation of the volume ratio, ζ, which was assumed to be constant throughout the analysis, is presented in Section 6.4. Section 6.5 displays the results of test of the pressurized 130-cell test article that was tested in longitudinal and lateral compression as well as in longitudinal tension. The chapter closes with the results of the wind tunnel tests on the pressure adaptive flap.

It is pointed out to the reader that an important set of tests is missing from this chapter. These are the experiments that should validate the stress-strain relations for pressurized honeycomb for the case of a constant mass of gas inside the pouch. Financial and manufacturing constraints prevented their inclusion. The manufacturing of a pouch with appropriate dimensions that is completely air tight over an extended period of time is difficult. For the presented set of experiments, vacuum-bag Mylar was heat-sealed, such as to act as a pouch. It was found that miniscule perforations around the seal existed that leaked very small amounts of air. By pressurizing these pouches, a constant pressure could be sustained during the experiments because a small mass flow was present. For the constant-mass case, these miniscule holes would be detrimental. In addition, experimental testing of such a specimen is fairly complicated. The testing could be done two ways. The first option would be to make one set of pouches that all hold the same amount of air. Stress-strain tests would need to be performed in an environment where the ambient pressure could be lowered (e.g. vacuum chamber). This poses obvious problems with test equipment inside a vacuum chamber. A second option would be to vary the mass of air inside the pouches, which comes down to pressurizing a pouch up to a certain pressure and then sealing the pouch. This would require a valve system on the pouch, similar to those found on bikes or car tires. Stress-strain testing could be done at a regular ambient pressure.

169

What is shown in Sections 6.1 through 6.5 is that the method that is presented in Chapter 4 can capture the behavior of pressurized honeycomb. Since the derivation for the constant-mass and constant-pressure models are identical, a validation of one of the models provides a high confidence level in the approach that is used and, consequently, the predictive capability of the other model.

6.1   Aluminum Honeycomb Test Results

The results of the tension test are presented in Figure 6.1 and are briefly discussed. Note the abbreviations for stainless steel (ss) and carbon steel (cs) in the subfigures. Each of the subfigures represents one specimen. The thickness, material, and honeycomb angle are displayed in the title. Each graph shows the experimental results and the predicted results. The solid line shows the prediction based on the material thickness as given in the title. The other two predictions account for a 10% offset in thickness, forming the bounds of the analytic predictions. Looking at the experimental data, it can be seen that six out of the eight specimens showed consistent linear behavior. The non-linear behavior that was observed for one of the 25.4μm thick specimens and the 12.7μm thick specimen was attributed to misalignment of the top and bottom sheets that made up the specimen. This resulted in slightly twisted specimens. Since the chucks of the Instron machine did not allow for any twist, under tension this resulted in a much higher resistance to the induced displacement, causing the non-linear behavior. The linearity that was shown by the other specimen validated the linear-elastic model that was presented in Section 4.1.
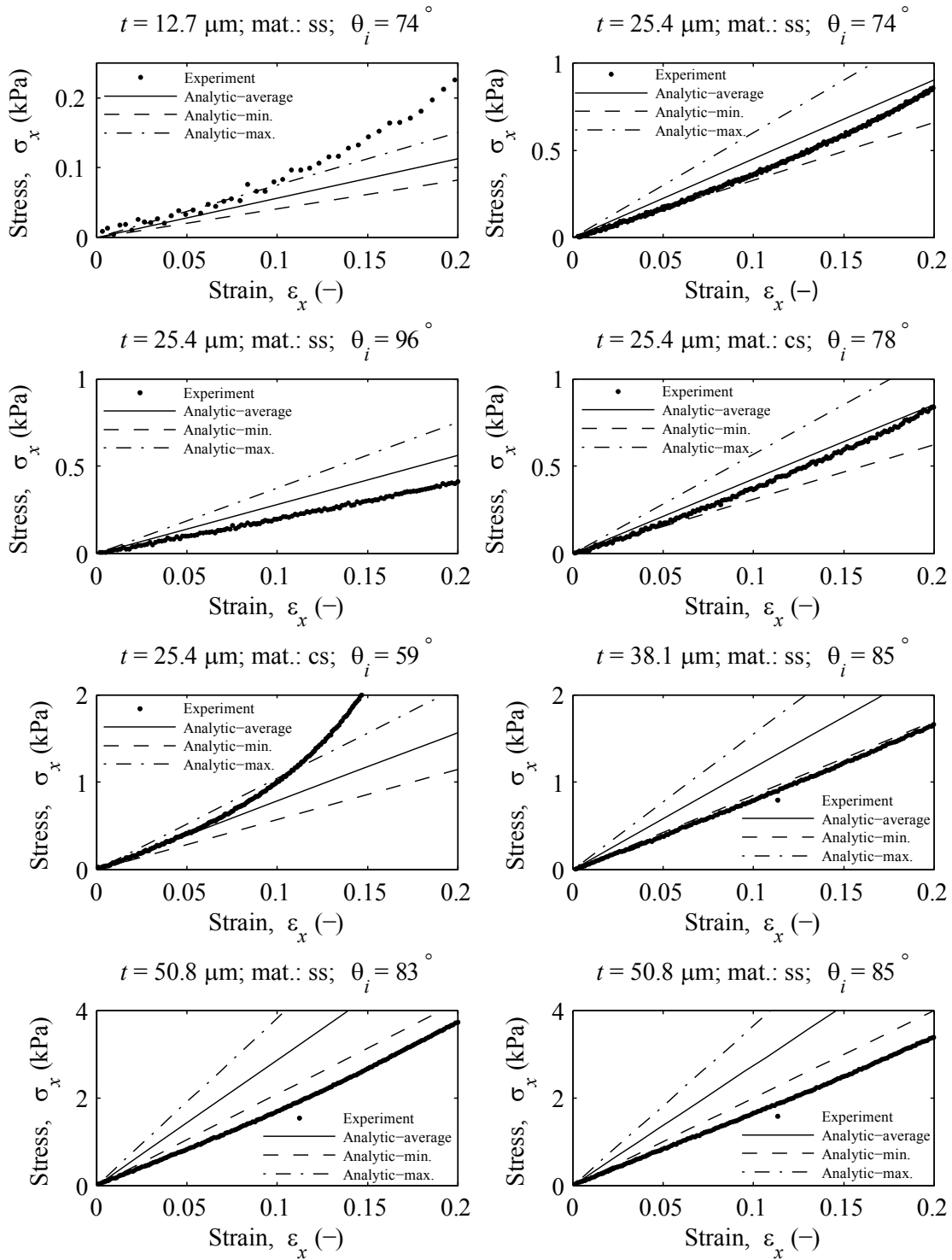
Figure 6.1   Experimental and Analytical Results for Tension Test of Steel Honeycomb

The experimental results generally fall between the predicted lower boundary and the predicted average. This shows that the analytic model of Section 0 could be used to predict the stiffness of the honeycomb structure. However, because of its sensitivity to sheet thickness the model should rather be used to predict a range of possible stiffnesses that can be expected. The 50.8μm specimens deviate beyond the predicted bounds and show a lower stiffness than expected. The reason for this lay in the fact that the top and bottom faces (which were assumed to stay undeformed in the analytic model) bent under the tensile load. Stiffening these faces even further could result in a closer correlation between experiment and analytic prediction.

6.2   Single-Cell Rigid-Member Pressurized Honeycomb

The goal of the single-cell experiment was to demonstrate the stress-strain relationship of pressurized honeycomb and to see how it correlated to the analytic model presented in Section 4.2. In addition, the single-cell experiment allowed for a test setup where tension and compression could be induced in one single run, without altering the boundary conditions. The rigid walls in this experiment were in agreement with the assumptions in the analytic model.

6.2.1 Longitudinal Compression-Tension Results and Correlation

The results of this experiment are presented in Figure 6.2. The CDPs that head each of the individual graphs are averages over the CDPs that were measured during the experiment. The y-axis of each of the graphs displays the relative stress, σ_x/p, where both σ_x and p were measured simultaneously during the experiment. The reason for doing this lies in the fact that the non-linear prediction (Eqs. 4.38 and 4.39) needs the CDP as an input to predict the stress. Since the pressure was not constant during the experiment, this resulted in a somewhat noisy prediction, especially at lower CDPs. Since this was deemed misleading, it was decided to divide both the experimental results and the analytic prediction by the CDP. By doing so, the experimental results consisted of pure experimentally obtained data, while the analytic prediction was totally independent of the experiment. This allowed for a better comparison between model and experiment at the various CDPs.
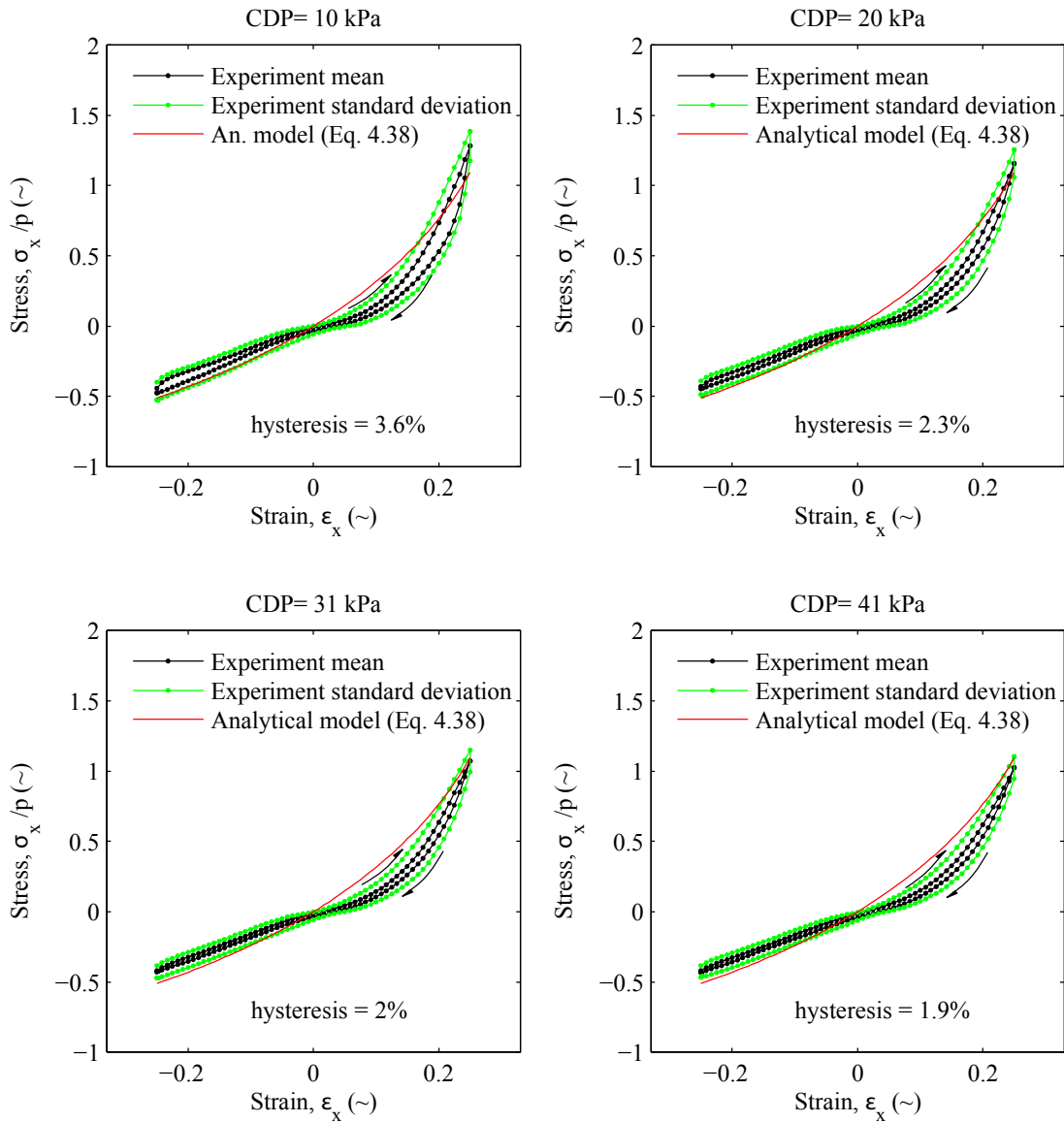
Figure 6.2   Results for Longitudinal Compression-Tension Tests

Each of the graphs in Figure 6.2 displays non-linear analytic prediction and the linearized analytic prediction. The theory of Section 4.2 was employed to create these predictive curves. It can be seen that the non-linear prediction is good over the entire set of CDPs, except for 5kPa. Correlation in the negative strain realm was better than in the positive realm. A possible explanation for the relatively flat plateau in the experimental curves is the fact that there could have existed some slop between the inflated pouch and the honeycomb wall. This

would have resulted in a delay in the onset of the pressure stiffness of the structure, which explains the discrepancy between the theoretical and experimental results.

6.2.2 Lateral Compression-Tension Results and Correlation

From the data obtained during the lateral test, the stress-strain relationship could be deduced. This is displayed in Figure 6.4. It can be seen that the model gives a fairly good prediction in the negative strain realm at CDPs beyond 30kPa. The experimental results did not show as much nonlinearity as the analytic model did. A possible explanation for this could be the fact that the faces of the honeycomb specimen were not as rigid as assumed in the model. As can be seen in Figure 6.3, bending in the top and bottom faces of the specimen could have lead to non-uniform loading over the span of the specimen as well as non-uniform displacement. This could be the source of discrepancy between the analytic model and the experimental results at higher strain values.
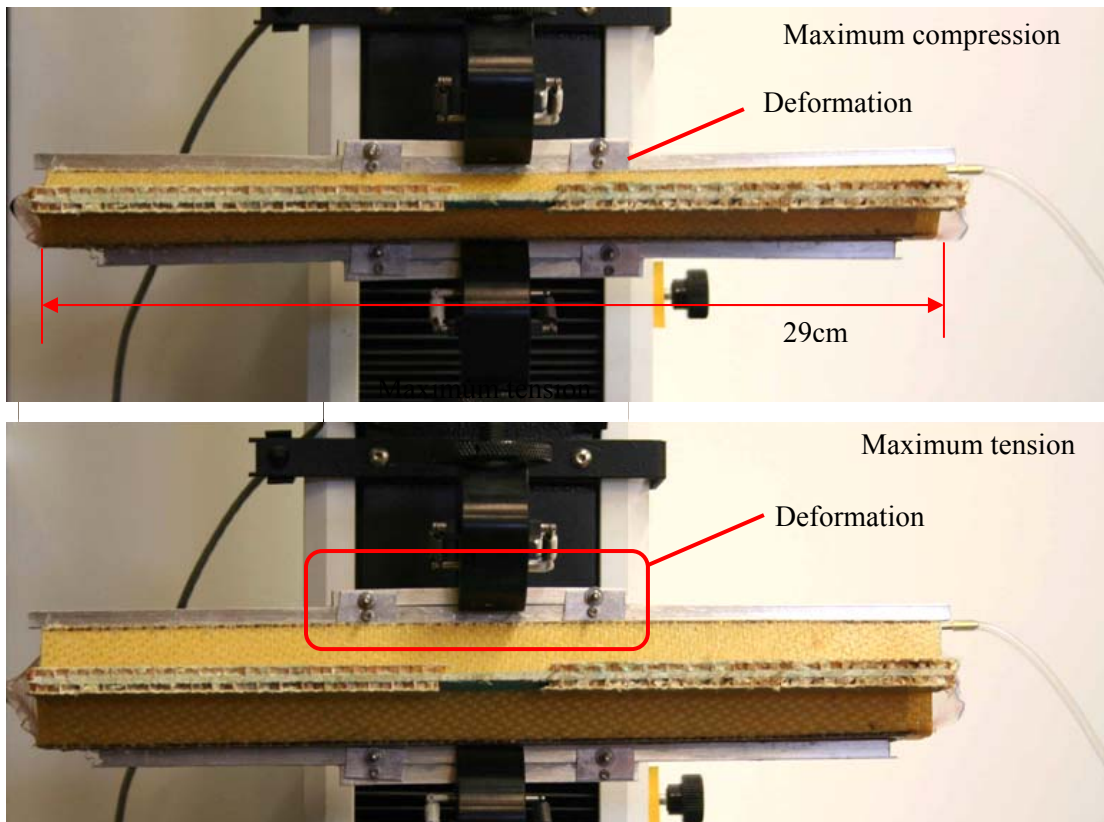
Figure 6.3   Deformations in Boundaries During Loading
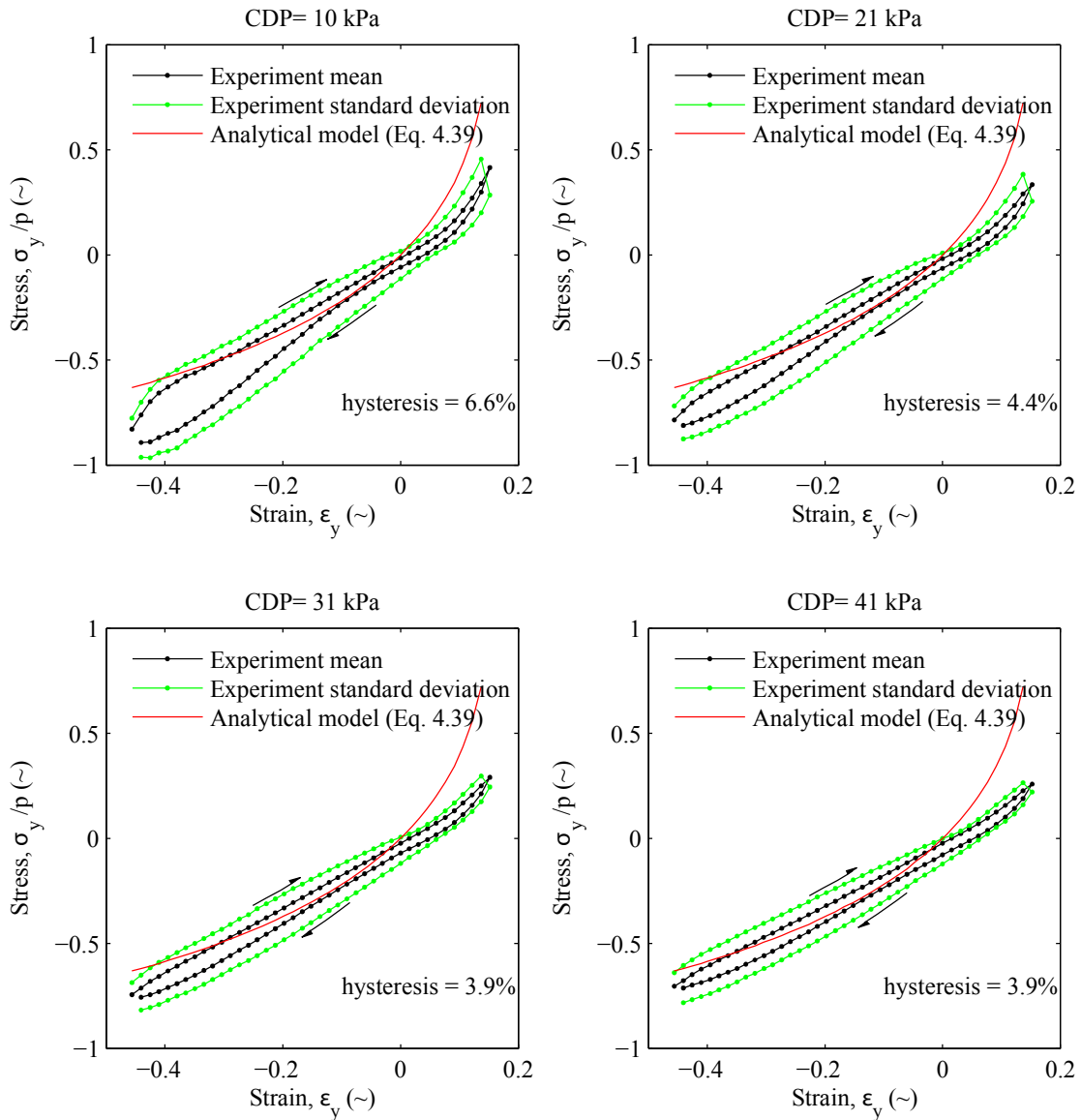
Figure 6.4   Results for Lateral Compression-Tension Tests

6.2.3 Hysteresis

Hysteresis is the amount of energy that is dissipated by the system as it performs mechanical work. For actuation purposes hysteresis is an important parameter because it shows how much of the invested energy can be regained when the system returns to its initial position. In its initial state, pressurized honeycomb consists of perfectly hexagonal cells. An applied load can induce a deformation. When the load disappears, the honeycomb returns to its initial state. However, in trying to do so, energy is dissipated because of friction between the pouch-

es and the honeycomb cells and, in this case, friction in the hinges of the honeycomb cells. Because of the lower energy availability the system does not completely return to its initial position.

The hysteresis was investigated during a full stroke in longitudinal direction. Figure 6.5 shows the stress-strain relations for a full compression-tension loop ranging between strains of ±30%. The difference between the upstroke and the downstroke is colored and is a visual indication of the amount of energy that is dissipated.
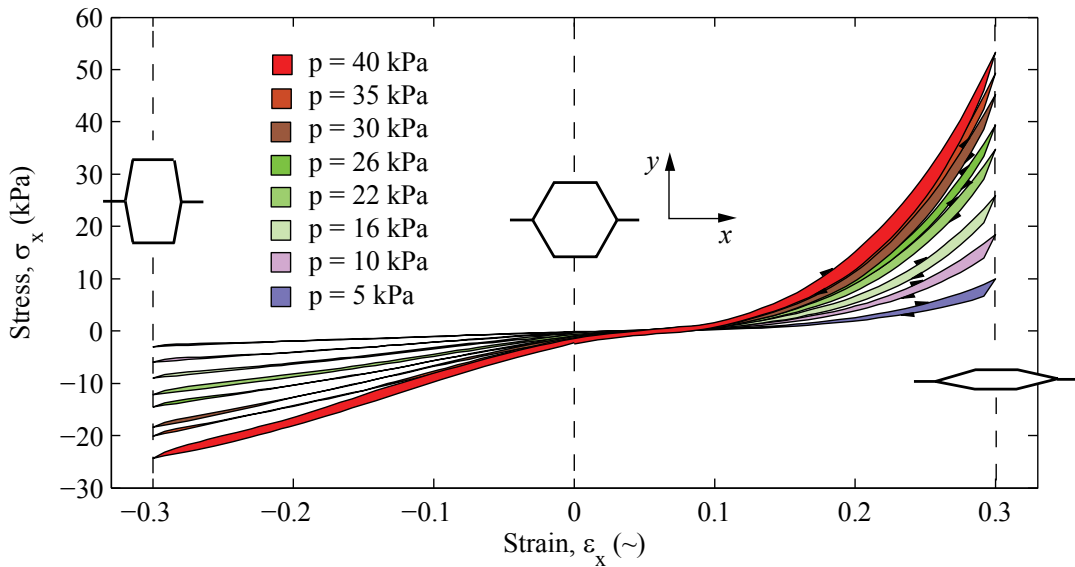
Figure 6.5   **Stress-Strain Loops in Pressure adaptive Honeycomb**

The amount of hysteresis is quantified as the area between the upstroke and the downstroke, divided by the area of the upstroke:

$$H = \left|\left(\int_0^{\varepsilon_{max}} \sigma_{down}\mathrm{d}\varepsilon \Big/ \int_0^{\varepsilon_{max}} \sigma_{up}\mathrm{d}\varepsilon\right) - 1\right| \tag{6.1}$$

Equation 6.1 was applied to the data that was obtained from the eight compression-tension experiments. At each of the four CDPs, the mean value of the hysteresis was calculated as well as the standard deviation. Figure 6.6 presents the findings of this experiment. There is a clear trend in hysteresis, in that it goes down with increased CDP. In addition, it can be seen that the hysteresis values are almost twice as large in the lateral direction as in the longitudinal direction. At 40kPa the hysteresis had decreased to 4% and 2%, respectively. It is pointed

out to the reader that this is just the hysteresis in the pressure adaptive honeycomb and that the hysteresis of the hinges has been filtered out.
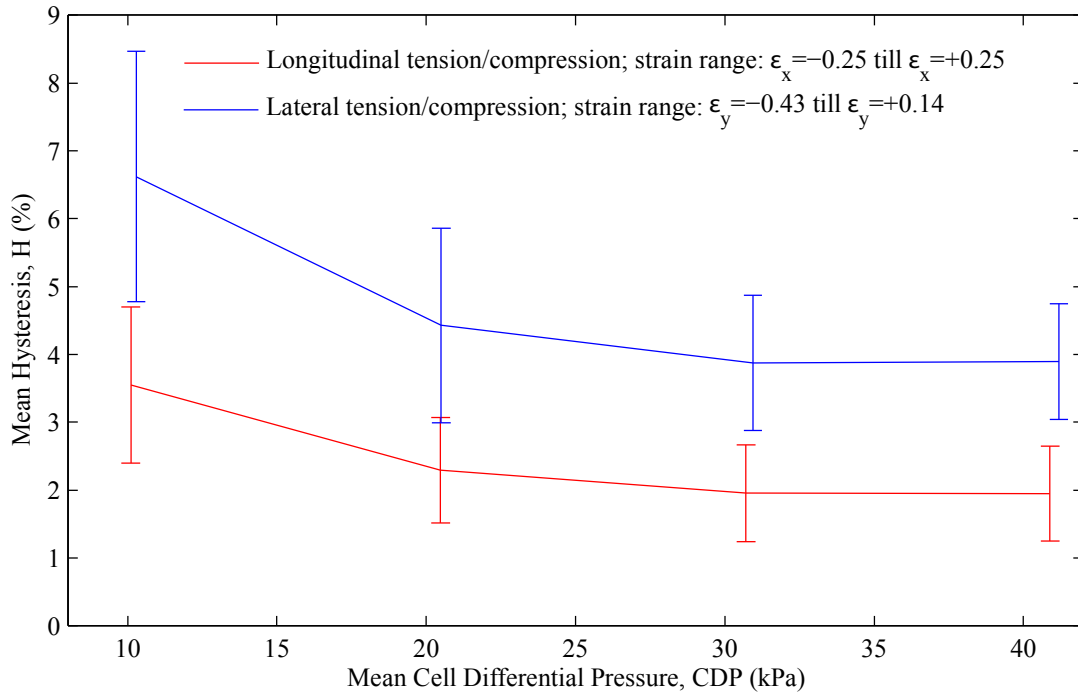
Figure 6.6   Hysteresis in Pressure adaptive Honeycomb

6.3   Multi-Cell Rigid-Member Pressurized Honeycomb

The results for the single cell experiment indicated that the analytic model predicted the stress-strain relationship quite accurately for the rigid-member honeycomb. To generalize these initial results two compression tests were carried out on a multi-cell test article. An overview of the stress-strain relations for selected CDPs is shown in Figure 6.7. Note that the CDPs that are presented in this figure are actually averages over the CDPs encountered during that specific stress-strain stroke. The irregularities in these graphs are attributed to the fact that the pressure was actively controlled during the experiment in an effort to keep it as close to the desired pressure as possible. However, some interventions resulted in relatively large changes in stiffness that caused the irregularities in the stress-strain curves. Despite those smoothness issues, the graphs give a very good indication of what is happening during pressurization of the honeycomb. It can be clearly seen that the slope of the stress-strain curves increases when the pressure increases, which means its stiffness modulus is magnified.
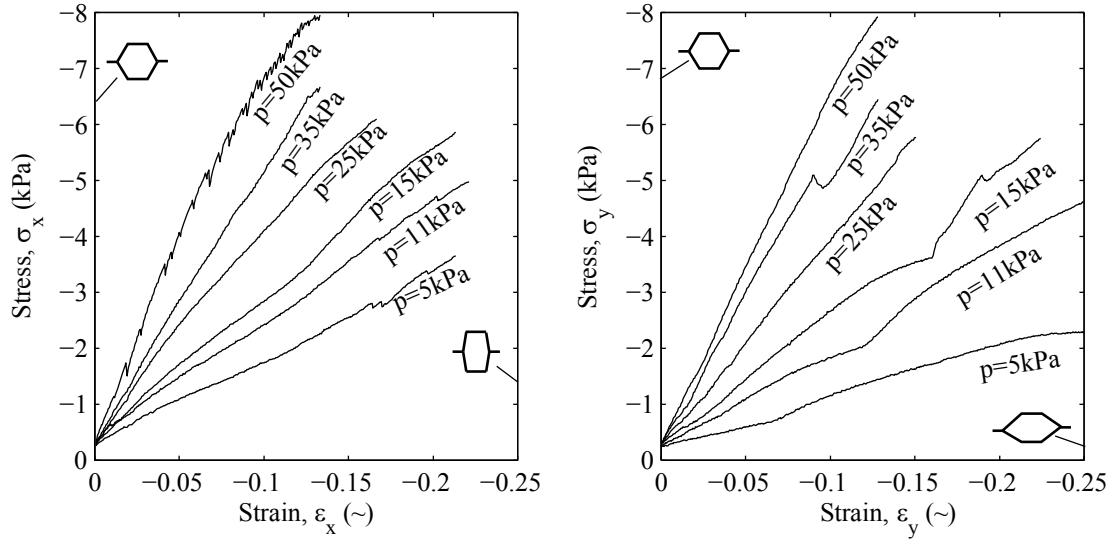
Figure 6.7   Stress-Strain Relations for Pressurized Honeycomb at Various CDPs

To compare the experimental results to the model presented in Section 4.2, the stress data from the experiment was normalized with respect to the CDP, as was done for the single-cell experiment. The stress was calculated by dividing the force by the effective area. Referring to Figure 5.8, the areas measured $156 \times 290 \text{mm}^2$ and $150 \times 290 \text{mm}^2$ for the areas perpendicular to the x and y axis, respectively. The reference volume occupied by the pouches amounted to $V_{ref} = 156 \times 150 \times 290 \text{mm}^3$. The initial volume could be calculated exactly by multiplying the number of cells, N, by their individual volume:

$$V_i = 2Nl^2 \sin \theta_i (1 + \cos \theta_i) \tag{6.2}$$

It was shown that the reference volume and the initial volume did not differ more than 1%. This validated the method of measuring the effective lengths of the honeycomb and consequently determining the reference areas that were mentioned above.

Since the non-linear model was based on the number of incremental sections (as defined in Figure 4.6), the volume considered by the model could be calculated according to:

$$V_{model} = N_x N_y l^2 \sin \theta_i (1 + \cos \theta_i) \tag{6.3}$$

Where N_x and N_y were the number of incremental sections in x and y direction, respectively. For this experiment $N_x = 6$ and $N_y = 10$. This resulted in an overestimation of volume con-

178

sidered by the model with respect to the true initial volume. The ratio between both volumes was calculated as follows:

$$\xi = \frac{V_i}{V_{model}} = \frac{2N}{N_x N_y}$$

(6.4)

Similar to the volume ratio between pouch and honeycomb (ζ), the initial to modeled volume ratio, ξ, was multiplied with the volume terms in the stress-strain equations (Eqs. 4.38 and 4.39).

6.3.1 Longitudinal Compression Results

The results of the compressive test in longitudinal direction are displayed in Figure 6.8. Although the curves are experimental, symbols are intentionally omitted in order for the reader to appreciate the difference between the predicted and experimentally obtained results. In addition, it might be observed that the lines do not start at the origin. This is because the specimen was loaded with a 10N pre-force before the testing started. At this force the displacement was zeroed. The displacement induced by this small initial load by multiplying it to the average slope of the experimental curve over the first 2% of compressive strain. At lower pressures this resulted in a higher offset in strain than at higher pressures, as can be seen from the difference between the individual subfigures in Figure 6.8.
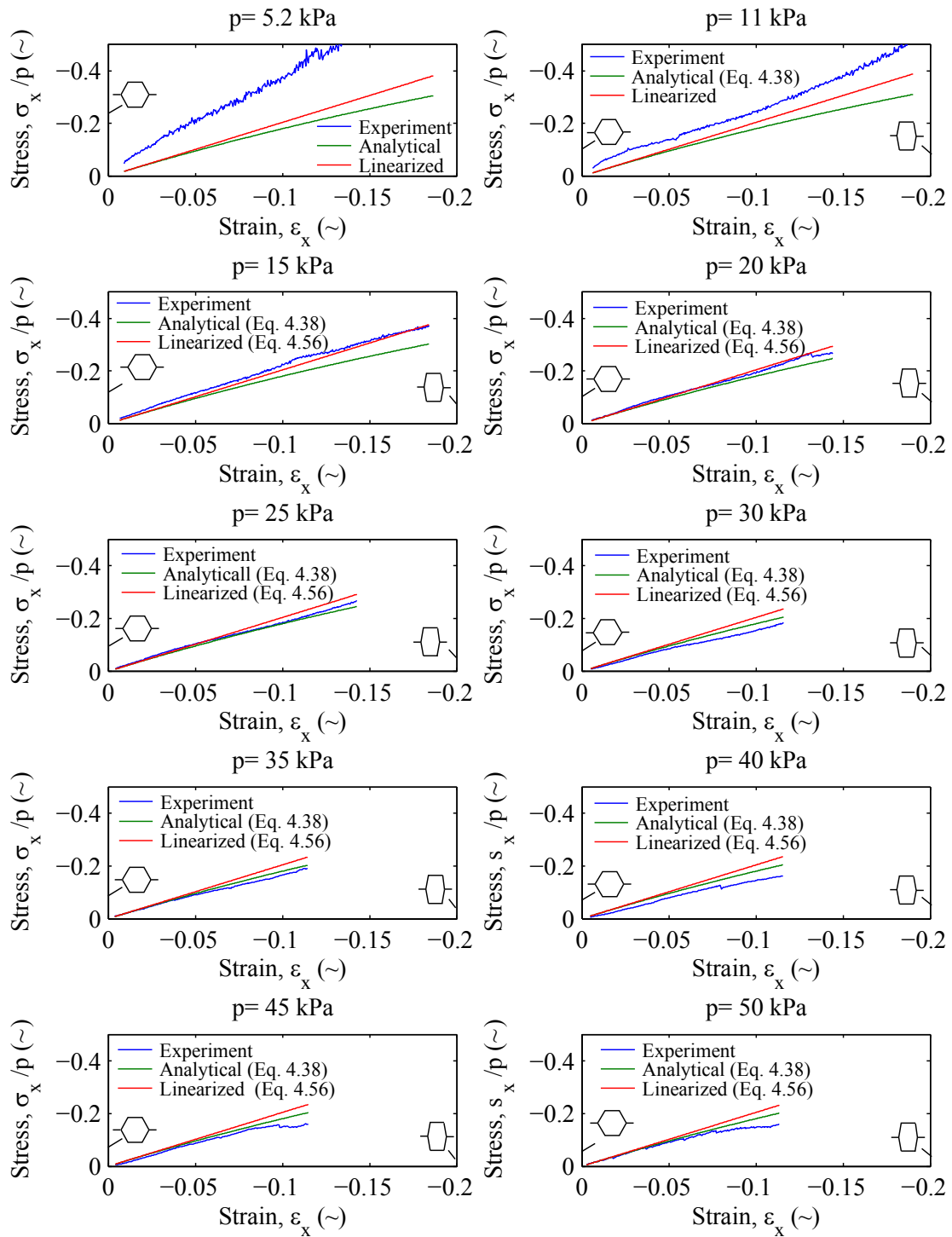
Figure 6.8   Correlation between Experiment and Theory in Longitudinal Direction

180

The graphs in Figure 6.8 generally demonstrate a good correlation between the non-linear analytic model and the experimental results in longitudinal direction. Similar to the results that were obtained for the single cell experiment, the correlation was rather poor at low CDPs (5 and 10kPa). It must be noted, however, that during this experiment the stiffness of the honeycomb structure itself contributed to the total stiffness of the system. Contrary to the single-cell experiment, this experiment, therefore, did not measure the pure pressure-induced stiffness. However, as CDP increased, the relative stiffness of the honeycomb structure diminished and the correlation between prediction and experiment improved. A remarkable close correlation up to 14% of compressive strain was obtained at 25kPa. At CDPs of 40kPa and higher the experimental results showed lower stress values beyond 7% of strain than the predicted values. One explanation for this might be that the pressure inside the pouches was in fact lower than the pressure measured by the sensor. In spite of efforts to perfectly seal all the pouches, it was found that miniscule holes existed in some of them through which, at high pressures, air was slowly leaking. At high pressures and stress, these holes might have leaked so much air that the average pressure in the structure decreased enough to induce the decrease in stiffness. The linearized model generally showed good correlation at low strains but its error with respect to the experimental data increased with strain. A linearization about a different strain point, for example half way between the minimum and maximum expected strain, could increase the overall correlation of the linearized model.

6.3.2 Lateral Compression Results

The experimental results and corresponding linearized and analytic models for the case of lateral compression are presented in Figure 6.9. Correlation between the analytic model and the experimental data is possibly even better in this direction than in the longitudinal direction. Again, it can be seen that correlation is less at lower CDPs than at higher CDPs. The linearized model over predicts the result and cannot properly capture the non-linearity in the experimental data set.
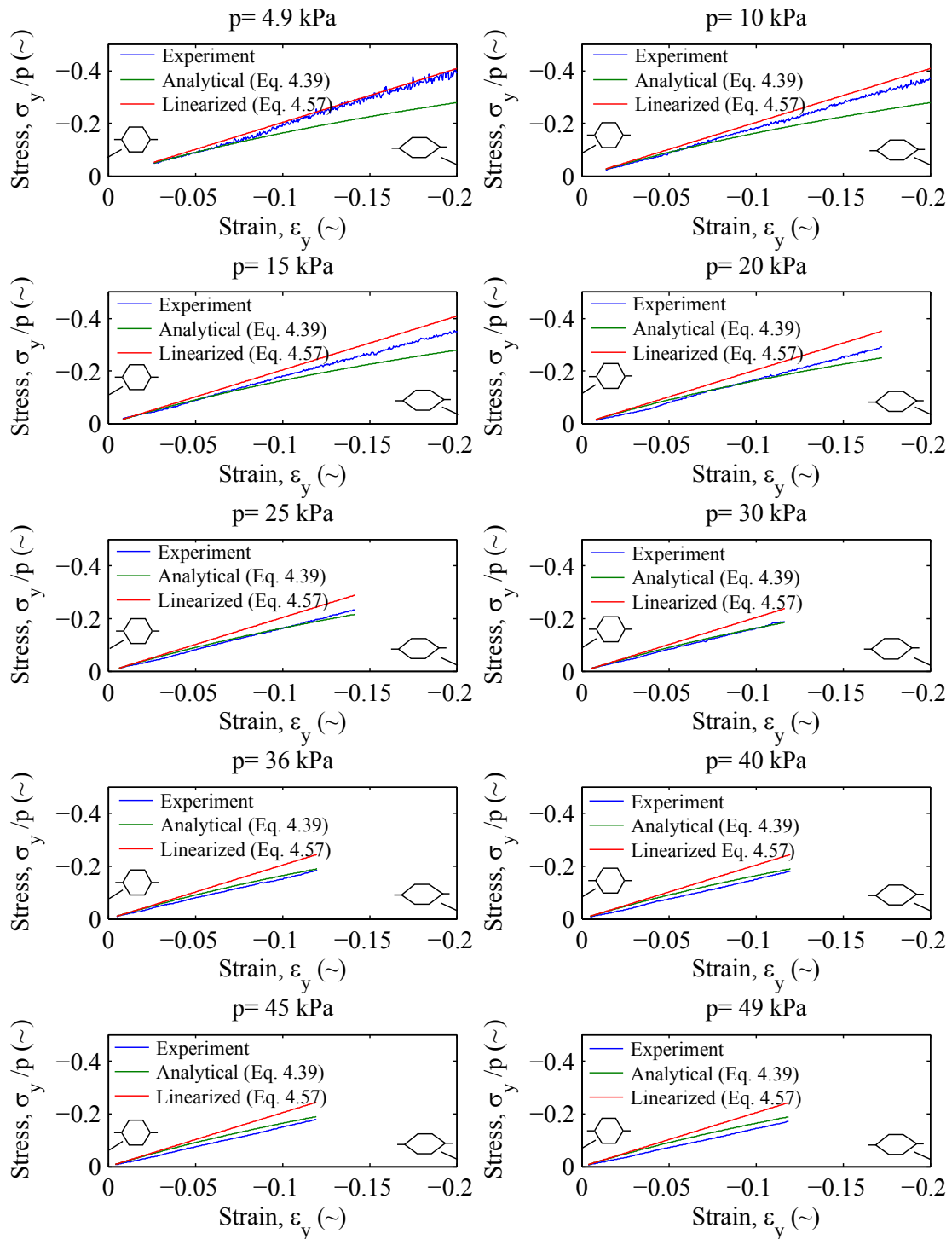
Figure 6.9   Correlation between Experiment and Theory in Lateral Direction

From these experiments it can be concluded that the findings of the single-cell experiment also hold for a multi-cell structure. It strengthens the claim that the non-linear model can properly predict the stress-strain behavior of the pressurized honeycomb. Even though the multi-cell experiment was not conducted over as wide of a range of strains, it demonstrated that the predictions were close to the actual measured data. This is a strong indication that the non-linear model can be used with confidence to predict the stiffness of pressurized honeycomb as a function of the CDP.

6.4 <u>Validation of Constant ζ Assumption</u>

The volume inside the honeycomb cell that is occupied by the pouch changes when the structure is deformed. An experiment was carried out to determine how much this volume changes with deformation. A metal hexagonal frame was produced consisting of 6 members that were hinged together, such that they formed a hexagon. A steel strip was bent to exactly fit inside the hexagon such that it touched each of the members exactly at their midpoints. The metal strip represented the pouch inside the hexagon. The frame was forced into 6 different positions, increasing the honeycomb angle between 20 and 70 degrees in steps of 10°. At every position the pouch perimeter and the internal frame bounds formed 6 triangles (one at each corner). The pouch perimeter formed one side of each of these triangles; therefore, conformal mapping was used to find the surface area. The triangular surface between the pouch perimeter and the hexagon was denoted with 6 characteristic coordinates: 3 at the corner points and 3 on the triangle members. It was assumed that the curved triangular members could be parameterized using a second order approximation. The conformal mapping technique allowed for accurate surface area predictions.

The results of this validation experiment are shown in Figure 6.10. The left hand graph depicts the variation of surface area with angular deformation. The excess area denoted in this graph refers to the area between the honeycomb and the pouch. As can be seen from this graph, the area of the pouch and the hexagon follow the same trend. The excess area is at a maximum when the honeycomb angle measures 60°. The graph on the right hand side of Figure 6.10 shows how the ratio between the pouch and the honeycomb areas changes with angular deformation. The variation of pouch volume does not fluctuate more than 7% of the total hexagon volume over the measured range. Given the trend shown in this graph, it is an-

ticipated that the total variation over the entire realm of honeycomb angles does not exceed 8%. However, since the ratio is minimized at an angle of 60° this is not perceived to be an appropriate average value. A value of $\zeta = 0.94$ would be accurate with a margin of $\pm 5\%$ over the entire realm of angular deformations. If only the realm beyond 60° is considered the change in volume ratio appears to be much smaller compared to the angles below 60°. A constant value much closer to the original value of ζ could be chosen with a lower margin.
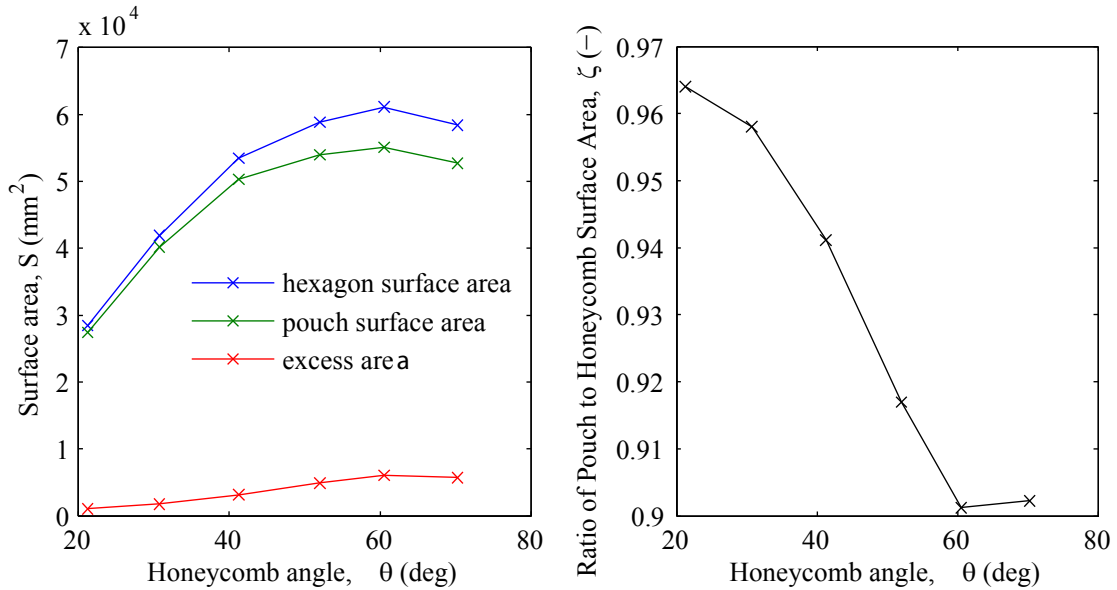
Figure 6.10   Results of Surface Area Experiment

6.5   Multi-Cell Pressurized Aluminum Honeycomb

The results presented in the previous sections demonstrated that the analytic model for pressurized honeycomb could be used to predict the stress-strain behavior of rigid-member honeycomb. In this section it is investigated if the expansion of this model to elastic honeycombs can also be used to predict the stress-strain relation of pressurized honeycomb. To that extent, three tests were carried out with a 130-cell test article (see Section 5.4.1): longitudinal compression and tension and lateral compression. Lateral tension was not carried out because it would have introduced high peel stresses on the bonded corrugated sheets that the honeycomb was made of. If debonding would have occurred the test article would have been severely damaged. The following subsections discuss the results of these experiments and their correlation to theory.

6.5.1 Longitudinal Tension Results

During the longitudinal tension test the strains were kept relatively small, because it was found that at strain levels beyond 5%, debonding between the corrugated sheets started to occur. Tests were conducted at four different CDPs and stress and strain could be deduced from the force and displacement measurements, respectively. The results of this test are presented in Figure 6.11
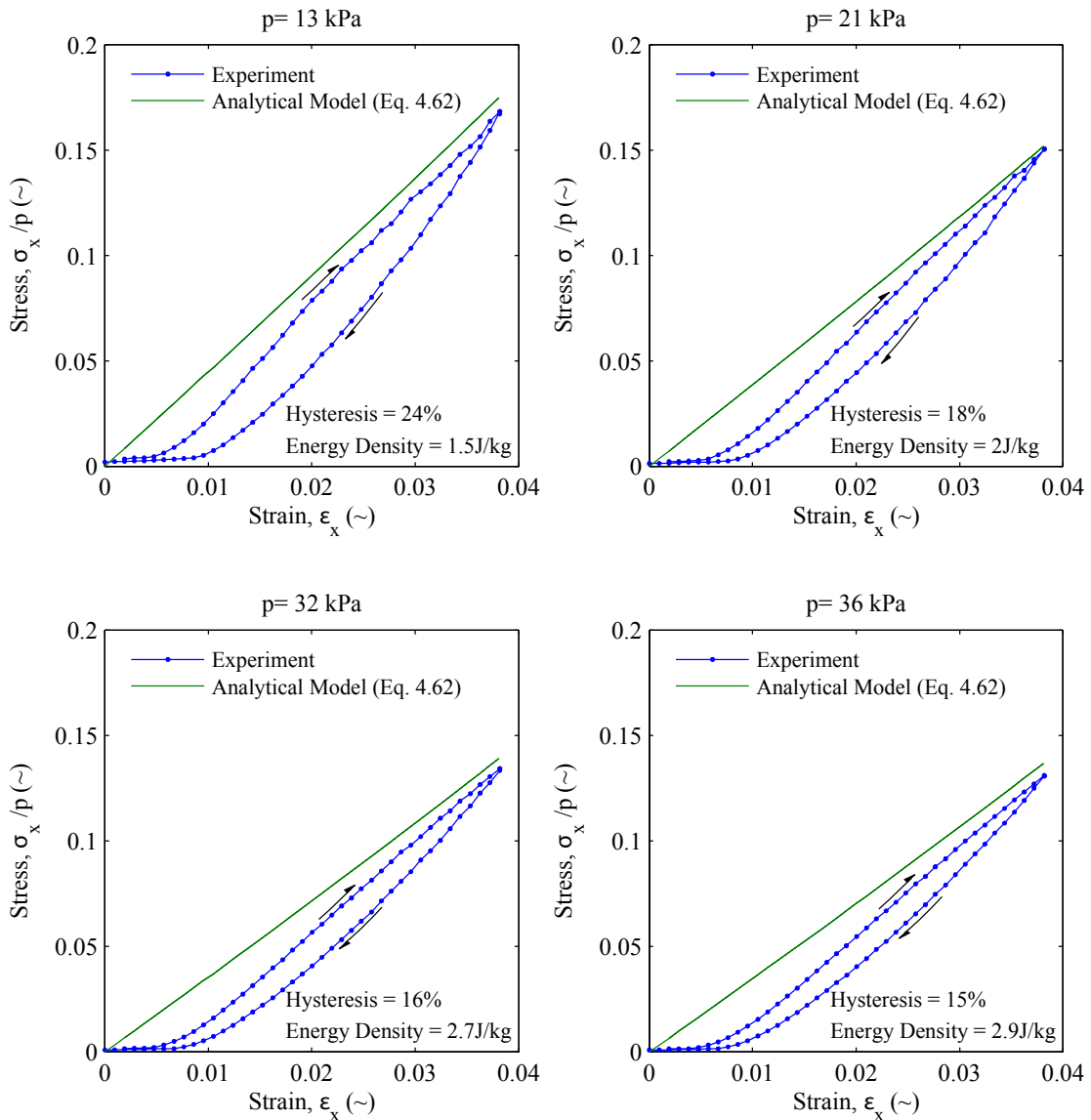
Figure 6.11   Raw Results of Longitudinal Tension Test

The most noticeable difference between the experimental results and the analytic model is the onset (where the stress remains close to zero while the strain changes). This onset was attributed to a settling phenomenon in the experimental setup. A second observation is that the slope of the experimental data was slightly steeper than what the analytic model predicted. In other words, the honeycomb was somewhat stiffer in longitudinal tension than was expected. With regards to the data obtained during the other experiments on this specimen, it could be concluded that this difference was caused by a slight difference in initial honeycomb angle, θ_i. Even though it was attemped to manufacture a honeycomb specimen with $\theta_i = 60°$, the reality was that that when no CDP was applied, the honeycomb assumed a shape with the (average) honeycomb angle being closer to 57°. This made the honeycomb somewhat stiffer when loaded in longitudinal direction and somewhat less stiff in lateral direction.

Each of the subplots of Figure 6.11 lists the energy density and the hysteresis. The energy density was calculated based on the area under the upstroke curve. Because the strains were small, the resulting energy density was not high compared to what is listed in Table 4.1. The reader is reminded, however, that the latter one is the maximum energy density, while the numbers mentioned in these plots are merely an indication of how much energy was required to induce the maximum amount of strain in the test article. The hysteresis is a measure of how much of this energy was dissipated. The same trend as in Figure 6.6 can be observed: hysteresis decreases with increasing CDP. The higher hysteresis compared to the rigid-wall experiment was attributed to the boundary conditions (slipping), friction between the pouch and the cell walls, as well as hysteresis in the honeycomb material itself.

In Figure 6.13 the nodal displacement of the finite element analysis is shown. This is to illustrate the mechanics of the honeycomb as it is loaded in longitudinal tension. The shape of the honeycomb and especially the bulging at the outer boundaries was a feature that was also observed during the experiments. The results presented in this figure were obtained by specifying a pressure on all the internal ligaments. Naturally, when pressure is applied at both sides of a ligament, there is no net effect in terms of displacement. An internal ligament of a pressurized honeycomb specimen, therefore, shows the same nodal displacement as an unpressurized honeycomb specimen. However, at the outer most ligaments one can see that the pressure causes the ligaments to form an arc.
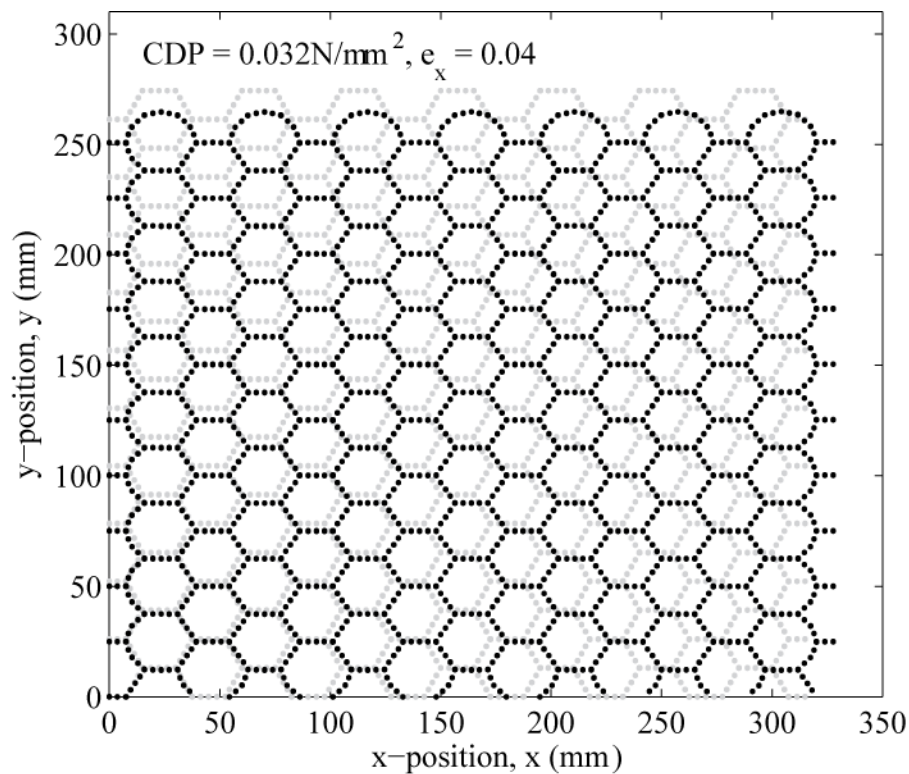
Figure 6.12   Nodal Displacements as Calculated by FEA at Maximum Prescribed Strain

6.5.2 Longitudinal Compression Results

The longitudinal compression test on the honeycomb did not suffer from the strain constraints that were limiting during the tension test. The limiting factor in this experiment was the maximum force that the Instron could provide (~2500N). Based on preliminary experiments at ~40kPa, the resulting maximum compressive strain at this force was set at 12.5%.

In Figure 6.13 the experimental stress-strain data is presented alongside the analytic prediction based on Equation 4.62. In addition, a third curve representing the finite element analysis is added. The next paragraph discusses the latter results. First, the reader is asked to compare the experimental results to the analytical model. It can be observed that the experimental curve shows a slightly steeper curve than the analytic model. This was also observed in the results of the tension test and was attributed to a small alteration in honeycomb angle. The overall shape of both curves is very similar and the analytical model could certainly be used to give a good prediction of the stress-strain relation in longitudinal compression.
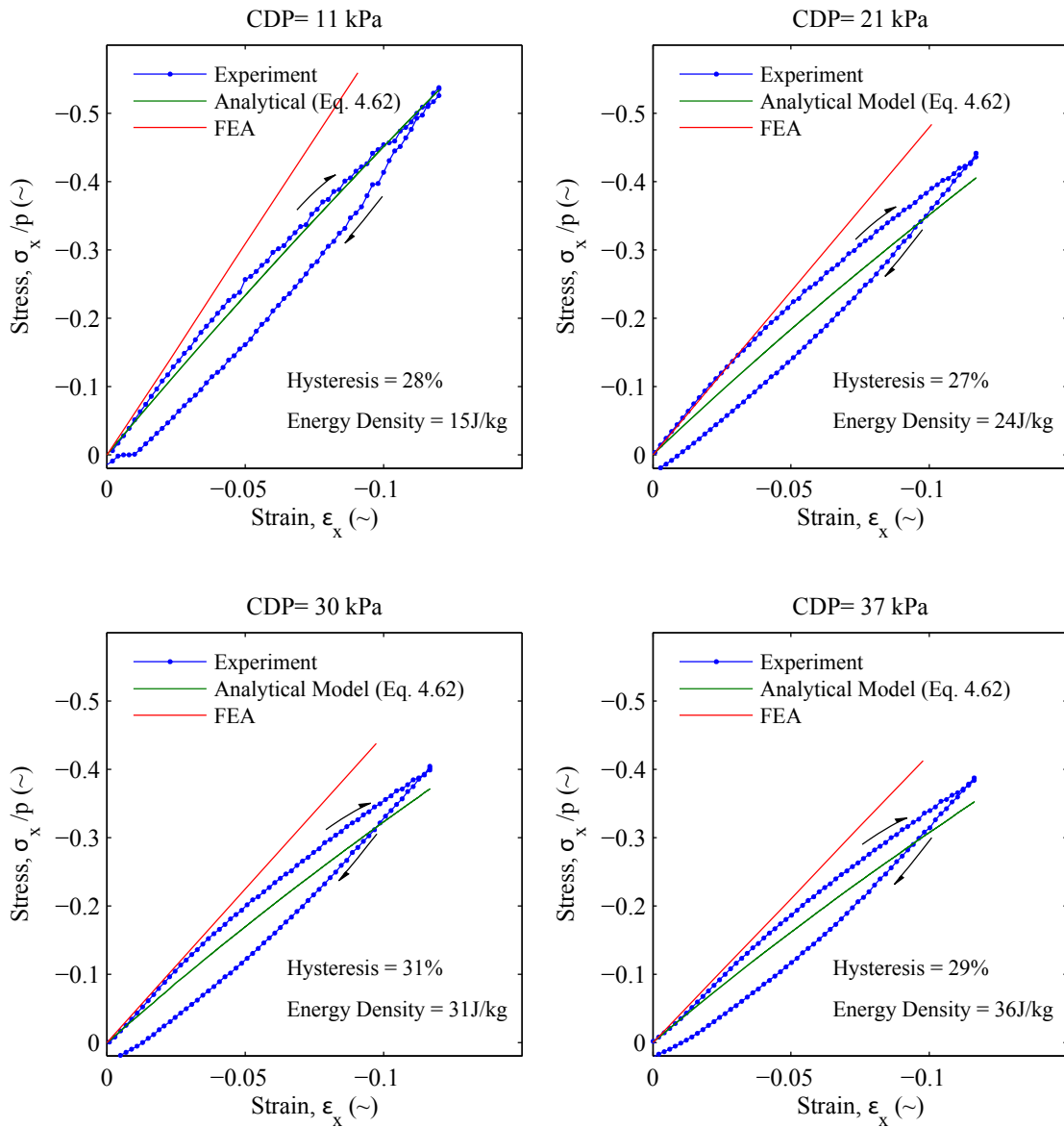
Figure 6.13   Results for Longitudinal Compression Test

The FEA curve in Figure 6.13 needs more explanation because this curve is not based on a physical model of the pressure adaptive honeycomb but relies on a homogenized, pressure-dependent material stiffness (as was explained in Section 4.5.4). In the present case, the material stiffness was extracted from the experimental results. The following steps were taken:

1. An average slope was determined of the upstroke stress-strain curves of Figure 6.13 by using a linear least squares fit. This resulted in a value of E_x at each of the 4 CDPs.

2. The CDP-E_x relation was plotted and linearly interpolated. At CDP = 0, the resulting $E_x = E_x^*$ (see Eq.4.6) was enforced, such that the stiffness of the pressurized honeycomb would degenerate to the stiffness of the plain, unpressurized honeycomb at zero CDP.

3. The resulting linear relationship between pressure and stiffness was correlated to an equivalent material stiffness via Eq. 4.79. Because this equivalent material stiffness was extracted from an the longitudinal compression experiment, it was conveniently denoted with E_{lon}. The following linear relation resulted: $E_{lon} = (9.71 \cdot 10^6)(p - p_a) + 70 \cdot 10^3$ [N/mm^2].

4. At each experimental CDP the resulting value of E_{lon} was inserted into the FE input file and the simulation was run with the externally applied loads and boundary conditions as presented in Figure 4.33. The resulting overall strain, ε_x, is what is plotted in Figure 6.13.

In summary, it can be stated that the FEA curves shown in Figure 6.13 are based on the experimental results in the same plots. It can be seen that this line forms a tangent to the experimental curve and is linear. The linearity is expected because the stress-strain relation was linearized in order to find a constant value of the stiffness. The discrepancy between the FEA and the experimental results can be attributed to the linearization of these relations as well as to the slight difference in honeycomb angle between what was assumed in the simulations and what was tested during the experiment. To give an impression of the cell deformations under the compressive strain, Figure 6.14 shows the nodal displacements as calculated by FINESSE.

$$CDP = 0.037 N/mm^2, e_x = -0.12$$
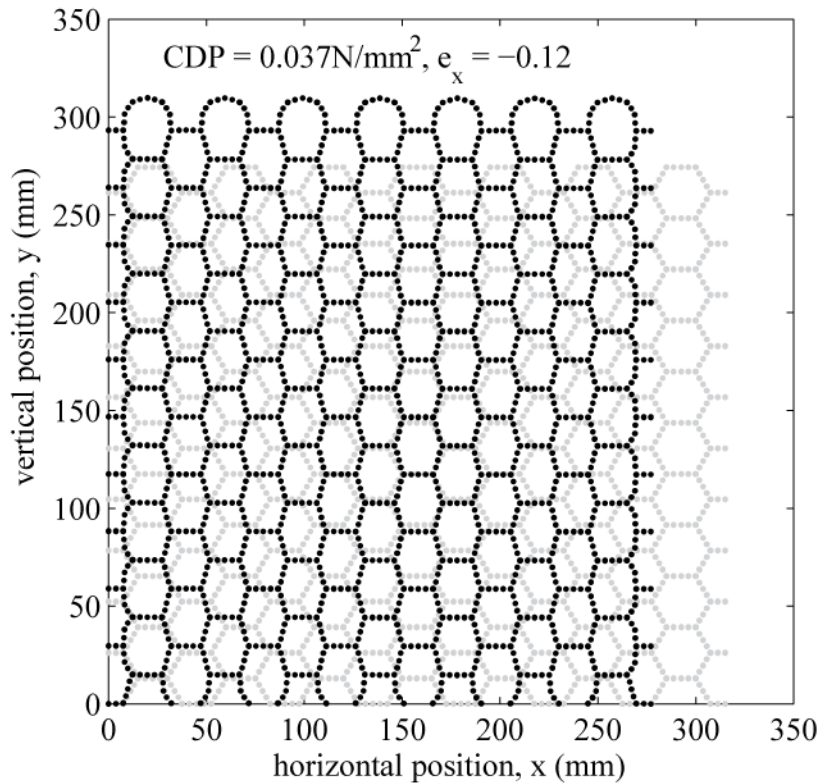
Figure 6.14 **Nodal Displacements as Calculated by FEA at Maximum Prescribed Strain and Maximum CDP**

6.5.3 Lateral Compression Results

The same 130-cell specimen was also tested in lateral compression. In Section 5.4.2 the experimental setup of this test can be found. In the case of lateral compression, the maximum compressive strain amounted to 16%. In Figure 6.15 the experimentally obtained stress-strain relationship can be seen along with the analytical prediction and the finite element analysis. It can be seen that there is quite a good correlation between the analytic model and the upstroke of the experimental results. In this case, the analytic model (Eq. 4.63) overpredicted the stiffness of the pressure adaptive honeycomb. This was attributed to the slight difference in honeycomb angle between theory and experiment. However, in general the model gave quite a good prediction of the stress-strain relation over a relative wide range of pressures and strains.
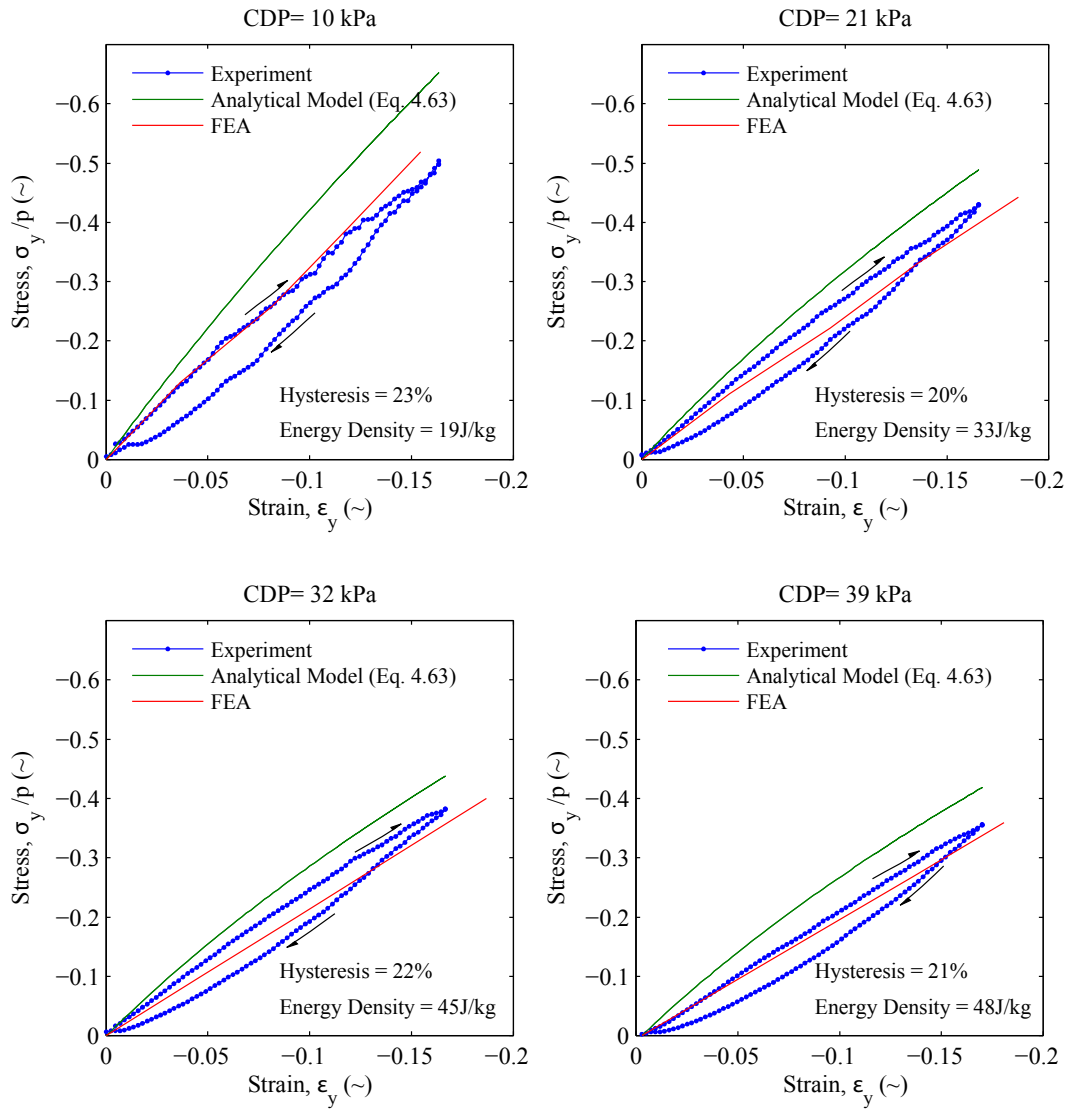
Figure 6.15   Results of Lateral Compression Test

The FEA prediction in Figure 6.15 was obtained by using the same step-by-step sequence as was laid out in the previous section for the case of longitudinal compression. In the present case a different linear relationship between the equivalent material stiffness and the CDP was obtained. With E_{lat} denoting the equivalent stiffness based on the lateral compression experiment, this relation was $E_{lat} = (5.31 \cdot 10^6)(p - p_a) + 70 \cdot 10^3$ [N/mm^2]. This equivalent stiffness was, in turn, substituted for the material stiffness of the honeycomb in the finite element analysis. With the constraints and loading as prescribed in Figure 4.32, the FEA resulted in the red line in Figure 6.15. As can be seen, the simulated stress-strain relationship is much

closer to the experimental data than for the case of longitudinal compression. It is thought that the reason for this lies in the fact that the latter stress-strain relation displayed a higher degree of nonlinearity than in the present case. The present lateral stress-strain relationship can be linearly approximated with a smaller least-squares error. It can be seen that the FEA line is virtually tangent to the experimental stress-strain curve as was the case for the longitudinal compression. In conclusion, Figure 6.16 gives an impression of the cell deformation during compressive loading. It shows the nodal displacement as calculated by FINESSE.
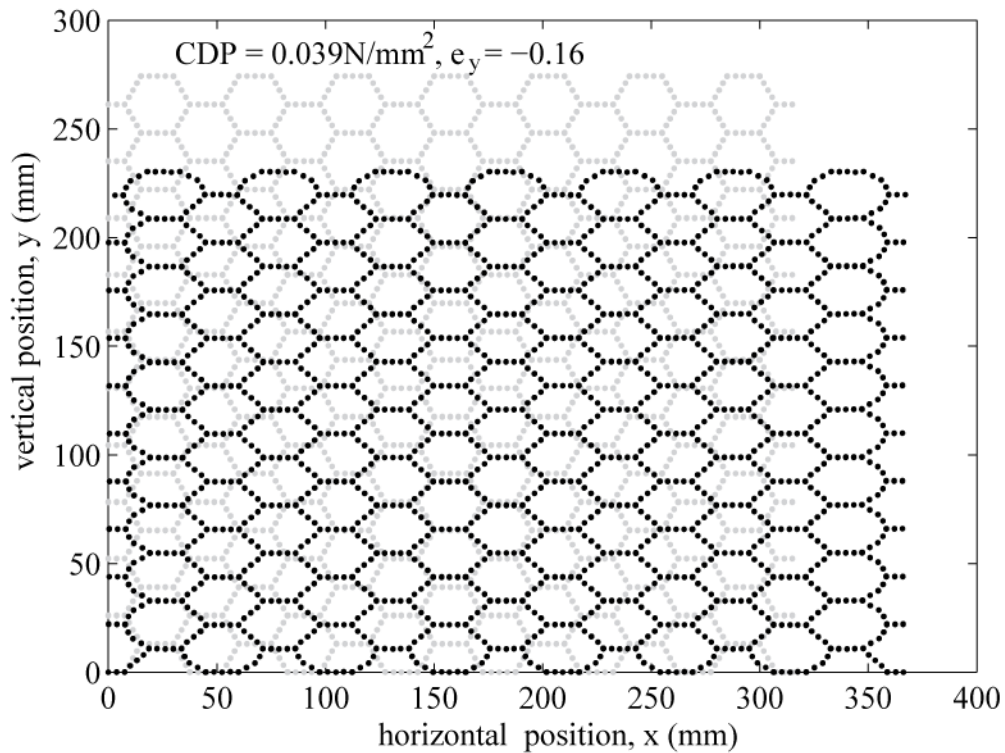
Figure 6.16 **Nodal Displacements as Calculated by FEA at Maximum Prescribed Strain and Maximum CDP**

6.5.4 Three-Point Bend Test

The longitudinal and lateral compression tests were used to establish a relationship between the equivalent material stiffness of the honeycomb and the CDP. To test if such an empirically obtained relationship could be useful in a more complex application of pressure adaptive honeycomb, a three-point bend test was carried out (see Section 5.4.5). A point load was distributed over a small area around the center of the test article. This force introduced a curvature in the beam, which was simply supported. A simulation of this experiment was con-

192

ducted by using a finite element analysis of the test article and the same loading and boundary conditions as during the experiment. Because the bending in the beam caused the cells to be compressed in longitudinal direction, the empirically obtained relation for the equivalent material stiffness (E_{lon}) was used in the calculations of FINESSE. In addition, the FEA with equivalent stiffness (E_{eq}) based on the linearization of the analytical model was investigated as well. The results of the experiment and finite element analyses are shown in Figure 6.17.
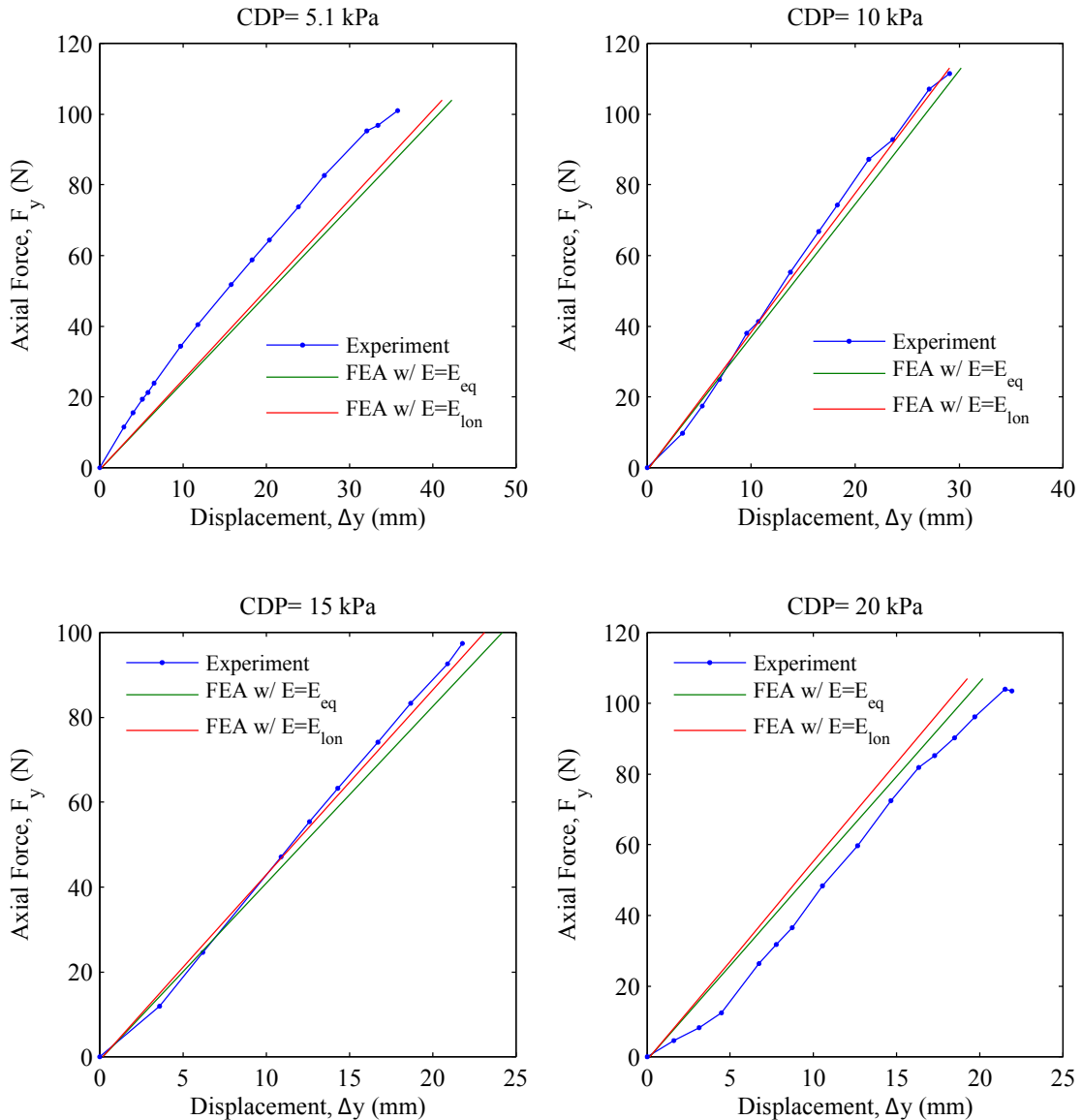
Figure 6.17   Results of Three-Point Bend Test and Correlation to FEA Results

From Figure 6.17 it can be observed that the correlation of the experimental results to the FEA-generated results is very good. Both FEA lines are very close because the linear equivalent-stiffness relation that was extracted from the results of the longitudinal compression test were in fact very close to what was predicted based on the linearization of the analytic model about the 60-degree honeycomb angle. From these experiments it can be concluded that the finite element analysis with the empirically obtained stiffness gives a very good approximation of the mechanics of pressure adaptive honeycomb and can be used with confidence in a finite element analysis of more complicated geometries. In addition, the present results also suggest that the linearization of the analytical model and the subsequent equivalent stiffness calculation also leads to a good prediction of the overall mechanics of pressure adaptive honeycomb (in this case). However, subsequent tests on a variety of different test articles should be carried out to confirm that this finding is true for any case.

In conclusion, Figure 6.18 demonstrates the nodal displacement of the honeycomb specimen during loading. It can be seen how the top row of cells displays the most deformation, while the shape of the bottom row remains almost unaltered. It is also pointed out that the cells at the outer most left and outer most right also show little to no deformation. This is mainly caused by the fact that there is no boundary enforced at either side. A gradual increase in deformation towards the center of the specimen can be observed, with maximum deformation taking place in the center cells of the top row.
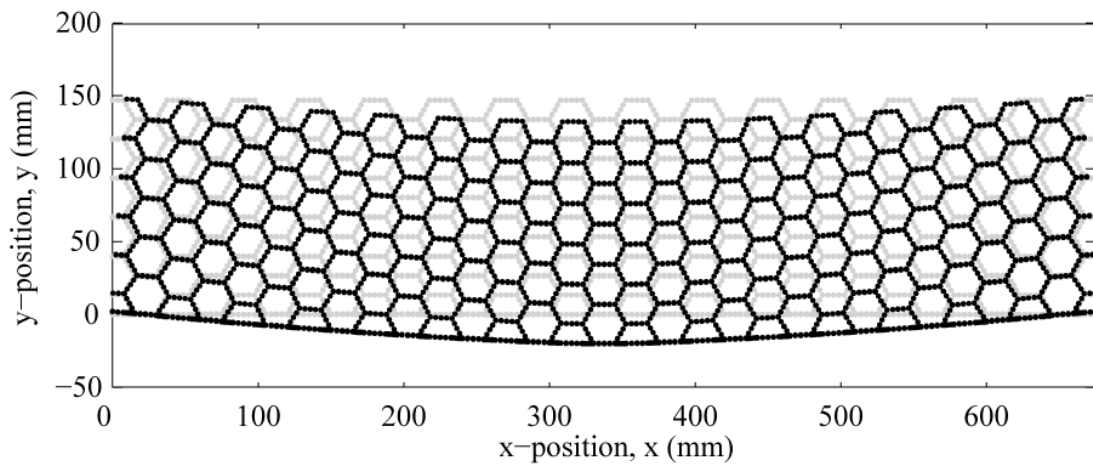
Figure 6.18   Nodal Displacement for F_y = 107N and CDP = 20kPa

The most strained honeycomb cells within this entire structure were the center cells in the top row of this test article. These cells showed 5% strain in longitudinal direction and 6% strain in lateral direction. The loading direction of these cells is predominantly in the longitudinal direction. If the reader recalls Figure 4.19 it can be seen that the linear stress-strain theory is still valid at 20kPa CDP and a longitudinal strain of 5%. However, it is evident that when higher finite strains are to be encountered, the present linear model (which forms the basis of the equivalent stiffness model) does not suffice. A more elaborate piecewise linear model can be formulated by changing the equivalent stiffness modulus as a function of the strain. This would, in turn, give a better approximation of the nonlinear stress-strain relations of pressure adaptive honeycomb.

6.5.5 Damaged Honeycomb

In light of possible damage to the honeycomb when in service, an experimental investigation was conducted to determine the effect of deflated pouches on the overall performance of the honeycomb. The same test setup was used as for the lateral compression test (see Section 5.4.2). A reference CDP of 30kPa was chosen for this test. The first benchmark test was done with all the pouches being fully inflated. In the subsequent tests the CDP was dropped to zero in randomly selected pouches up to a maximum of 5.4% of all the pouches. The compression test was carried out and force and displacement were recorded, translated to stress-strain values, and plotted in Figure 6.19. A brief discussion follows.

As can be seen from the top left plot in Figure 6.19, the benchmark test closely correlates to the analytical model. In subsequent plots the analytic model is plotted as a reference to the reader. The first observation that is made when looking at the plots of the test article with deflated cells is that there was an increased amount of onset strain. This meant that while the specimen strained, the stress hardly changed. This onset strain increased with a higher percentage of deflated cells. This was attributed due to the fact that with the few deflated cells, the specimen re-adjusted itself by disproportionally straining the walls of the deflated cells. Therefore, only the stiffness of the aluminum honeycomb was encountered, which was significantly lower than the stiffness of the inflated honeycomb.

The second observation that can be made is that the slope of the stress-strain curved became shallower with increased number of deflated cells. This was expected based on the lower total inflated volume of the honeycomb (see Eq. 4.25).
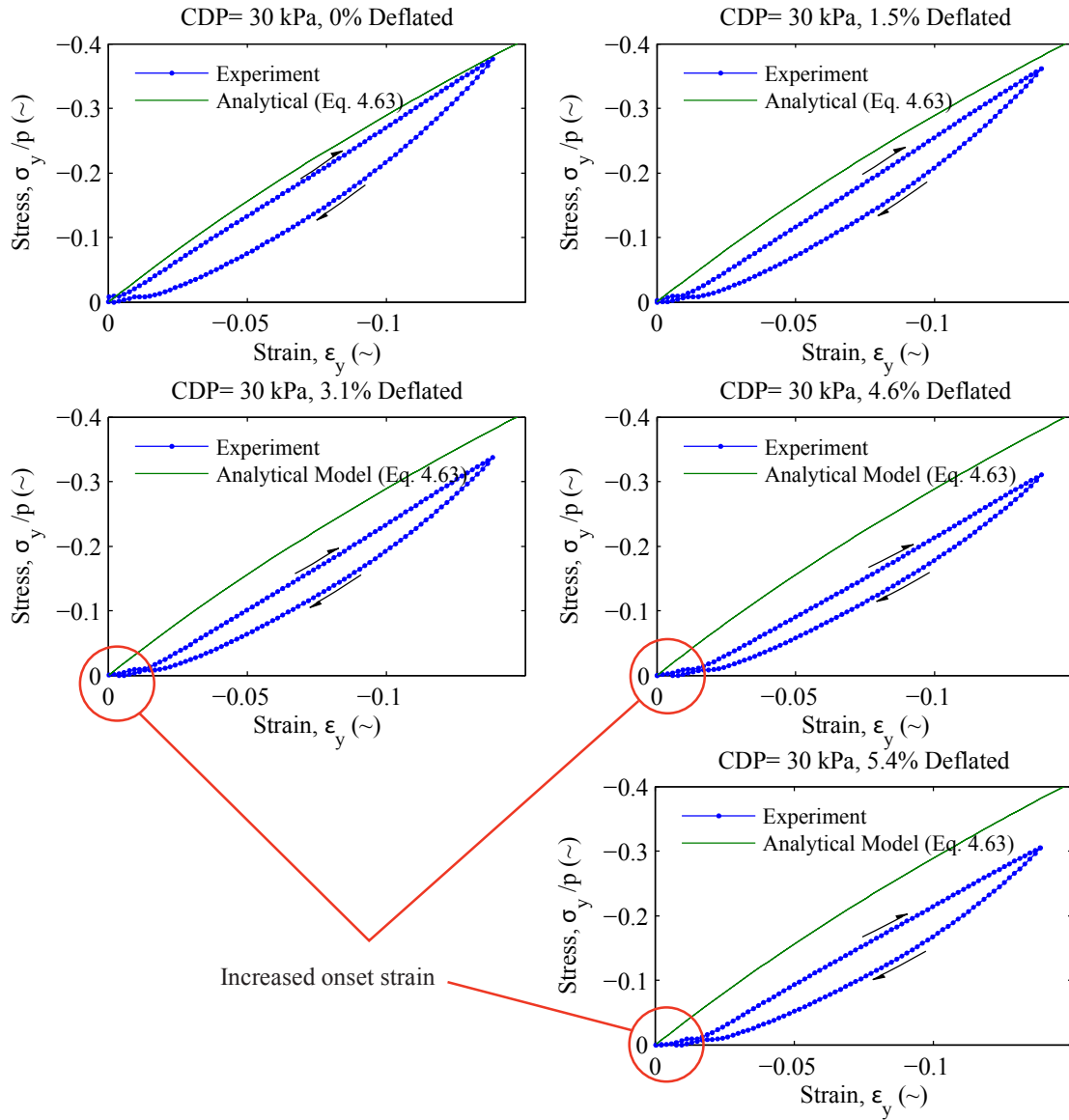
Figure 6.19   Stress-Strain Curves for Randomly Damaged Honeycomb Cells

6.5.6   General Discussion and Lessons Learned

During the set of experiments a few general observations were made that could be beneficial for future investigations into pressure adaptive honeycomb. The first observation was the ex-

perimental results are very sensitive to the geometry and (relative) dimension of the test article. For example, the honeycomb angle should be very accurately induced in the sheet metal and preferably be the same in every fold. This was not always the case in the for the test articles that were used for these experiments, which might have been a cause for the difference between the predictions and the experimental results.

Another example is the relative dimension of the pouch with respect to the cell. Both should be manufactured such that the pouch forms a perfect circle within a perfect hexagon when inflated. In that case, there exist no peel stresses on the bonded corrugated sheets that make up the honeycomb. However, if the pouches are made a little to big, they attempt to form a circle which is larger than the honeycomb can allow. The peel stresses that are thus created are easily large enough to tear apart the individual layers of corrugated sheets. Conversely, if the pouches are made slightly too small, there occurs a small range of strains where the pressurized honeycomb has very low stiffness (similar to what is pointed out in Figure 6.19). Accordingly, the margin of error in fabricating the pouches and the honeycomb should be kept very small in order to obtain good results without damaging the test article.

In line with the previous observation, it was also noted that bonding two corrugated sheets together is not the most optimal way of constructing a honeycomb grid for pressure adaptive honeycomb. The adhesive (in this case Hysol 9412) could not provide the adequate strength to prevent debonding during a combination of high external loading and high CDP. Figure 6.20 shows an example of debonding that took place on the 145-cell rectangular test article at a CDP of 25kPa. Based on this observation, it is advised to use an alternative way of constructing the honeycomb grid. A possible alternative is to stitch the two corrugated sheets together using Kevlar thread. This would significantly increase the peel strength of the bonded corrugated sheets and make the structure more robust.
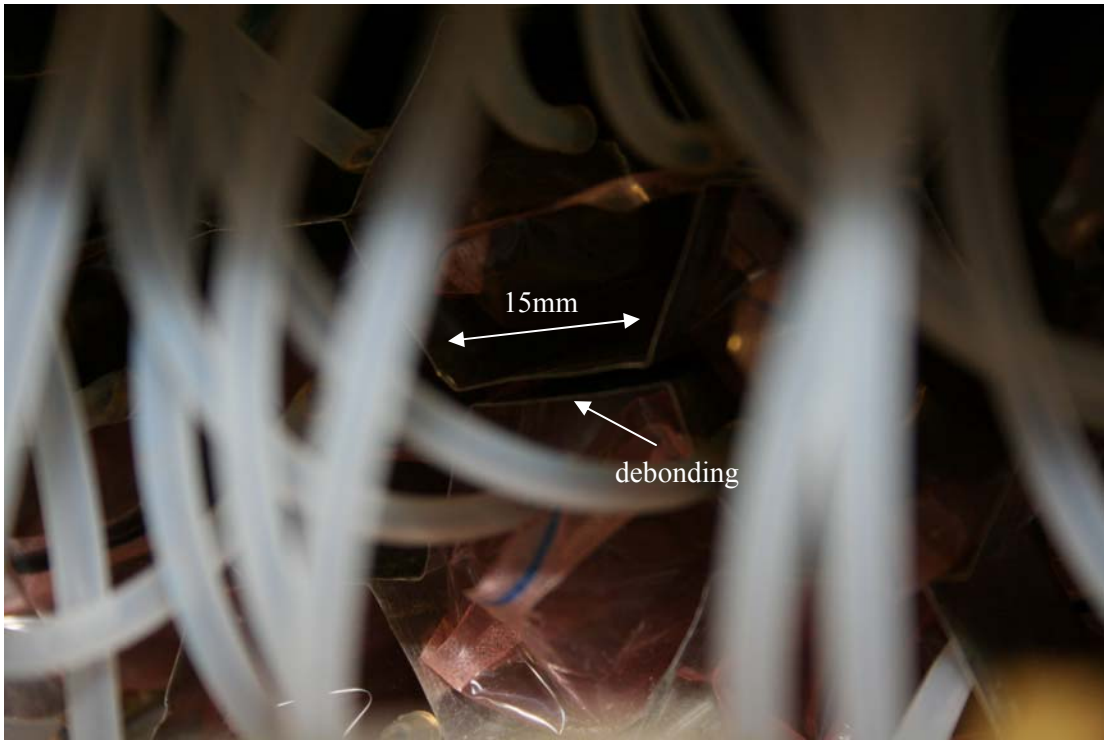
Figure 6.20   Debonding of Corrugated Sheets Due to High Peel Stresses

6.6   Pressure Adaptive Flap in Wind Tunnel

In Section 5.5 the experimental setup of the wind tunnel model was presented. The goal of this test was to demonstrate how a pressure adaptive flap could alter the gross aerodynamic performance of the wing. This, in turn, would prove that pressure adaptive honeycomb could be successfully used in an aerospace application to induce gross changes in performance. This section details the results of the test and how they were corrected for wind tunnel boundary conditions. During the test three variables were introduced: cell differential pressure (CDP), angle of attack, and free-stream velocity (or Reynolds number). To analyze the effects of each of these, the same data is presented in two subsequent sections: first at a constant angle-of-attack and secondly at a constant Reynolds number. These sections are preceded by a section on wind tunnel wall corrections and followed by a closing section about the general lessons that were learned from this experiment.

To put the results in perspective, Figure 6.21 and Figure 6.22 show the aerodynamic coefficients for a NACA 2412 section. The geometry of the wind tunnel model was based on this airfoil. The first 64% of the model was identical to the 2412, while the shape of the (re-

tracted) flap deviated due to manufacturing imperfections. However, the values presented in Figure 6.21 and Figure 6.22 function as a reference for the wind tunnel data that is presented in the following sections.
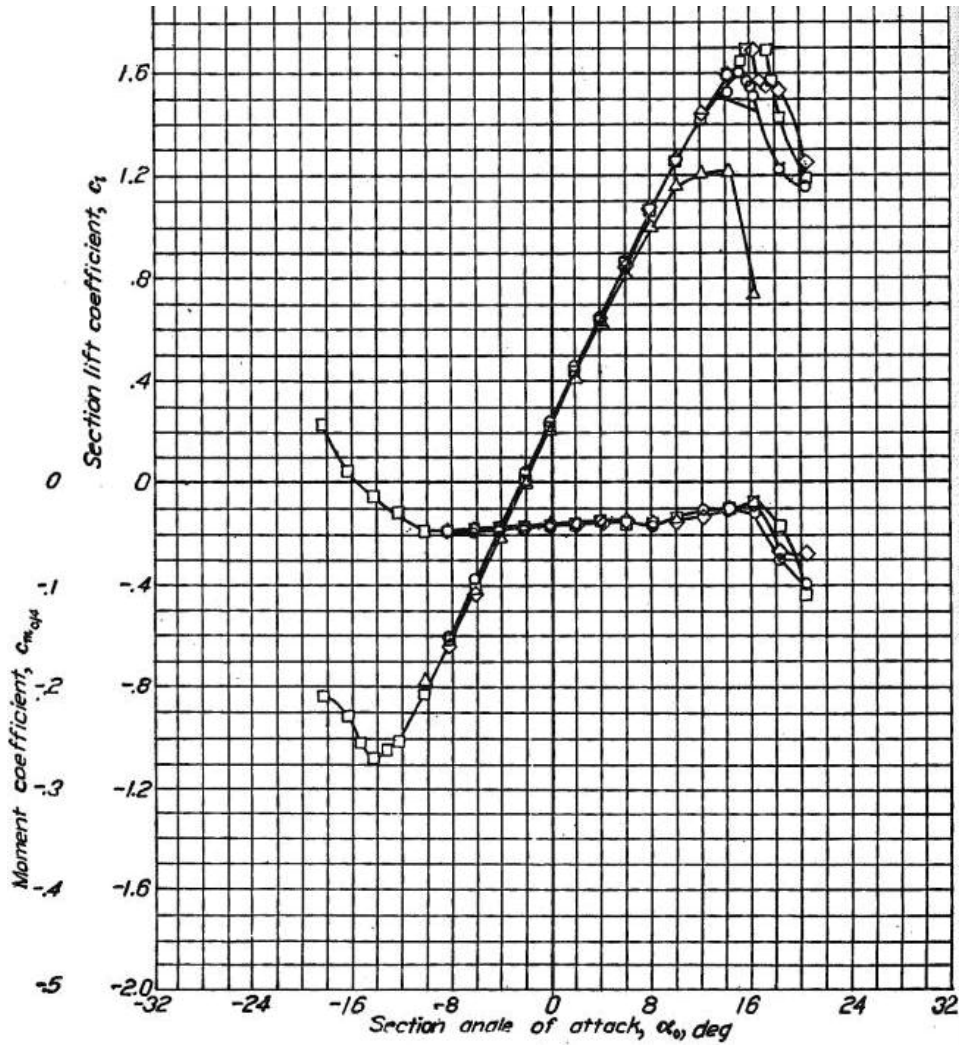
Figure 6.21   NACA 2412 Section (Copied from p. 478 in Ref. 47)
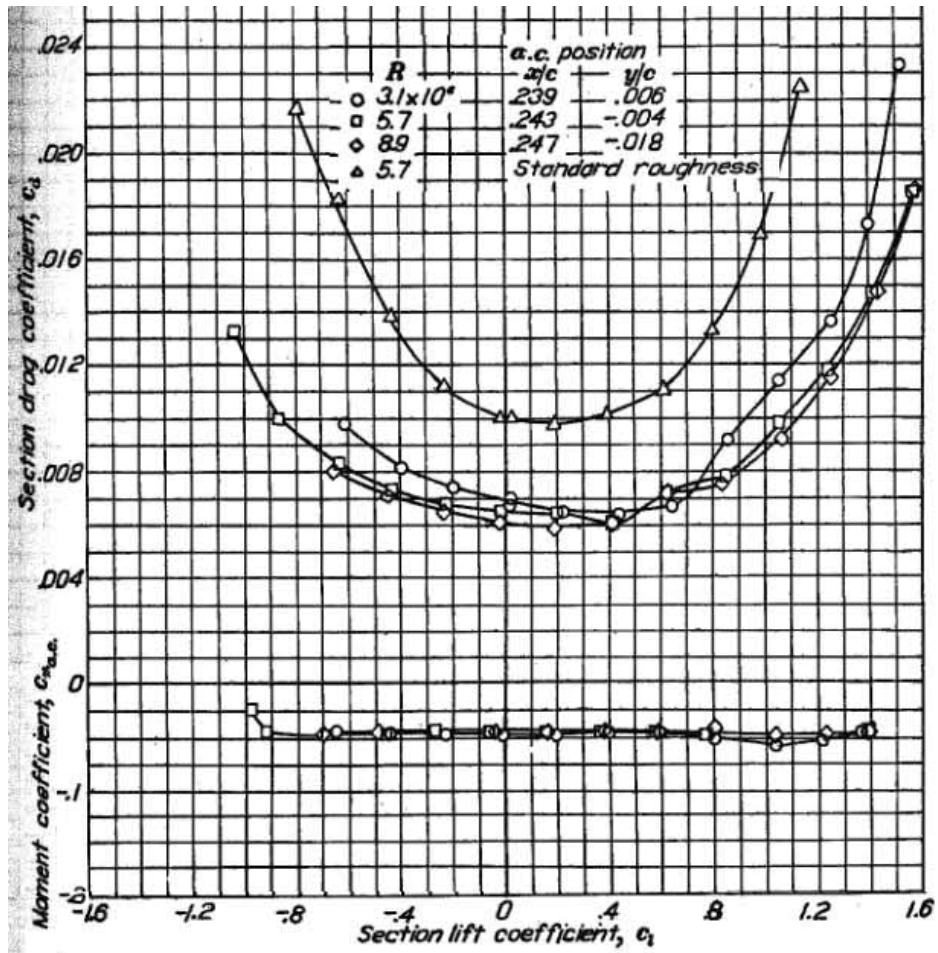
Figure 6.22   NACA 2412 Wing Section (Copied from p. 479 in Ref. 47)

6.6.1 Raw Data and Wall Corrections

The raw data that was taken during the wind tunnel experiment is presented in Appendix C.
From the raw data, the aerodynamic coefficients of the wing section were determined. Since
the model was sandwiched between two large end plates it was assumed that there was essen-
tially no flow around the edges of the wing (two-dimensional flow). The uncorrected (sub-
script u) lift, drag and moment coefficient were calculated according to:

$$c_{lu} = \frac{2L}{\rho V_u^2 S} \tag{6.5}$$

$$c_{du} = \frac{2D}{\rho V_u^2 S} \tag{6.6}$$

$$c_{mu} = \frac{2M}{\rho V_u^2 Sc} \tag{6.7}$$

Where ρ, V_u, L, D, and M were recorded during the experiment. The uncorrected data needed to be corrected for wind tunnel boundary effects. There were multiple effects that the wind tunnel model encountered that were different from free-flight conditions. There was a buoyancy effect that altered the drag force, a solid blockage effect, and a wake blockage effect that altered free-stream velocity and all aerodynamic coefficients. In addition there was a streamline effect that altered the effective angle of attack. The buoyancy and wake blockage effects were not included in the evaluation of the results. To determine the additional drag caused by buoyancy, the static pressure decay over the wind tunnel wall needed to be measured. This was not done during the experiment and the buoyancy could therefore not be accurately calculated. The wake blockage effect relied on the value of the uncorrected section drag coefficient. This coefficient was not measured accurately in this test setup due to the addition of the end plates and the poles of the test stand. The added friction and pressure drag of those items gave an overestimated value of the drag force. Because the resulting drag coefficient was unreliable an accurate determination of the wake blockage coefficient could not be obtained. The solid blockage coefficient (ε_{sb}) was calculated as follows (see Ref. 144):

$$\varepsilon_{sb} = \Lambda\sigma \tag{6.8}$$

In this equation Λ was the body shape factor according to Allen and Vincenti which was determined from Figure 9.17 in Ref. 144 and amounted to 0.24 for a NACA 2412 airfoil. The value of σ was constant and was based on the wind tunnel height (h) and the wing chord:

$$\sigma = \frac{\pi^2}{48}\left(\frac{c}{h}\right)^2 \tag{6.9}$$

Since it was decided that only the solid blockage effects would be taken into account, the total blockage coefficient equaled the solid blockage coefficient:

$$\varepsilon = \varepsilon_{sb} \tag{6.10}$$

Following the approach laid out in Ref. 144 the following flow parameters were calculated with solid blockage accounted for:

$$V = \varepsilon_{sb}(1 + \varepsilon) \tag{6.11}$$

$$Re = Re_u(1 + \varepsilon) \tag{6.12}$$

$$c_l = c_{lu}(1 - \sigma - 2\varepsilon) \tag{6.13}$$

$$c_d = c_{du}(1 - 3\varepsilon_{sb}) \tag{6.14}$$

$$c_m = c_{mu}(1 - 2\varepsilon) + \frac{1}{4}\sigma c_l \tag{6.15}$$

In addition to blockage effects, the fact that the wind tunnel was in place had an effect on the streamlines of the flow. The presence of ceiling and floor prevented the normal curvature of the free air that occurs about any lifting body. Relative to the straightened flow at the floor and ceiling, the body therefore appeared to have more camber than it actually had. From simple vortex theory it could be deduced that this resulted in an increased angle of attack (see Ref. 144). The resulting angle of attack (in degrees) was:

$$\alpha = \alpha_u + \frac{57.3\sigma}{2\pi}(c_{lu} + 4c_{mu}) \tag{6.16}$$

The previous equations were used to determine the corrected wind tunnel data. It has been shown that they work very well as long all conditions of a two-dimensional test are fulfilled. In this case, not all those requirements were fulfilled. For example, the end plates that were used did not span the entire height of the tunnel. In the correction theory it is assumed that these end plates were the same as putting the model between the two vertical tunnel walls. Obviously, there was a discrepancy between what the theory assumed and what actually happened during the test. It is therefore likely that the blockage coefficient that was calculated is overestimated by the theory. Also, there existed a small ~2mm gap at either side between the flap and the end plates. This small slot ensured that the flap could travel freely up and down without being constrained by the end plates. However, it also allowed for some air to flow from the bottom of the model to the top side. Due to these effects, the reader is cautioned that the results that are presented in the following sections should be evaluated with these considerations in mind.

6.6.2 Results at Constant Angle of Attack

The results presented in Figure 6.23 represent best how the wind tunnel experiment was carried out. More specifically, the angle of attack was set, a wind speed was set, and the pressure

was increased with increments of 10kPa. This figure demonstrates how the lift coefficient varied with CDP. It can be observed that the change in lift coefficient was much greater for the lowest Reynolds number than for the highest Reynolds number. Deflation of the flap from 40kPa down to 0 resulted in an increase of c_l of approximately 0.3 for a Reynolds number around 1×10^6. At a Reynolds number of 2×10^6 this changed to $\Delta c_l \approx 0.15$. These values can be seen across the entire range of angles of attack. The main reason for the decrease of Δc_l with Reynolds number lies in the fact that the aerodynamic forces increased with a factor of four while the CDP and elastic forces in the flap remained unchanged. In other words, the elastic and CDP forces did not scale with the airspeed. During the test at 61kts the higher aerodynamic forces caused the (elastic) flap to flex upwards. Since the maximum flap deflection was merely a balance between the elastic forces in the skin and the aerodynamic forces acting on the skin, it was evident that higher aerodynamic forces would change the geometry of the flap.

Each of the plots in Figure 6.23 shows generally the same behavior: a decrease in lift coefficient with increased CDP and a decrease in lift coefficient with increased Reynolds number. However in the last plot (23 degree angle of attack) it can be seen this latter trend is disturbed at higher CDP. This behavior was attributed to flow separation which is likely to have occurred at this high angle of attack. Flow separation at the lowest Reynolds number explains the lower lift coefficient compared to those at higher Reynolds numbers.
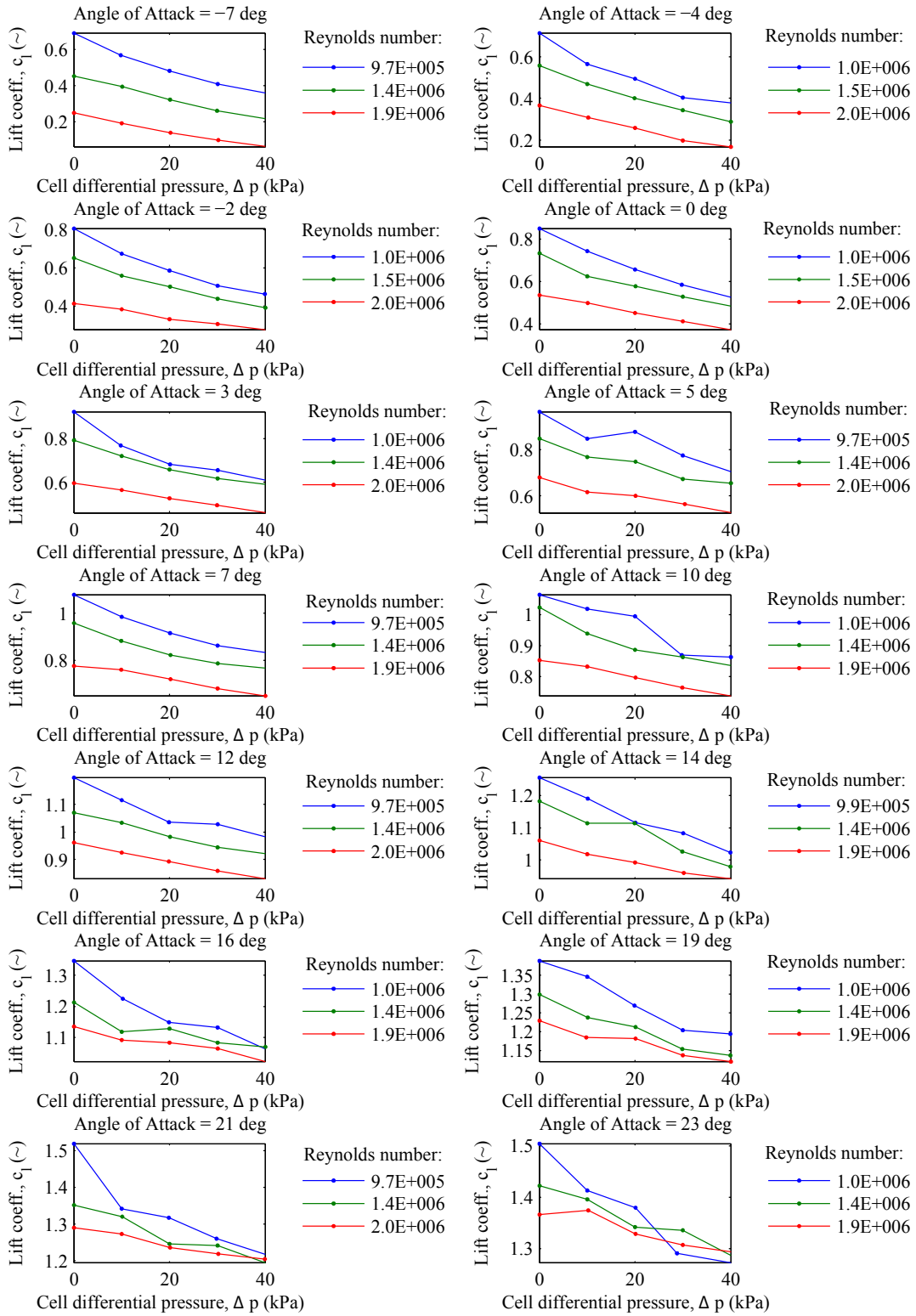
Figure 6.23   Lift Coefficient versus CDP at Various (Corrected) Angles of Attack

204

In Figure 6.24 (p. 206) the variation of drag coefficient with CDP is shown. It can be seen across all the angles of attack and Reynolds numbers that the drag coefficient decreased with increasing CDP. This was expected because the higher the CDP the closer the flap was to total retraction, the lower the drag coefficient. The influence of the Reynolds number was of interest because it appeared to have a different effect at low angles of attack ($\alpha \leq 12°$) where the higher Reynolds numbers demonstrated a lower value of the drag coefficient. However, at the higher angles of attack this relationship appeared to reverse. This is believed to be caused by the location of separation. It appears that at higher Reynolds number the flow separates over a larger portion of the wing, creating a larger wake and consequently a higher drag coefficient. However, no flow-visualization experiment was carried out to confirm this assumption.

The pitching moment coefficient (measured about the quarter chord point) and its variation with CDP is shown in Figure 6.25 (p. 207). It can be seen how a deployed flap (CDP = 0 kPa) generated a high negative pitching moment. This was expected because the deployed flap generated higher aft loading over the airfoil and consequently a higher nose down moment. This behavior could be seen across all angles of attack. When the pressure was increased, the flap retracted, the aft loading decreased, and the negative pitching moment decreased. At high angles of attack, the pressure peak (in negative sense) over the first quarter of the airfoil became so large that a positive pitching moment resulted, regardless of flap position. A typical increase in pitching moment coefficient of 0.04 could be observed between maximum flap deployment and retraction.
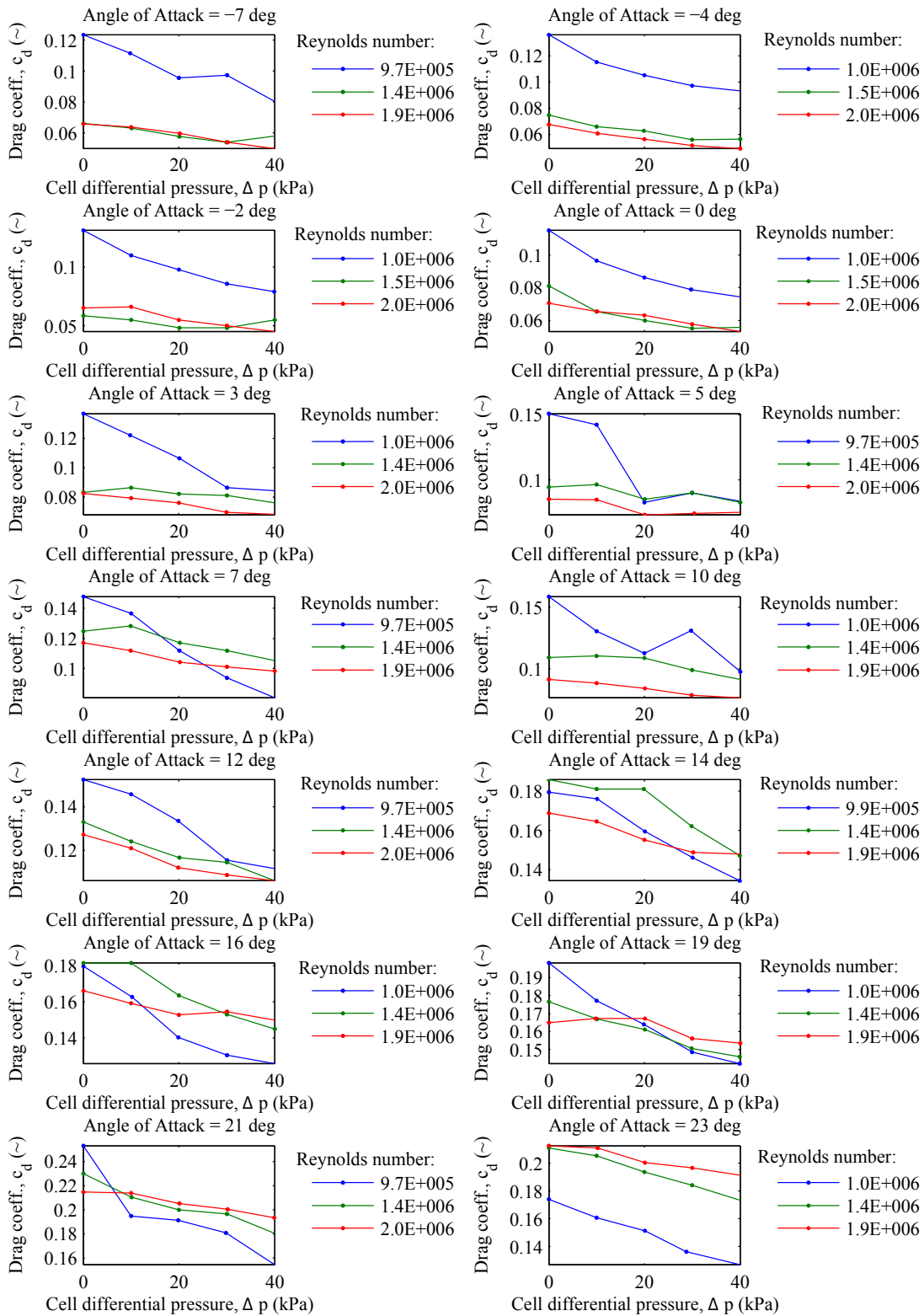
Figure 6.24   Drag Coefficient versus CDP

206
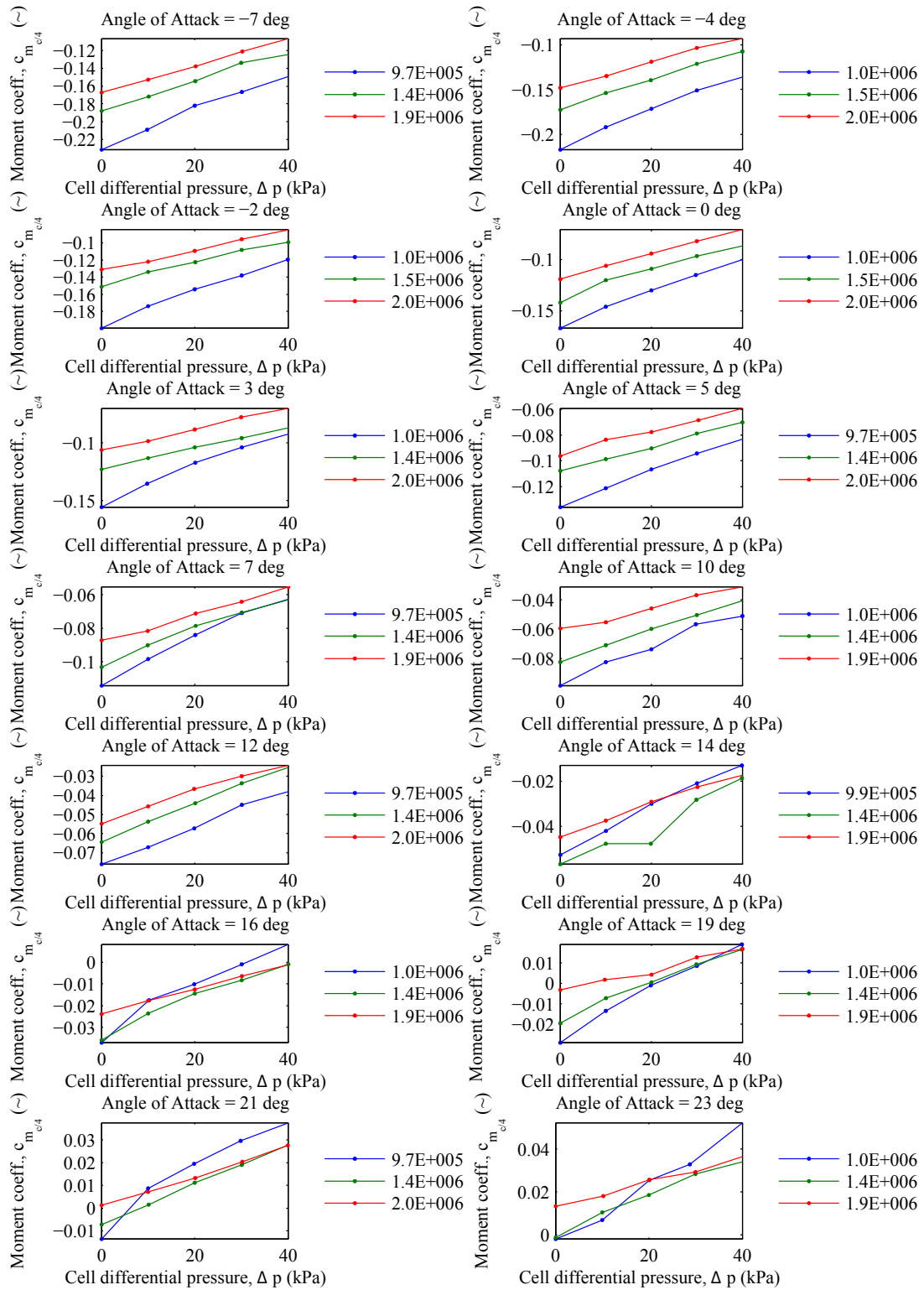
Figure 6.25   Moment Coefficient versus CDP

6.6.3 Results at Constant Velocity

In this section, the same results as in Section 6.6.2 are presented. This time, however, it is from a different point of view, namely a constant velocity (or Reynolds number). Therefore, the reader can appreciate the variation of the aerodynamic coefficients with angle of attack under various CDPs. The graphs that are presented here are more commonly used and might give the reader a more comprehensive perspective of the results.

Figure 6.26 shows the change in lift coefficient with angle of attack. In addition, the shape change of the airfoil is presented at characteristic combinations of angle of attack and CDP. These shapes were obtained from photographs of the wing section shape during the experiment. It can be clearly seen that an increase in CDP shifts the c_l-α line down. This is in accordance with conventional flap behavior where a flap retraction causes a downward shift of the c_l-α curve. If the three individual plots of Figure 6.26 are compared, the effect of Reynolds number becomes evident. At higher dynamic pressures, the effect of the pressure and elastic forces becomes smaller and smaller. Scaling the elastic and CDP-induced forces such that they are tailored towards the expected dynamic pressures can counter this problem. Ideally, the pressure and elastic forces would be an order of magnitude higher than the aerodynamic forces. In that case, the aerodynamic forces would have little influence on the geometry of the flap geometry and more robust control could be achieved in all flight regimes.
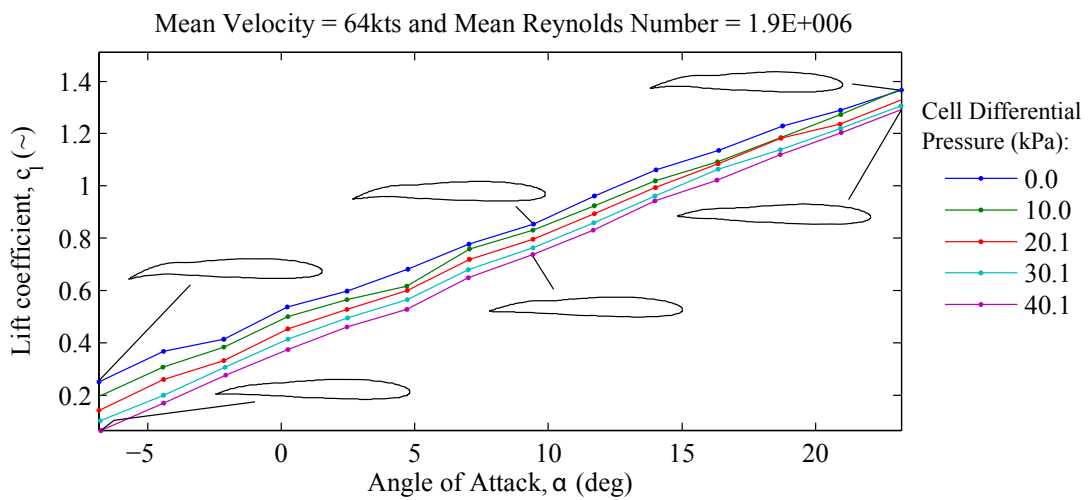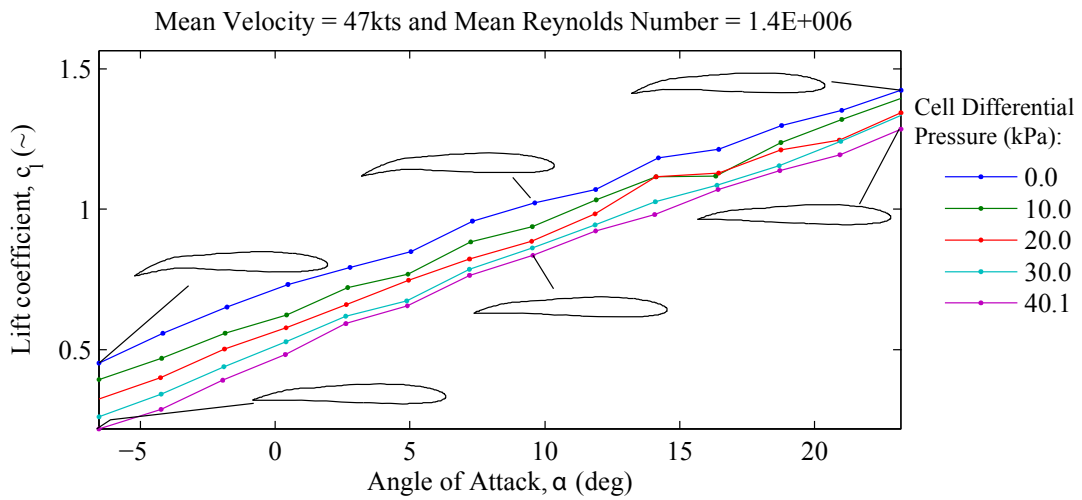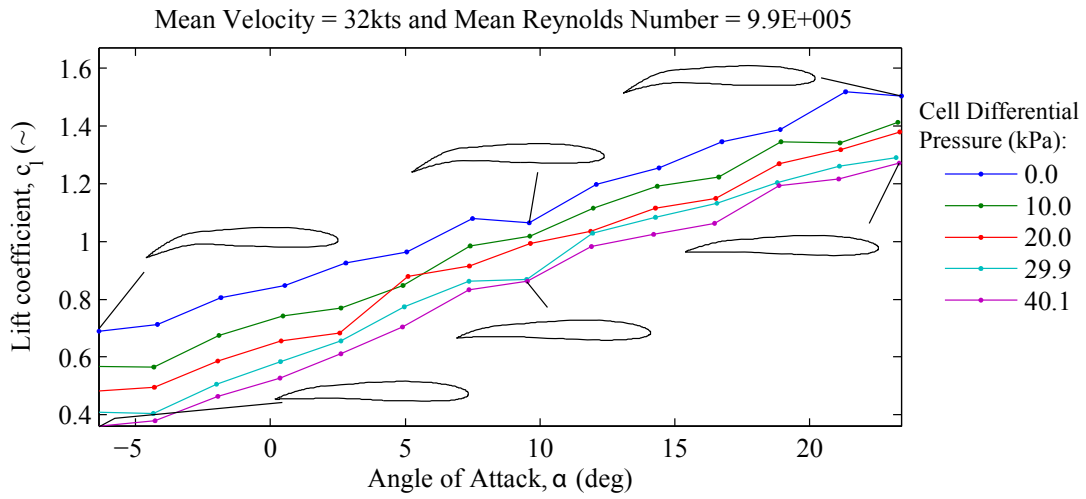
Figure 6.26   Section Lift Coefficient Versus Angle-of-Attack

The reader might have observed that the c_l-α curves in Figure 6.26 are more shallow than would be expected from two-dimensional airfoil theory (where $c_{l\alpha} \approx 2\pi$). In Table 6.1 the lift curve slopes are presented for different Reynolds numbers and CDPs. These numbers were obtained by using a linear least-squares fit of the data between $\alpha = -4$ and $\alpha = 14$, which is according to Figure 6.21 well within the linear realm of the NACA 2412 airfoil. As can be seen from this table, the values of $c_{l\alpha}$ are very much below what was expected for this test.

Table 6.1   Lift-Curve Slopes (1/rad) for Pressure adaptive Wing

		Reynolds Number (x10^6)		
		1.0	1.4	1.9
Cell Differential Pressure, CDP (kPa)	0	1.7	1.8	2.2
	10	1.8	1.9	2.2
	20	1.9	2.1	2.3
	30	2.0	2.1	2.3
	40	2.0	2.1	2.4

The following parameters could have caused the large discrepancy between theory and experiment:

- The flexing of the flap under aerodynamic loading. The absolute geometry of the model was not constant during the experiment because of the flexible flap. The flap flexed under aerodynamic loading and could not keep its original shape.

- Imperfect boundary conditions. The presented results assume purely two-dimensional flow, which was not fully achieved. Flow around the endplates, as well as flow through the gaps between flap and end plate led to three-dimensional effects that were not accounted for in the present analysis

- Inaccurate balance calibration. The wind tunnel balance was calibrated by comparing present wind tunnel test results on a small aircraft model (Cessna 210) to results obtained under the same conditions during tests a long time ago. The adaptive flap

model had an order of magnitude larger surface area and therefore exceeded the calibrated regime.

- Inadequate correction factors for boundary conditions. According to Ref. 144 a typical value for the ratio of frontal area to total area of the tunnel is 0.05. At zero angle-of-attack the present model had a frontal-area to tunnel-area ratio of 0.17 (discarding the tunnel area outside the end plates). Large values of blockage result in additional surface stresses on the model. The present blockage correction does not account for a change of surface stresses as a result of the finite area ratio and is therefore inadequate.

In the authors opinion, the present results clearly demonstrate the effect of the pressure adaptive flap on the aerodynamic characteristics of the section. Even though the absolute values of the coefficients might not be accurate for a free-flight model, they still proof the concept of the pressure adaptive flap. Additional wind tunnel tests (for example in an open jet wind tunnel or a large low-speed wind tunnel) have to be carried out in order to obtain the absolute aerodynamic characteristics of this wing.

In Figure 6.27 the drag coefficient is shown as a function of angle-of-attack. The trend with angle-of-attack was as expected. Generally speaking, it can be seen that the lines of different pressures are much closer together in the last plot of Figure 6.27 than in the first plot. This is the same as in the c_l-α plots of Figure 6.26. It demonstrates that at a higher dynamic pressure the flap is already partially retracted. Deploying the flap by decreasing the CDP therefore has less effect on the aerodynamic coefficients of the model.

Figure 6.28 (p. 213) shows the variation of the pitching moment coefficient (about the quarter chord point) with angle of attack. In case of an ordinary, rigid airfoil one would expect the value of the pitching moment coefficient to be constant up to the point where the airfoil enters the stall region. Obviously, the plotted curves in Figure 6.28 do not show a constant behavior, but show a distinct trend with angle of attack. This is attributed to the fact that the flap flexed upwards with higher angle of attack, instead of keeping its original shape. This resulted in a lower (in absolute sense) pitching moment, then would be expected based on the assumption of a rigid flap. It can be seen that increasing the CDP results in a shift of the c_m-α curve upwards. This shift amounted to approximately 0.05 at low angles of attack for a change in CDP of 40kPa.
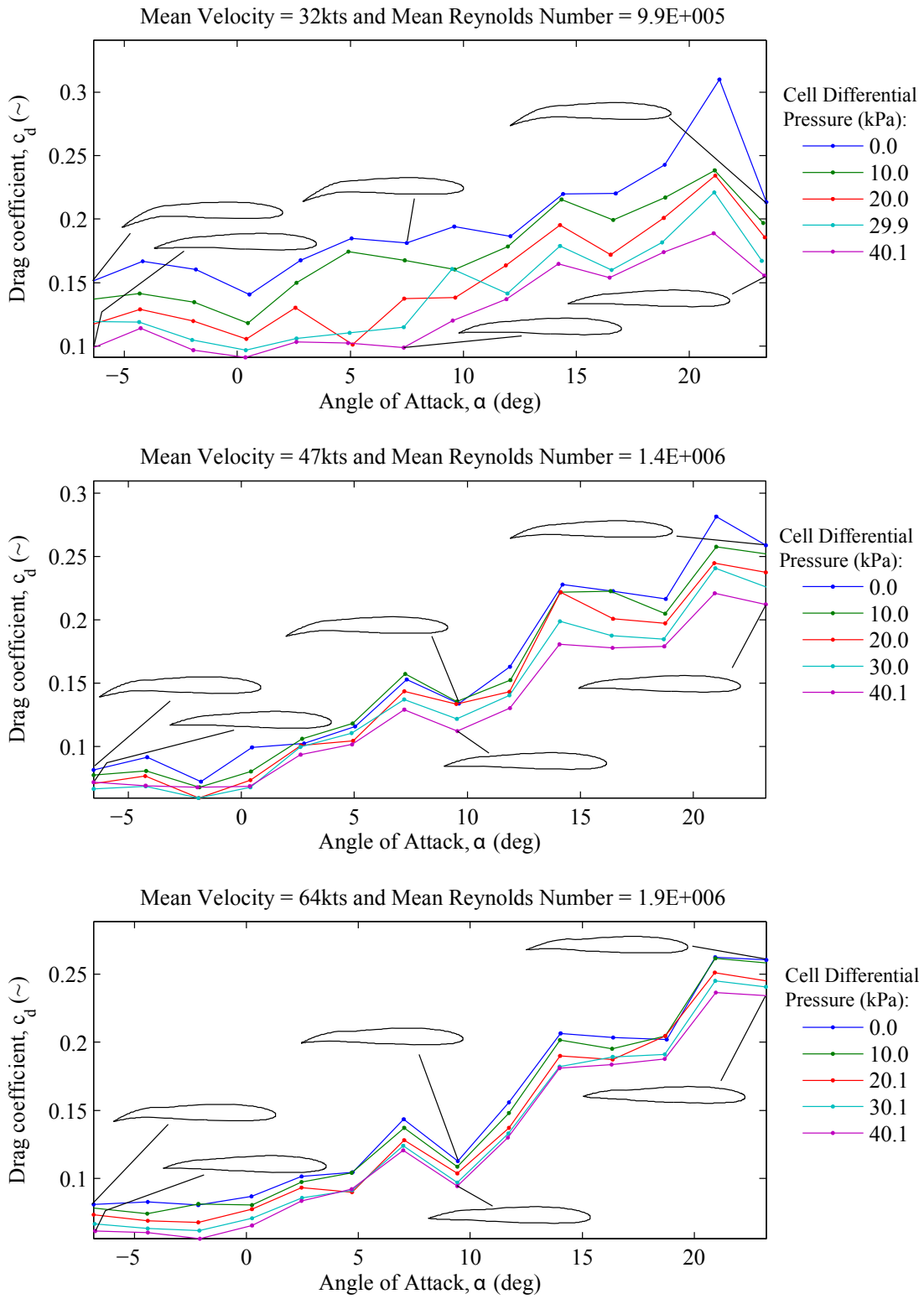
Figure 6.27   Section Drag Coefficient Versus Angle-of-Attack

212
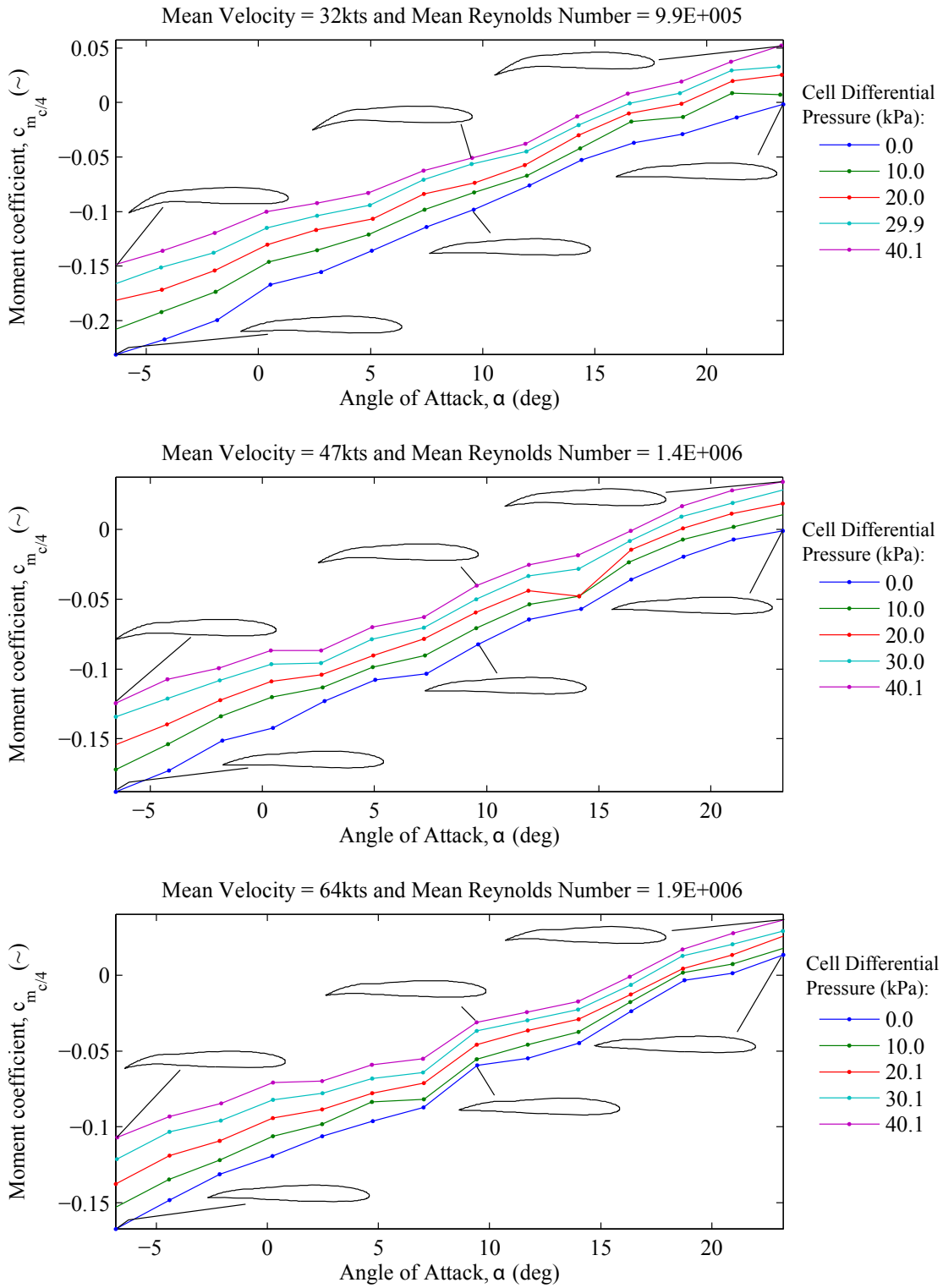
Figure 6.28   Section Pitching Moment Coefficient Versus Angle-of-Attack

6.6.4 Comparison to Xfoil Results

The experiments that were done in the wind tunnel were modeled using Xfoil (see Section 4.6). The geometry of the flap was extracted from photographs taken during the experiment. The resulting two-dimensional airfoil geometry was subjected to the corrected Reynolds number, Mach number, and angle of attack. Xfoil generated a pressure distribution over the airfoil geometry and calculated the resulting lift, drag, and pitching moment coefficient. The following input parameters were used in Xfoil (see Section 4.6 for details):

- Maximum number of Newton iterations: 150

- Number of panels: 200

- Critical amplification factor: $\tilde{n} = 9$

In Figure 6.29 through Figure 6.42 each of the pressure distributions, airfoil geometry, and aerodynamic coefficients is displayed. The reader can observe how the airfoil geometry changed with changing velocity and CDP. Each figure comprises of 15 plots: three Reynolds numbers (horizontal) times five CDPs (vertical). Fourteen different angles of attack were run and each figure shows the result for one of them. The reader might observe that at negative angles of attack Xfoil did not converge to a solution. Those figures lack a pressure distribution and only list the aerodynamic coefficients that were measured experimentally. A possible explanation for the lack of convergence could be found in the fact that at negative angles of attack and a deflected flap, the flow separates from the wing. Since Xfoil does not have a law-of-the-wake boundary layer formulation, it cannot accurately predict the pressure distribution when the flow is separated. This should also be kept in mind when observing the data at higher angles of attack.
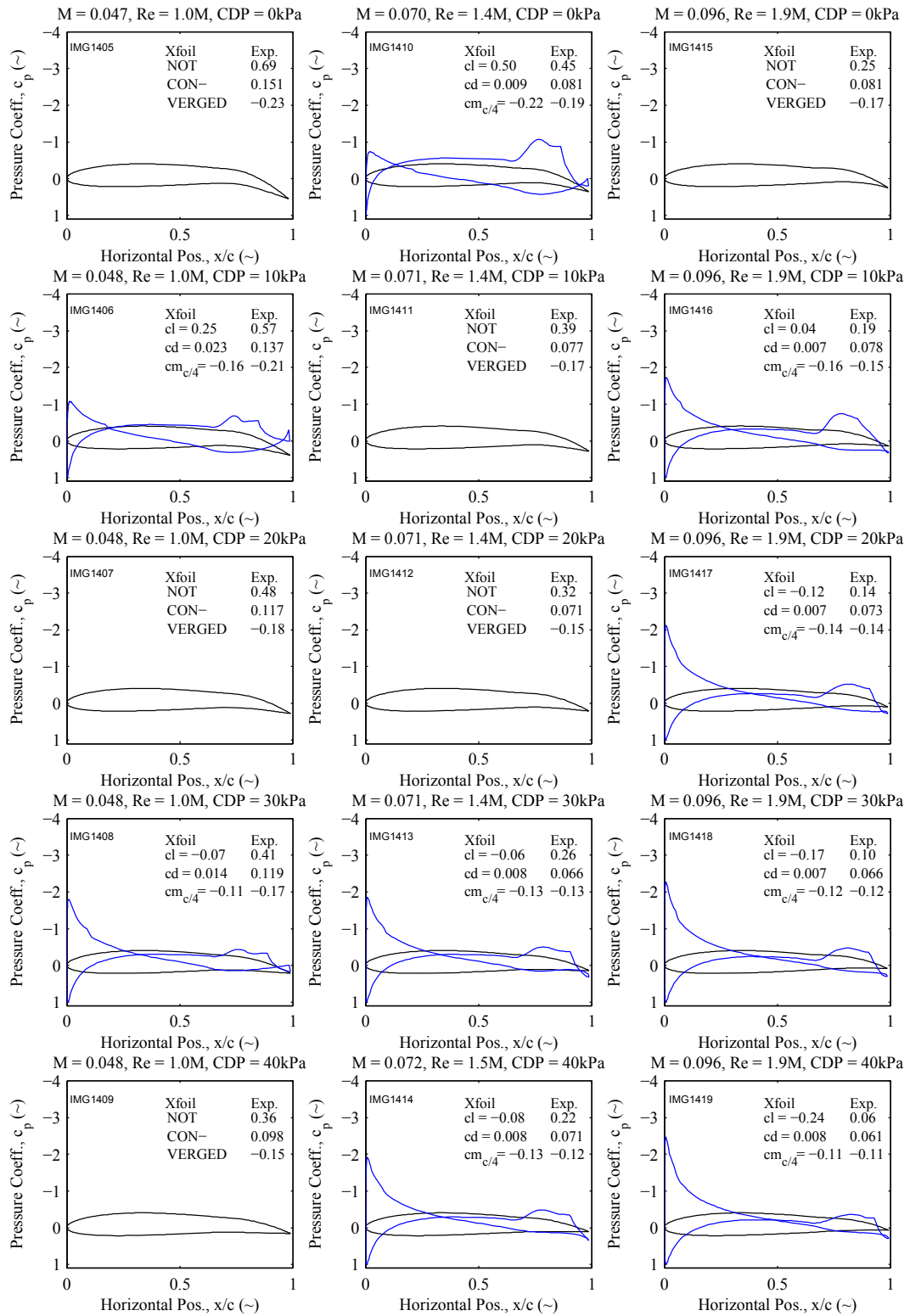
Figure 6.29   Pressure Distributions for -6º Angle of Attack

215
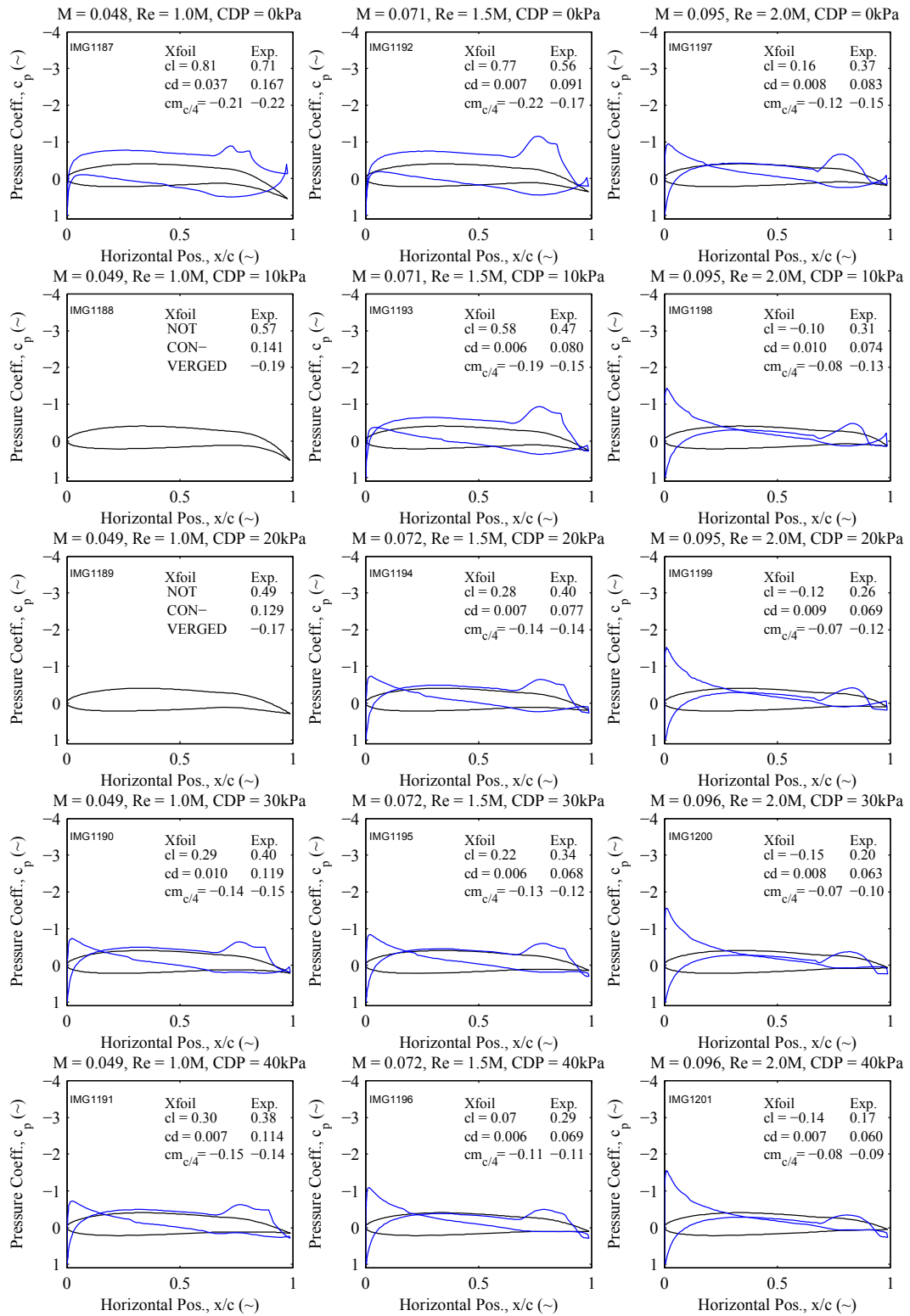
Figure 6.30   Pressure Distributions for -4º Angle of Attack
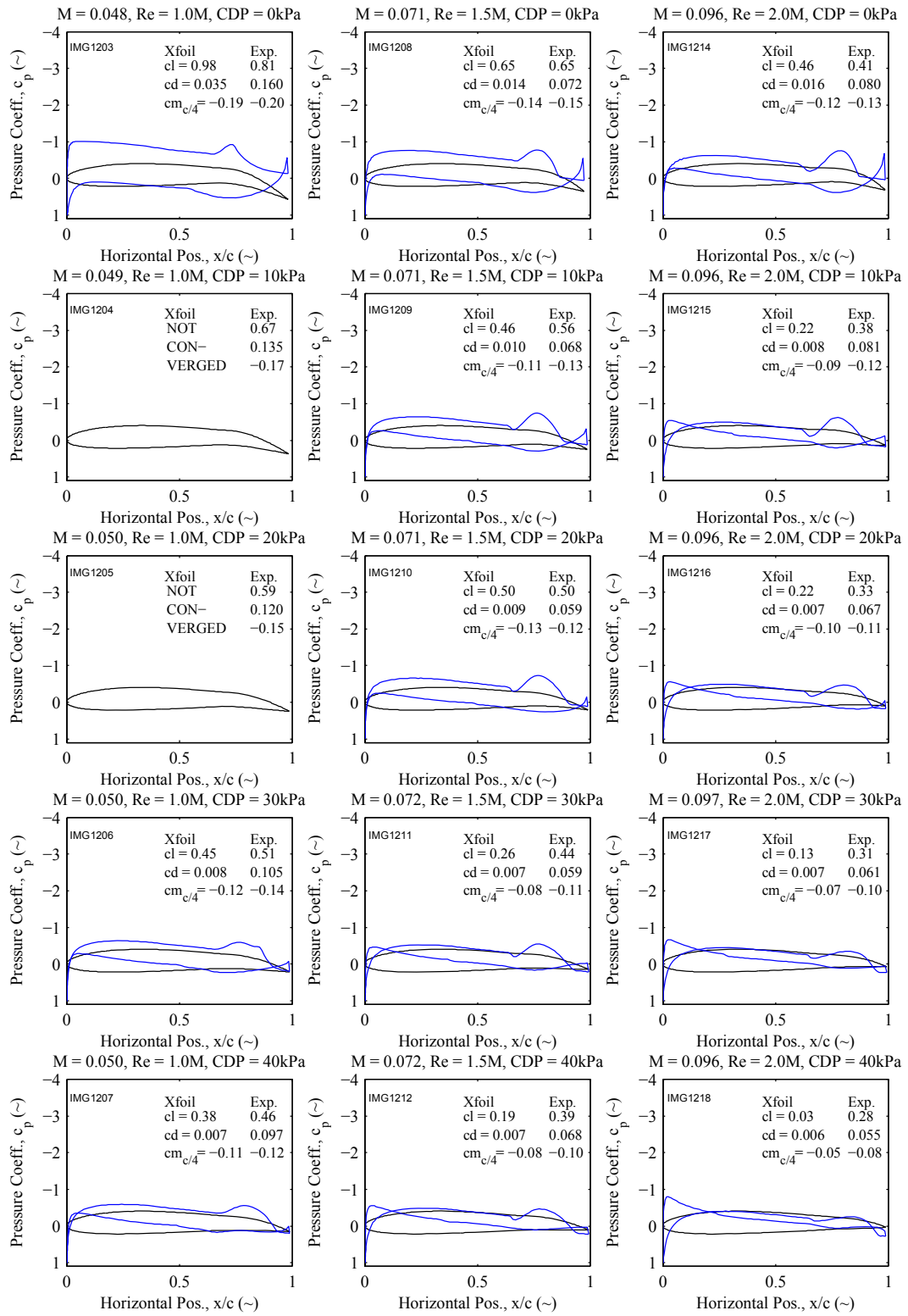
Figure 6.31   Pressure Distributions for -2° Angle of Attack
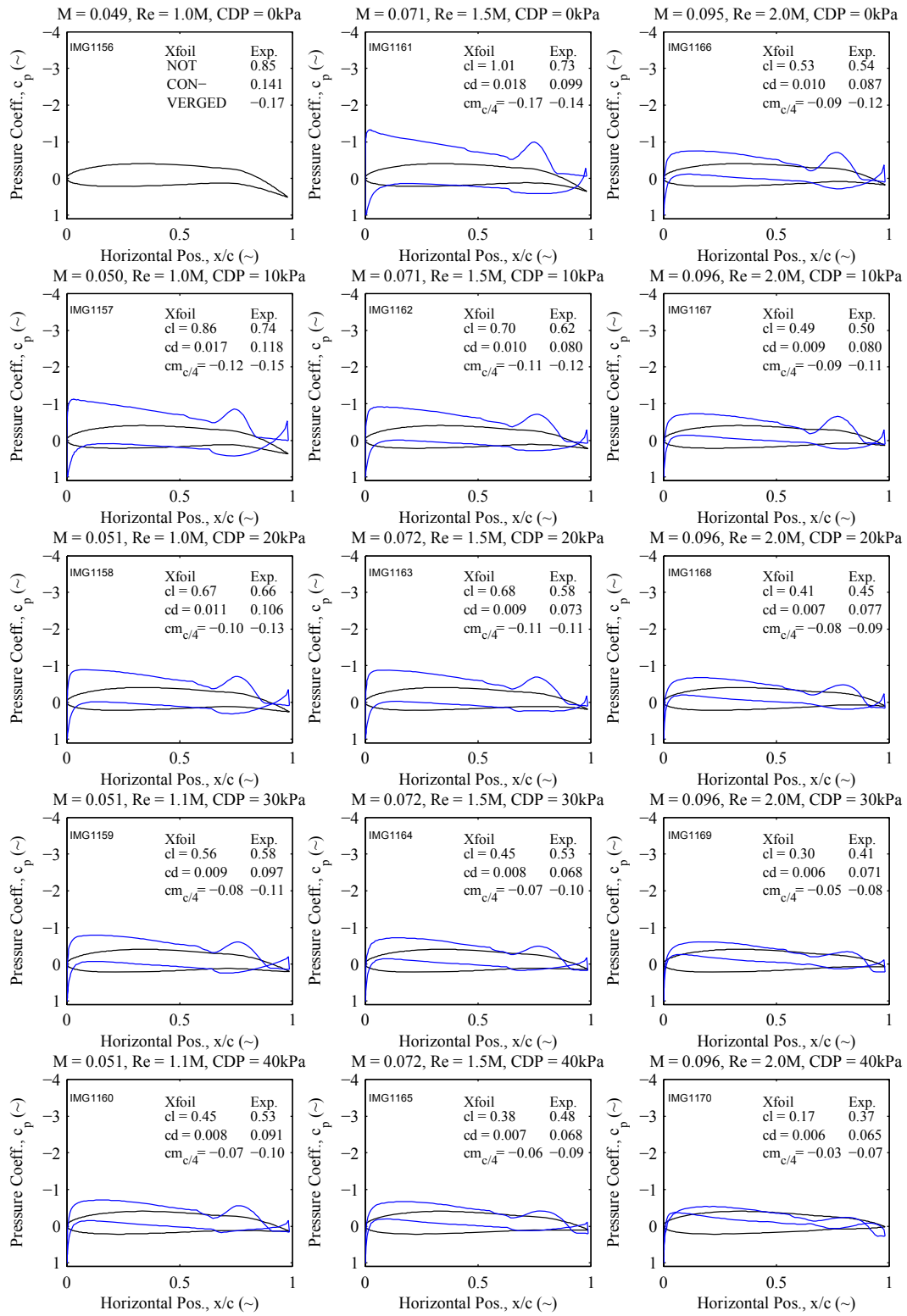
Figure 6.32   Pressure Distributions for 0° Angle of Attack

218
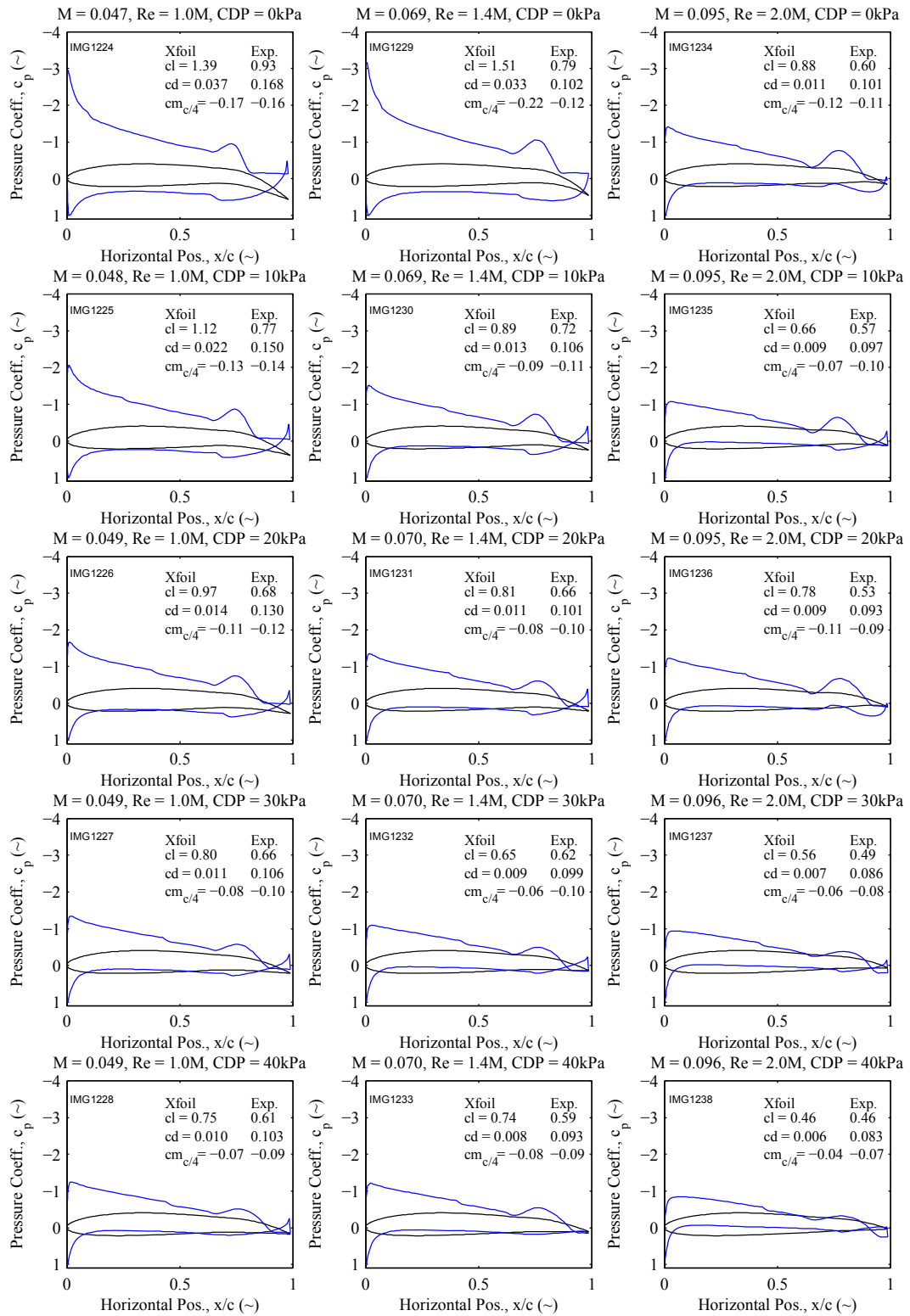
Figure 6.33   Pressure Distributions for 2º Angle of Attack

M = 0.046, Re = 1.0M, CDP = 0kPa

IMG1248

	Xfoil	Exp.
cl =	1.58	0.96
cd =	0.040	0.185
$cm_{c/4}$ =	−0.16	−0.14

Pressure Coeff., c_p (~)

Horizontal Pos., x/c (~)

M = 0.069, Re = 1.4M, CDP = 0kPa

IMG1253

	Xfoil	Exp.
cl =	1.25	0.85
cd =	0.020	0.116
$cm_{c/4}$ =	−0.11	−0.11

Pressure Coeff., c_p (~)

Horizontal Pos., x/c (~)

M = 0.096, Re = 2.0M, CDP = 0kPa

IMG1258

	Xfoil	Exp.
cl =	0.95	0.68
cd =	0.012	0.104
$cm_{c/4}$ =	−0.08	−0.10

Pressure Coeff., c_p (~)

Horizontal Pos., x/c (~)

M = 0.047, Re = 1.0M, CDP = 10kPa

IMG1249

	Xfoil	Exp.
cl =	1.32	0.85
cd =	0.025	0.174
$cm_{c/4}$ =	−0.12	−0.12

Pressure Coeff., c_p (~)

Horizontal Pos., x/c (~)

M = 0.070, Re = 1.4M, CDP = 10kPa

IMG1254

	Xfoil	Exp.
cl =	1.16	0.77
cd =	0.016	0.118
$cm_{c/4}$ =	−0.10	−0.10

Pressure Coeff., c_p (~)

Horizontal Pos., x/c (~)

M = 0.096, Re = 2.0M, CDP = 10kPa

IMG1259

	Xfoil	Exp.
cl =	0.89	0.62
cd =	0.010	0.104
$cm_{c/4}$ =	−0.07	−0.08

Pressure Coeff., c_p (~)

Horizontal Pos., x/c (~)

M = 0.047, Re = 1.0M, CDP = 20kPa

IMG1250

	Xfoil	Exp.
	NOT	0.88
	CON−	0.101
	VERGED	−0.11

Pressure Coeff., c_p (~)

Horizontal Pos., x/c (~)

M = 0.070, Re = 1.4M, CDP = 20kPa

IMG1255

	Xfoil	Exp.
cl =	1.11	0.75
cd =	0.014	0.104
$cm_{c/4}$ =	−0.10	−0.09

Pressure Coeff., c_p (~)

Horizontal Pos., x/c (~)

M = 0.096, Re = 2.0M, CDP = 20kPa

IMG1260

	Xfoil	Exp.
cl =	0.89	0.60
cd =	0.010	0.090
$cm_{c/4}$ =	−0.07	−0.08

Pressure Coeff., c_p (~)

Horizontal Pos., x/c (~)

M = 0.048, Re = 1.0M, CDP = 30kPa

IMG1251

	Xfoil	Exp.
cl =	1.11	0.77
cd =	0.015	0.110
$cm_{c/4}$ =	−0.09	−0.09

Pressure Coeff., c_p (~)

Horizontal Pos., x/c (~)

M = 0.070, Re = 1.5M, CDP = 30kPa

IMG1256

	Xfoil	Exp.
cl =	1.02	0.67
cd =	0.011	0.110
$cm_{c/4}$ =	−0.09	−0.08

Pressure Coeff., c_p (~)

Horizontal Pos., x/c (~)

M = 0.096, Re = 2.0M, CDP = 30kPa

IMG1261

	Xfoil	Exp.
cl =	0.90	0.56
cd =	0.009	0.091
$cm_{c/4}$ =	−0.08	−0.07

Pressure Coeff., c_p (~)

Horizontal Pos., x/c (~)

M = 0.048, Re = 1.0M, CDP = 40kPa

IMG1252

	Xfoil	Exp.
cl =	1.10	0.70
cd =	0.014	0.102
$cm_{c/4}$ =	−0.09	−0.08

Pressure Coeff., c_p (~)

Horizontal Pos., x/c (~)

M = 0.071, Re = 1.5M, CDP = 40kPa

IMG1257

	Xfoil	Exp.
cl =	0.95	0.66
cd =	0.010	0.101
$cm_{c/4}$ =	−0.08	−0.07

Pressure Coeff., c_p (~)

Horizontal Pos., x/c (~)

M = 0.097, Re = 2.0M, CDP = 40kPa

IMG1262

	Xfoil	Exp.
cl =	0.90	0.53
cd =	0.009	0.092
$cm_{c/4}$ =	−0.08	−0.06

Pressure Coeff., c_p (~)

Horizontal Pos., x/c (~)

Figure 6.34   Pressure Distributions for 4º Angle of Attack

220
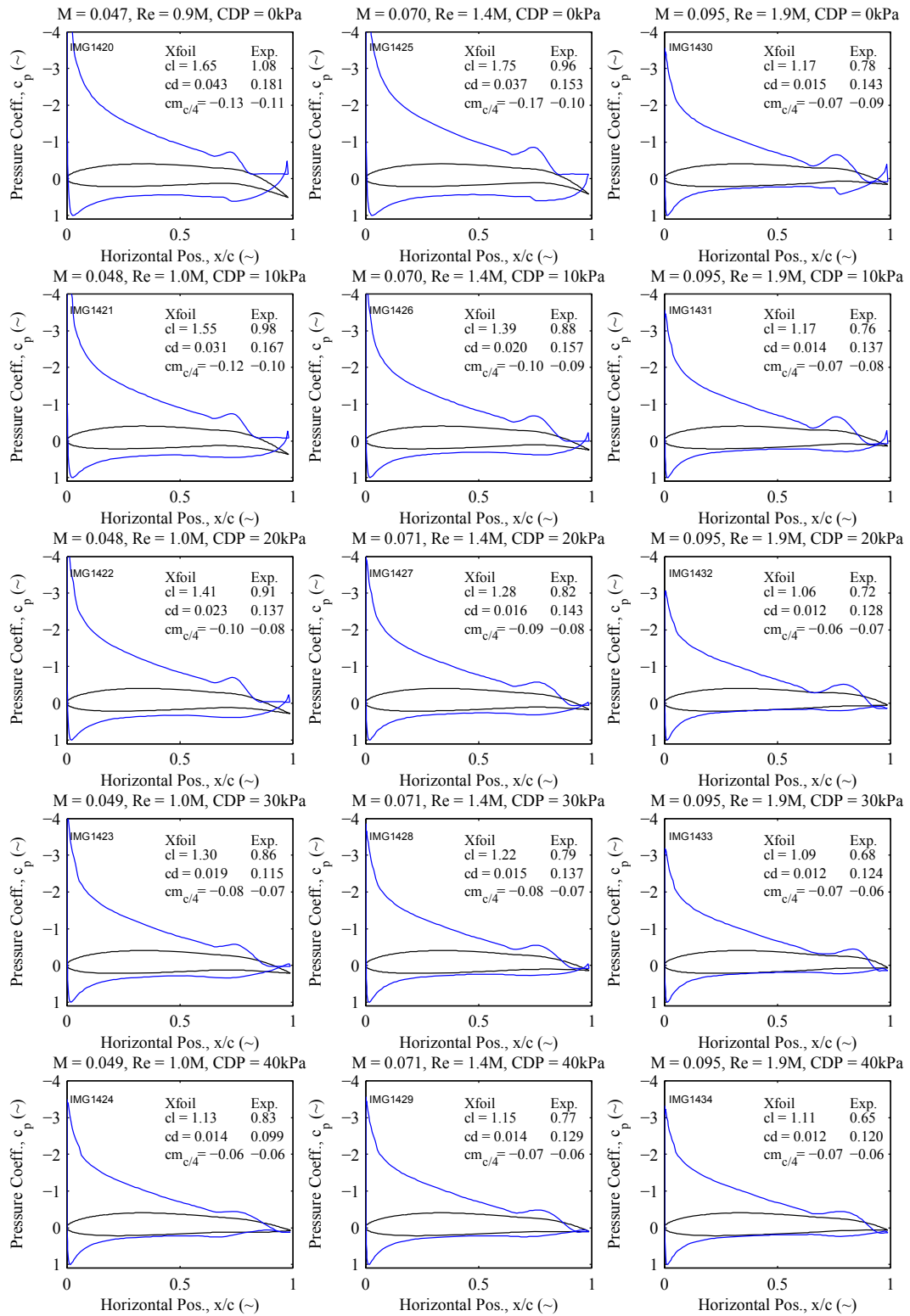
Figure 6.35 Pressure Distributions for 6° Angle of Attack
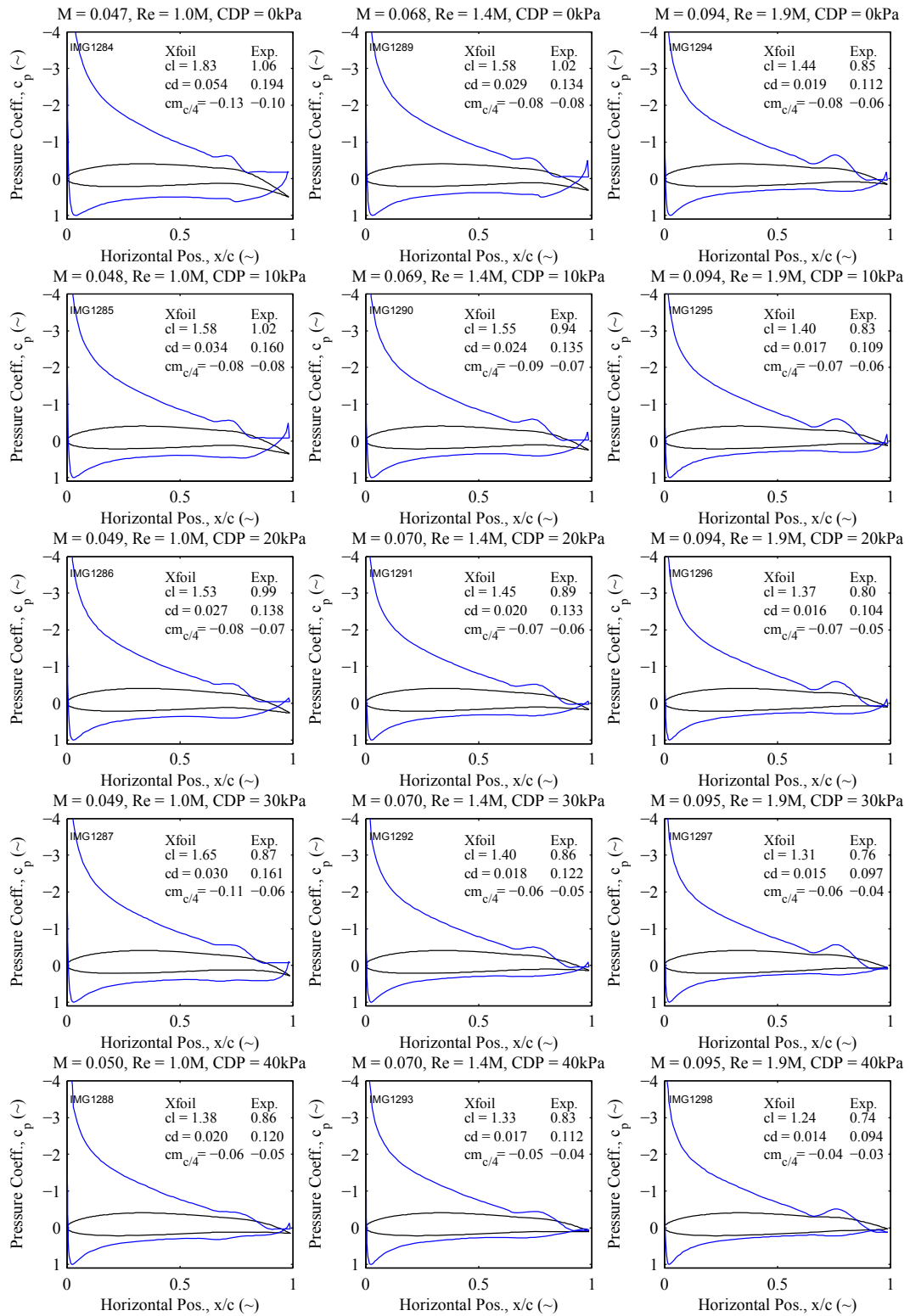
Figure 6.36 Pressure Distributions for 8° Angle of Attack
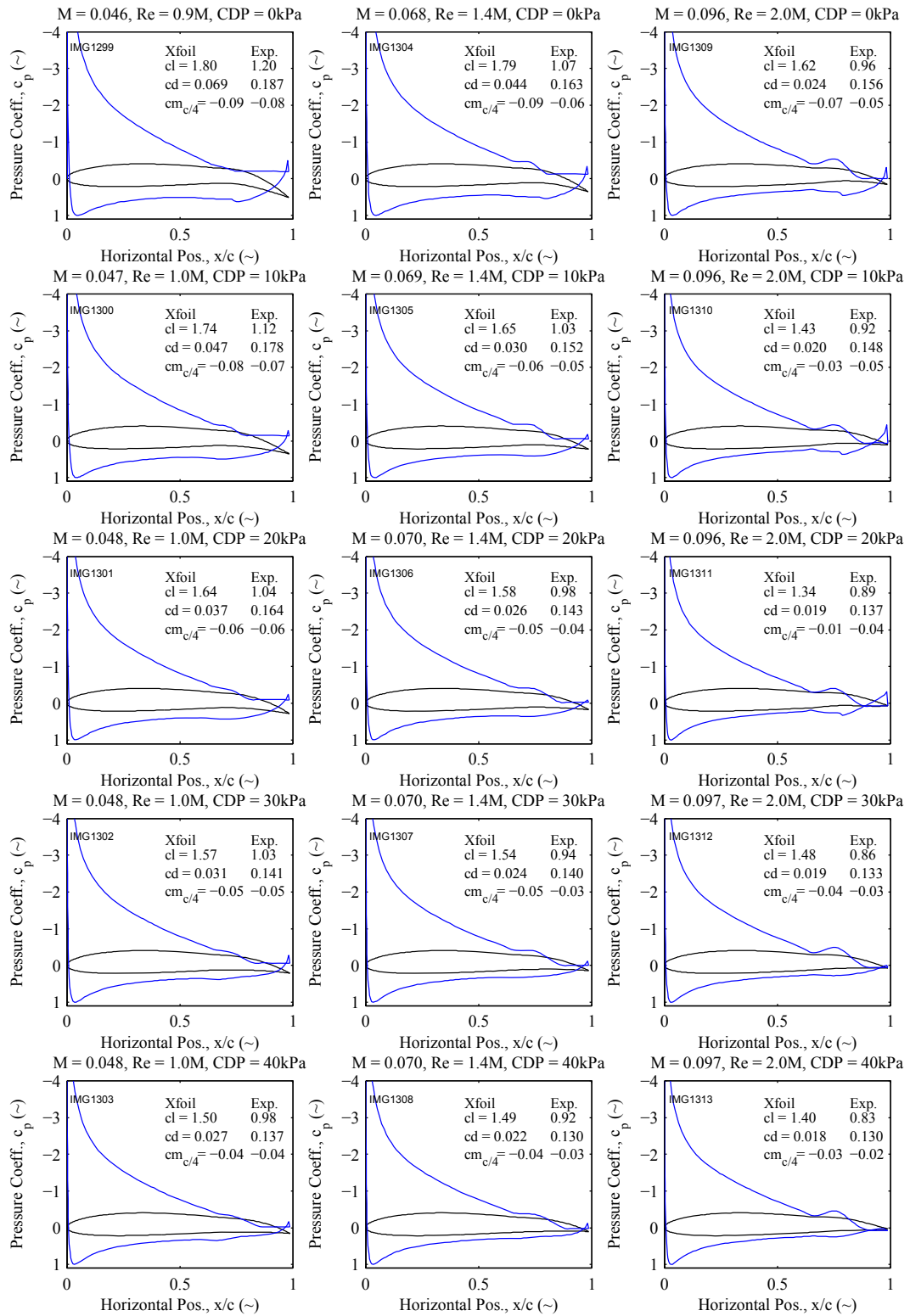
Figure 6.37   Pressure Distributions for 10º Angle of Attack

223
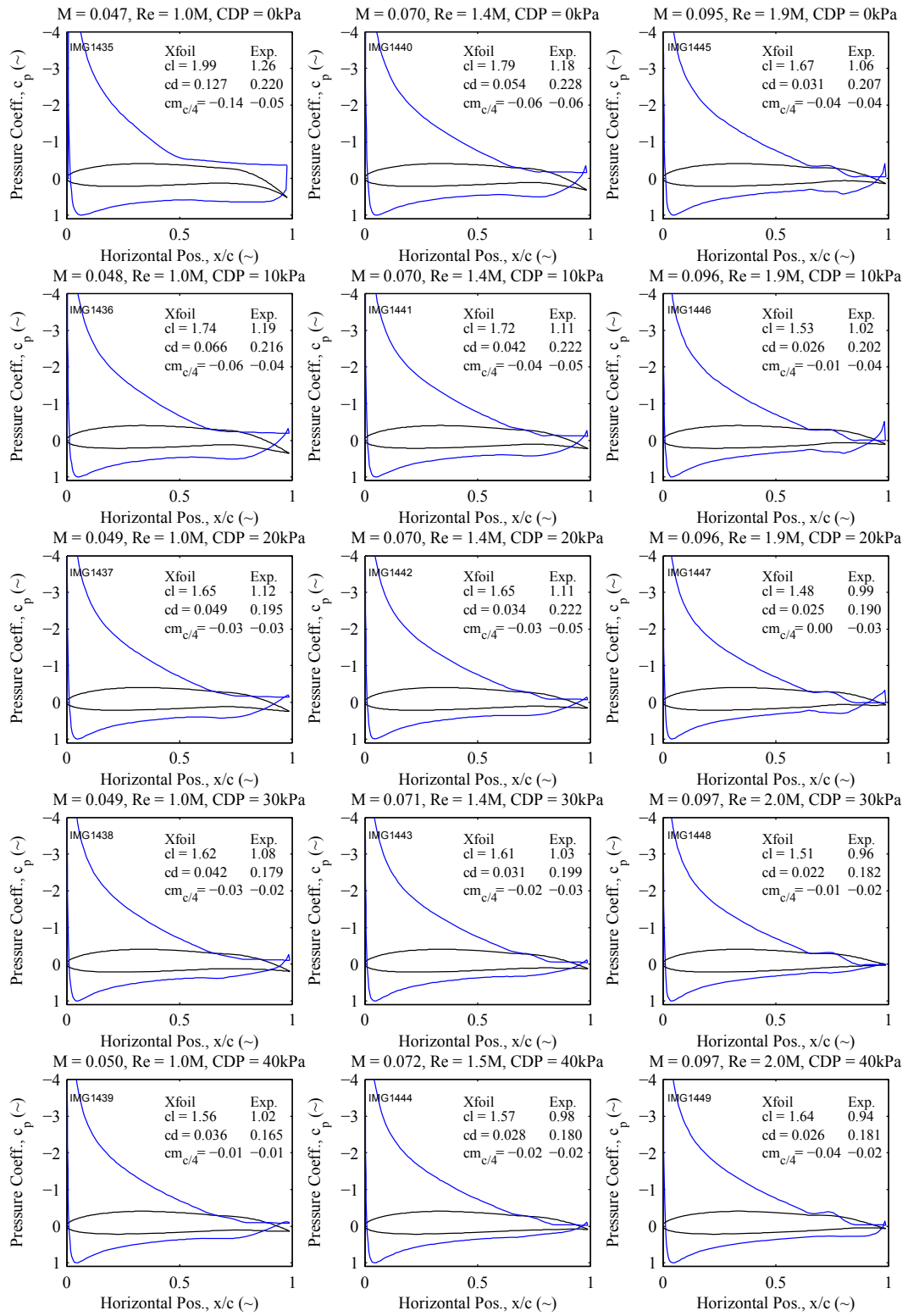
Figure 6.38   Pressure Distributions for 12° Angle of Attack

224
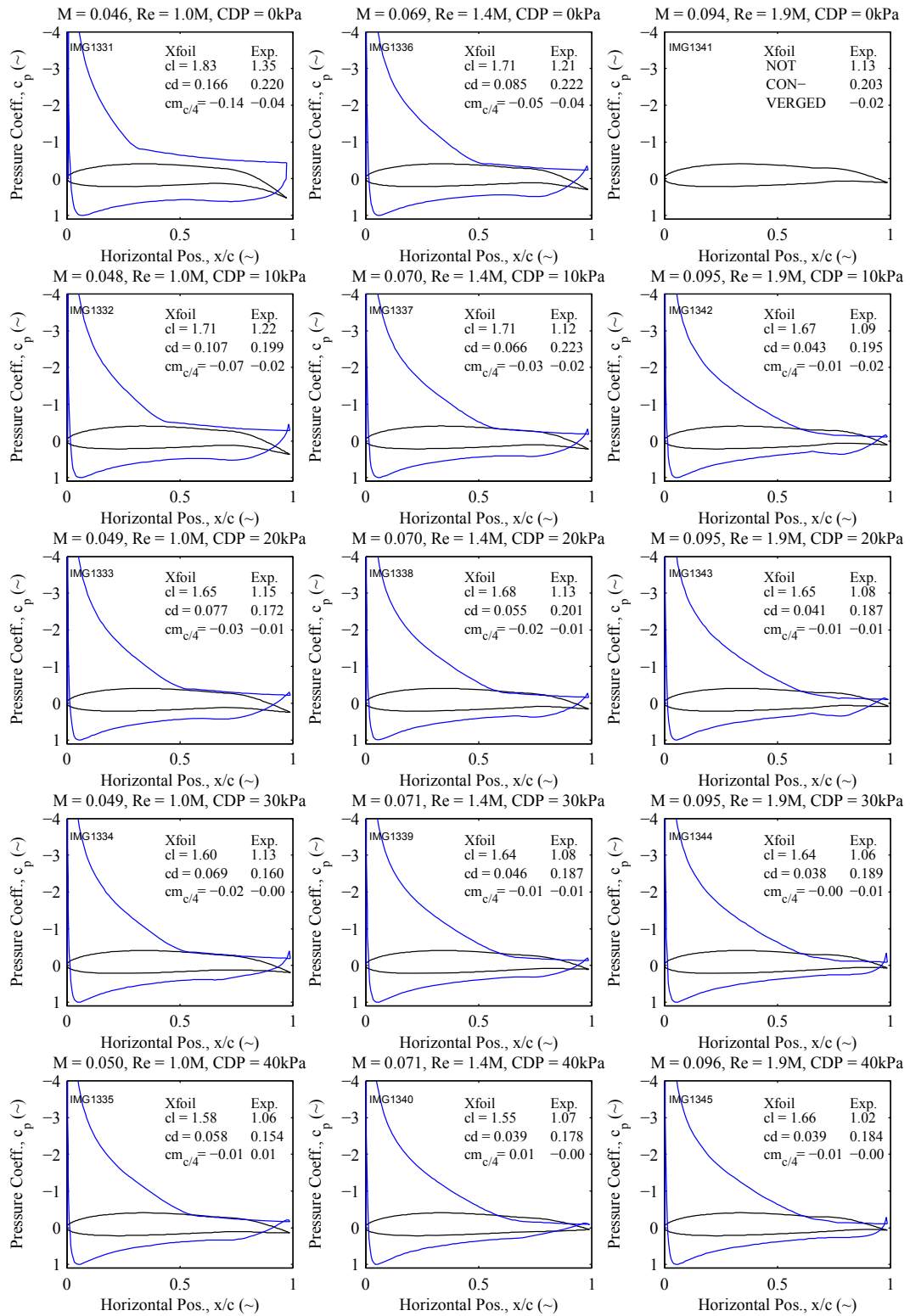
Figure 6.39   Pressure Distributions for 14° Angle of Attack

225

M = 0.047, Re = 1.0M, CDP = 0kPa

IMG1346

	Xfoil	Exp.
cl =	1.62	1.39
cd =	0.188	0.243
$cm_{c/4}$=	−0.13	−0.03

M = 0.069, Re = 1.4M, CDP = 0kPa

IMG1351

	Xfoil	Exp.
cl =	1.62	1.30
cd =	0.124	0.216
$cm_{c/4}$=	−0.06	−0.02

M = 0.094, Re = 1.9M, CDP = 0kPa

IMG1356

	Xfoil	Exp.
cl =	1.63	1.23
cd =	0.085	0.202
$cm_{c/4}$=	−0.03	−0.00

M = 0.048, Re = 1.0M, CDP = 10kPa

IMG1347

	Xfoil	Exp.
cl =	1.60	1.35
cd =	0.155	0.217
$cm_{c/4}$=	−0.10	−0.01

M = 0.070, Re = 1.4M, CDP = 10kPa

IMG1352

	Xfoil	Exp.
cl =	1.59	1.24
cd =	0.108	0.205
$cm_{c/4}$=	−0.04	−0.01

M = 0.095, Re = 1.9M, CDP = 10kPa

IMG1357

	Xfoil	Exp.
cl =	1.62	1.19
cd =	0.078	0.205
$cm_{c/4}$=	−0.02	0.00

M = 0.049, Re = 1.0M, CDP = 20kPa

IMG1348

	Xfoil	Exp.
cl =	1.52	1.27
cd =	0.126	0.201
$cm_{c/4}$=	−0.05	−0.00

M = 0.071, Re = 1.4M, CDP = 20kPa

IMG1353

	Xfoil	Exp.
cl =	1.56	1.21
cd =	0.097	0.197
$cm_{c/4}$=	−0.03	0.00

M = 0.095, Re = 1.9M, CDP = 20kPa

IMG1358

	Xfoil	Exp.
cl =	1.60	1.18
cd =	0.074	0.205
$cm_{c/4}$=	−0.01	0.00

M = 0.050, Re = 1.0M, CDP = 30kPa

IMG1349

	Xfoil	Exp.
cl =	1.51	1.20
cd =	0.108	0.182
$cm_{c/4}$=	−0.03	0.01

M = 0.071, Re = 1.5M, CDP = 30kPa

IMG1354

	Xfoil	Exp.
cl =	1.57	1.15
cd =	0.080	0.185
$cm_{c/4}$=	−0.01	0.01

M = 0.095, Re = 1.9M, CDP = 30kPa

IMG1359

	Xfoil	Exp.
cl =	1.56	1.14
cd =	0.066	0.191
$cm_{c/4}$=	0.00	0.01

M = 0.050, Re = 1.0M, CDP = 40kPa

IMG1350

	Xfoil	Exp.
cl =	1.49	1.19
cd =	0.102	0.174
$cm_{c/4}$=	−0.02	0.02

M = 0.071, Re = 1.5M, CDP = 40kPa

IMG1355

	Xfoil	Exp.
cl =	1.57	1.14
cd =	0.080	0.179
$cm_{c/4}$=	−0.02	0.02

M = 0.095, Re = 1.9M, CDP = 40kPa

IMG1360

	Xfoil	Exp.
cl =	1.58	1.12
cd =	0.069	0.188
$cm_{c/4}$=	−0.01	0.02

The vertical axes are labeled "Pressure Coeff., c_p (~)" and the horizontal axes are labeled "Horizontal Pos., x/c (~)".

Figure 6.40   Pressure Distributions for 16º Angle of Attack
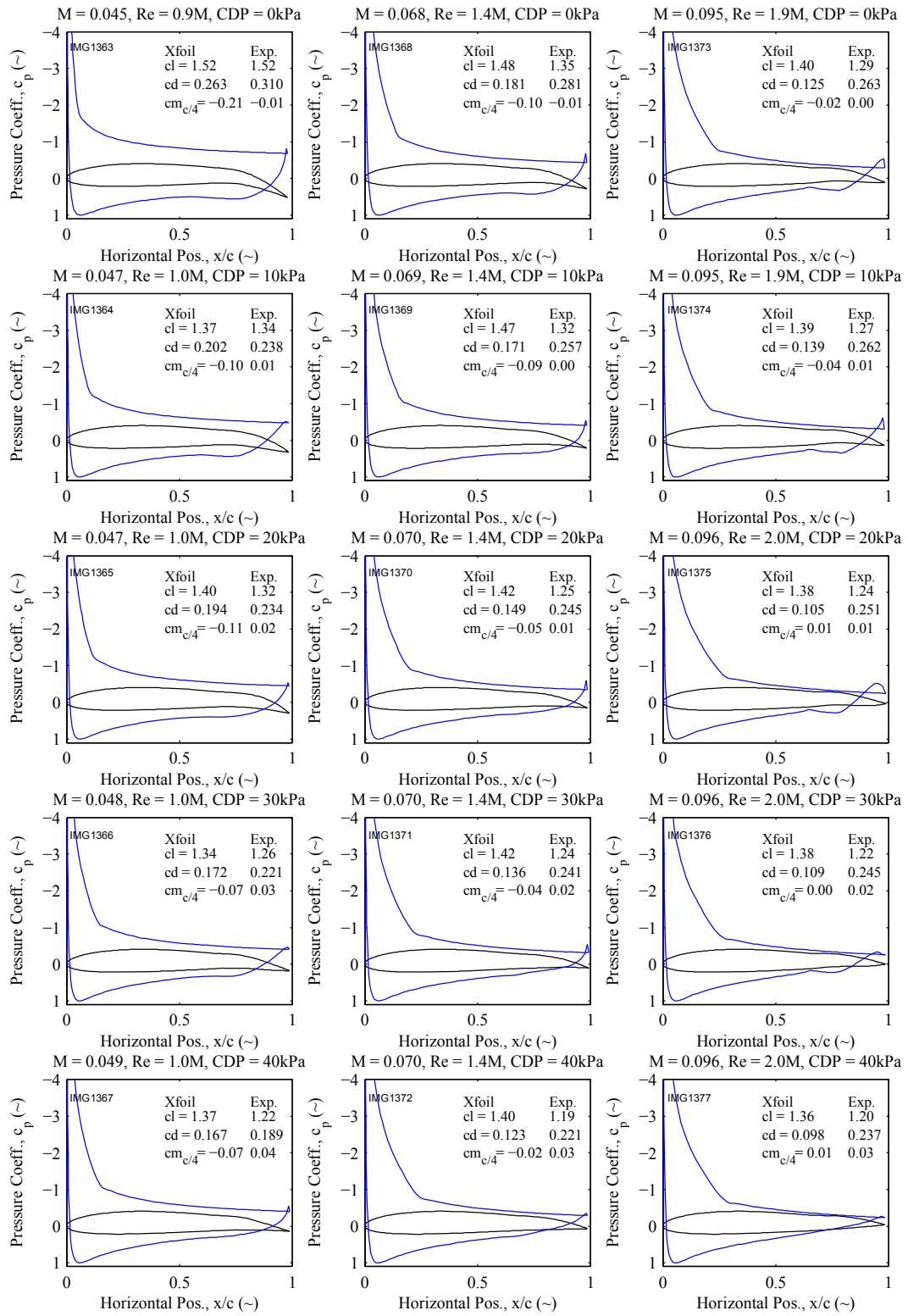
Figure 6.41   Pressure Distributions for 18º Angle of Attack

227
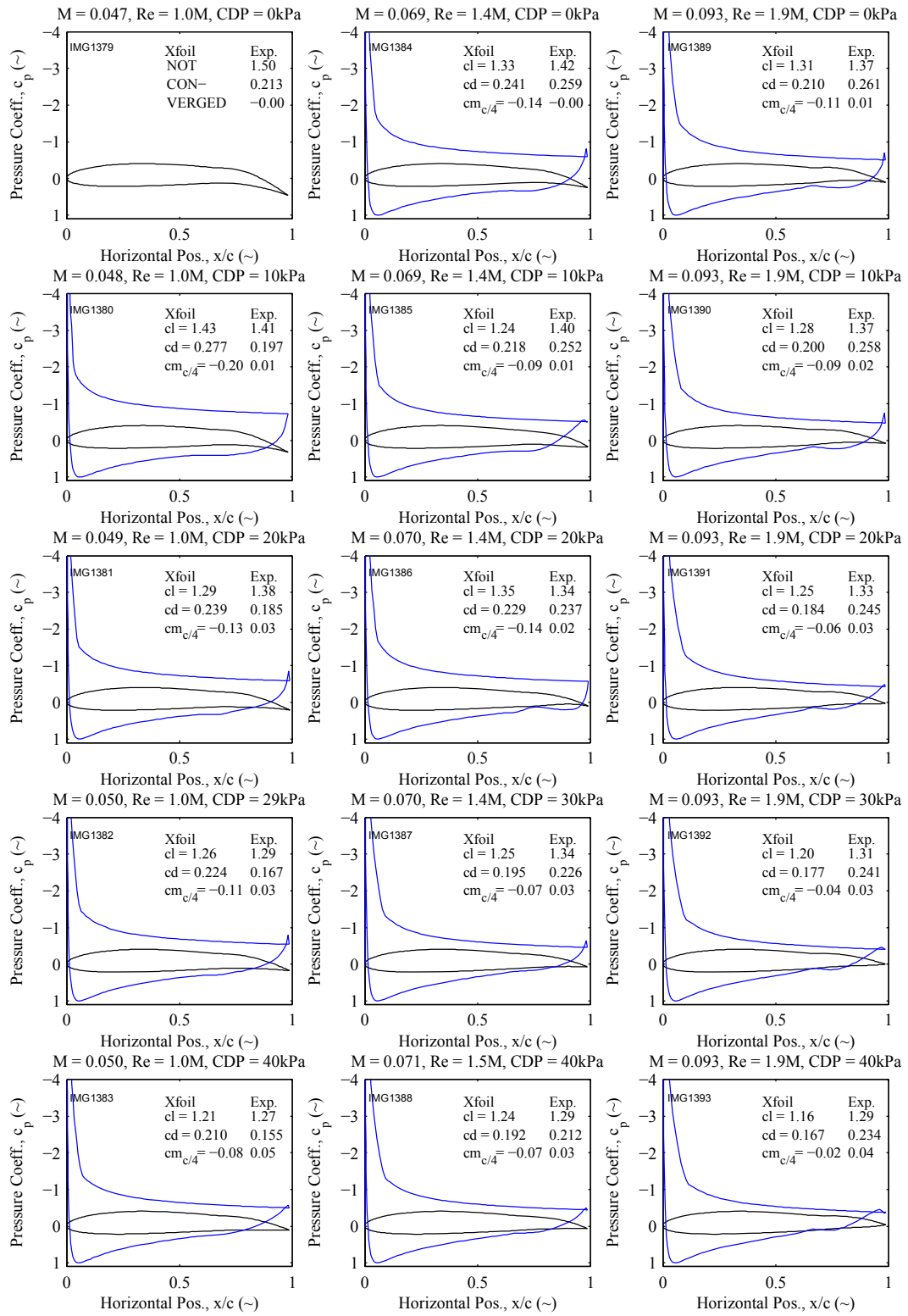
Figure 6.42   Pressure Distributions for 20º Angle of Attack

228

6.6.5 General Discussion and Lessons Learned

The results of the wind tunnel experiment proved that pressure adaptive honeycomb can be used to make gross alterations in airfoil geometry and can influence the aerodynamic coefficients substantially. The present model, however, was still flawed in many ways and could be substantially improved. This section discusses ideas for possible improvement and the implications this has for the structure.

If it is desired to fix the shape of the flap at any arbitrary value of angle-of-attack or dynamic pressure, then it is evident that the pressure forces and elastic forces need to be increased. The present model used a constant-thickness, curved upper and lower skin to induce the flap camber under zero loading. It was observed during the tests that at high dynamic pressures, the flap flexed upwards, particularly near the root. Increasing the skin thickness near the root would potentially solve this problem. Near the root of the flap the moment generated by aerodynamic loading and CDP is greatest. Near the trailing edge, both become very small. It would therefore make sense to tailor the stiffness (or thickness) of the skins such that the flap would not flex up as much as it did in this experiment. In lieu of increasing the thickness of the skin, a similar effect could be achieved by increasing the thickness-to-length ratio of the honeycomb itself. This would have a similar effect. Of course, a combination of both measures could also be a possibility. The most important limit to keep in mind is the fact that the material should stay in the elastic range when it is deformed. This limits the absolute thickness of skin for a given geometric alteration.

At the same time that the elastic stiffness is increased, the pressure stiffness of the honeycomb should also increase. That would mean that the CDP should exceed 40kPa. The pouch material that was used in this pressurized honeycomb yielded at approximately 45kPa. Therefore, tests could not be conducted at such high CDPs. However, that does not necessarily mean that a different material needs to be chosen or that the pouch needs to be made thicker. A smaller cell size would also decrease the circumferential stresses in the pouches substantially and allow for higher CDPs. In addition, a smaller cell size would increase the thickness-to-length ratio of the honeycomb and would contribute to a higher stiffness of the flap.

A third benefit of a smaller cell size would be the fact that the space between the top and bottom skin could then be occupied more efficiently by honeycomb cells. In the present model, over 30% of the available space was not filled with pressurized honeycomb. This means that

229

there is potential to fill this space more efficiently with smaller cells and hence generate a larger moment when the pouches are inflated. The disadvantage of making smaller cells (assuming the thickness remains unaltered) is that the amount of material per volume increases and that the structure as a whole becomes heavier.

With respect to the wind tunnel experiment itself a few things can be done to improve the current setup. The current model was large with respect to the size of the tunnel. The main reason for this was that the model could not be made smaller because then it would become very difficult to manufacture the pressure adaptive flap. However, from the discussion in Section 6.6.3 it could be concluded that the top and bottom wall introduced boundary effects that could not be appropriately accounted for. It would therefore be a good idea to test a future specimen in an open jet facility or at a much larger low-speed wind tunnel. In that case, the wall effects would be much smaller and the morphing effect would be less compromised.

In addition, it needs to be made sure that the wind tunnel balance is calibrated properly. The current experimental setup relied on a calibration which was done for much smaller models.

CHAPTER 7   CONCLUSIONS AND FUTURE WORK

7.1   <u>Conclusions</u>

A new type of adaptive aerostructure for civil aircraft has been presented. This adaptive structure has the potential of adapting wing, empennage or nacelle shape as a function of the ambient pressure only. It has been shown that two possibilities exist to actuate this structure. The first approach relies on a constant mass of gas within the honeycomb cells, while the latter relies on an enforced, yet constant cell pressure. While the first approach relies solely on the ambient pressure change between cruise and take-off altitude, the second option requires a control mechanism that actively regulates the pressure in the pouches.

The following items sum up the main conclusions of the present research:

- Longitudinal strains up to 54% can be achieved without plastic deformation of the cell walls (see Figure 7.1).

- Lateral strains up to 76% can be achieved without plastic deformation of the cell walls (see Figure 7.1).
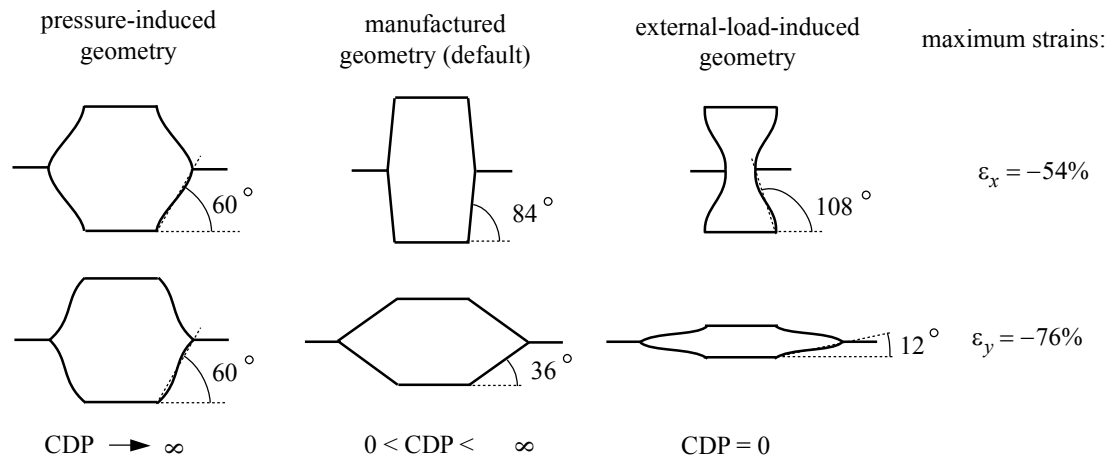
Figure 7.1   Maximum Deformations of Pressure adaptive Honeycomb

- In the case of constant mass and a 40kPa decline in atmospheric pressure, the maximum blocked force amounts to 70kPa with a resulting mass-specific energy density of 1.1J/g, assuming maximum lateral strain.

- In the case the honeycomb is pressurized from the compressor stage of a gas turbine, the maximum blocked pressure that can be produced amounts to 0.82MPa, resulting in a mass-specific energy density of 12.4J/g (on the par with shape memory alloy), assuming maximum lateral strain.

- Pressure-induced hysteresis declines with increasing cell differential pressure to 2% at 40kPa when loaded in longitudinal direction and 4% when loaded in lateral direction.

- Wind tunnel test demonstrated that on a NACA 2412 wing with a 25%c pressure adaptive flap the maximum lift coefficient increased from 1.27 to 1.52 (after wall corrections) due to pressure-induced morphing of the flap.

7.2 Advances in the State of the Art in Pressurized Honeycomb Modeling

It was demonstrated that the effective properties of pressurized honeycomb could be modeled by assuming that the material-induced stiffness and pressure-induced stiffness were independent and could therefore be added. The material-induced stiffness could be found from classical cellular material theory. A model based on the conservation of mechanical energy was developed to determine the pressure-induced stiffness of pressurized honeycomb. The resulting stress-strain relations showed nonlinear behavior. For small strains a linearization was employed about the zero-strain geometry. This resulted in a constant total stiffness modulus of the pressurized honeycomb. To simplify the finite element analysis, this modulus was translated to a new effective stiffness of the cell walls by using the inverse of classical cellular material theory. This allowed the generation of a finite-element honeycomb structure without the explicit definition of pouches or pressure loading and the same geometry as ordinary (non-pressurized) honeycomb. For small strains this model was shown to correlate well to experimental results from a three-point bend test on honeycomb beam test article.

7.3 Future Work

Continuing work needs to be carried out in order to utilize the potential of pressure adaptive honeycomb. First of all, a database of experimental data should be established that relates to the mechanical properties of pressure adaptive honeycomb. In this dissertation a beginning of this database has been presented. However, more diligent testing needs to be done over the

entire anticipated strain range of the material. In order to accomplish this in a repeatable fashion, a manufacturing method needs to be established that results in honeycomb with a constant geometry. This includes a device that can accurately create a pre-defined honeycomb angle as well as a device that can bond the corrugated sheets accurately together. When those prerequisites are met, it becomes possible to create test articles of various cell sizes, honeycomb angles, and overall size. These test articles can consequently be subjected to tension and compression tests at various pressures. This way the properties of pressure adaptive honeycomb can be characterized.

The presented equivalent stiffness model needs to be expanded such that it can be used for finite strains that are on the par with those shown in Figure 7.1. To that extent the equivalent stiffness needs to be determined at various strain levels. That way, a table of effective moduli can be constructed. Based on the strain that an element encounters during deformation, a different effective modulus needs to be implemented. A finite element analysis can find the appropriate modulus in an iterative manner where the solution converges to a point where modulus and strain are in agreement. It should be investigated if such a method would give good predictions of the behavior of complex pressurized honeycomb structures, such as those encountered in the pressure adaptive flap.

A third area of research is the material choice and manufacturing of the pouch inside the honeycomb. In the present dissertation the focus was not to use the best possible material for the pouch, but rather something that functioned well enough to demonstrate the principle of pressure-induced morphing. Future research should be directed towards choosing an appropriate material to be used for the pouch as well. For low-pressure applications various kinds of aerospace-graded nylon could be considered. For high-pressure applications other options, including metallic pouches should be taken into consideration. In those applications an appropriate system should be designed that feeds air to the pouches without any pressure loss due to leaks.

With the three steps outlined above, a solid basis can be created for the application of pressure adaptive honeycomb in aerospace structures. The next logical step would be to implement pressure adaptive honeycomb into the design of a high-lift device. Finite element analysis of the embedded pressure adaptive honeycomb can aid the designer in determining the different geometric shapes that can be achieved by altering the pressure inside the cells.

When it comes to applications of pressure adaptive honeycombs the author believes various a variety of aircraft could benefit. Light sport aircraft, for example, could use a solid state flap system based on pressure adaptive honeycomb. For minimum cost, complexity and power requirements, the flap system could be made such as to satisfy the stall requirements. A simple powered version of a pressure adaptive flap could be made by using the engine's exhaust manifold pressure in combination with a simple pilot-controlled valve to regulate the pressure and hence the deployment of the flap. A similar system could be used in larger general aviation aircraft.

However, pressure adaptive honeycomb is not limited to propeller aircraft but could also be used in business jets and commercial transport aircraft. It is acknowledged that the simple adaptive flap that was tested in the present research will likely not be enough to create the lift coefficient that is required in these types of aircraft. However, pressure adaptive honeycomb inside of an aft-translating flap could induce some additional camber in the flap, which in turn increases the lift coefficient. For every percent of lift coefficient that is gained, the wing surface area can be made one percent smaller and hence the drag coefficient in cruise also decreases with a percent. Alternatively, pressure adaptive honeycomb could be used in small tabs such as the pressure adaptive Gurney flap that was presented in this document. It is up to future researchers and designers to fully explore the benefits of pressure adaptive honeycomb for aircraft performance.

REFERENCES

[1]   Ruijgrok, G.J.J., *Elements of Airplane Performance*, Delft University Press, Delft, The Netherlands, 1996.

[2]   Rudolph, P.K.C., "High-Lift Systems on Commercial Subsonic Airliners," NASA Contractor Report 4746, September, 1996.

[3]   Lentink, D., "Exploring the biofluiddynamics of swimming and flight," Wageningen University and Research Centre, Wageningen, Sept. 9, 2008.

[4]   Schairer, G.S., "Aircraft Design - Present and Future," *Journal of Aircraft*, Vol. 2, No. 5, 1965, pp. 361-367.

[5]   Barrett, R.M., "Adaptive Aerostructures Course Notes," Delft University of Technology, Delft, The Netherlands, Fall, 2003.

[6]   Morgan, N.B. and Broadley, M., "Taking the art out of smart! - Forming processes and durability issues for the application of NiTi shape memory alloys in medical devices," *Materials & Processes for Medical Devices Conference*, Anaheim, CA, 2003, ASM International.

[7]   Barrett, R.M., Burger, C., and Melian, J.P., "Recent Advances in Uninhabited Aerial Vehicle Flight Control with Aeroadaptive Aerostructures," *Proceedings of the 2001 Conference on Smart Technology, Demonstrators and Devices*, Edinburgh, 2001.

[8]   Kudva, J.N., "Overview of the DARPA Smart Wing Project," *Journal of Intelligent Material Systems and Structures*, Vol. 15, 2004, pp. 261-267.

[9]   Martin, C.A., Hallam, B.J., Flanagan, J.S., and Bartley-Cho, J., "Design, Fabrication, and Testing of a Scaled Wind Tunnel Model for the Smart Wing Project," *Journal of Intelligent Material Systems and Structures*, Vol. 15, 2004, pp. 269-278.

[10]   Bartley-Cho, J.D., Wang, D.P., Martin, C.A., Kudva, J.N., and West, M.N., "Development of High-rate, Adaptive Trailing Edge Control Surface for the Smart Wing Phase 2 Wind Tunnel Model," *Journal of Intelligent Material Systems and Structures*, Vol. 15, 2004, pp. 279-291.

[11]   Sanders, B., Cowan, D., and Scherer, L., "Aerodynamic Performance of the Smart Wing Control Effectors," *Journal of Intelligent Material Systems and Structures*, Vol. 15, 2004, pp. 293-303.

[12]   Rediniotis, O.K., Wilson, L.N., Lagoudas, D.C., and Khan, M.M., "Development of a Shape-Memory-Alloy Actuated Biomimetic Hydrofoil," *Journal of Intelligent Material Systems and Structures*, Vol. 13, 2002, pp. 35-49.

[13]   Ramrakhyani, D.S., Leisieutre, G.A., Frecker, M., and Bharti, S., "Aircraft Structural Morphing Using Tendon-Actuated Compliant Cellular Trusses," *Journal of Aircraft*, Vol. 42, No. 6, 2005, pp. 1615-1621.

[14]   Strelec, J.K., Lagoudas, D.C., Khan, M.A., and Yen, J., "Design and Implementation of a Shape Memory Alloy Actuated Reconfigurable Airfoil," *Journal of Intelligent Material Systems and Structures*, Vol. 14, 2003, pp. 257-273.

[15]   Calkins, F.T. and Butler, G.W., "Variable Geometry Chevrons for Jet Noise Reduction," *12th AIAA/CEAS Aeroacoustics Conference*, Cambridge, Massachusetts, 2006, AIAA Paper 2006-2546.

[16]   Calkins, F.T., Mabe, H.H., and Butler, G.W., "Boeing's Variable Geometry Chevron: morphing aerospace structures for jet noise reduction," *SPIE Smart Structures and Materials Conference*, San Diego, CA, 2006, SPIE, Vol. 6171.

[17]   Mabe, H.H., Calkins, F.T., and Butler, G.W., "Boeing's Variable Geometry Chevron: morphing aerospace structures for jet noise reduction," *47th AIAA/ASME/ASCE/AHS/ASC Structures, Structural Dynamics, and Materials Conference*, Newport, RI, 1-4 May, 2006, AIAA 2006-2142.

[18]   Taylor, C.J. and Washington, G.N., "A Comprehensive Piezoceramic Actuator Review," *Smart Structures and Materials*, 2002, SPIE, Vol. 4701, pp. 443-454.

[19]   Barrett, R., "Active Plate and Missile Wing Development Using DAP Elements," *AIAA Journal*, Vol. 32, No. 3, pp. 601 - 609.

[20]   Barrett, R.M., "Method and Apparatus for Structural Actuation and Sensing in a Desired Direction," University of Maryland, United States Patent 5,440,193, Aug. 8, 1995.

[21]   Barrett, R., "Active Plate and Missile Wing Development Using EDAP Elements," *Journal of Smart Materials and Structures*, Vol. 1, No. 3, 1996, pp. 214-226.

[22]   Barrett, R.M., "Adaptive Aerostructures: Improving High Performance Subscale Military UAVs," *45th AIAA/ASME/ASCE/AHS/ASC Structures, Structural Dynamics & Materials Conference*, Palm Springs, California, 2004, AIAA 2004-1886.

[23]   Barrett, R. and Lee, G., "Design Criteria, Aircraft Design, Fabrication and Testing of Sub-Canopy and Urban Micro-Aerial Vehicles," *AIAA/AHS International Powered Lift Conference*, Alexandria, Virginia, Nov. 1, 2000, AIAA.

[24]   Barrett, R., Brozoski, F., and Gross, R.S., "Design and Testing of Subsonic All-Moving Smart Flight Control Surfaces," *proceedings of the 36th Structures, Structural Dynamics and Materials Conference*, New Orleans, LA, 1995, AIAA-1995-1081, pp. 2289 - 2296.

[25]   Vos, R. and Barrett, R., "Post-Buckled Precompressed Techniques in Adaptive Aerostructures: An Overview," *ASME 2008 Conference on Smart Materials, Adaptive Structures and Intelligent Systems*, Ellicot City, MD, 28-30 October, 2008, SMASIS08-458.

[26]   Vos, R., Barrett, R., De Breuker, R., and Tiso, P., "Post-buckled precompressed elements: a new class of control actuators for morphing wing UAVs," *Journal of Smart Materials and Structures*, Vol. 16, 2007, pp. 919–926.

[27]   Vos, R., De Breuker, R., Barrett, R., and Tiso, P., "Morphing Wing Flight Control Via Postbuckled Precompressed Piezoelectric Actuators," *Journal of Aircraft*, Vol. 44, No. 4, 2007, pp. 1060-1068.

[28]   Barrett, R., "Improvements to Commercial and General Aviation via Adaptive Aerostructures," *7th AIAA Aviation Technology, Integration and Operations Conference (ATIO)*, Belfast, Northern Ireland, 18 - 20 September, 2007, AIAA 2007-7873, pp. 251-260.

[29]   Barrett, R. and Vos, R., "Design, Development and Testing of a Transonic Missile Fin Employing PBP/DEAS Actuators," *Smart Structures and Materials*, San Diego, California, 2008, SPIE, Vol. 6930-37.

[30]   Anon., "Comparison of EAPs with Other Actuator Technologies," SRI International and DARPA,   [cited: May 30, 2009]; Available from: ndeaa.jpl.nasa.gov/nasa-nde/lommas/eap/.

[31]   Anon., "Comparison of EAPs with Other Actuator Technologies," SRI International and DARPA, 2009 [cited: May 30, 2009]; Available from: ndeaa.jpl.nasa.gov/nasa-nde/lommas/eap/.

[32]   Vlot, A., Vogelesang, B., and De Vries, A.J., "Towards the application of fiber metal laminates in large aircraft," *Aircraft Engineering and Aerospace Technology: International Edition*, Vol. 71, No. 6, 1999, pp. 558-570.

[33]   Wright, O. and Kelly, F.C., *How We Invented the Airplane: An Illustrated History*, Dover Publications, New York, 1988.

[34]   Akhilesh, K.J. and Kudva, J.N., "Morphing Aircrat Concepts, Classification, and Challenges," *SPIE Smart Structures and Materials Conference*, San Diego, 2004, SPIE, Vol. 5388.

[35]   Lednicer, D., "The Incomplete Guide to Airfoil Usage," 2007 [cited: 7 January, 2007]; Available from: http://www.ae.uiuc.edu/m-selig/ads/aircraft.html.

[36]   Selig, M., "UIUC Airfoil Coordinate Database, Version 2.0," 2006 [cited: 20 December, 2006]; Available from: http://www.ae.uiuc.edu/m-selig/ads/coord_database.html.

[37]   Wortmann, F.X., *The Quest for High Lift*, The Soaring Society of America, Los Angeles, CA, 1974.

[38]   Roskam, J., *Airplane Design, part 6: Preliminary calculation aerodynamic, thrust and power characteristics*, DARcorp, Lawrence, KS, 1990.

[39]   Obert, E., *Vormgeving en Gebruik van Vliegtuigen*, Delft University of Technology, Delft, The Netherlands, 1989.

[40]   Liebeck, R.H., "Design of Subsonic Airfoils for High Lift," *Journal of Aircraft*, Vol. 15, No. 9, 1978, pp. 547-561.

[41]   Roskam, J., *Airplane Design, Part 3: Layout Design of Cockpit, Fuselage, Wing and Empennage: Cutaways and Inboard Profiles*, DARcorp, Lawrence, KS, 2002.

[42] Roskam, J., *Airplane Design, Part 2: Preliminary Configuration Design and Integration of the Propulsion System*, DARCorp, Lawrence, KS, 2006.

[43] Jenkinson, L.R., Simpkin, P., and Rhodes, D., *Civil jet aircraft design*, American Institute of Aeronautics and Astronautics, Reston, VA, 1999.

[44] NASA Dryden Flight Research Center, "The Supercritical Airfoil," NASA Dryden Technical Facts, NASA, 2004 [cited: 13 September, 2007]; Available from: http://www.nasa.gov/centers/dryden/about/Organizations/Technology/Facts/TF-2004-13-DFRC.html.

[45] Jackson, P., ed. *Jane's all the world aircraft*, McGraw-Hill: New York, 2007.

[46] Taylor, M.J.H., ed. *Brassey's world aircraft & system directory*, Brassey's: London, UK, 1999.

[47] Abbot, I.H. and VonDoenhoff, A.E., *Theory of Wing Sections*, ed. 1, Dover Publications, Inc, New York, 1959.

[48] Kientz, O.L., "Aeroplane Wing," United States Patent 1,790,309, Jan. 27, 1931.

[49] Krall, K.M., "Airfoil Construction," Vought Corporation, United States Patent 4,296,900, Oct. 27, 1981.

[50] Ferguson, S.R., "Airfoil having Adjustable Shape," Northrop Corporation, United States Patent 4,582,278, Apr. 15, 1986.

[51] Hoak, D.E. and Finck, R.D., "USAF Stability and Control Datcom," Flight Control Division, Airfoirce Flight Dynamics Laboratory, Wright Patterson AFB, Ohio, 1978.

[52] Demele, F.A. and Sutton, F., "The effects of increasing the leading-edge radius and adding forward camber on the aerodynamic characteristics of a wing with 35 degrees of sweepback," NACA, Ames Aeronautical Laboratory, Moffett Field, CA, 9 February, 1951.

[53] Parker, H.F., "The Parker Variable Camber Wing," National Advisory Committee for Aeronautics, Washington D.C., 1920.

[54] Lyon, D.G., "Variable Shaped Airfoil," United States Patent 3,179,357, April 20, 1965.

[55]   Rodriguez, A.R., "Morphing Aircraft Technology Survey," *45th AIAA Aerospace Sciences Meeting and Exhibit*, Reno, NV, 2007, AIAA Paper 2007-1258.

[56]   DeCamp, R.W. and Hardy, R., "Mission adaptive wing advanced research concepts, "*A collection of Technical Papers (AIAA Atmospheric Flight Mechanics Conference)*, American Institute of Aeronautics and Astronautics, Washington D.C., 1984.

[57]   Gould, D.K., "Mission Adaptive Wing Flight Demonstration Program," *SAE Aerospace Congress & Exposition*, Anaheim California, 1981, SAE-811035.

[58]   Lewis, G.E., Thomasson, R.E., and Nelson, D.W., "Win Lift/Drag Optimization System," The Boeing Company, United States Patent 4,899,284, Feb. 6, 1990.

[59]   Powers, S.G. and Webb, L.D., "Flight Wing Surface Pressure and Boundary-Layer Data Report from the F-111 Smooth Variable-Camber Supercritical Mission Adaptive Wing," NASA Technical Memorandum 4789, June, 1997.

[60]   Lu, K.-K. and Kota, S., "Design of Compliant Mechanisms for Morphing Structural Shapes," *Journal of Intelligent Material Systems and Structures*, Vol. 14, 2003, pp. 379-391.

[61]   Campanile, L.F. and Sachau, D., "The Belt-Rib Concept: A Structronic Approach to Variable Camber," *Journal of Intelligent Material Systems and Structures*, Vol. 11, 2000, pp. 215-224.

[62]   Murray, G. and Gandhi, F., "Flexible Matrix Composite Skins for One-Dimensional Wing Morphing," *48th AIAA/ASME/ASCE/AHS/ASC Structures, Structural Dynamics, and Materials Conference*, Honolulu, HW, 2007, AIAA Paper 2007-1737.

[63]   Reich, G.W. and Sanders, B., "Development of Skins for Morphing Aircraft Applications via Topology Optimization," *48th AIAA/ASME/ASCE/AHS/ASC Structures, Structural Dynamics, and Materials Conference*, Honolulu, HW, 2007, AIAA Paper 2007-1738.

[64]   Kota, S., Hetrick, J.A., and Osborn, R.F., "Adaptive structures: Moving into the mainstream," *Aerospace America*, American Institute of Aeronautics and Astronautics, Washington, DC, September, 2006.

[65]   Maki, R. and Hunton, L.W., "An Investigation of Subsonic Speed of Several Modifications to the Leading-Edge Region of the NACA 64 A010 Airfoil Section," NACA, Ames Aeronautical Laboratory, Moffett Field, CA, December, 1956.

[66]   Kelly, J.A., "Effects of modifications to the leading-edge region on the stalling characteristics of the NACA 63(sub 1)-012 airfoil section," NACA, November, 1950.

[67]   Hicks, R.M., Mendoza, J.P., and Bandettini, A., "Effects of forward contour modification on the aerodynamic characteristics of the NACA 641-212 airfoil section," NASA, Ames Research Center, 1 September, 1975.

[68]   Kota, S., Hetrick, J.A., and Jr., R.F.O., "Adaptive structures: Moving into the mainstream," *Aerospace America*, American Institute of Aeronautics and Astronautics, Washington, DC, September, 2006.

[69]   Cole, J.B., "Variable Camber Leading Edge Assembly for an Airfoil," The Boeing Company, United States Patent 4,475,702, Oct. 9, 1984.

[70]   Sanders, B., Crowe, R., and Garcia, E., "Defense Advanced Research Projects Agency – Smart Materials and Structures Demonstration Program Overview," *Journal of Intelligent Material Systems and Structures*, Vol. 15, 2004, pp. 227-233.

[71]   Garcia, H.M., Abdulrahim, M., and Lind, R., "Roll control for a Micro Air Vehicle using Active Wing Morphing," *AIAA Guidance, Navigation, and Control Conference and Exhibit*, Austin, TX, 11-14 August, 2003, AIAA-2003-5347.

[72]   Cadogan, D., Smith, T., Uhelsky, F., and MacKusick, M., "Morphing Inflatable Wing Development for Compact Package Unmanned Aerial Vehicles," *45th AIAA/ASME/ASCE/AHS/ASC Structures, Structural Dynamics and Materials Conference*, Palm Springs, CA, April 19-22, 2004, AIAA 2004-1807.

[73]   Jirasek, A., "Vortex-Generator Model and Its Application to Flow Control," *Journal of Aircraft*, Vol. 42, No. 6, 2005, pp. 1486-1491.

[74]   Barrett, R.M., "An Experimental Evaluation of Smart Tetrahedral Vortex Generators," *Department of Aerospace Engineering*, The University of Kansas, Lawrence, KS, 1993.

[75]   Barrett, R. and Farokhi, S., "Subsonic Aerodynamics and Performance of a Smart Vortex Generator System," *Journal of Aircraft*, Vol. 33, No. 2, 1996, pp. 393-398.

[76]   Nikolic, V.R., "Additional Aerodynamic Features of Wing-Gurney Flap Flows," *Journal of Aircraft*, Vol. 43, No. 5, 2006, pp. 1325-1333.

[77]   Cavanaugh, M.A., Robertso, P., and Mason, W.H., "Wind Tunnel Test of Gurney Flaps and T-Strips on an NACA 23012 Wing," *25th AIAA Applied Aerodynamics Conference*, Miami, FL, 2007, AIAA Paper 2007-4175.

[78]   Van Dam, C.P., Yen, D.T., and Vijgen, P.M.H.W., "Gurney Flap Experiments on Airfoil and Wings," *Journal of Aircraft*, Vol. 36, No. 2, 1999, pp. 484-486.

[79]   Traub, L.W., Miller, A.C., and Rediniotis, O., "Preliminary Parametric Study of Gurney-Flap Dependencies," *Journal of Aircraft*, Vol. 43, No. 4, 2006, pp. 1242-1244.

[80]   Ashby, D.L., "Effect of Lift-Enhancing Tabs on a Two-Element Airfoil," *International Journal of Aerospace Engineering*, Vol. 16, 1996, pp. 31-37.

[81]   Katz, J. and Largman, R., "Effect of 90 Degree Flap on the Aerodynamics of a Two-Element Airfoil," *Journal of Fluid Engineering*, Vol. 111, 1989, pp. 93,94.

[82]   Vu, P. and Chavez, F., "Investigation of the effects of stiffness on control power via a morphing wing technology," *46th AIAA/ASME/ASCE/AHS/ASC Structures, Structural Dynamics, and Materials Conference*, Austin, TX, 18-21April, 2005, AIAA Paper 2005-2039.

[83]   Pendleton, E., Bessett, D., Field, P., Miller, G., and Griffin, K., "Active Aeroelastic Wing Flight Research Program: Technical Program and Model Analytical Development," *Journal of Aircraft*, Vol. 37, No. 4, 2000, pp. 554-561.

[84]   Andersen, G., Forster, E., Kolonay, R., and Eastep, F., "Multiple Control Surface Utilization in Active Aeroelastic Wing Technology," *Journal of Aircraft*, Vol. 34, No. 4, 1997, pp. 552-557.

[85]   Noll, T.E. and Eastep, F.E., "Active Flexible Wing Program," *Journal of Aircraft*, Vol. 32, No. 1, 1995, pp. 9.

[86] Voracek, D., Pendleton, E., Reichenbach, E., Griffin, D.K., and Welch, L., "The Active Aeroelastic Wing Phase I Flight Research Through January 2003," NASA, 2003.

[87] Chen, P.C., Sarhaddi, D., Jha, R., Liu, D.D., Griffin, K., and Yurkovich, R., "Variable Stiffness Spar Approach for Aircraft Maneuver Enhancement Using ASTROS," *Journal of Aircraft*, Vol. 37, No. 5, 2000, pp. 865.

[88] Vos, R., Hodigere-Siddaramaiah, V., and Cooper, J., "Aeroelastic Flight Control for Subscale UAVs," *48th AIAA/ASME/ASCE/AHS/ASC Structures, Structural Dynamics, and Materials Conference*, Honolulu, Hawaii, 23 - 26 April, 2007, AIAA paper 2007-1706.

[89] Amprikidis, M. and Cooper, J.E., "Experimental Validation of Wing Twist Control using Adaptive Internal Structures," *45th AIAA/ASME/ASCE/AHS/ASC Structures, Structural Dynamics, and Materials Conference* Palm Springs, CA, 2004, AIAA Paper 2004-1884.

[90] Phillips, W.F., "Lifting-Line Analysis for Twisted Wings and Washout-Optimized Wings," *Journal of Aircraft*, Vol. 41, No. 1, 2004, pp. 128-136.

[91] Kudva, J.N., Appa, K., Martin, C.A., and Jardine, A.P., "Design, Fabrication, and Testing of the DARPA / Wright Lab "Smart Wing" Wind Tunnel Model," *38th AIAA/ASME/ASCE/AHS/ASC Structures, Structural Dynamics, and Materials Conference and Exhibit*, Kissimmee, FL, Apr. 7-10, 1997.

[92] Vos, R., Gurdal, Z., and Abdalla, M., "A Novel Mechanism for Wing Warping," *49th AIAA/ASME/ASCE/AHS/ASC Structures, Structural Dynamics, and Materials Conference*, Schaumburg, IL, Apr. 7-10, 2008, AIAA-2008-1879.

[93] Phillips, W.F., "Minimizing Induced Drag with Geometric and Aerodynamic Twist on a Wing of Arbitrary Planform," Department of Mechanical and Aerospace Engineering, Utah State University, Logan, 2003.

[94] Bowman, J., Sanders, B., Cannon, B., Kudva, J., Joshi, S., and Weisshaar, T., "Development of Next Generation Morphing Aircraft Structures," *48th AIAA/ASME/ASCE/AHS/ASC Structures, Structural Dynamics, and Materials Conference*, Honolulu, Hawaii, 2007, AIAA Paper 2007-1707.

243

[95]   Flanagan, J.S., Strutzenberg, R.C., Myers, R.B., and Rodrian, J.E., "Development and Flight Testing of a Morphing Aircraft, the NextGen MFX-1," *48th AIAA/ASME/ASCE/AHS/ASC Structures, Structural Dynamics, and Materials Conference*, Honolulu Hawaii, 2007, AIAA Paper 2007-1707.

[96]   NextGen Aeronautics," 2007 [cited: 09-23, 2007]; Available from: http://www.nextgenaero.com/.

[97]   Bye, D.R. and McClure, P.D., "Design of a Morphing Vehicle," *48th AIAA/ASME/ASCE/AHS/ASC Structures, Structural Dynamics, and Materials Conference*, Honolulu, HW, 23-26 April, 2007, AIAA Paper 2007-1728.

[98]   Love, M.H., Zink, P.S., Stroud, R.L., Bye, D.R., Rizk, S., and White, D., "Demonstration of Morphing Technology through Ground and Wind Tunnel Tests," *48th AIAA/ASME/ASCE/AHS/ASC Structures, Structural Dynamics, and Materials Conference*, Honolulu, HW, 23-26 April, 2007, AIAA Paper 2007-1729.

[99]   Ivanco, T.G., Scott, R.C., Love, M.H., Zink, S., and Weisshaar, T.A., "Validation of the Lockheed Martin Morphing Concept with Wind Tunnel Testing," *48th AIAA/ASME/ASCE/AHS/ASC Structures, Structural Dynamics, and Materials Conference*, Honolulu, Hawaii, 2007, AIAA Paper 2007-2235.

[100]   Anon., "Boeing 2707," 2008 [cited: 8 September, 2008]; Available from: http://en.wikipedia.org/wiki/Boeing_2707.

[101]   Thomas, G., "The New 747," *Airways*, Vol. 122, April 2006, pp. 16-22.

[102]   Anon., "Lost Classics - Boeing 2707-200 SST," [cited: September 8, 2008]; Available from: http://www.unrealaircraft.com/classics/sst.php.

[103]   Farokhi, S., *Aircraft Propulsion*, ed. 1, Wiley, New York, 2008.

[104]   Oort, A.H. and Rasmusson, E.M., "Atmospheric Circulation Statistics," US Deparment of Commerce, National Oceanic and Atmospheric Administration, Rockville, MD, September, 1971.

[105]   Anon., "Reference atmospheres for aerosapce use," International Organization for Standardization, 15 April, 1982.

[106]   Shavelson, R.J., *Statistical Reasoning for the Behavioral Sciences*, ed. 3, Allyn and Bacon, Boston, 1995.

[107]   Norris, R.K. and Pulliam, W.J., "Historical Perspective on Inflatable Wing Structures," *50th AIAA/ASME/ASCE/AHS/ASC Structures, Structural Dynamics, and Materials Conference*, Palm Springs, California, 4 - 7 May, 2009.

[108]   Sebrell, W.A., "Inflatable Wing," United States Energy Research and Development Administration, United States Patent 3,957,232, May 18, 1976.

[109]   Priddy, T.G., "Inflatable Wing," United States Department of Energy, United States Patent 7,725,021, Feb. 16, 1988.

[110]   Ritter, D.L., "Light Weight Pneumatic Airplane," United States Patent 2,886,265, May 12, 1959.

[111]   Bain, B.K., "Inflatable Airplane," United States Patent 3,106,373, Oct. 8, 1963.

[112]   Chutter, R.R., "Pneumatic Tubular Construction," United States Patent 3,473,761, Oct. 21, 1969.

[113]   Reinhard, A., To, F.E., Ramseier, O., and Kammer, R., "Adaptive Pneumatic Wing for Fixed Wing Aircraft," Prospective Concepts AG, United States Patent 6,199,796B1, Mar. 13, 2001.

[114]   Woods, B.K.S., Bubert, E.A., Kothera, C.S., and Wereley, N.M., "Design and Testing of a Biologically Inspired Pneumatic Trailing Edge Flap System," *49th AIAA/ASME/ASCE/AHS/ASC Structures, Structural Dynamics, and Materials Conference*, Schaumburg, IL, 7 - 10 April 2008, 2008.

[115]   Khire, R.A., Dessel, S.V., Messac, A., and Mullur, A.A., "Study of a Honeycomb-Type Rigidified Inflatable Structure for Housing," *Journal of Structural Engineering*, Vol. 132, No. 10, 2006, pp. 1664-1672.

[116]   Atli, B. and Gandhi, F., "Energy Absorption of Cellular Honeycombs with Various Cell Angles under In-Plane Compressive Loading," *49th AIAA/ASME/ASCE/AHS/ASC Structures, Structural Dynamics, and Materials*, Schaumburg, IL, 7 - 10 April, 2008.

[117] Shaw, J.A., Churchill, C., Grummon, D., Triantafyllidis, N., Michailidis, P., and Foltz, J., "Shape memory alloy honeycombs: experiments & simulation," *48th AIAA/ASME/ASCE/AHS/ASC Structures, Structural Dynamics, and Materials Conference*, Honolulu, Hawaii, 23 - 26 April, 2007.

[118] Turner, T.L., Buehrle, R.D., Cano, R.J., and Fleming, G.A., "Modeling, Fabrication, and Testing of a SMA Hybrid Composite Jet Engine Chevron Concept," *Journal of Intelligent Material Systems and Structures*, Vol. 17, 2006, pp. 483-497.

[119] Brentjes, J., "Honeycomb as an Energy Absorbing Material," *AIAA/ASME 8th Structures, Structural Dynamics & Materials Conference*, Palm Springs, California, March 1967, 1967, pp. 468-473.

[120] Goldsmith, W. and Sackman, J.L., "An Experimental Study of Energy Absorption in Impact on Sandwich Plates," *Int. J. Impact Eng.*, Vol. 12, No. 2, 1992, pp. 241-262.

[121] Atli, B. and Gandhi, F., "Energy Absorption of Cellular Honeycombs with Various Cell Angles under In-Plane Compressive Loading," *49th AIAA/ASME/ASCE/AHS/ASC Structures, Structural Dynamics, and Materials Conference*, Schaumburg, IL, 7 - 10 April, 2008.

[122] Olympio, K.R. and Gandhi, F., "Zero-ν Cellular Honeycomb Flexible Skins for One-Dimensional Wing Morphing," *48th AIAA/ASME/ASCE/AHS/ASC Structures, Structural Dynamics, and Materials Conference*, Honolulu, Hawaii, 23 - 26 April 2007, 2007, AIAA 2007-1735.

[123] Bubert, E.A., Woods, B.K.S., Kothera, C.S., and Wereley, N.M., "Design and Fabrication of a Passive 1-D Morphing Aircraft Skin," *49th AIAA/ASME/ASCE/AHS/ASC Structures, Structural Dynamics, and Materials Conference*, Schaumburg, IL, 7 - 10 April, 2008, AIAA 2007-1737.

[124] Anon., "Jabiru J250 Sportplane," 2008 [cited: 8 September, 2008]; Available from: http://www.jabirupacific.com/specs/j250sp.htm.

[125] Gruensfelder, C.A. and Wille, R.H., "Mission adaptive Inlet," The Boeing Company, United States Patent 6,260,567 B1, 2001.

[126] Monner, H.P., Kintscher, M., Lorkowski, T., and Storm, S., "Design of a Smart Droop Nose as Leading Edge High Lift System for Transportation Aircrafts," *50th AIAA/ASME/ASCE/AHS/ASC Structures, Structural Dynamics, and Materials Conference*, Palm Springs, CA, 4-7 May, 2009, AIAA.

[127] Anon., "El Alto International Airport," 2007 [cited: 13 October, 2007]; Available from: http://en.wikipedia.org/wiki/El_Alto_International_Airport.

[128] Pulliam, W.J.," Personal Communication, Palm Springs, CA, May 4, 2009.

[129] Gibson, L.J. and Ashby, M.F., *Cellular Solids, Structure and Properties*, ed. 1, Cambridge University Press, 1988.

[130] Rolle, K.C., *Thermodynamics and Heat Power*, ed. 6, Pearson Prentice Hall, Upper Saddle River, NJ, 2005.

[131] Olympio, K. and Gandhi, F., "Zero-v Cellular Honeycomb Flexible Skins for One-dimensional Wing Morphing," *48th AIAA/ASME/ASCE/AHS/ASC Structures, Structural Dynamics, and Materials Conference*, Honolulu, HI, 23 - 26 April, 2007, AIAA 2007-1735.

[132] Anon., "Linear Servo Actuators L16 Series 2"&3" Stroke 6 to 200+ Lbf Loads," Craig Kackert Design Tech., Inc., Simi Valley, CA, 2008.

[133] Surana, K.S., Ahmadi, A.R., and Reddy, J.N., "The K-Version of Finite Element Method for Self-Adjoint Operators in BVP," *International Journal of Computational Engineering Science*, Vol. 3, No. 3, 2002, pp. 155-218.

[134] Moody, T.C., "Local Estimation of Modeling Error in Multi-Scale Modeling of Heterogeneous Elastic Solids," *Mechanical Engineering Department*, The University of Kansas, Lawrence, KS, 27 February 2008, 2008.

[135] Giles, M.B. and Drela, M., "Two-Dimensional Transonic Aerodynamic Design Method," *AIAA Journal*, Vol. 25, No. 9, 1987, pp. 1199-1206.

[136] Drela, M., "Two-Dimensional Transonic Aerodynamic Design and Analysis Using the Euler Equations," February, 1986.

[137] Drela, M. and Giles, M.B., "Viscous-Inviscid Analysis of Transonic and Low Reynolds Number Airfoils," *AIAA Journal*, Vol. 25, No. 10, 1987, pp. 1347-1355.

[138]   Anderson, J.D., *Fundamentals of Aerodynamics*, ed. 2, McGraw-Hill, New York, 1991.

[139]   Swafford, T.W., "Analytical Approximation of Two-Dimensional Separated Turbulent Boundary-Layer Velocity Profiles," *AIAA Journal*, Vol. 21, 1983, pp. 923-926.

[140]   Schlichting, H. and Gersten, K., *Boundary-Layer Theory*, ed. 8, Springer, Heidelberg, 2000.

[141]   Drela, M. and Youngren, H., "XFOIL 6.94 User Guide," MIT Aero & Astro, 2001.

[142]   Anon., "Stainless Steel Shim Tolerances," Precision Brand, 2008 [cited: 15 May, 2008]; Available from: http://www.precisionbrand.com/.

[143]   Anon., "Shim Stock- Metal Steel Shim Stock Hard cold rolled SAE 101 Steel, Rockwell B-90," Small Parts, Inc, 2008 [cited: 15 May, 2008]; Available from: http://www.smallparts.com/.

[144]   Barlow, J.B., Rae, W.H., and Pope, A., *Low-Speed Wind Tunnel Testing* ed. 3, Wiley & Sons, New York, 1999.

APPENDIX A <u>EARTH LATITUDES</u>

To remind the reader how the latitudes are distributed geographically, the figure below shows a detailed overview. Note that both Europe and the United States fall within the 30-60° latitude band.
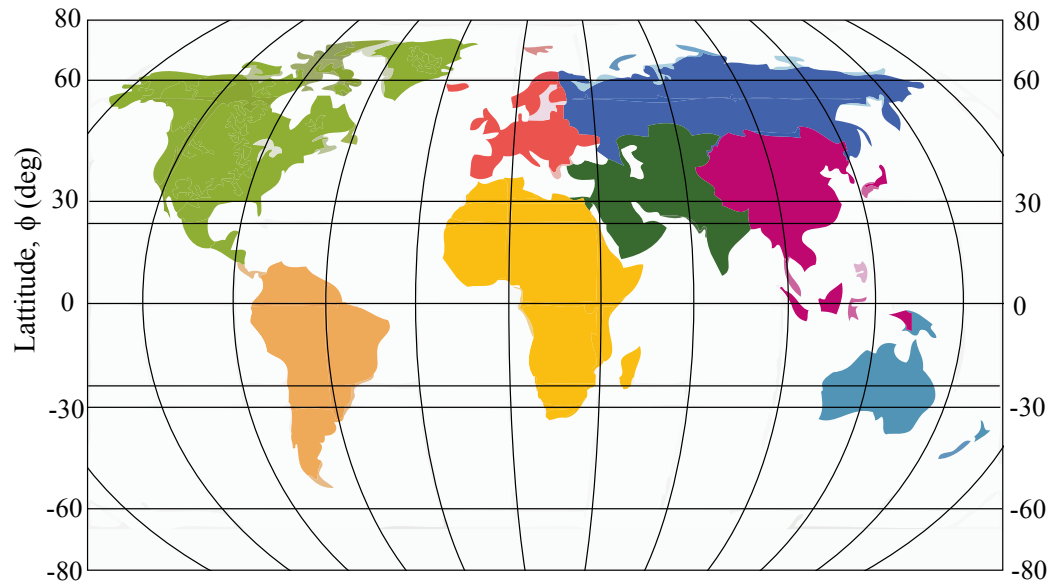
Figure A. 1   Definition of Earth Latitudes

APPENDIX B <u>PRESSURE STIFFNESS CALCULATION</u>

B.1   In-Plane Principal Stiffnesses

This section details how the normal in-plane pressure stiffness is derived. First, recall the expression for longitudinal, resp., lateral stiffness from Chapter 4:

$$E_x = \frac{d\sigma_x}{d\varepsilon_x} = \frac{d\sigma_x}{d\theta}\frac{d\theta}{d\varepsilon_x} \tag{4.44}$$

$$E_y = \frac{d\sigma_y}{d\varepsilon_y} = \frac{d\sigma_y}{d\theta}\frac{d\theta}{d\varepsilon_y} \tag{4.45}$$

Using the expressions for stress and strain laid out in Section 4.2.4, the following substitutions are introduced:

$$s_x = \cos\theta \quad s_y = \sin\theta \quad C_x = 1/l^2 \sin\theta_i \quad C_y = 1/l^2(1 + \cos\theta_i)$$

If a constant mass is considered, the stress derivatives can be solved to read the following:

$$\frac{d\sigma_x}{d\theta} = C_x \frac{(mRT/V - p_a)dV/d\theta - [mRT\ln(V/V_i) - p_a(V - V_i)]ds_x/d\theta}{(s_x - s_{xi})^2} \tag{B.1}$$

$$\frac{d\sigma_y}{d\theta} = C_y \frac{(mRT/V - p_a)dV/d\theta - [mRT\ln(V/V_i) - p_a(V - V_i)]ds_y/d\theta}{\left(s_y - s_{yi}\right)^2} \tag{B.2}$$

Note that the subscript "i" refers to the initial condition, or when $\theta = \theta_i$. Furthermore, Equation 4.29 is employed to calculate the volume as a function of the honeycomb angle, θ. If the pressure remains constant during deformation, the above relations change to:

$$\frac{d\sigma_x}{d\theta} = C_x(p - p_a) \frac{(s_x - s_{xi})dV/d\theta - (V - V_i)ds_x/d\theta}{(s_x - s_{xi})^2} \tag{B.3}$$

$$\frac{d\sigma_y}{d\theta} = C_y(p - p_a) \frac{(s_y - s_{yi})dV/d\theta - (V - V_i)ds_y/d\theta}{\left(s_y - s_{yi}\right)^2} \tag{B.4}$$

Elaborating on the derivatives that appear in the above equations yields the following relationships:

$$\frac{dV}{d\theta} = \zeta l^2(\cos\theta + \cos 2\theta) \tag{B.5}$$

$$\frac{\mathrm{d}s_x}{\mathrm{d}\theta} = -l\sin\theta \tag{B.6}$$

$$\frac{\mathrm{d}s_y}{\mathrm{d}\theta} = l\cos\theta \tag{B.7}$$

The strain derivatives are evaluated next:

$$\frac{\mathrm{d}\theta}{\mathrm{d}\varepsilon_x} = -\frac{1+\cos\theta_i}{\sin\theta} \tag{B.8}$$

$$\frac{\mathrm{d}\theta}{\mathrm{d}\varepsilon_y} = \frac{\sin\theta_i}{\cos\theta} \tag{B.9}$$

When substituting the above equations and the stress-derivatives in Equations 4.44 and 4.45 a relation between the stiffness, E, and the honeycomb, θ, is found. Since the strain is coupled geometrically to the honeycomb angle, a graphical relation can be shown between strain and stiffness. This relation is presented in Figure 4.11.

B.2   In-plane Shear Stiffness

This section details how the in-plane shear stiffness is derived. Recall from Chapter 4 that the shear stiffness is defined as follows:

$$G_{xy} = \frac{\mathrm{d}\tau_{xy}}{\mathrm{d}\gamma}\frac{\mathrm{d}\gamma}{\mathrm{d}\gamma_{xy}} \tag{4.52}$$

Now, this derivative can be evaluated similarly to the analysis laid out in the previous section. If a constant mass is present Equation 4.52 results in the following expression:

$$\frac{\mathrm{d}\tau_{xy}}{\mathrm{d}\gamma_{xy}} = \frac{\sin\gamma(mRT/V-p_a)\mathrm{d}V/\mathrm{d}\gamma - [mRT\ln(V/V_i)-p_a(V-V_i)]\cos\gamma}{2l^2\sin\theta_i\sin^2\gamma} \tag{B.10}$$

The above equation is a function of γ only. All the remaining terms are constants or depend on the shear strain. In addition, the subscripts on γ are dropped for convenience.

When the pressure is held constant the above equation changes to:

$$\frac{\mathrm{d}\tau_{xy}}{\mathrm{d}\gamma_{xy}} = (p - p_a)\frac{\sin\gamma\,\mathrm{d}V/\mathrm{d}\gamma - (V-V_i)\cos\gamma}{2l^2\sin\theta_i\sin^2\gamma} \tag{B.11}$$

251

Notice that the volume and volume derivative are different from those in the previous section. In the case of shear deformation, the volume is given by Equation 4.48 and its derivative with respect to the shear strain reads:

$$\frac{dV}{d\gamma} = -\zeta l^2 \sin\theta_i \sin\gamma \tag{B.12}$$

The inverse of the shear strain derivative, with respect to the angle, γ, is calculated as follows:

$$\frac{d\gamma}{d\gamma_{xy}} = \frac{1 + 2\cos\theta_i \cos\gamma + \cos^2\theta_i}{1 + \cos\theta_i \cos\gamma} \tag{B.13}$$

Appropriate substitution of the above expressions into Equation 4.52 results in an analytic expression that relates the shear stiffness to the honeycomb angle and a set of constants.

APPENDIX C <u>WIND TUNNEL DATA</u>

This appendix presents the wind tunnel data that was gathered as well as the data that was gathered from Xfoil. Section C.1 shows the raw wind tunnel data, while in Section C.2 the uncrorrected, wall-corrected, and predicted aerodynamic coefficients are presented.

C.1   Raw Wind Tunnel Data

Table C. 1   Tabulated Raw Wind Tunnel Data

Lift (lb)	Drag (lb)	Pitch (lbin)	Side Force (lb)	Roll (lbin)	Yaw (lbin)	AoA (deg)	speed (ft/s)	Mean Temperature (R)	Reynolds number (1/ft)	Density (slug/ft³)	Picture #	CDP (kPa)
19	3.4	-206	-2.2	130	-35	-6	51	532	3.03E+05	0.00228	1405	0.0
16	3.2	-188	-2.0	134	-38	-6	51	532	3.06E+05	0.00228	1406	9.8
14	2.8	-167	-1.9	128	-33	-6	52	532	3.10E+05	0.00228	1407	20.0
12	2.8	-152	-1.9	128	-33	-6	52	532	3.11E+05	0.00228	1408	30.1
11	2.4	-137	-2.0	125	-31	-6	52	532	3.12E+05	0.00228	1409	40.2
28	4.1	-363	-4.2	224	-38	-6	76	533	4.52E+05	0.00228	1410	0.0
25	3.9	-334	-4.2	229	-37	-6	76	533	4.54E+05	0.00228	1411	10.1
20	3.7	-301	-4.0	222	-36	-6	77	533	4.57E+05	0.00228	1412	20.1
17	3.5	-262	-3.8	216	-33	-6	77	533	4.59E+05	0.00228	1413	29.9
14	3.7	-242	-3.6	212	-33	-6	77	533	4.59E+05	0.00228	1414	40.2
28	7.5	-571	-5.7	277	-55	-6	103	533	6.12E+05	0.00227	1415	0.0
22	7.3	-517	-5.8	271	-52	-6	103	533	6.13E+05	0.00227	1416	10.0
16	6.9	-463	-5.6	263	-46	-6	104	533	6.14E+05	0.00227	1417	20.2
12	6.2	-405	-5.4	260	-42	-6	104	534	6.15E+05	0.00227	1418	30.2
7	5.8	-354	-5.3	259	-38	-6	104	534	6.15E+05	0.00227	1419	40.3
21	3.9	-203	-1.8	87	-27	-4	51	532	3.12E+05	0.00233	1187	0.0
17	3.5	-185	-1.7	94	-30	-4	52	532	3.18E+05	0.00233	1188	10.0
15	3.2	-167	-1.7	96	-31	-4	53	532	3.21E+05	0.00233	1189	20.0
12	3.0	-147	-1.4	92	-29	-4	53	532	3.22E+05	0.00233	1190	30.0
12	2.9	-134	-1.5	91	-28	-4	53	532	3.24E+05	0.00233	1191	40.1
36	4.8	-358	-3.8	192	-33	-4	76	532	4.64E+05	0.00233	1192	0.0

30	4.3	-321	-3.7	194	-33	-4	77	532	4.67E+05	0.00232	1193	10.0
26	4.1	-291	-3.5	196	-33	-4	77	533	4.69E+05	0.00232	1194	19.9
22	3.7	-254	-3.4	189	-31	-4	77	533	4.70E+05	0.00232	1195	30.0
19	3.7	-224	-3.3	189	-31	-4	78	533	4.71E+05	0.00232	1196	40.0
42	7.7	-533	-5.6	275	-52	-4	102	533	6.21E+05	0.00232	1197	0.0
35	7.0	-483	-5.6	271	-49	-4	103	533	6.22E+05	0.00232	1198	10.2
30	6.5	-426	-5.5	272	-45	-4	103	533	6.23E+05	0.00232	1199	20.0
23	6.0	-368	-5.4	258	-38	-4	103	533	6.25E+05	0.00232	1200	30.0
20	5.8	-331	-5.4	262	-33	-4	104	533	6.26E+05	0.00232	1201	40.0
24	3.9	-197	-1.7	81	-26	-2	52	529	3.18E+05	0.00234	1203	0.0
21	3.4	-178	-1.4	84	-28	-2	53	529	3.24E+05	0.00234	1204	10.0
18	3.1	-161	-1.4	86	-27	-2	53	529	3.29E+05	0.00234	1205	20.0
16	2.7	-144	-1.3	87	-24	-2	54	529	3.30E+05	0.00234	1206	30.0
15	2.5	-127	-1.1	83	-20	-2	54	529	3.31E+05	0.00234	1207	39.9
41	3.7	-326	-3.3	185	-29	-2	76	530	4.65E+05	0.00234	1208	0.0
36	3.6	-292	-3.7	189	-33	-2	77	530	4.70E+05	0.00234	1209	10.0
33	3.1	-268	-3.1	181	-26	-2	77	530	4.71E+05	0.00233	1210	20.1
29	3.2	-238	-3.1	177	-27	-2	77	530	4.73E+05	0.00233	1211	30.0
26	3.6	-218	-2.8	172	-28	-2	77	530	4.73E+05	0.00233	1212	40.0
48	7.6	-493	-5.2	240	-39	-2	103	531	6.29E+05	0.00233	1214	0.0
45	7.7	-459	-6.6	255	-53	-2	103	531	6.28E+05	0.00232	1215	10.0
39	6.5	-412	-4.9	235	-34	-2	103	531	6.30E+05	0.00233	1216	20.0
36	5.9	-368	-5.0	235	-36	-2	104	531	6.34E+05	0.00233	1217	30.0
33	5.3	-324	-4.3	221	-29	-2	104	531	6.32E+05	0.00232	1218	40.3
26	3.6	-181	-1.4	70	-13	0	53	530	3.24E+05	0.00234	1156	0.0
24	3.1	-164	-1.3	75	-15	0	54	530	3.30E+05	0.00233	1157	10.0
21	2.8	-148	-1.2	75	-16	0	54	531	3.33E+05	0.00233	1158	20.0
19	2.6	-132	-1.1	74	-16	0	55	531	3.34E+05	0.00233	1159	29.8
18	2.5	-118	-0.9	74	-17	0	55	531	3.37E+05	0.00233	1160	40.1
46	5.1	-317	-3.3	155	-22	0	76	531	4.64E+05	0.00233	1161	0.0
40	4.2	-274	-3.0	164	-24	0	77	531	4.68E+05	0.00233	1162	10.0
38	3.9	-252	-3.0	163	-24	0	77	531	4.70E+05	0.00233	1163	20.1
35	3.6	-225	-2.9	161	-25	0	77	531	4.71E+05	0.00233	1164	30.0
32	3.7	-204	-2.8	162	-26	0	77	531	4.72E+05	0.00233	1165	40.1
62	8.2	-473	-6.0	261	-48	0	103	532	6.24E+05	0.00232	1166	0.0
58	7.6	-428	-5.7	249	-48	0	103	532	6.26E+05	0.00232	1167	10.1
53	7.4	-384	-5.7	267	-47	0	104	533	6.28E+05	0.00232	1168	20.0
49	6.8	-338	-5.6	261	-45	0	104	533	6.29E+05	0.00232	1169	30.0
44	6.3	-295	-5.5	256	-43	0	104	533	6.29E+05	0.00232	1170	40.1

26	3.9	-161	-1.5	78	-12	2	51	531	3.11E+05	0.00233	1224	0.0
23	3.6	-144	-1.5	78	-13	2	52	531	3.17E+05	0.00233	1225	9.8
21	3.2	-129	-1.6	84	-17	2	53	531	3.21E+05	0.00233	1226	20.1
20	2.6	-117	-1.3	82	-18	2	53	531	3.22E+05	0.00233	1227	30.1
19	2.6	-106	-1.5	84	-17	2	53	531	3.23E+05	0.00233	1228	40.1
48	5.0	-273	-2.7	172	-12	2	74	531	4.51E+05	0.00233	1229	0.0
44	5.3	-254	-2.7	171	-24	2	75	531	4.54E+05	0.00233	1230	10.0
41	5.1	-236	-2.6	170	-32	2	75	531	4.57E+05	0.00233	1231	20.0
38	5.0	-219	-2.6	167	-37	2	75	531	4.58E+05	0.00232	1232	30.0
37	4.7	-202	-2.5	163	-36	2	75	531	4.58E+05	0.00232	1233	40.1
68	9.4	-433	-4.7	246	-46	2	102	531	6.20E+05	0.00232	1234	0.0
65	9.1	-406	-4.8	245	-47	2	102	532	6.22E+05	0.00232	1235	10.0
61	8.8	-370	-4.8	245	-48	2	103	532	6.23E+05	0.00232	1236	20.0
57	8.1	-333	-4.8	249	-50	2	103	532	6.25E+05	0.00232	1237	29.9
53	7.9	-302	-4.6	235	-47	2	103	532	6.25E+05	0.00232	1238	40.2
26	4.1	-139	-1.6	76	-11	4	50	531	3.02E+05	0.00232	1248	0.0
24	4.0	-127	-1.5	71	-10	4	50	531	3.07E+05	0.00232	1249	10.0
25	2.4	-121	-0.9	73	-10	4	51	531	3.11E+05	0.00232	1250	20.0
22	2.6	-108	-1.3	78	-13	4	51	531	3.13E+05	0.00232	1251	30.0
21	2.4	-97	-1.0	75	-10	4	52	531	3.14E+05	0.00232	1252	40.1
52	5.8	-256	-2.9	158	-4	4	75	531	4.53E+05	0.00232	1253	0.0
48	6.0	-238	-2.9	165	-22	4	75	531	4.57E+05	0.00232	1254	10.0
47	5.3	-223	-2.3	159	-21	4	76	531	4.59E+05	0.00232	1255	20.1
42	5.7	-198	-2.6	164	-26	4	76	531	4.60E+05	0.00232	1256	30.0
41	5.2	-182	-2.3	157	-26	4	76	531	4.61E+05	0.00232	1257	40.0
79	9.9	-422	-4.8	225	-35	4	103	532	6.23E+05	0.00231	1258	0.0
72	9.9	-374	-5.2	229	-42	4	103	532	6.26E+05	0.00231	1259	10.0
70	8.6	-353	-4.5	222	-39	4	104	532	6.26E+05	0.00231	1260	20.1
66	8.7	-318	-4.9	225	-40	4	104	533	6.27E+05	0.00231	1261	30.4
62	8.9	-282	-4.9	222	-40	4	104	533	6.28E+05	0.00231	1262	40.2
30	4.1	-129	-1.7	114	-18	6	50	532	3.01E+05	0.00228	1420	0.0
28	3.9	-118	-1.5	103	-14	6	52	532	3.07E+05	0.00228	1421	10.0
27	3.3	-106	-1.5	110	-15	6	52	532	3.10E+05	0.00228	1422	20.1
25	2.8	-95	-1.5	110	-12	6	52	532	3.12E+05	0.00228	1423	30.0
25	2.4	-87	-1.1	106	-11	6	53	532	3.13E+05	0.00228	1424	40.1
58	7.6	-257	-3.1	225	-38	6	75	532	4.47E+05	0.00228	1425	0.0
55	7.9	-233	-3.1	219	-41	6	76	533	4.52E+05	0.00228	1426	9.9
52	7.3	-210	-2.7	217	-45	6	76	533	4.55E+05	0.00228	1427	20.2
50	7.1	-195	-2.3	213	-42	6	77	533	4.57E+05	0.00227	1428	30.1
49	6.7	-180	-2.5	216	-41	6	77	533	4.57E+05	0.00227	1429	40.1

87	13.1	-395	-1.8	275	-61	6	102	533	6.06E+05	0.00227	1430	0.0
85	12.6	-376	-1.5	272	-64	6	102	533	6.06E+05	0.00227	1431	9.9
81	11.8	-338	-1.8	269	-64	6	103	533	6.08E+05	0.00227	1432	20.2
77	11.5	-311	-1.6	270	-61	6	103	533	6.09E+05	0.00227	1433	30.0
73	11.1	-279	-1.8	268	-61	6	103	534	6.09E+05	0.00227	1434	40.0
30	4.5	-121	-1.6	75	-10	8	51	532	3.09E+05	0.00231	1284	0.0
30	3.9	-111	-1.1	70	-10	8	52	532	3.16E+05	0.00231	1285	10.0
30	3.4	-104	-0.9	70	-11	8	53	532	3.18E+05	0.00231	1286	20.0
27	4.0	-86	-1.8	80	-13	8	53	532	3.21E+05	0.00231	1287	29.8
27	3.0	-82	-1.3	74	-10	8	53	532	3.23E+05	0.00231	1288	40.0
60	6.5	-222	-2.3	133	-10	8	74	532	4.45E+05	0.00231	1289	0.0
57	6.7	-200	-2.3	131	-13	8	75	532	4.50E+05	0.00231	1290	10.0
54	6.7	-179	-2.4	138	-13	8	75	532	4.53E+05	0.00231	1291	20.0
53	6.1	-162	-2.6	139	-19	8	75	532	4.55E+05	0.00231	1292	30.0
52	5.7	-144	-2.4	140	-18	8	76	532	4.56E+05	0.00231	1293	40.2
95	10.2	-319	-4.3	213	-17	8	101	533	6.09E+05	0.00230	1294	0.0
93	9.9	-303	-4.3	220	-20	8	101	533	6.08E+05	0.00230	1295	10.0
89	9.5	-271	-4.2	219	-22	8	102	533	6.11E+05	0.00230	1296	20.1
86	8.9	-238	-4.1	219	-25	8	102	533	6.12E+05	0.00230	1297	29.9
83	8.7	-217	-4.0	222	-27	8	102	533	6.12E+05	0.00230	1298	40.2
32	4.0	-102	-1.0	84	-14	10	49	532	2.98E+05	0.00231	1299	0.0
31	4.1	-97	-1.3	78	-12	10	51	532	3.05E+05	0.00231	1300	10.0
30	3.8	-88	-1.3	79	-12	10	51	532	3.09E+05	0.00231	1301	19.9
30	3.4	-79	-1.1	78	-10	10	52	532	3.12E+05	0.00231	1302	30.1
29	3.3	-72	-0.9	74	-10	10	52	532	3.13E+05	0.00231	1303	40.1
63	7.9	-197	-2.0	148	-11	10	74	532	4.44E+05	0.00230	1304	0.0
62	7.5	-179	-2.3	150	-16	10	75	533	4.49E+05	0.00230	1305	10.0
60	7.1	-161	-2.3	153	-17	10	75	533	4.52E+05	0.00230	1306	20.1
59	7.1	-142	-2.6	160	-19	10	76	533	4.55E+05	0.00230	1307	30.0
58	6.6	-126	-2.3	155	-21	10	76	533	4.56E+05	0.00230	1308	40.1
111	14.6	-333	-3.9	257	-43	10	103	533	6.18E+05	0.00229	1309	0.0
108	14.1	-302	-4.0	264	-44	10	104	533	6.21E+05	0.00229	1310	10.0
104	13.1	-268	-3.7	263	-46	10	104	533	6.22E+05	0.00229	1311	19.8
101	12.8	-242	-4.0	268	-47	10	104	533	6.25E+05	0.00229	1312	30.0
98	12.6	-220	-3.8	264	-48	10	105	534	6.26E+05	0.00229	1313	40.1
35	5.0	-91	-1.6	113	-10	12	51	533	3.03E+05	0.00227	1435	0.0
35	5.1	-83	-1.5	106	-11	12	52	533	3.10E+05	0.00227	1436	10.1
34	4.8	-73	-1.4	108	-11	12	53	533	3.14E+05	0.00227	1437	20.1
33	4.4	-64	-1.3	107	-10	12	53	533	3.17E+05	0.00227	1438	30.1

256

32	4.2	-57	-1.2	108	-11	12	54	533	3.19E+05	0.00227	1439	39.9
71	11.2	-197	-2.2	215	-45	12	75	533	4.47E+05	0.00227	1440	0.0
69	11.2	-181	-1.9	205	-47	12	76	533	4.51E+05	0.00227	1441	10.0
69	11.2	-181	-1.9	205	-47	12	76	533	4.51E+05	0.00227	1442	19.9
65	10.3	-143	-1.7	207	-44	12	77	534	4.57E+05	0.00227	1443	29.9
64	9.6	-125	-1.8	215	-44	12	78	534	4.59E+05	0.00227	1444	39.9
120	19.1	-313	-0.5	283	-68	12	103	534	6.09E+05	0.00226	1445	0.0
118	19.0	-288	-0.3	281	-73	12	104	534	6.13E+05	0.00226	1446	10.0
115	17.9	-257	-0.6	272	-71	12	104	534	6.14E+05	0.00226	1447	20.0
113	17.5	-235	-0.5	273	-71	12	105	534	6.17E+05	0.00226	1448	30.2
111	17.4	-215	-0.2	271	-74	12	105	534	6.19E+05	0.00226	1449	40.1
37	4.9	-81	-0.9	65	6	14	50	530	3.06E+05	0.00231	1331	0.0
36	4.8	-66	-1.5	83	-3	14	52	530	3.16E+05	0.00231	1332	10.2
35	4.3	-59	-1.2	79	1	14	53	530	3.21E+05	0.00231	1333	19.9
35	4.0	-50	-0.8	75	3	14	53	530	3.24E+05	0.00231	1334	30.0
34	4.0	-41	-1.1	83	0	14	54	530	3.26E+05	0.00231	1335	40.1
72	10.8	-162	-1.9	165	-25	14	74	531	4.47E+05	0.00230	1336	0.0
68	11.1	-138	-2.9	179	-32	14	75	531	4.51E+05	0.00230	1337	10.0
69	10.0	-123	-2.2	175	-28	14	75	531	4.55E+05	0.00230	1338	20.0
68	9.6	-112	-1.8	169	-26	14	76	531	4.57E+05	0.00230	1339	30.0
67	9.1	-98	-1.6	166	-26	14	76	531	4.59E+05	0.00230	1340	40.0
126	18.4	-253	-2.2	293	-60	14	101	532	6.08E+05	0.00230	1341	0.0
123	18.0	-232	-2.2	290	-61	14	102	532	6.10E+05	0.00230	1342	10.0
122	17.2	-214	-1.5	286	-55	14	102	532	6.12E+05	0.00229	1343	20.0
120	17.4	-191	-1.8	283	-61	14	102	532	6.14E+05	0.00229	1344	30.1
117	17.2	-171	-1.6	280	-63	14	103	532	6.15E+05	0.00229	1345	40.1
39	5.6	-79	-0.9	76	-2	16	51	532	3.06E+05	0.00230	1346	0.0
40	5.2	-67	-0.7	79	-4	16	52	532	3.16E+05	0.00230	1347	10.0
39	5.0	-56	-0.9	87	-5	16	53	532	3.20E+05	0.00230	1348	19.9
38	4.7	-47	-0.6	83	-2	16	54	532	3.24E+05	0.00230	1349	30.0
38	4.5	-37	-0.6	86	-4	16	54	532	3.26E+05	0.00230	1350	39.9
77	10.5	-143	-1.1	168	-14	16	74	532	4.44E+05	0.00230	1351	0.0
76	10.2	-120	-1.4	173	-18	16	75	532	4.49E+05	0.00230	1352	10.1
76	10.1	-108	-1.1	168	-19	16	76	532	4.58E+05	0.00230	1353	20.1
74	9.7	-90	-1.2	182	-20	16	77	532	4.60E+05	0.00230	1354	29.9
73	9.4	-75	-1.5	183	-20	16	77	532	4.63E+05	0.00230	1355	39.9
136	18.2	-204	-0.9	290	-49	16	101	533	6.08E+05	0.00229	1356	0.0
133	18.8	-185	-1.2	287	-52	16	102	533	6.09E+05	0.00229	1357	9.8
133	18.8	-177	-1.4	294	-55	16	102	533	6.11E+05	0.00229	1358	20.1

257

131	17.9	-146	-0.9	282	-50	16	103	533	6.13E+05	0.00229	1359	30.0
129	17.6	-130	-1.0	290	-51	16	103	533	6.14E+05	0.00229	1360	40.0
40	6.6	-66	-0.9	45	12	18	49	532	2.95E+05	0.00230	1363	0.0
38	5.5	-47	-1.1	66	5	18	51	532	3.06E+05	0.00230	1364	10.0
37	5.4	-38	-1.4	74	4	18	51	532	3.10E+05	0.00230	1365	19.8
37	5.3	-29	-1.1	78	3	18	52	532	3.13E+05	0.00230	1366	29.8
37	4.7	-21	-1.1	78	4	18	53	532	3.16E+05	0.00230	1367	40.1
78	13.3	-123	-1.8	146	-18	18	73	532	4.42E+05	0.00230	1368	0.0
79	12.5	-110	-1.6	154	-20	18	74	532	4.47E+05	0.00230	1369	10.1
76	12.2	-90	-1.6	155	-20	18	75	533	4.50E+05	0.00230	1370	20.0
76	12.0	-76	-1.7	154	-19	18	75	533	4.53E+05	0.00230	1371	30.0
75	11.3	-59	-1.6	161	-20	18	76	533	4.56E+05	0.00230	1372	40.1
148	24.6	-207	-0.7	254	-57	18	103	533	6.13E+05	0.00229	1373	0.0
145	24.4	-185	-0.2	249	-57	18	103	535	6.14E+05	0.00228	1374	10.0
144	23.9	-163	-0.1	259	-60	18	104	535	6.16E+05	0.00228	1375	20.1
142	23.3	-137	0.0	247	-59	18	104	535	6.18E+05	0.00228	1376	30.2
140	22.5	-111	0.1	246	-59	18	104	535	6.20E+05	0.00228	1377	39.9
42	4.9	-62	0.2	67	12	20	51	534	3.04E+05	0.00229	1379	0.0
41	4.7	-53	0.2	66	10	20	52	534	3.12E+05	0.00229	1380	10.0
42	4.6	-38	0.0	76	9	20	53	534	3.17E+05	0.00229	1381	20.1
41	4.3	-30	-0.2	77	8	20	54	534	3.20E+05	0.00229	1382	28.8
40	4.0	-12	-0.6	94	3	20	54	534	3.23E+05	0.00229	1383	40.1
84	12.5	-122	0.6	197	-42	20	74	534	4.43E+05	0.00229	1384	0.0
85	12.5	-103	0.7	202	-45	20	75	534	4.48E+05	0.00229	1385	10.0
84	12.1	-88	0.8	203	-41	20	76	534	4.52E+05	0.00229	1386	20.0
83	11.5	-70	0.7	203	-41	20	76	534	4.55E+05	0.00229	1387	30.0
82	11.1	-57	0.7	201	-39	20	77	534	4.57E+05	0.00229	1388	40.2
148	23.0	-171	2.9	279	-71	20	100	535	5.96E+05	0.00229	1389	0.0
148	22.7	-157	3.0	269	-69	20	100	535	5.97E+05	0.00228	1390	10.2
146	22.0	-130	3.1	269	-70	20	101	535	6.00E+05	0.00228	1391	20.1
144	21.6	-116	3.4	259	-70	20	101	535	6.02E+05	0.00228	1392	30.0
142	21.0	-92	3.2	256	-70	20	101	535	6.03E+05	0.00228	1393	40.1

C.2 Experimental and Predicted Aerodynamic Coefficients

Table C. 2 Uncorrected, Wall-Corrected, and Predicted Aerodynamic Coefficients; Note, 'n/c' means 'not converged'

Angle of Attack (deg)	CDP (kPa)	Reynolds number *10^{-6}	Mach number	Lift coefficient , cl			Drag coefficient, cd			Moment coeff., cm$_{c/4}$		
				Uncorrected	Corrected	Xfoil	Uncorrected	Corrected	Xfoil	Uncorrected	Corrected	Xfoil
-6	0	1	0.047	0.99	0.69	n/c	0.178	0.151	n/c	-0.3	-0.23	n/c
-6	0	1.4	0.07	0.65	0.45	0.5	0.095	0.081	0.009	-0.23	-0.19	-0.22
-6	0	1.9	0.096	0.36	0.25	n/c	0.095	0.081	n/c	-0.2	-0.17	n/c
-6	10	1	0.048	0.82	0.57	0.25	0.16	0.137	0.023	-0.26	-0.21	-0.16
-6	10	1.4	0.071	0.57	0.39	n/c	0.091	0.077	n/c	-0.21	-0.17	n/c
-6	10	1.9	0.096	0.28	0.19	0.04	0.092	0.078	0.007	-0.18	-0.15	-0.16
-6	20	1	0.048	0.69	0.48	n/c	0.137	0.117	n/c	-0.23	-0.18	n/c
-6	20	1.4	0.071	0.46	0.32	n/c	0.083	0.071	n/c	-0.19	-0.15	n/c
-6	20	1.9	0.096	0.2	0.14	-0.12	0.086	0.073	0.007	-0.16	-0.14	-0.14
-6	30	1	0.048	0.59	0.41	-0.07	0.14	0.119	0.014	-0.21	-0.17	-0.11
-6	30	1.4	0.071	0.37	0.26	-0.06	0.078	0.066	0.008	-0.16	-0.13	-0.13
-6	30	1.9	0.096	0.14	0.1	-0.17	0.078	0.066	0.007	-0.14	-0.12	-0.12
-6	40	1	0.048	0.52	0.36	n/c	0.115	0.098	n/c	-0.19	-0.15	n/c
-6	40	1.5	0.072	0.31	0.22	-0.08	0.084	0.071	0.008	-0.15	-0.12	-0.13
-6	40	1.9	0.096	0.09	0.06	-0.24	0.072	0.061	0.008	-0.12	-0.11	-0.11
-4	0	1	0.048	1.03	0.71	n/c	0.196	0.167	n/c	-0.28	-0.22	n/c
-4	0	1.5	0.071	0.8	0.56	0.77	0.107	0.091	0.007	-0.22	-0.17	-0.22
-4	0	2	0.095	0.53	0.37	0.16	0.097	0.083	0.008	-0.19	-0.15	-0.12
-4	10	1	0.049	0.81	0.57	n/c	0.166	0.141	n/c	-0.25	-0.19	n/c
-4	10	1.5	0.071	0.67	0.47	0.58	0.094	0.08	0.006	-0.2	-0.15	-0.19
-4	10	2	0.095	0.44	0.31	-0.1	0.087	0.074	0.01	-0.17	-0.13	-0.08
-4	20	1	0.049	0.71	0.49	n/c	0.151	0.129	n/c	-0.22	-0.17	n/c
-4	20	1.5	0.072	0.58	0.4	0.28	0.09	0.077	0.007	-0.18	-0.14	-0.14
-4	20	2	0.095	0.37	0.26	-0.12	0.081	0.069	0.009	-0.15	-0.12	-0.07
-4	30	1	0.049	0.58	0.4	0	0.14	0.119	NaN	-0.19	-0.15	0
-4	30	1.5	0.072	0.49	0.34	0.22	0.08	0.068	0.006	-0.15	-0.12	-0.13
-4	30	2	0.096	0.28	0.2	-0.15	0.074	0.063	0.008	-0.13	-0.1	-0.07
-4	40	1	0.049	0.54	0.38	0.3	0.134	0.114	0.007	-0.17	-0.14	-0.15
-4	40	1.5	0.072	0.41	0.29	0.07	0.081	0.069	0.006	-0.14	-0.11	-0.11
-4	40	2	0.096	0.24	0.17	-0.14	0.071	0.06	0.007	-0.11	-0.09	-0.08
-2	0	1	0.048	1.16	0.81	0.98	0.188	0.16	0.035	-0.27	-0.2	-0.19
-2	0	1.5	0.071	0.94	0.65	0.65	0.084	0.072	0.014	-0.21	-0.15	-0.14
-2	0	2	0.096	0.59	0.41	0.46	0.094	0.08	0.016	-0.17	-0.13	-0.12

259

-2	10	1	0.049	0.97	0.67	n/c	0.158	0.135	n/c	-0.23	-0.17	n/c
-2	10	1.5	0.071	0.8	0.56	0.46	0.079	0.068	0.01	-0.18	-0.13	-0.11
-2	10	2	0.096	0.55	0.38	0.22	0.095	0.081	0.008	-0.16	-0.12	-0.09
-2	20	1	0.05	0.84	0.59	n/c	0.14	0.12	n/c	-0.2	-0.15	n/c
-2	20	1.5	0.071	0.72	0.5	0.5	0.069	0.059	0.009	-0.16	-0.12	-0.13
-2	20	2	0.096	0.48	0.33	0.22	0.079	0.067	0.007	-0.14	-0.11	-0.1
-2	30	1	0.05	0.73	0.51	0.45	0.123	0.105	0.008	-0.18	-0.14	-0.12
-2	30	1.5	0.072	0.63	0.44	0.26	0.069	0.059	0.007	-0.15	-0.11	-0.08
-2	30	2	0.097	0.44	0.31	0.13	0.072	0.061	0.007	-0.12	-0.1	-0.07
-2	40	1	0.05	0.67	0.46	0.38	0.114	0.097	0.007	-0.16	-0.12	-0.11
-2	40	1.5	0.072	0.56	0.39	0.19	0.079	0.068	0.007	-0.13	-0.1	-0.08
-2	40	2	0.096	0.4	0.28	0.03	0.065	0.055	0.006	-0.11	-0.08	-0.05
0	0	1	0.049	1.22	0.85	n/c	0.165	0.141	n/c	-0.23	-0.17	n/c
0	0	1.5	0.071	1.05	0.73	1.01	0.116	0.099	0.018	-0.2	-0.14	-0.17
0	0	2	0.095	0.77	0.54	0.53	0.102	0.087	0.01	-0.16	-0.12	-0.09
0	10	1	0.05	1.07	0.74	0.86	0.139	0.118	0.017	-0.2	-0.15	-0.12
0	10	1.5	0.071	0.9	0.62	0.7	0.094	0.08	0.01	-0.17	-0.12	-0.11
0	10	2	0.096	0.72	0.5	0.49	0.094	0.08	0.009	-0.15	-0.11	-0.09
0	20	1	0.051	0.94	0.66	0.67	0.124	0.106	0.011	-0.18	-0.13	-0.1
0	20	1.5	0.072	0.83	0.58	0.68	0.086	0.073	0.009	-0.15	-0.11	-0.11
0	20	2	0.096	0.65	0.45	0.41	0.091	0.077	0.007	-0.13	-0.09	-0.08
0	30	1.1	0.051	0.84	0.58	0.56	0.114	0.097	0.009	-0.16	-0.11	-0.08
0	30	1.5	0.072	0.76	0.53	0.45	0.079	0.068	0.008	-0.14	-0.1	-0.07
0	30	2	0.096	0.59	0.41	0.3	0.083	0.071	0.006	-0.11	-0.08	-0.05
0	40	1.1	0.051	0.76	0.53	0.45	0.107	0.091	0.008	-0.14	-0.1	-0.07
0	40	1.5	0.072	0.69	0.48	0.38	0.08	0.068	0.007	-0.12	-0.09	-0.06
0	40	2	0.096	0.54	0.37	0.17	0.076	0.065	0.006	-0.1	-0.07	-0.03
2	0	1	0.047	1.33	0.93	1.39	0.197	0.168	0.037	-0.23	-0.16	-0.17
2	0	1.4	0.069	1.14	0.79	1.51	0.12	0.102	0.033	-0.18	-0.12	-0.22
2	0	2	0.095	0.86	0.6	0.88	0.119	0.101	0.011	-0.15	-0.11	-0.12
2	10	1	0.048	1.11	0.77	1.12	0.176	0.15	0.022	-0.19	-0.14	-0.13
2	10	1.4	0.069	1.04	0.72	0.89	0.124	0.106	0.013	-0.17	-0.11	-0.09
2	10	2	0.095	0.81	0.57	0.66	0.114	0.097	0.009	-0.14	-0.1	-0.07
2	20	1	0.049	0.98	0.68	0.97	0.153	0.13	0.014	-0.17	-0.12	-0.11
2	20	1.4	0.07	0.95	0.66	0.81	0.118	0.101	0.011	-0.15	-0.1	-0.08
2	20	2	0.095	0.76	0.53	0.78	0.109	0.093	0.009	-0.13	-0.09	-0.11
2	30	1	0.049	0.94	0.66	0.8	0.124	0.106	0.011	-0.15	-0.1	-0.08
2	30	1.4	0.07	0.89	0.62	0.65	0.117	0.099	0.009	-0.14	-0.1	-0.06
2	30	2	0.096	0.71	0.49	0.56	0.1	0.086	0.007	-0.11	-0.08	-0.06
2	40	1	0.049	0.88	0.61	0.75	0.121	0.103	0.01	-0.14	-0.09	-0.07
2	40	1.4	0.07	0.85	0.59	0.74	0.109	0.093	0.008	-0.13	-0.09	-0.08
2	40	2	0.096	0.66	0.46	0.46	0.098	0.083	0.006	-0.1	-0.07	-0.04
4	0	1	0.046	1.39	0.96	1.58	0.217	0.185	0.04	-0.21	-0.14	-0.16
4	0	1.4	0.069	1.22	0.85	1.25	0.136	0.116	0.02	-0.17	-0.11	-0.11
4	0	2	0.096	0.98	0.68	0.95	0.123	0.104	0.012	-0.15	-0.1	-0.08
4	10	1	0.047	1.22	0.85	1.32	0.205	0.174	0.025	-0.18	-0.12	-0.12
4	10	1.4	0.07	1.1	0.77	1.16	0.138	0.118	0.016	-0.15	-0.1	-0.1
4	10	2	0.096	0.89	0.62	0.89	0.122	0.104	0.01	-0.13	-0.08	-0.07

4	20	1	0.047	1.26	0.88	n/c	0.119	0.101	n/c	-0.17	-0.11	n/c
4	20	1.4	0.07	1.07	0.75	1.11	0.123	0.104	0.014	-0.14	-0.09	-0.1
4	20	2	0.096	0.86	0.6	0.89	0.105	0.09	0.01	-0.12	-0.08	-0.07
4	30	1	0.048	1.11	0.77	1.11	0.129	0.11	0.015	-0.15	-0.09	-0.09
4	30	1.5	0.07	0.97	0.67	1.02	0.13	0.11	0.011	-0.13	-0.08	-0.09
4	30	2	0.096	0.81	0.56	0.9	0.107	0.091	0.009	-0.11	-0.07	-0.08
4	40	1	0.048	1.01	0.7	1.1	0.12	0.102	0.014	-0.13	-0.08	-0.09
4	40	1.5	0.071	0.94	0.66	0.95	0.119	0.101	0.01	-0.12	-0.07	-0.08
4	40	2	0.097	0.76	0.53	0.9	0.108	0.092	0.009	-0.1	-0.06	-0.08
6	0	0.9	0.047	1.55	1.08	1.65	0.213	0.181	0.043	-0.19	-0.11	-0.13
6	0	1.4	0.07	1.38	0.96	1.75	0.179	0.153	0.037	-0.17	-0.1	-0.17
6	0	1.9	0.095	1.12	0.78	1.17	0.168	0.143	0.015	-0.14	-0.09	-0.07
6	10	1	0.048	1.41	0.98	1.55	0.197	0.167	0.031	-0.17	-0.1	-0.12
6	10	1.4	0.07	1.27	0.88	1.39	0.184	0.157	0.02	-0.15	-0.09	-0.1
6	10	1.9	0.095	1.09	0.76	1.17	0.161	0.137	0.014	-0.13	-0.08	-0.07
6	20	1	0.048	1.31	0.91	1.41	0.161	0.137	0.023	-0.15	-0.08	-0.1
6	20	1.4	0.071	1.18	0.82	1.28	0.168	0.143	0.016	-0.13	-0.08	-0.09
6	20	1.9	0.095	1.03	0.72	1.06	0.15	0.128	0.012	-0.12	-0.07	-0.06
6	30	1	0.049	1.24	0.86	1.3	0.135	0.115	0.019	-0.13	-0.07	-0.08
6	30	1.4	0.071	1.13	0.79	1.22	0.161	0.137	0.015	-0.12	-0.07	-0.08
6	30	1.9	0.095	0.98	0.68	1.09	0.146	0.124	0.012	-0.11	-0.06	-0.07
6	40	1	0.049	1.2	0.83	1.13	0.116	0.099	0.014	-0.12	-0.06	-0.06
6	40	1.4	0.071	1.1	0.77	1.15	0.151	0.129	0.014	-0.11	-0.06	-0.07
6	40	1.9	0.095	0.93	0.65	1.11	0.141	0.12	0.012	-0.1	-0.06	-0.07
8	0	1	0.047	1.53	1.06	1.83	0.228	0.194	0.054	-0.17	-0.1	-0.13
8	0	1.4	0.068	1.47	1.02	1.58	0.157	0.134	0.029	-0.15	-0.08	-0.08
8	0	1.9	0.094	1.23	0.85	1.44	0.132	0.112	0.019	-0.11	-0.06	-0.08
8	10	1	0.048	1.46	1.02	1.58	0.188	0.16	0.034	-0.15	-0.08	-0.08
8	10	1.4	0.069	1.35	0.94	1.55	0.159	0.135	0.024	-0.13	-0.07	-0.09
8	10	1.9	0.094	1.2	0.83	1.4	0.128	0.109	0.017	-0.11	-0.06	-0.07
8	20	1	0.049	1.43	0.99	1.53	0.162	0.138	0.027	-0.14	-0.07	-0.08
8	20	1.4	0.07	1.27	0.89	1.45	0.157	0.133	0.02	-0.12	-0.06	-0.07
8	20	1.9	0.094	1.14	0.8	1.37	0.121	0.104	0.016	-0.1	-0.05	-0.07
8	30	1	0.049	1.25	0.87	1.65	0.188	0.161	0.03	-0.11	-0.06	-0.11
8	30	1.4	0.07	1.24	0.86	1.4	0.143	0.122	0.018	-0.1	-0.05	-0.06
8	30	1.9	0.095	1.1	0.76	1.31	0.114	0.097	0.015	-0.08	-0.04	-0.06
8	40	1	0.05	1.24	0.86	1.38	0.141	0.12	0.02	-0.11	-0.05	-0.06
8	40	1.4	0.07	1.2	0.83	1.33	0.131	0.112	0.017	-0.09	-0.04	-0.05
8	40	1.9	0.095	1.06	0.74	1.24	0.111	0.094	0.014	-0.08	-0.03	-0.04
10	0	0.9	0.046	1.72	1.2	1.8	0.219	0.187	0.069	-0.15	-0.08	-0.09
10	0	1.4	0.068	1.54	1.07	1.79	0.191	0.163	0.044	-0.13	-0.06	-0.09
10	0	2	0.096	1.38	0.96	1.62	0.183	0.156	0.024	-0.12	-0.05	-0.07
10	10	1	0.047	1.6	1.12	1.74	0.21	0.178	0.047	-0.14	-0.07	-0.08
10	10	1.4	0.069	1.49	1.03	1.65	0.179	0.152	0.03	-0.12	-0.05	-0.06
10	10	2	0.096	1.33	0.92	1.43	0.174	0.148	0.02	-0.1	-0.05	-0.03
10	20	1	0.048	1.49	1.04	1.64	0.192	0.164	0.037	-0.12	-0.06	-0.06
10	20	1.4	0.07	1.41	0.98	1.58	0.168	0.143	0.026	-0.1	-0.04	-0.05
10	20	2	0.096	1.28	0.89	1.34	0.161	0.137	0.019	-0.09	-0.04	-0.01

10	30	1	0.048	1.48	1.03	1.57	0.166	0.141	0.031	-0.11	-0.05	-0.05
10	30	1.4	0.07	1.36	0.94	1.54	0.165	0.14	0.024	-0.09	-0.03	-0.05
10	30	2	0.097	1.23	0.86	1.48	0.156	0.133	0.019	-0.08	-0.03	-0.04
10	40	1	0.048	1.41	0.98	1.5	0.161	0.137	0.027	-0.1	-0.04	-0.04
10	40	1.4	0.07	1.33	0.92	1.49	0.153	0.13	0.022	-0.08	-0.03	-0.04
10	40	2	0.097	1.19	0.83	1.4	0.152	0.13	0.018	-0.07	-0.02	-0.03
12	0	1	0.047	1.8	1.26	1.99	0.258	0.22	0.127	-0.13	-0.05	-0.14
12	0	1.4	0.07	1.7	1.18	1.79	0.267	0.228	0.054	-0.13	-0.06	-0.06
12	0	1.9	0.095	1.53	1.06	1.67	0.243	0.207	0.031	-0.11	-0.04	-0.04
12	10	1	0.048	1.71	1.19	1.74	0.253	0.216	0.066	-0.11	-0.04	-0.06
12	10	1.4	0.07	1.6	1.11	1.72	0.26	0.222	0.042	-0.12	-0.05	-0.04
12	10	1.9	0.096	1.46	1.02	1.53	0.237	0.202	0.026	-0.1	-0.04	-0.01
12	20	1	0.049	1.6	1.12	1.65	0.229	0.195	0.049	-0.1	-0.03	-0.03
12	20	1.4	0.07	1.6	1.11	1.65	0.26	0.222	0.034	-0.12	-0.05	-0.03
12	20	1.9	0.096	1.43	0.99	1.48	0.223	0.19	0.025	-0.09	-0.03	0
12	30	1	0.049	1.56	1.08	1.62	0.21	0.179	0.042	-0.09	-0.02	-0.03
12	30	1.4	0.071	1.47	1.03	1.61	0.233	0.199	0.031	-0.09	-0.03	-0.02
12	30	2	0.097	1.38	0.96	1.51	0.214	0.182	0.022	-0.08	-0.02	-0.01
12	40	1	0.05	1.47	1.02	1.56	0.193	0.165	0.036	-0.07	-0.01	-0.01
12	40	1.5	0.072	1.41	0.98	1.57	0.212	0.18	0.028	-0.08	-0.02	-0.02
12	40	2	0.097	1.35	0.94	1.64	0.213	0.181	0.026	-0.07	-0.02	-0.04
14	0	1	0.046	1.93	1.35	1.83	0.258	0.22	0.166	-0.12	-0.04	-0.14
14	0	1.4	0.069	1.74	1.21	1.71	0.261	0.222	0.085	-0.11	-0.04	-0.05
14	0	1.9	0.094	1.63	1.13	n/c	0.239	0.203	n/c	-0.09	-0.02	n/c
14	10	1	0.048	1.76	1.22	1.71	0.234	0.199	0.107	-0.09	-0.02	-0.07
14	10	1.4	0.07	1.61	1.12	1.71	0.261	0.223	0.066	-0.09	-0.02	-0.03
14	10	1.9	0.095	1.57	1.09	1.67	0.229	0.195	0.043	-0.08	-0.02	-0.01
14	20	1	0.049	1.65	1.15	1.65	0.202	0.172	0.077	-0.08	-0.01	-0.03
14	20	1.4	0.07	1.62	1.13	1.68	0.235	0.201	0.055	-0.08	-0.01	-0.02
14	20	1.9	0.095	1.56	1.08	1.65	0.22	0.187	0.041	-0.08	-0.01	-0.01
14	30	1	0.049	1.63	1.13	1.6	0.188	0.16	0.069	-0.07	0	-0.02
14	30	1.4	0.071	1.56	1.08	1.64	0.22	0.187	0.046	-0.07	-0.01	-0.01
14	30	1.9	0.095	1.53	1.06	1.64	0.222	0.189	0.038	-0.07	-0.01	0
14	40	1	0.05	1.53	1.06	1.58	0.181	0.154	0.058	-0.05	0.01	-0.01
14	40	1.4	0.071	1.54	1.07	1.55	0.209	0.178	0.039	-0.06	0	0.01
14	40	1.9	0.096	1.47	1.02	1.66	0.216	0.184	0.039	-0.06	0	-0.01
16	0	1	0.047	2	1.39	1.62	0.285	0.243	0.188	-0.11	-0.03	-0.13
16	0	1.4	0.069	1.87	1.3	1.62	0.254	0.216	0.124	-0.1	-0.02	-0.06
16	0	1.9	0.094	1.77	1.23	1.63	0.237	0.202	0.085	-0.07	0	-0.03
16	10	1	0.048	1.93	1.35	1.6	0.255	0.217	0.155	-0.09	-0.01	-0.1
16	10	1.4	0.07	1.78	1.24	1.59	0.24	0.205	0.108	-0.08	-0.01	-0.04
16	10	1.9	0.095	1.7	1.19	1.62	0.24	0.205	0.078	-0.07	0	-0.02
16	20	1	0.049	1.82	1.27	1.52	0.236	0.201	0.126	-0.07	0	-0.05
16	20	1.4	0.071	1.74	1.21	1.56	0.231	0.197	0.097	-0.07	0	-0.03
16	20	1.9	0.095	1.7	1.18	1.6	0.24	0.205	0.074	-0.06	0	-0.01
16	30	1	0.05	1.73	1.2	1.51	0.213	0.182	0.108	-0.06	0.01	-0.03
16	30	1.5	0.071	1.66	1.15	1.57	0.217	0.185	0.08	-0.06	0.01	-0.01
16	30	1.9	0.095	1.64	1.14	1.56	0.224	0.191	0.066	-0.05	0.01	0

262

16	40	1	0.05	1.72	1.19	1.49	0.204	0.174	0.102	-0.05	0.02	-0.02
16	40	1.5	0.071	1.63	1.14	1.57	0.21	0.179	0.08	-0.05	0.02	-0.02
16	40	1.9	0.095	1.61	1.12	1.58	0.221	0.188	0.069	-0.05	0.02	-0.01
18	0	0.9	0.045	2.18	1.52	1.52	0.364	0.31	0.263	-0.1	-0.01	-0.21
18	0	1.4	0.068	1.94	1.35	1.48	0.33	0.281	0.181	-0.09	-0.01	-0.1
18	0	1.9	0.095	1.85	1.29	1.4	0.308	0.263	0.125	-0.07	0	-0.02
18	10	1	0.047	1.93	1.34	1.37	0.28	0.238	0.202	-0.07	0.01	-0.1
18	10	1.4	0.069	1.9	1.32	1.47	0.302	0.257	0.171	-0.07	0	-0.09
18	10	1.9	0.095	1.83	1.27	1.39	0.307	0.262	0.139	-0.06	0.01	-0.04
18	20	1	0.047	1.89	1.32	1.4	0.275	0.234	0.194	-0.05	0.02	-0.11
18	20	1.4	0.07	1.79	1.25	1.42	0.287	0.245	0.149	-0.06	0.01	-0.05
18	20	2	0.096	1.78	1.24	1.38	0.295	0.251	0.105	-0.06	0.01	0.01
18	30	1	0.048	1.81	1.26	1.34	0.259	0.221	0.172	-0.04	0.03	-0.07
18	30	1.4	0.07	1.78	1.24	1.42	0.282	0.241	0.136	-0.05	0.02	-0.04
18	30	2	0.096	1.75	1.22	1.38	0.288	0.245	0.109	-0.05	0.02	0
18	40	1	0.049	1.75	1.22	1.37	0.221	0.189	0.167	-0.03	0.04	-0.07
18	40	1.4	0.07	1.72	1.19	1.4	0.259	0.221	0.123	-0.04	0.03	-0.02
18	40	2	0.096	1.73	1.2	1.36	0.278	0.237	0.098	-0.04	0.03	0.01
20	0	1	0.047	2.16	1.5	n/c	0.25	0.213	n/c	-0.09	0	n/c
20	0	1.4	0.069	2.04	1.42	1.33	0.304	0.259	0.241	-0.08	0	-0.14
20	0	1.9	0.093	1.96	1.37	1.31	0.306	0.261	0.21	-0.06	0.01	-0.11
20	10	1	0.048	2.03	1.41	1.43	0.231	0.197	0.277	-0.07	0.01	-0.2
20	10	1.4	0.069	2.01	1.4	1.24	0.295	0.252	0.218	-0.07	0.01	-0.09
20	10	1.9	0.093	1.98	1.37	1.28	0.303	0.258	0.2	-0.06	0.02	-0.09
20	20	1	0.049	1.98	1.38	1.29	0.218	0.185	0.239	-0.05	0.03	-0.13
20	20	1.4	0.07	1.93	1.34	1.35	0.279	0.237	0.229	-0.06	0.02	-0.14
20	20	1.9	0.093	1.91	1.33	1.25	0.288	0.245	0.184	-0.05	0.03	-0.06
20	29	1	0.05	1.86	1.29	1.26	0.196	0.167	0.224	-0.04	0.03	-0.11
20	30	1.4	0.07	1.92	1.34	1.25	0.265	0.226	0.195	-0.04	0.03	-0.07
20	30	1.9	0.093	1.88	1.31	1.2	0.283	0.241	0.177	-0.04	0.03	-0.04
20	40	1	0.05	1.83	1.27	1.21	0.182	0.155	0.21	-0.01	0.05	-0.08
20	40	1.5	0.071	1.85	1.29	1.24	0.249	0.212	0.192	-0.04	0.03	-0.07
20	40	1.9	0.093	1.86	1.29	1.16	0.275	0.234	0.167	-0.03	0.04	-0.02

APPENDIX D MANUFACTURING TECHNIQUES FOR PRESSURE ADAPTIVE HONEYCOMB

D.1 Manufacturing Honeycomb from Aluminum Sheets
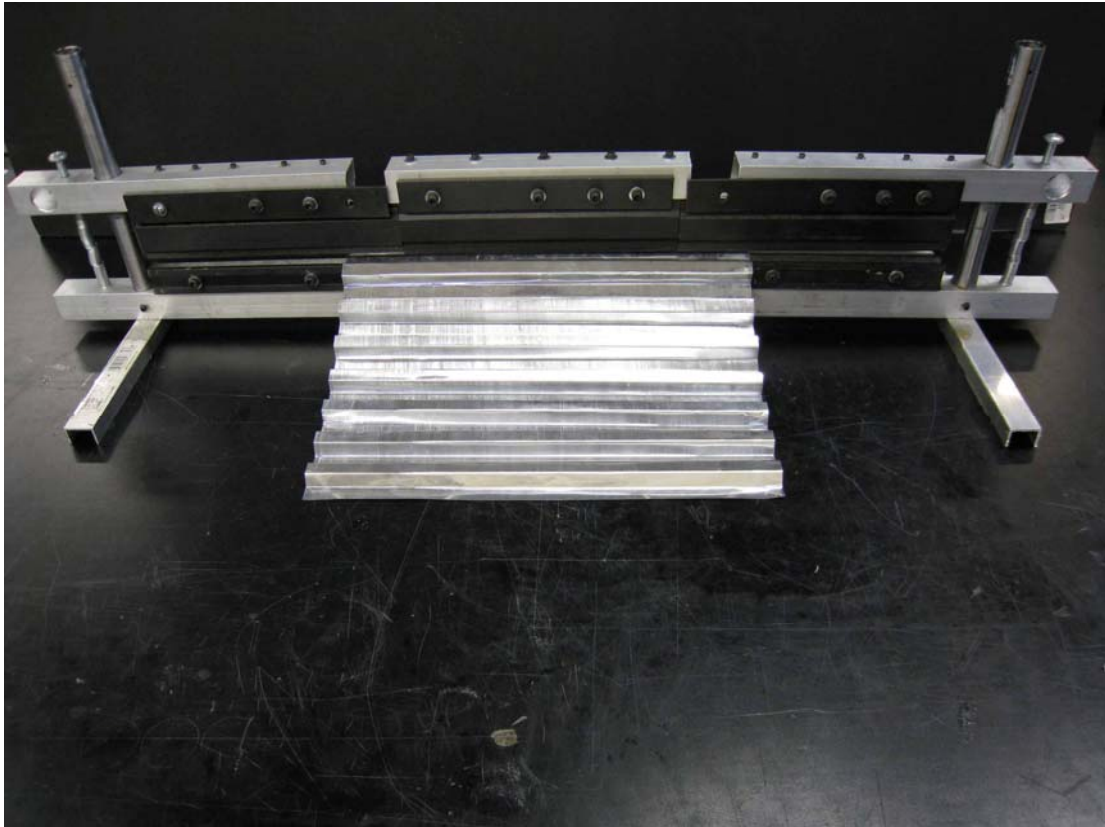
Figure D. 1   A press break is used to induce folds into the aluminum sheet.
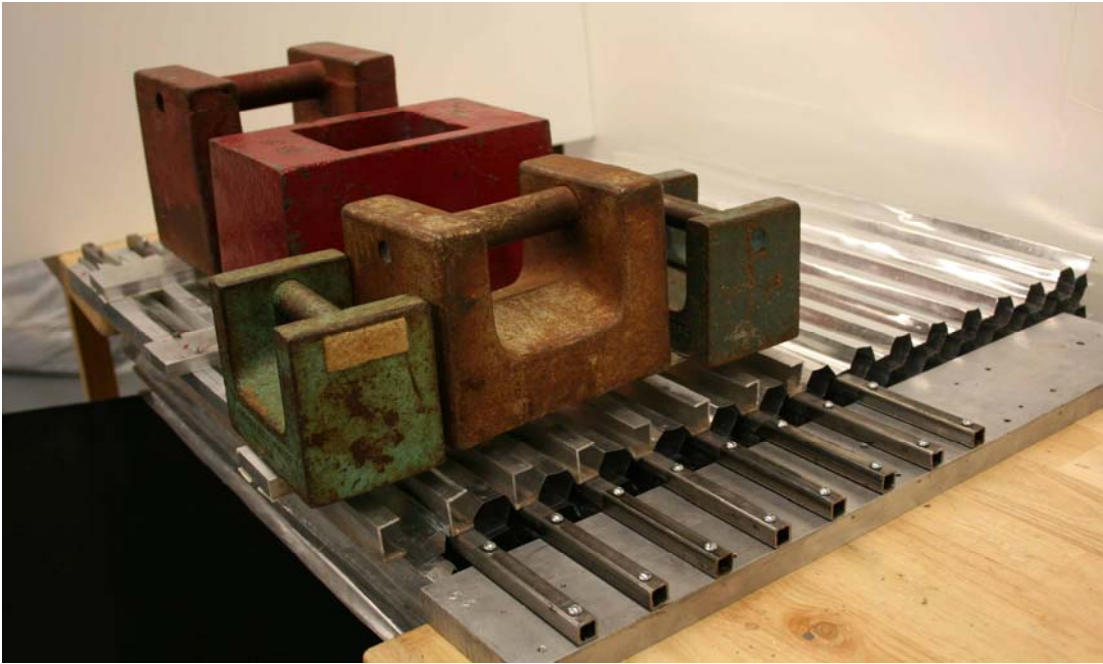
Figure D. 2The corrugated sheets are bonded together using a steel frame and 660N of applied weight

D.2 Manufacturing Pouches

Figure D. 3 A brass tube is pierced through the plastic

Figure D. 4 Brass tube pulled through the plastic

Figure D. 5 Duct tape patches applied on the inside of the pouch

Figure D. 6 Duct tape patches applied on the outside of the pouch

Figure D. 7 Air tight connection between brass tube and plastic
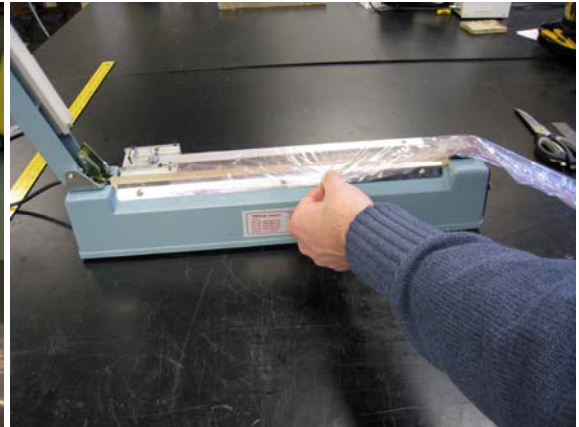
Figure D. 8 Plastic is positioned in heat sealer
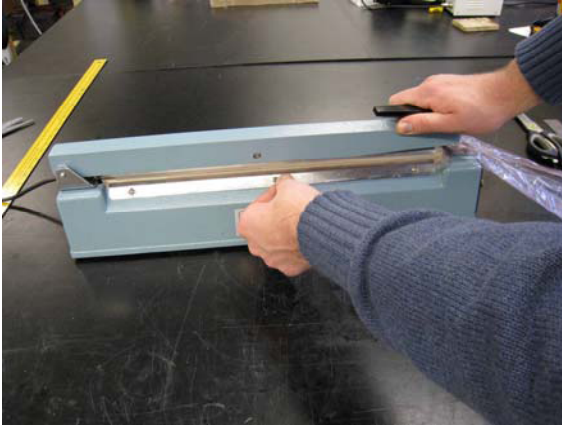
Figure D. 9 Heat sealer is closed to melt the two sides together
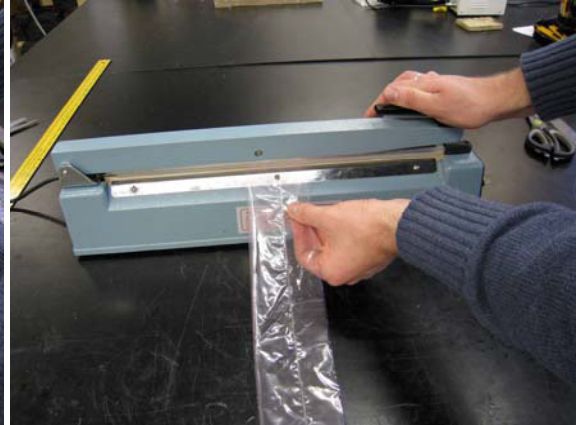
Figure D. 10 Either edge is sealed

Figure D. 11 45 degree angles are introduced between the seams

Figure D. 12 The pouch is trimmed

267